Sensitivity enhancement of the CUORE experiment via the development of Cherenkov hybrid TeO bolometers

Valentina Novati

université PARIS-SACLAY

NNT: 2018SACLS412

Thèse de doctorat

Sensitivity enhancement of the CUORE experiment via the development of Cherenkov hybrid TeO_2 bolometers

Thèse de doctorat de l'Université Paris-Saclay
préparée à l'Université Paris-Sud au sein du
Centre des Sciences Nucléaires et de
Sciences de la Matière (CSNSM)

École doctorale n^o 576
Particles, Hadrons, Energy, Nuclei, Instrumentation,
Imaging, Cosmos et Simulation (PHENIICS)
Spécialité de doctorat: Physique des particules.

Thèse présentée et soutenue à Orsay, le 21 Novembre 2018, par

Valentina Novati

Composition du Jury:

M. Jacques Dumarchez Directeur de Recherche, Université Paris-Sorbonne (LPNHE)	Président et Rapporteur
M. Juan José Gómez Cadenas Professeur, Universitat de València (IFIC)	Rapporteur
Mme. Maryvonne De Jésus Chargee de recherche, Université Claude Bernard (IPNL)	Examinatrice
Mme. Claire Marrache-Kikuchi Maitre de Conferences, Université Paris-Saclay (CSNSM)	Examinatrice
Mme. Christine Marquet Chargée de Recherche, Université de Bordeaux (CENBG)	Examinatrice
M. Emiliano Olivieri Ingénieur de Recherche, Université Paris-Saclay (CSNSM)	Examinateur
M. Andrea Giuliani Directeur de Recherche, Université Paris-Saclay (CSNSM)	Directeur de thèse

Résumé

CUORE (*Cryogenic Underground Observatory for Rare Events*) cherche à mettre en évidence la désintégration double bêta sans neutrino du ^{130}Te. Cette hypothétique transition nucléaire n'a jamais été observée et sa découverte aurait des conséquences décisives sur la scène actuelle de la physique fondamentale. D'abord elle permettrait de déterminer l'échelle de masse du neutrino. Par ailleurs, ce processus révèlerait la nature des neutrinos (s'ils sont des particules de Dirac ou de Majorana) : en effet l'existence de la désintégration double bêta sans neutrino nécessite que le neutrino soit sa propre antiparticule (c'est-à-dire qu'il s'agirait alors d'une particule de Majorana). De plus, ce serait la première découverte d'un phénomène physique qui ne conserve pas le nombre de leptons. Un processus créant des leptons — comme la désintégration double bêta sans neutrino — donnerait un fort crédit à la théorie de la leptogénèse, qui essaye de rendre compte de l'asymétrie entre matière et antimatière observée dans l'Univers.

La signature de cette désintégration est un pic à la Q-valeur de la réaction, qui dans le cas du ^{130}Te — l'isotope étudié par l'expérience CUORE — correspond à une energie de 2527 keV. Le ^{130}Te a une abondance isotopique d'environ 34% — correspondant au plus haut taux parmi les candidats à la désintégration double bêta sans neutrino — ce qui permet à CUORE d'être compétitif sur la scène internationale même avec l'utilisation de cristaux non enrichis. Les bolomètres — des détecteurs cryogéniques fonctionnant à des températures de l'ordre de 10 mK — sont utilisés pour détecter la désintégration double bêta sans neutrino par l'expérience CUORE. Ce choix a été fait en raison de la haute résolution de ces détecteurs (de l'ordre de 0,2% FWHM à 2.6 MeV), indispensable pour identifier le pic correspondant au signal attendu. Les bolomètres sont des détecteurs calorimétriques constitués d'un absorbeur, dans le cas de l'expérience CUORE, faits de TeO_2. Lorsqu'il y a un événement dans l'absorbeur, sa température augmente proportionellement à l'energie deposée et est mesurée avec un capteur de température. Dans l'expérience CUORE, ces capteurs sont des thermistance de germanium "Neutron Transmutation Doped" (NTD-Ge) : des senseurs en germanium dopé au moyen d'une irradiation de neutrons dans un réacteur nucléaire. L'expérience CUORE est la première

expérience à l'échelle d'une tonne qui utilise des bolomètres pour une masse totale de 742 kg de TeO_2. L'expérience CUORE a débuté en 2017 et est en cours d'acquisition de données dans les laboratoires nationaux du Gran Sasso. Cette expérience a fixé la limite la plus stricte sur la demi-vie de la double désintégration bêta sans neutrino du ^{130}Te : $1.5{\times}10^{25}$ années. Également, pour la première fois, CUORE a démontré la faisabilité de la mise en oeuvre de 988 bolomètres.

L'amélioration de la sensibilité de CUORE a été considerés dans le cadre de plusieurs R&D en vue de l'expérience qui lui succédera : CUPID (*CUORE Upgrade with Particle IDentification*). L'amélioration de la sensibilité de CUORE sera atteinte en agissant sur deux fronts principaux dans le programme de CUPID : l'augmentation du nombre de noyaux candidats à la désintégration double bêta sans neutrino et la réduction du fond. Actuellement, le fond dominant de l'expérience CUORE est dû à des particules α émises par des contaminations en surface, avec une énergie dégradée similaire à celle de la transition recherchée. Le fonds α contribue pour environ 10^{-2} counts/(keV kg yr) dans la région proche du signal. Un fond de 10^{-4} counts/(keV kg yr) sera requis afin de couvrir complètement l'échelle de masses des neutrinos dans la hiérarchie inversée (qui représente le but des expériences de nouvelle génération) dans l'expérience proposée CUPID.

L'expérience CUPID a envisagé différentes options pour le rejet du fond α. Une possibilité consiste à utiliser le même absorbeur utilisé par l'expérience CUORE : les cristaux de TeO_2. Ce matériau est bien connu et a démontré une performance particulièrement intŕessante. De plus, la haute abondance isotopique du ^{130}Te nécessiterait des coûts d'enrichissement moins élevés. Une autre possibilité est de changer d'isotope. Différentes options ont été étudiées dans le cadre de l'expérience CUPID : ^{82}Se incorporé dans du $Zn^{82}Se$, ^{100}Mo avec des cristaux de $Zn^{100}MoO_4$ et $Li_2{}^{100}MoO_4$ et du ^{116}Cd dans des cristaux de $^{116}CdWO_4$. Ces isotopes ont une Q-valeur supérieure à 2,6 MeV — correspondant au point final du fond naturel γ — qui leur permet d'atteindre des niveaux de fond plus faibles avec moins d'efforts. De plus, avec ces matériaux, le fond α est rejeté grâce aux propriétés de scintillation des cristaux qui ont un rendement lumineux différent entre les événements $\beta(\gamma)$ et α.

Ce travail a été consacré à l'option TeO_2 avec deux approches différentes : la réduction du fond α et l'étude du modèle thermique. Concernant la problématique du fond, la lumière due à la scintillantion dans cristaux de TeO_2 ne suffit pas pour séparer les signaux du fond. Dans la première partie de ce travail, on étudie la possibilité de détecter la faible lumière Cherenkov émise par les cristaux de TeO_2 pour rejeter les événements α. La lumière Cherenkov est émise seulement lors d'événements $\beta(\gamma)$ — notre signal — mais pas par les événements α. En effet, le signal recherché, ayant une énergie de

2527 keV, dépasse le seuil pour la production de lumière Cherenkov (50 keV pour des électrons) alors que les particules α avec la même énergie doivent surmonter une énergie plus élevée (400 MeV). Le défi consiste dans la détection d'un signal Cherenkov lumineux qui, une fois émis en correspondance d'un événement dans le bolomètre principal, dépose 100 eV dans un détecteur de lumière avec un NTD-Ge comme senseur. Ces détecteurs de lumière sont caractérisés généralement par un bruit sur ligne de base de l'ordre de 100 eV et peuvent atteindre 50 eV dans les meilleurs cas. Cette question a été résolue avec l'emploi de l'effet Neganov-Trofimov-Luke pour abaisser le seuil d'énergie du détecteur de lumière et améliorer son rapport signal-sur-bruit. Cet effet exploite la présence d'un champ électrique appliqué dans un semiconducteur pour amplifier les signaux thermiques du bolomètre.

Un ensemble de six détecteurs a été étudié et caractérisé dans différents cryostats (en surface) pour évaluer leurs performances. Ils ont montré des performances uniformes en termes de sensibilité ($\sim$0.9 μV/keV), de résolution à la ligne X de 5,9 keV ($\sim$300 eV RMS) et de gain dans le régime Neganov-Trofimov-Luke ($\sim$ 13 à 50 V), démontrant que la technologie est mature et que les résultats sont reproductibles.

De plus, deux mesures souterraines ont été effectuées pour tester la réjection du fond α. Dans la première mesure, deux cristaux enrichis de $^{130}TeO_2$ avec une masse de 435 g ont été utilisés. Les deux bolomètres ont montré de bonnes performances (4.3 et 6.5 keV FWHM à 2.6 MeV) et une radiopurité élevée (^{228}Th et ^{226}Ra $< 3,1$ μBq/kg). Les détecteurs de lumière fonctionnaient en régime Neganov-Trofimov-Luke avec un bruit de base de 25 et 35 eV avec respectivement une polarisation de 55 et 25 V. La capacité d'identification des événements α a été prouvée avec cette mesure : le 78,8% et 98,3% des événements $\beta(\gamma)$ ont été collectées avec un rejet du 99,9% des α. Cette mesure a démontré que la technologie — requise par CUPID dans le cas des détecteurs faits de TeO_2 — peut être constituée par des détecteurs de lumière au germanium équipés de NTD-Ge en utilisant l'amplification Neganov-Trofimov-Luke avec de très bonnes perspectives.

Une deuxième mesure souterraine a été réalisée au Laboratoire Souterrain de Modane (France). Un détecteur de lumière amélioré par l'effet Neganov-Trofimov-Luke a été couplé à un bolomètre du TeO_2 caracterisé par la même taille de détecteurs utilisés par CUORE. Ce crystal avait un rendement lumineux inférieur aux deux précédents en raison de sa masse plus importante (784 g). Le détecteur de lumière a atteint un bruit de base de 10 eV et un gain de 12,7 dans le régime Neganov-Trofimov-Luke avec une polarisation de 60 V. Cette performance élevée a permis l'acceptation de 96% de signaux $\beta(\gamma)$ avec le rejet de 99,9 % d'événements α. La séparation complète entre les événements α et $\beta(\gamma)$ a été obtenue pour la première fois avec un bolomètre TeO_2 identique à celui utilisé par

l'expérience CUORE. Nous avons démontré que le fond α peut être réduit d'un facteur 10^3 en ajoutant des détecteurs de lumière renforcés par l'effet Neganov-Trofimov-Luke en conservant la configuration actuelle de CUORE.

Le rapport signal sur bruit amélioré et le seuil bas de ces dispositifs dans le régime Neganov-Trofimov-Luke peuvent être utilisés pour d'autres applications, comme par exemple la réjection de l'empilement dans des détecteurs caractérisés par un taux d'événements élevé. À cette fin, un détecteur de lumière assisté par l'effet Neganov-Trofimov-Luke a été couplé à un bolomètre en $LiInSe_2$ avec une masse de 10,3 g. Ce détecteur était intéressant pour la désintégration β de ^{115}In, dont la forme à basse énergie peut contraindre le valeur de la constante de couplage axiale g_A. La difficulté de cette mesure est due au taux élevé d'événements ($\sim$1 Hz) et à l'empilement résultant, qui modifie la forme du spectre énergétique.

Une autre application interessante de ces dispositifs est leur utilisation avec des détecteurs caractérisées par un faible rendement lumineux. La collection de lumière peut être améliorée grâce à l'amplification réalisable par ces photo-bolomètres. Un bolomètre de $Na_2(MoO_3)_4O$ avec une masse de 1,6 g a été testé comme un candidat potentiel pour une expérience de nouvelle génération dans le champ de la double desintegration bêta sans neutrino. L'échantillon était si petit que le senseur NTD-Ge au sommet réduisait la collecte de lumière. Nous avons montré qu'une meilleure discrimination pouvait être obtenue en exploitant l'amplification génerée par l'effet Neganov-Trofimov-Luke.

En plus, un autre type de détecteur de lumière équipé d'un capteur de température différent — un TES (*Transition Edge Sensor*) composé de NbSi — a été étudié dans ce travail. La mesure du premier TES avec une grande surface déposée directement sur l'absorbeur principal présentait de bonnes performances : une sensibilité de 4,3 μV/keV a été obtenue avec un bruit de base de 173 eV RMS et un temps de montée de 150 μs. L'inconvénient de ce dispositif était sa température de transition élevée ($\sim$140 mK). Ce dispositif pourrait être intéressant pour la réjection de l'empilement grâce à sa sensibilité élevée et à ses signaux rapides, mais une température de transition plus basse serait indispensable pour être compatible avec les applications bolométriques décrites dans ce travail. Son bruit de base n'en fait pas un bon candidat pour la détection des signaux très faibles de lumière Cherenkov produit par les bolomètres en TeO_2.

Dans la deuxième partie de ce travail, on présente une étude du modèle thermique décrivant les bolomètres équipés par des senseurs de NTD-Ge avec l'objectif de mieux comprendre la réponse des détecteurs. En fait, les bolomètres sont des détecteurs étonnants utilisés pour un grand nombre d'applications en raison de leurs performances élevées,

néanmoins leur modélisation et simulation sont loin d'être complètement abouties. Deux étùdes ont été menées afin d'évaluer expérimentalement deux paramètres du modèle thermique : la conductance de la colle — utilisée pour coller le senseur sur le détecteur — et le couplage entre les électrons et les phonons dans le senseur. Ces paramètres ont été mesurés pour la première fois dans un montage imitant les détecteurs de l'expérience CUORE.

Lors de la première mesure, une conductance électron-phonon $G_{el-ph} = 0,74\ T[K]^{5,5}$ [W/(K mm^3)] a été trouvée. En ce qui concerne la conductance de la colle, nous avons rencontré un problème inattendu : sa valeur ne dépend pas de la surface de la colle. Nous avons supposé que cela était dû à notre technique de collage : le processus n'était pas reproductible. Conséquentement, une deuxième mesure a été effectuée en changeant la technique de collage. Cette fois, les résultats de conductance de la colle étaient cohérents : $G_{glue} = 1,2(5) \times 10^{-3} T[K]^{3,1(1)}$ [W/(K mm^2)]. La conductance électron-phonon a été à nouveau mesurée en obtenant : $G_{el-ph} = 1,44\ T[K]^{5,3}$ [W/(K mm^3)]. Etant donné que plusieurs des paramètres thermiques des bolomètres n'ont initialement pas été optimisés en raison des long temps nécessaires pour la préparation et la réalisation des mesures bolométriques, cette mesure est un premier pas vers la modélisation des détecteurs qui pourrait conduire dans l'avenir à l'amélioration de leur sensibilité.

Contents

1 Introduction

This chapter is meant to show the importance of neutrino physics and to introduce the neutrinoless double-β decay. The present state of the art about the neutrino physics and the main discoveries related to it are summarised in Sec. 1.1. The introduction to the problem of the neutrino-mass measurement and the possible experimental techniques for its determination are illustrated in Sec. 1.2. Then, the neutrinoless double-β decay is presented in Sec. 1.3.

1.1 Neutrino

The neutrino is an elusive particle: W. E. Pauli, who theorised it in 1930, affirmed that he had done a terrible thing by postulating a particle that cannot be detected [1]. Its existence has been proposed to explain the non-conservation of the β-decay energy. This proposal was made in a letter to the "radioactive ladies and gentlemen" of the Federal Institute of Technology in Zürich, reported in Ref. [2]. In fact β events produce an electron with a continuum energy spectrum, opposite to the α decay for which the energy conservation is immediately visible as α particles have a well defined energy. Pauli proposed the existence of a second particle participating to the decay that was taking away the missing energy. He proposed to call this particle "neutron" because of its charge absence, imposed by the charge conservation in the β decay. But just two years later, this name has been used by J. Chadwick to describe the neutral nucleons present in the atoms, that he discovered in 1932 [3]. Therefore, when E. Fermi included the particle — theorised by W. E. Pauli — in his theory on β decay, he decided to call it neutrino [4].

Luckily W. E. Pauli was not completely right and this particle is detectable: in 1946 B. Pontecorvo suggested to observe it through the inverse electron capture/β^+ decay [5]. In particular he proposed to use the two following reactions:

$$\nu_e + {}^{37}Cl \rightarrow e^- + {}^{37}Ar, \tag{1.1}$$

$$\nu_e + {}^{79-81}Br \rightarrow e^- + {}^{79-81}Kr. \tag{1.2}$$

Their products were easily distinguishable and measurable after a chemical extraction. Pontecorvo's idea triggered the research for the neutrino interactions, that led C. L. Cowan and F. Reines to detect the antineutrino in 1956 for the first time [6]. They employed the inverse neutron β decay:

$$\bar{\nu}_e + p \rightarrow e^+ + n, \tag{1.3}$$

with a cadmium-loaded-water target [7] to detect the antineutrinos emitted by the Hanford nuclear reactor.

The reaction proposed by B. Pontecorvo was employed by R. Davis in 1968 to measure the Sun electron-neutrino flux. At that time, there was a debate about the nuclear processes occurring in the Sun. Two main theories were popular: the CNO cycle and the proton-proton chain. The CNO (*carbon-nitrogen-oxygen*) cycle is a process occurring in the stars that was suggested by H. Bethe in 1939 [8]. As it will be discovered later, it is the main mechanism of energy production in heavy stars[1] [9]. The

[1] Stars with a mass larger than three solar masses.

proton-proton chain is a set of nuclear fusion reactions occurring in smaller stars. This process converts hydrogen in helium and then successively to heavier elements. The light reaching the Earth is produced at the Sun surface and cannot be used to investigate the reactions occurring inside. On the contrary, neutrinos — produced in the Sun inner-core reactions — manage to reach to Earth and are the perfect probe to investigate the Sun.

R. Davis employed a 615-tonne tetrachloroethylene-filled tank in the Homestake mine in South Dakota to detect the neutrino flux from the Sun [10]. The choice of the location was suggested by the experience acquired in 1955, when R. Davis tried to measure the cross-section of antineutrinos coming from the Savannah River reactor and fixed an upper limit on the Sun neutrino flux [11]. The theoretical neutrino flux according to the Standard Solar model was of (7.9 ± 2.6) SNU[2] [12], where the SNU (*Solar Neutrino Unit*) is the number of neutrinos detected in one second employing 10^{36} target atoms. R. Davis detected a flux of (2.3 ± 0.75) SNU [13], corresponding to one third of the expected value. This effect was observed also by the GALLEX [14], GNO [15] and SAGE [16] experiments. These three experiments used the inverse electron capture of ^{71}Ga, characterised by a lower threshold for the solar-neutrino detection (corresponding to 236 keV instead of the 814 keV of ^{37}Cl). The solar neutrino flux predicted for a such threshold corresponds to 131 ± 11 SNU [17]. Also in this case, the measured flux was lower than the foreseen one, in particular GALLEX measured $77.5 \pm 6.2^{+4.3}_{-4.7}$ SNU [14], GNO $62.9^{+6.0}_{-5.9}$ SNU [15] and SAGE $70.8^{+5.3}_{-5.2}$ (stat) $^{+3.7}_{-3.2}$ (sys) SNU [16].

A possible explanation to the underestimation of the Sun electron-neutrino flux was proposed by B. Pontecorvo in 1968 [18]. He suggested that the electron neutrino can change flavour, becoming for example a muon or a tau neutrino, during their time of flight between the Sun and the Earth. The described experiments were insensitive to these other flavours and this could have explained the underestimation of the flux. The phenomenon proposed by B. Pontecorvo is referred to as neutrino oscillations: a neutrino can be seen as a mix of three different neutrino states from a quantum mechanics point of view. A neutrino is produced as a flavour eigenstate (ν_e, ν_μ, ν_τ), but then it propagates in a mass (free-particle) eigenstate (ν_1, ν_2, ν_3) that is a combination of all the possible flavours. When the neutrino interacts with matter, for example with a detector, it is again the flavour component of its wave function that drives the interaction. The relationship between the mass eigenstates and the flavour ones is regulated by the PNMS (Pontecorvo, Maki, Nakagawa e Sakata) matrix:

$$\begin{bmatrix} \nu_e \\ \nu_\mu \\ \nu_\tau \end{bmatrix} = \begin{bmatrix} c_{12}c_{13} & s_{12}c_{13} & s_{13}e^{-i\delta} \\ -s_{12}c_{23} - c_{12}s_{23}s_{13}e^{i\delta} & c_{12}c_{23} - s_{12}s_{23}s_{13}e^{i\delta} & s_{23}c_{13} \\ s_{12}s_{23} - c_{12}c_{23}s_{13}e^{i\delta} & -c_{12}s_{23} - s_{12}c_{23}s_{13}e^{i\delta} & c_{23}c_{13} \end{bmatrix} \times diag(1, e^{i\alpha_1}, e^{i\alpha_2}) \begin{bmatrix} \nu_1 \\ \nu_2 \\ \nu_3 \end{bmatrix}, \quad (1.4)$$

where $c_{ji} = \cos\theta_{ji}$ and $s_{ji} = \sin\theta_{ji}$. This matrix depends on three angles (θ_{12}, θ_{23}, θ_{13}) and three phases (δ, α_1, α_2) if the neutrino is a Majorana particle (i. e. the neutrino coincide with its antiparticle). If the neutrino is a Dirac particle (i. e. neutrino and antineutrino are two different particles), the parameters become only four: the three angles and one phase (δ).

The oscillation probability can be defined as in Eq. (1.5) in the simplified case of a two-neutrino model instead of our three-neutrino model. This simplification does not impact on the consideration that will follow, as in many cases neutrino-oscillation phenomena can be described in a two-neutrino framework with a reasonable accuracy.

$$P(\nu_e \to \nu_\mu) = sin^2 2\theta sin^2 \frac{(p_2 - p_1)L}{2} \simeq sin^2 2\theta sin^2 \frac{\delta m^2_{12} L}{4E}, \quad (1.5)$$

where p_1 and p_2 are the neutrino momenta, that can be approximated to $p_i \simeq E_i - m_i^2/2E$, L is the distance between the source and the detector and θ the only mixing angle in a two-neutrino model. The

[2] 1 SNU (Solar Neutrino Unit) corresponds to 1 ν / (10^{36} atoms $\cdot$ s)

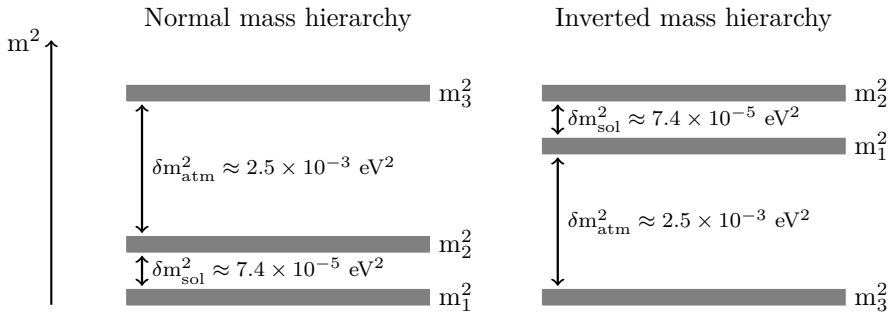

Fig. 1.1: Normal (*left*) and inverted (*right*) mass hierarchy scheme.

measurement of the oscillation probability between two states provides information on the square mass difference and the mixing angle.

Table 1.1 presents the most recent experimental results on the three mixing angles, the two square mass differences and the Dirac phase. The square mass differences (δm^2_{sol} and δm^2_{atm}) differ of around two orders of magnitude. There are two neutrinos closer in mass (m_1 and m_2) and a third one (m_3) whose mass is farther with respect to the previous two. Depending on the sign of the square mass difference δm^2_{atm}, three cases are distinguishable:

Direct hierarchy. The lightest neutrino mass state is m_1 if $\delta m^2_{atm} > 0$. The hierarchy of the mass states becomes: $m_1 < m_2 \ll m_3$.

Inverted hierarchy. The lightest neutrino mass state is m_3 when $\delta m^2_{atm} < 0$. The mass state can be ordered as: $m_3 \ll m_1 < m_2$.

Degenerate hierarchy. The lightest neutrino mass state is m_1. The degenerated ordering is verified when the square mass differences are negligible with respect to the neutrino masses: $m_1 \simeq m_2 \simeq m_3$.

Refer to Fig. 1.1 for a graphical scheme of the normal and inverted hierarchy.

The decisive proof of the neutrino-oscillation existence has been brought by the Super-Kamiokande [19] experiment in 1998 followed by the SNO [20] experiment in 2001. Super-Kamiokande observed the oscillations of atmospheric neutrinos with a 50-ktonne water-Cherenkov detector hosted in the Kamioka mine [21]. The Super-Kamiokande experiment observed a ν_μ disappearance in the atmospheric neutrino flux. The SNO experiment — hosted in the Sudbury laboratory — demonstrated the oscillations of the solar neutrinos [22] with a 12-m-diameter balloon filled with 100 tonnes of heavy water, which scintillation light was read by 456 photomultipliers. The solar neutrino oscillation was demonstrated thanks to a detection of a ν_e flux lower than the total neutrino flux measured with a flavour independent process. Moreover the total neutrino flux was compatible with the Solar Model predictions. This measurement was permitted by the different interacting channels of the SNO detector: a precise measurement of the ν_e flux was performed with the charged-current reaction $\nu_e + D \to p + p + e^-$; the elastic scattering on electrons was mainly sensitive to ν_e but also able to detect the other two flavours and the neutral-current reaction $\nu + D \to p + n + \nu$ was sensitive to all neutrino flavours.

Atmospheric and solar neutrino oscillation measurements give access to the determination of two angles (θ_{12} and θ_{23}) and two square mass differences (δm^2_{12} and δm^2_{23}). The angle θ_{13} is measured with reactor and accelerator measurements. Among the three angles, θ_{13} is the smallest and has the highest error. The information on the mass hierarchy and the phase δ — that can be measured with accelerator-based experiments — are not yet known. However, presently the direct ordering for the mass hierarchy is

Tab. 1.1: Oscillations parameters for a three-neutrino model from Ref. [23]. The best-fit value and its 3σ interval is reported for each value. Note that the interval of δ/π corresponds to 2σ.

Parameter	best-fit [3σ interval]			
	direct hierarchy		inverted hierarchy	
δm^2_{21} [$\times 10^{-5}$ eV^2]	7.37 [6.93 − 7.96]			
$\lvert\delta m^2_{23}\rvert$ [$\times 10^{-3}$ eV^2]	2.56	[2.45 − 2.69]	2.54	[2.42 − 2.66]
$\sin^2\theta_{12}$	0.297 [0.250 − 0.354]			
$\sin^2\theta_{23}$	0.425	[0.381 − 0.615]	0.589	[0.384 − 0.636]
$\sin^2\theta_{13}$	0.0215	[0.0190 − 0.0240]	0.0216	[0.0190 − 0.0242]
δ/π	1.38	[1.0 − 1.9]	1.31	[0.92 − 1.88]

favoured with respect to the inverted one. A parameter, to which all these measurements are insensitive, is the neutrino mass that will be introduced in the following section.

1.2 The neutrino mass and its measurement

The Standard Model describes neutrinos as neutral and massless Dirac fermions which interact only by weak force. The neutrino and the antineutrino are two different particles as they have a different lepton number. The only neutrino states — which couples to other fermions via weak interactions — are the left-handed neutrino (ν_L) and the right-handed antineutrino ($\bar{\nu}_R$). Being neutrinos massless in the baseline version of the Standard Model, the state ν_L ($\bar{\nu}_R$) has exactly negative (positive) helicity. If neutrinos are massive, the ν_L and the $\bar{\nu}_R$ states do not have definite helicity any more. Then the question arises if the feature of neutrino interactions is determined by the lepton number or by the helicity.

E. Majorana theorised that the neutrino is equal to its antiparticle in 1937 [24]. In this case, the relevant parameter to describe neutrino interactions is not the lepton number — which looses any physical meaning — but the helicity. It is clear, then, that an open and fundamental question of neutrino physics is if the neutrino is a Dirac or a Majorana particle. The answer to this question by experiments is extremely difficult because the neutrino mass is very small and the two descriptions tend to coincide.

Different theories about the process that generates the neutrino mass have been elaborated. The three more interesting are here summarised. The mass term has to be added by hand to the Lagrangian that describes free neutrinos:

$$\mathcal{L} = \bar{\psi}\left(i\gamma^\mu \frac{\partial}{\partial x^\mu} - m\right)\psi, \tag{1.6}$$

where ψ is the spinor describing the particle and m its mass. We can define then the following mass terms:

Dirac mass. The mass term can be written assuming that the neutrino has a Dirac nature as done in the baseline version of the Standard Model. In this case there will be two spinors for the neutrino: ψ_L and ψ_R, the first one participates to weak interactions while the second can only interact through gravity. The Lagrangian mass term looks like:

$$\mathcal{L} = m_D\left(\bar{\psi}_L\psi_R + \bar{\psi}_R\psi_L\right). \tag{1.7}$$

The corresponding mass matrix is not diagonal: the flavour mixing appears when the matrix is diagonalised according to the mass eigenvalues.

Majorana mass. If the neutrino is a Majorana particle, two additional components are available $\bar{\psi}\psi^C$ and $\bar{\psi}^C\psi$. The Lagrangian mass term can assume the following form:

$$\mathcal{L} = \frac{1}{2}\left(m_M\bar{\psi}\psi^C + m_M^*\bar{\psi}^C\psi\right), \tag{1.8}$$

where m_M is the Majorana mass. The projections on the left and right-handed states transform the last Lagrangian in:

$$\mathcal{L} = \frac{1}{2}m_L\left(\bar{\psi}_L\psi_R^C + \bar{\psi}_R^C\psi_L\right) + \frac{1}{2}m_R\left(\bar{\psi}_L^C\psi_R + \bar{\psi}_R\psi_L^C\right). \tag{1.9}$$

Also in this case, the oscillation can be extracted redefining the mass eigenstate as: $\phi_1 = \psi_L + \psi_R^C$ and $\phi_2 = \psi_R + \psi_L^C$.

A more general case. At this point, we can imagine to have a more general model that includes both the Dirac and the Majorana mass terms. Its Lagrangian would be the sum of the two Lagrangians that can be summarised as:

$$\mathcal{L} = \begin{bmatrix}\bar{\psi}_L & \bar{\psi}_L^C\end{bmatrix}\begin{bmatrix}m_L & m_D\\ m_D & m_R\end{bmatrix}\begin{bmatrix}\psi_R^C\\ \psi_R\end{bmatrix}. \tag{1.10}$$

Also in this case, the flavour mixing can be obtained with a diagonalisation of this matrix.

From this definition we can briefly summarise four possible neutrino mass models:

- Pure Dirac neutrino model corresponds to the case in which $m_L = m_R = 0$, this case has been described above.
- Pseudo-Dirac neutrino model occurs when the Majorana mass components are negligible with respect to the Dirac one: $m_D \gg m_L, m_R$.
- Pure Majorana neutrino model requires that $m_D = 0$, also this case has been explained above.
- The most general case (presence of both Dirac and Majorana) is very interesting from the point of view of physics and it is related to the so called see-saw mechanism in which one fixes $m_R \gg m_D$ and $m_L = 0$. This model foresees the existence of yet-not-observed heavy neutrino states with a mass m_R and light neutrino states with a mass m_D^2/m_R. The light neutrino states coincide with the three neutrinos that we have observed and which undergo flavour oscillations. Both light and heavy neutrinos are Majorana particles. This is an elegant solution to explain the big mass difference present between neutrinos and the other known particles.

As we have seen in the previous section, oscillation experiments do not provide information about the neutrino mass, since they are sensitive only to the square mass difference. Three other viable techniques — sensitive to the neutrino mass — are used to investigate this parameter:

Cosmological measurements. The sum of the three-neutrino masses $\Sigma = \sum_{i=1}^{3} m_i$ can be evaluated from cosmological measurements. This is possible thanks to the neutrinos produced after the Big Bang, that influenced the Universe evolution and affect quantities such as the cosmic microwave background and the cosmological matter density. The sum of the neutrino masses evaluated with cosmological measurements is strongly model dependent, different limits can be put depending on the theoretical models considered. The most recent limit on Σ — released by the Planck experiment [25] — ranges between $0.12 - 0.6$ eV.

β decay. The spectrum of the β decay is another parameter sensitive to the electron-neutrino mass. The endpoint of the β spectrum depends on the neutrino mass, in fact a part of the total energy of the decay is taken away from the neutrino that is not detected. The neutrino mass thus measured can be expressed by:

$$m_\beta = \sqrt{\left(\sum_{i=1}^{3} |U_{1i}|^2 m_i^2\right)}. \tag{1.11}$$

This is a sort of effective average mass due to the fact that all the today's conceivable experiments do not have a sufficient resolution to separate the three neutrino mass eigenvalues. This parameter is investigated with two main experimental techniques: electrostatic-retarding spectrometers (in the following called spectrometers) and low-temperature calorimeters. The first one performs an energy measurement of the electrons emitted by an external source. The second approach consists in the use of a source directly embedded in a cryogenic detector. The β-decay isotope should have a low Q-value to increase the relative counting rate in the end-point spectral region. Spectrometers use typically ^{3}He while ^{187}Re and ^{163}Ho are employed for the low-temperature calorimeters. The most stringent limits on the m_β mass have been imposed by the Troitsk and Mainz experiments, respectively $m_\beta \leq 2.05$ eV (95 % C.L.) [26] and $m_\beta \leq 2.3$ eV (95 % C.L.) [27]. The KATRIN experiment has just started and employs the longest spectrometer ever built — with a total lenght of 70 m [28] — that will allow us to reach a sensitivity to the neutrino mass of the order of 0.2 eV at the 90 % C.L. [29]. The PROJECT 8 collaboration is investigating the possibility to use the cyclotron radiation emission to measure the energies at the ^{3}He-spectrum end-point and improve the sensitivity to the neutrino mass down to 40 meV [30].

The ^{187}Re isotope has been employed by the MANU and MiBeta experiments, they respectively set the following limits on the neutrino mass direct measurement: $m_\beta < 26$ eV/c^2 at 95 % C.L. [31] and $m_\beta < 15$ eV/c^2 at 90 % C.L. [32]. The MARE experiment followed these two experiments. After a first phase that continued the investigation of ^{187}Re, it started the investigation of a different isotope, the ^{163}Ho[3] [33]. Concerning ^{163}Ho, the present limit on the neutrino mass corresponds to 225 eV [34]. Nevertheless new results are expected soon from the ECHo [35] and HOLMES [36] experiments, that are supposed to reach sub-eV sensitivities [36, 37] with a micro-calorimeter technology.

Neutrinoless double-β decay. If the neutrino is a Majorana particle, this process is probably the most promising technique for the evaluation of the neutrino mass scale. Next-generation experiments are supposed to cover the complete inverted hierarchy reaching neutrino masses down to about 20 meV. The neutrino mass measured with this decay is expressed by:

$$\langle m_\nu \rangle = \left| \sum_{i=1}^{3} U_{1i}^2 m_i \right|. \tag{1.12}$$

The $0\nu2\beta$ decay requires that the neutrino is a Majorana particle and therefore the terms U_{1i}^2 from the PNMS matrix have to include also the Majorana phases. This process is described in detail in the following section.

Direct measurements of ν_μ and ν_τ masses have been performed analysing the kinematic of the following decays: $\pi^+ \to \mu^+ + \nu_\mu$ and $\tau^- \to \nu_\tau + 5\pi$ but also $\tau^- \to \nu_\tau + 3\pi$. The limit on the ν_μ mass is 0.17 MeV at 90 % C.L. [38] and the one on the ν_τ mass is 18.2 MeV at 95 % C.L. [39].

[3] Actually holmium undergoes an electron capture decay. The particle measured in the final state is a X-ray photon and not an electron as in the case of rhenium.

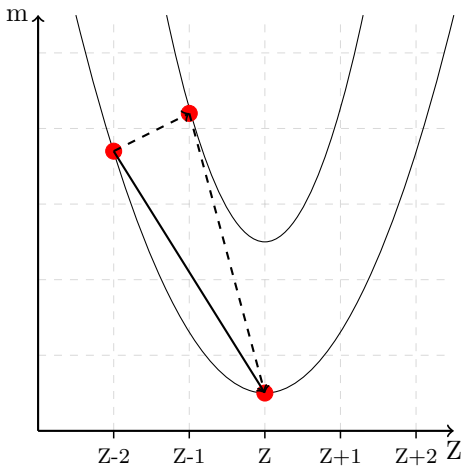

Fig. 1.2: Double parabola produced by the paring term in the Bethe-Weizsacker formula for even-even nuclei. A β decay from the Z-2 atom to the Z-1 one is forbidden. The only possible decay allowed for a Z-2 atom is a double-β decay.

1.3 The neutrinoless double-β decay

After Fermi's theory on the β decay, M. Goeppert-Mayer proposed the existence of the double-β decay in 1935 [40]. This decay consists in two simultaneous β decays:

$$(A, Z) \rightarrow (A, Z+2) + 2e^{-} + 2\bar{\nu}_e. \tag{1.13}$$

The existence of the double-β decay has been demonstrated for the first time in 1950 with a geochemical experiment: ^{130}Xe was found in geologically old tellurium samples [41]. The definitive confirmation of the double-β decay existence has been proved 37 years later for ^{82}Se with a time-projection chamber [42]. These decays are characterised by a long lifetime of the order of $10^{18} - 10^{21}$ yr.

The double-β decay detection is favoured for nuclei whose β decay is forbidden because of energy conservation. The nuclei belonging to this category are characterised by an even number of protons and neutrons, the so-called even-even nuclei. In order to understand the reason of this, we should consider the Bethe-Weizsacker formula that expresses the nucleus mass as a function of its number of protons Z, neutrons N and the binding energy E_B:

$$m = Z\ m_p + N\ m_n - \frac{E_B}{c^2}, \tag{1.14}$$

where m_p and m_n are respectively the masses of the proton and the neutron. The binding energy can be expressed according to:

$$E_B = a_v A - a_s A^{2/3} - a_c Z(Z-1)A^{-1/3} - a_{sym}\frac{(A-2Z)^2}{A} + \delta, \tag{1.15}$$

where A is the atomic mass, a_v, a_s, a_c, a_{sym} are in the order the volume, the surface, the Coulomb and the symmetry terms, and δ is the pairing term [43]. Eq. (1.14) becomes a parabola as a function of Z for atoms with the same atomic mass. All the nuclei with a mass higher than the one at the parabola

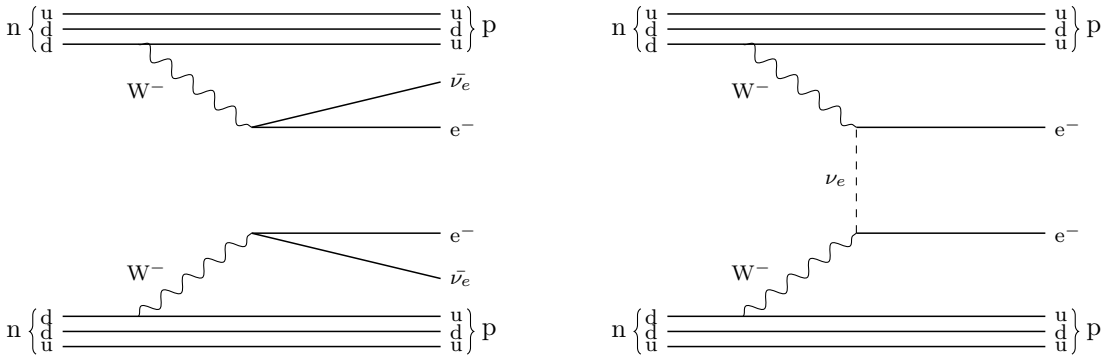

Fig. 1.3: Feynman diagram of double-β decay (*left*) and neutrinoless double-β decay (*right*).

minimum tends to decay β^+ and β^- toward the lowest energy state. In presence of even-even (odd-odd) nuclei, the parabola is split in two parabolas due to the pairing term δ that assumes a positive (negative) value for even-even (odd-odd) nuclei. Fig. 1.2 shows an example of double parabola for an even-even nuclei. Given this assumption, sometimes an atom characterised by a proton number $Z-1$ can have a mass higher than the state $Z-2$. The single β decay from the $Z-2$ state to $Z-1$ one is forbidden, the $Z-2$ atom can only decay through a double-β decay to the Z atom.

W. H. Furry proposed the existence of the neutrinoless double-β decay in 1939 assuming that the neutrino is a Majorana particle [44]. The neutrinoless double-β ($0\nu2\beta$) decay is a nuclear transition that transforms two neutrons in two protons with the emission of two electrons:

$$(A, Z) \rightarrow (A, Z+2) + 2e^-. \tag{1.16}$$

This decay is forbidden according to the Standard Model because it does not conserve the lepton number. Fig. 1.3 compares the Feynman diagrams of the double-β ($2\nu2\beta$) and the $0\nu2\beta$ decays. In the first case two antineutrinos are emitted together with the two electrons, conserving the lepton number in the nuclear transition. In the second case, an antineutrino is emitted from a vertex and it is absorbed as a neutrino in the second vertex. This process is possible only if the neutrino is a Majorana particle. Moreover the neutrino must have a mass in order that the process is not forbidden by a strict helicity conservation.

The signature of the $0\nu2\beta$ decay is a monochromatic peak at the sum energy of the two electrons, corresponding to the reaction Q-value ($Q_{\beta\beta}$). Fig. 1.4 shows the $0\nu2\beta$ signal and the $2\nu2\beta$ spectrum, that is continuous with an end-point at the reaction Q-value minus the mass of the two antineutrinos. The continuous spectrum is due to the fact that the antineutrino energy cannot be measured by the detector. This plot represents an ideal condition without deformation of the $2\nu2\beta$-spectrum end-point and enlargement of the $0\nu2\beta$ peak due to the detector energy resolution. For this reason the discovery of the $0\nu2\beta$ decay requires detectors characterised by a good energy resolution able to extract the peak signal.

The discovery of the $0\nu2\beta$ decay would:

- allow an evaluation of the neutrino mass scale;
- demonstrate the existence of a process that does not conserve the lepton number;
- prove the Majorana nature of neutrino.

The discovery of the lepton-number violation — and the consequent possibility of creating leptons — would have important consequences on the matter-antimatter asymmetry discussion. Our Universe is

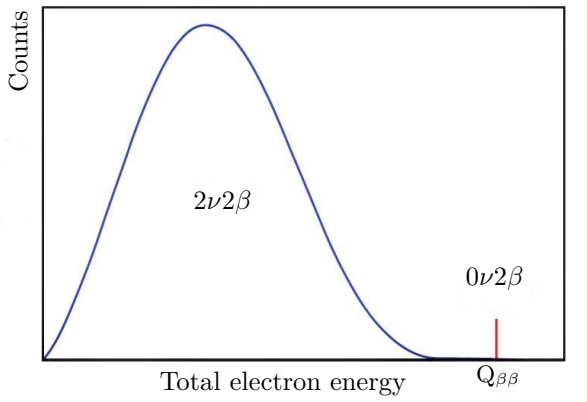

Fig. 1.4: The $0\nu2\beta$ and $2\nu2\beta$ decay spectra. The signature of the $0\nu2\beta$ decay is a peak at the Q-value of the reaction ($Q_{\beta\beta}$). The plot has been adapted from Ref. [45].

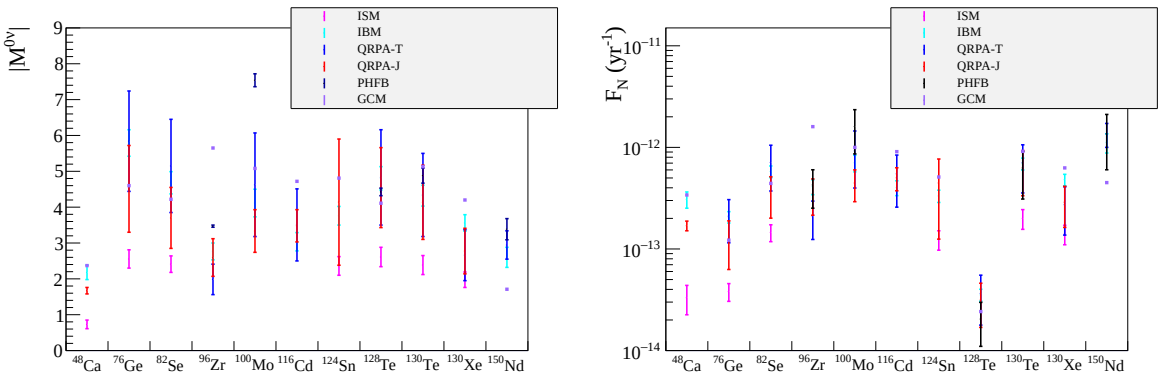

Fig. 1.5: *Left panel*: nuclear matrix elements for the main $0\nu2\beta$ isotopes. *Right panel*: F_N term — from Eq. (1.17) — for the main $0\nu2\beta$ isotopes. The error bands are due to the uncertainties on the nuclear matrix element and axial coupling constant g_A.

mainly constituted by matter and this fact cannot be explained according to any of the known physical laws. The leptogenesis [46] is one of the theories that could explain this observed asymmetry.

The Majorana neutrino mass $\langle m_\nu \rangle^2$ — defined in Eq. (1.12) — is connected to the $0\nu2\beta$ rate as:

$$[T^{0\nu}_{1/2}]^{-1} = \frac{g_A^4 G^{0\nu} |M^{0\nu}|^2 \langle m_\nu \rangle^2}{m_e^2} = \frac{F_N \langle m_\nu \rangle^2}{m_e^2}, \tag{1.17}$$

when the only involved mechanism is an exchange of a light Majorana neutrino. In this equation, m_e is the electron mass, $G^{0\nu}$ the phase space factor, g_A the axial coupling and $|M^{0\nu}|^2$ the nuclear matrix element terms that will be now described in more detail:

Nuclear matrix element. This parameter takes into account the nuclear interactions involved in the decay. This parameter can be redefined as:

$$M^{0\nu} = M^{0\nu}_{GT} - \frac{g_V^2}{g_A^2} M^{0\nu}_F, \tag{1.18}$$

where $M^{0\nu}_{GT}$ and $M^{0\nu}_F$ are the Gamow-Teller and the Fermi matrix element, g_V and g_A are respectively the vector and the axial coupling constants. In the case of a free nucleon approximation, g_V and g_A are taken respectively equal to 1 and ~ 1.26 [47]. The value of g_A is influenced by the many-body interactions occurring inside the nucleus. For this reason, usually an effective g_A value is considered in order to take into account the nuclear interactions. The effective g_A is usually defined as $g_A^{eff} = q\ g_A^{free}$. This effective value is evaluated both from theoretical and experimental analysis. Since the $0\nu2\beta$ rate depends on the fourth power of the axial coupling constant, this parameter can strongly affect the half life estimation, making them much longer than what was predicted up to now.

The evaluation of nuclear matrix element is particularly complicated because the nuclear physics involved cannot be treated in a simple and exact way. We can only elaborate models that try to reconstruct approximately the many-body interactions. The nuclear-matrix-element calculation will be fundamental for the evaluation of the neutrino mass when the $0\nu2\beta$ decay will be discovered. For this reason many models are currently under study; the most used ones are here presented:

- Nuclear Shell Model (NSM) uses a shell model — in analogy with the one used to account for the electrons behaviour in the atoms — to describe the behaviour of neutrons and protons inside the nucleus. The shell model provides a good explanation for the extra-binding energy of some nuclei (magic numbers) [48] and of many other nuclear properties.
- neutron-proton Quasiparticle Random Phase Approximation (npQRPA) is one of the most popular methods. This model is useful for the heavy-nuclei calculations that are unfeasible with the full shell model [49]. This model considers the proton and neutron as a two-quasiparticle system, which interaction strength is controlled by a free parameter that is obtained by the real data fit.
- Interacting Boson Model (IBM) interprets the interaction inside the nucleus as a number N of boson that interact via two- and three-body interactions. A refinement of this model introduces a distinction between the proton and the neutron. This model — as the previous one — is simpler than the shell model and requires less computing power [50].

Other nuclear models have been recently introduced to better interpret the nuclear behaviour as the Projected Hartree-Fock-Bogoliubov (PHFB) approach [51] and the Energy Density Functional - Generating Coordinate Method (EDF-GCM) [52]. The nuclear matrix elements for the main $0\nu2\beta$ isotopes are reported in Fig. 1.5 (*left*). The uncertainties are still big and not all the models give compatible results.

Tab. 1.2: Summary of the phase space factors $G^{0\nu}$ for relevant $0\nu2\beta$-decay nuclei from Ref. [53].

Nucleus	$G^{0\nu}$ [$\times10^{-15}$ yr]	Nucleus	$G^{0\nu}$ [$\times10^{-15}$ yr]	Nucleus	$G^{0\nu}$ [$\times10^{-15}$ yr]
^{48}Ca	24.81	^{116}Cd	16.70	^{150}Nd	63.03
^{76}Ge	2.363	^{124}Sn	9.040	^{154}Sm	3.015
^{82}Se	10.16	^{128}Te	0.5878	^{160}Gd	9.559
^{96}Zr	20.58	^{130}Te	14.22	^{198}Pt	7.556
^{100}Mo	15.92	^{136}Xe	14.58	^{232}Th	13.93
^{110}Pd	4.815	^{148}Nd	10.10	^{238}U	33.61

Phase space factor. This parameter considers the kinematic of the decay. The phase space factor can be calculated precisely and its complete formula can be found in Ref. [53]. Its values are reported in Table 1.2 for different isotopes and are practically free of uncertainties. A graphical representation of the F_N parameter (that includes the phase space factor and the nuclear matrix element) is reported in Fig. 1.5 (*right*) for the main $0\nu2\beta$ isotopes.

The sensitivity to the $0\nu2\beta$ decay of an experiment can be expressed as:

$$S = ln2 \; \epsilon \; T \frac{N_{\beta\beta}}{n_B}, \tag{1.19}$$

where ϵ and T are respectively the detection efficiency and the experiment live time, and $N_{\beta\beta}$ and n_B are the number of nuclei that can decay and the upper limit — at a given confidence level — on the number of counts of the double-β-decay transition. In case of non-zero background, n_B depends on the number of background counts. The number of background counts N_B depends on the width of the energy region close to the Q-value — that can be approximated as the energy resolution of the detector ΔE — the measurement time and the experiment mass M: $N_B = BI \; \Delta E \; T \; M$. BI is the background rate over mass, energy resolution and time, the so-called Background Index. The number of nuclei can be rewritten also as a function of the mass, considering the number of isotope atoms x in the molecule, the molecular weight A and the $0\nu2\beta$-candidate isotopic abundance IA: $N_{\beta\beta} = IA \; x \; N_A \; M/A$, where N_A is the Avogadro number. Considering a Poissonian statistics to evaluate the upper limit on the number of signal counts, the formula can be rewritten as:

$$S = ln2 \; \epsilon \; IA \; \frac{x \; N_A}{A} \sqrt{\frac{T \; M}{\Delta E \; BI}}. \tag{1.20}$$

The following parameters of Eq. (1.20) are fundamental for the design of a $0\nu2\beta$ experiment and the evaluation of its performance:

Mass. An approach used to increase the sensitivity is to employ a detector with a large isotope mass. In order to explore the inverse hierarchy as goal for the next generation experiments, masses from hundred kilograms up to tonnes are needed depending on the technology used.

Isotopic abundance. This parameter takes into account the percentage of the $0\nu2\beta$ isotope employed by the experiment. Fig. 1.6 (*top-left*) shows the isotopic abundance of the main $0\nu2\beta$ isotopes. The isotope with the highest natural abundance is ^{130}Te, several experiments use or are considering this isotope because a good sensitivity can be achieved without enrichment. When the $0\nu2\beta$ isotopes have an isotopic abundance lower than or of the order of 10 %, a source enrichment is usually recommended. The material enrichment is usually done by centrifugation. The problem is that not all the isotopes can be enriched easily with reasonable costs. ^{48}Ca, ^{96}Zr and ^{150}Nd enter this category, even if they are interesting because of their high Q value (above the γ natural radioactivity and in a radon-free region) they are not widely employed because of their difficult enrichment.

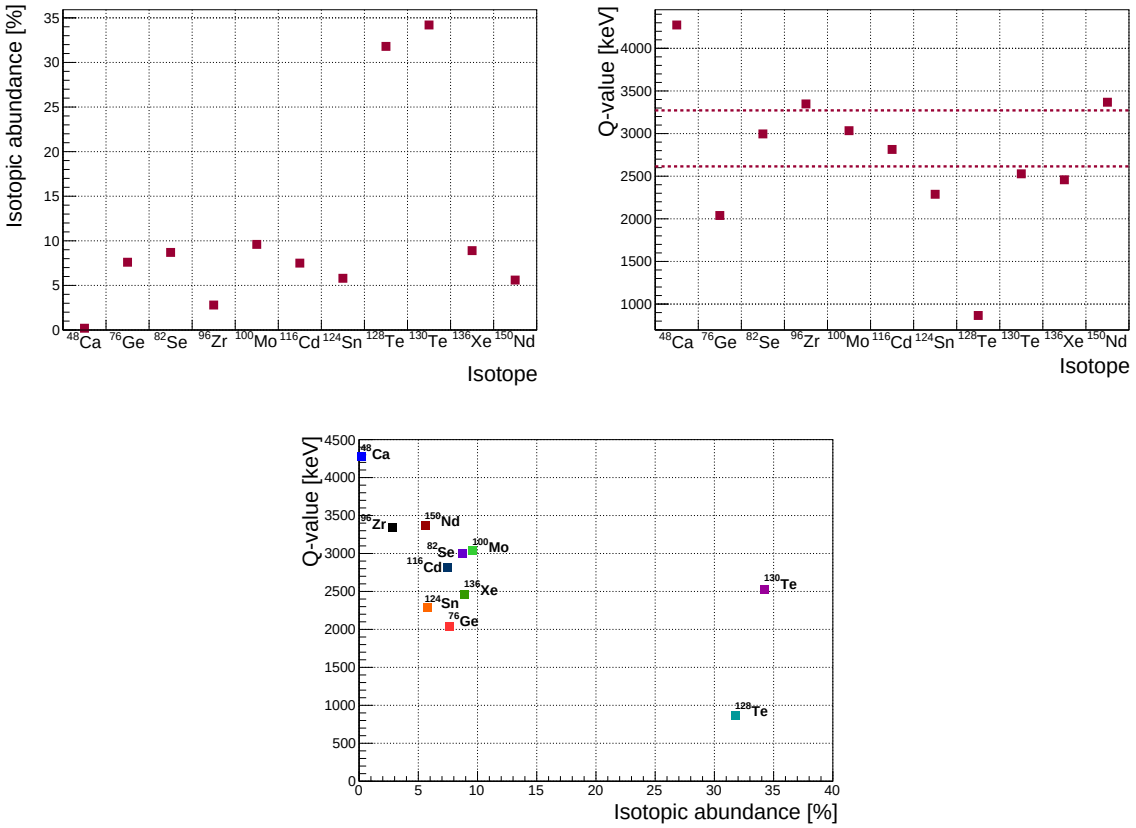

Fig. 1.6: *Top-left panel*: Isotopic abundance for the main $0\nu2\beta$ isotopes. *Top-right panel*: Q-value for the main $0\nu2\beta$ isotopes. The two dashed lines represent the 2615-keV γ quanta of ^{208}Tl and 3272-keV Q_β end-point of ^{214}Bi. *Bottom panel*: Q-value as a function of the isotopic abundance for the main $0\nu2\beta$ isotopes.

Energy resolution. As shown in Fig. 1.4 (*left*) the signature of the $0\nu2\beta$ decay is a peak at the reaction Q-value. A good energy resolution is a key point for the peak identification and background control.

Live time. The sensitivity is proportional to the square root of the experiment live time. Obviously a long detection time increases the sensitivity but its gain is no longer interesting after a few years. For this reason, the live time target is usually fixed to $5 - 10$ yr. Doubling the sensitivity of an experiment that has worked for 5 years would require and additional running time of 75 years.

Background index. This parameter provides information on the background level in the $0\nu2\beta$ region of interest. Its dimension is expressed as counts/(keV yr kg). By multiplying this parameter by the isotope mass, the energy resolution and the experiment live time, we can deduce the expected number of background counts. The zero-background condition at the 90 % C.L. is accomplished on average when the region of interest is expected to contain less than 0.1 counts during the experiment live time. Obviously it depends on the background index, but also on the experiment mass, its live time and energy resolution. Presently a good and challenging target for the background index can be considered 10^{-4} counts/(keV kg yr). Even if this could not be sufficient for a next-generation zero-background experiment. In fact if a 400-kg mass is employed for 5 years with an energy resolution of 5 keV, there will be 1 count in the region of interest. This experiment can not be considered without background. In the approximation of a zero-background experiment, the Eq. (1.20) can be rewritten as:

$$S = ln2 \; \epsilon \; IA \; \frac{x \; N_A}{A} \frac{T \; M}{n_L}, \tag{1.21}$$

where n_L is an upper limit on the number of background counts observable. The advantage of a zero-background experiment is that the sensitivity becomes linear with the experiment live time and mass.

A short comment about the $0\nu2\beta$ candidate is needed before moving to the experiment discussion. 35 isotopes with an even-even nuclei are allowed to undergo double-β decay but not all of them are interesting candidates. The main nuclei usually considered are: ^{48}Ca, ^{76}Ge, ^{82}Se, ^{96}Zr, ^{100}Mo, ^{116}Cd, ^{124}Sn, ^{128}Te, ^{130}Te, ^{136}Xe, ^{150}Nd. Fig. 1.6 shows their isotopic abundances and Q-values. The background level in the $0\nu2\beta$ region is influenced also by isotope Q-value. We can distinguish three main groups:

- the isotopes with a Q-value higher than 3272 keV — corresponding to the end-point of ^{214}Bi β spectra — are in a region without γ background and free from radon-induced natural radioactivity. ^{48}Ca, ^{96}Zr, ^{150}Nd belong to this group, but as we have seen their enrichment is a complicated issue.

- the isotopes with a Q-value lower than 3272 keV but higher than 2615 keV, the end point of the γ natural background corresponding to the γ quanta of ^{208}Tl. ^{82}Se, ^{100}Mo, ^{116}Cd enter in this category.

- the group of notable isotopes for $0\nu2\beta$ includes also ^{76}Ge, ^{130}Te and ^{136}Xe. These isotopes remain interesting and competitive even at the price of a higher background in the region of interest, that has to be controlled more carefully. Germanium can reach impressively good radio-purity levels thanks to the R&D triggered by its large use in germanium detectors. Tellurium is also an attractive isotope thanks to its high isotopic abundance that is competitive without the need of enrichment. Xenon is a noble gas that can be easily enriched and purified.

Each isotope has different phase spaces and nuclear matrix elements, as shown in Fig. 1.5. Considering the space phase factor has a leading term proportional to the fifth power of the Q-value [53], the $0\nu2\beta$ isotopes with a high transition energy are favoured. Concerning the nuclear matrix element, it is not taken into account in the isotope choice given the big uncertainties connected to its calculation.

1.3.1 Experiments

Presently the $0\nu2\beta$ decay has not been discovered yet. The most famous claim of $0\nu2\beta$ decay detection has been made by a part of the Heidelberg-Moscow collaboration [72] in 2001 and then it has been strongly refused by the community, Ref. [73] reports a summary of the verbal crossfire that occurred. Today this claim is ruled out by the GERDA results. Even if this is the most famous case, it is not the first: several paper claiming the $0\nu2\beta$ decay detection appeared in journals, Ref. [74] lists an interesting historical collection of disproved discoveries. Presently several experiments are looking for the $0\nu2\beta$ decay given the big impact its discovery would have. Different technologies are employed, a short overview of the present and future situation is here presented:

Homogeneous detectors. The experiments belonging to this category are characterised by detectors containing $0\nu2\beta$ isotope. Five main technologies can be distinguished in this category:

Liquid-loaded scintillators. The detector is constituted by a scintillator loaded with the $0\nu2\beta$ isotope. This technology can easily employ large quantity of isotope with a consequent increase of the $0\nu2\beta$ sensitivity. The drawback of this technique is the low energy resolution. The KamLAND-Zen experiment [69] belongs to this detector family and is leading the field with the most stringent neutrino-mass limit [69]. Other two experiments will employ the same technology: the SNO+ experiment [75] is expected to start in 2019 and the THEIA experiment [76] is still in a R&D phase. Both are supposed to employ the ^{130}Te as candidate isotope.

Time-Projection Chamber (TPC). This kind of detectors can be used with liquid or gaseous isotopes (usually xenon) and in both cases an electric field is employed to drift the two electrons produced by the double-β decay. A double read-out is used in TPC detectors: a light and an ionisation signals are collected. After the decay, a prompt scintillation light signal is produced by xenon and points out the beginning of the event. The two emitted electrons ionise the medium along their tracks, creating an electric cloud of secondary electrons that are drifted by the electric field. In the case of a liquid TPC, the electrons are collected by the anode providing a signal proportional to the collected charge. In the case of a gaseous TPC, the electrons are accelerated in a dedicated volume close to the anode producing light by electroluminescence. This light is used to measure the energy and the track in the X–Y plane. This is the original approach adopted by the NEXT collaboration which provides energy resolutions less than 1 % FWHM in the region of interest. The energy resolution for liquid TPC is worst by about one order of magnitude. This technology is employed by the EXO-200 [70] experiment with a liquid TPC and the NEXT [77], PANDA-X III [78] and AXEL [79] experiments with a gaseous TPC. We remark however that PANDA-X III does not use electroluminescence but a "traditional" gain TPC.

Semiconductor detectors. Semiconductor diodes are interesting detectors for the $0\nu2\beta$-decay detection. The advantage of this technology is the good energy resolution. The leading experiments are GERDA [57] and MAJORANA [87] that are using germanium detectors. Their foreseen upgrade will be the LEGEND experiment [80]. The ^{76}Ge has a small Q-value compared to other nuclei (i. e. 2039 keV [88]), that falls in a region characterised by a more complicated background. Nevertheless the high purity of germanium semiconductor detectors and the leading techniques for the background rejection allows the GERDA experiment to have the lowest background index among all the $0\nu2\beta$ experiments, corresponding to 5.6×10^{-4} counts/(keV kg yr) [89]. Also semiconductors containing other $0\nu2\beta$ isotopes can be employed. For example the COBRA [90] experiment is employing Cd(Zn)Te.

Scintillators The $0\nu2\beta$ decay has also been investigated with scintillators where the $0\nu2\beta$ was embedded in the crystal. In this category of experiments we have to list the AURORA [65]

Tab. 1.3: Present limits set by the main experiments on the Majorana neutrino mass. For each experiment the technique used, the isotope studied with its mass, the exposure time and the resolution are listed. Note that the mass and the exposure are referred only to the $0\nu2\beta$ isotope. Currently the following experiments are presently running: CUORE, EXO-200, CUPID-0, GERDA and MAJORANA.

Experiment	technique	isotope	mass [kg]	exposure [kg yr]	FWHM [keV]	lim $T^{0\nu2\beta}_{1/2}$ [yr]	lim $\langle m_{\beta\beta} \rangle$ [eV]	Ref.
CANDLES-III	Scintillators	^{48}Ca	0.3	NA	111	6.2×10^{22}	$3.4 - 13.7$	[54]
ELEGANT VI	Scintillators	^{48}Ca	0.008	13.5	~ 213	5.8×10^{22}	$3.5 - 22$	[55]
NEMO-3	Tracking calorimeter	^{48}Ca	0.007	0.037	~ 679	2.0×10^{22}	$6.0 - 26$	[56]
GERDA	Ge diodes	^{76}Ge	31	47	$3 - 4$	8.0×10^{25}	$0.12 - 0.26$	[57]
MAJORANA	Ge diodes	^{76}Ge	27	26	2.5	2.7×10^{25}	$0.20 - 0.43$	[58]
CUPID-0	Scintillating bolometers	^{82}Se	5	3.4	23	4.0×10^{24}	$0.29 - 0.60$	[59]
NEMO-3	Tracking calorimeter	^{82}Se	0.9	4.9	~ 794	2.5×10^{23}	$1.2 - 3.0$	[60]
NEMO-3	Tracking calorimeter	^{96}Zr	0.009	0.031	~ 520	9.2×10^{21}	$7.2 - 19.5$	[61]
NEMO-3	Tracking calorimeter	^{100}Mo	7	34	~ 809	1.1×10^{24}	$0.33 - 0.62$	[62]
LUMINEU	Scintillating bolometers	^{100}Mo	0.45	0.1	$5 - 6$	0.7×10^{23}	$1.4 - 2.4$	[63, 64]
AURORA	Scintillators	^{116}Cd	0.3	4.7	~ 170	2.2×10^{23}	$1.0 - 1.7$	[65]
NEMO-3	Tracking calorimeter	^{116}Cd	0.4	0.02	~ 722	1.0×10^{23}	$1.4 - 2.5$	[66]
Solotvina	Scintillators	^{116}Cd	0.1	143	218	1.7×10^{23}	1.7	[67]
CUORE	Bolometers	^{130}Te	206	86	7.7	1.5×10^{25}	$0.11 - 0.52$	[68]
KamLAND-Zen	liquid scintillator	^{136}Xe	400	126	270	1.07×10^{26}	$0.06 - 0.17$	[69]
EXO-200	liquid TPC	^{136}Xe	75	178	~ 78	1.8×10^{25}	$0.15 - 0.40$	[70]
NEMO-3	Tracking calorimeter	^{150}Nd	0.04	0.19	~ 535	2.0×10^{22}	$1.6 - 5.3$	[71]

Tab. 1.4: Summary of the main future experiments searching for the $0\nu2\beta$ decay. The status label is meant to give an indication of the time scale: if the experiment is in a project (proj.) state, under construction (constr.), or in a demonstrator (demonst.) phase.

Experiment	technique	isotope	mass [kg]	lim $\langle m_{\beta\beta} \rangle$ [meV]	status	Ref.
LEGEND-200	Ge diodes	^{76}Ge	200	$30 - 93$	R&D	[58]
LEGEND-1000	Ge diodes	^{76}Ge	1000	$< 15 - 50$	proj.	[58, 80]
SuperNEMO	Tracking calorimeter	^{82}Se, ^{150}Nd	140	$70 - 73$	demonst.	[81]
CUPID	Bolometer + part. ID	^{100}Mo(^{130}Te)	250 (550)	~ 10	demonst.	[82]
AMoRE-II	Scintill. bolometers	^{100}Mo	100	$20 - 50$	R&D	[83]
THEIA	liquid scintillator	^{130}Te	12500	< 6.3	proj.	[76]
SNO+	liquid scintillator	^{130}Te	1200	$35 - 140$	constr.	[75, 84]
n-EXO	TPC	^{136}Xe	4000	$6 - 18$	R&D	[85]
KamLAND-Zen 800	liquid scintillator	^{136}Xe	750	~ 40	constr.	[86]
KamLAND2-Zen	liquid scintillator	^{136}Xe	1000	~ 20	proj.	[86]
NEXT-100	gaseous TPC	^{136}Xe	91	$46 - 170$	constr.	[77, 84]
NEXT-2.0	gaseous TPC	^{136}Xe	~ 1000	$17 - 40$	proj.	[84]
Panda-X III	gaseous TPC	^{136}Xe	180	$90 - 230$	R&D	[78]

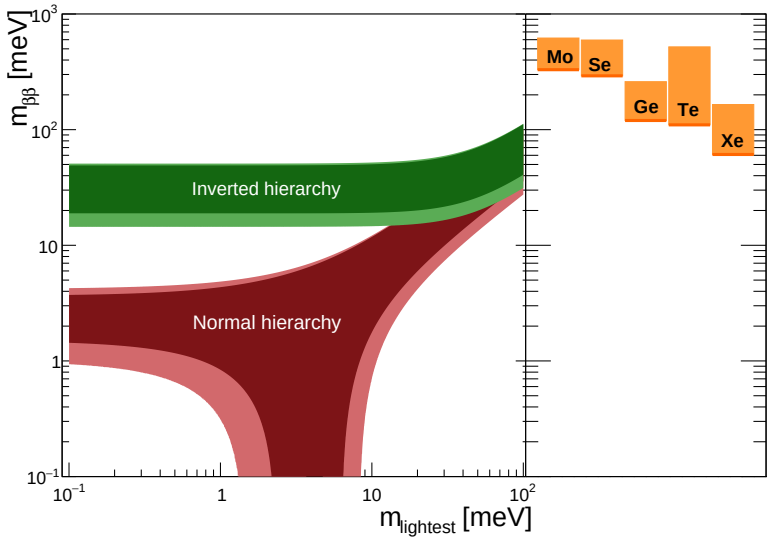

Fig. 1.7: Majorana mass as a function of the lightest neutrino mass (m_1 in case of direct hierarchy and m_3 in case of inverted hierarchy). The two bands represent the case of normal and inverted hierarchy. This plot has been adapted from Ref. [68]. The references considered for the limits on the Majorana neutrino mass are [57] for ^{76}Ge, [59] for ^{82}Se, [62] for ^{100}Mo, [68] for ^{130}Te and [69] for ^{136}Xe.

and Solotvina [67] experiments investigating ^{116}Cd with $^{116}CdWO_4$ crystals, and the ELEGANT VI [55] and CANDLE-III [54] experiments studying ^{48}Ca with CaF_2 scintillators.

Bolometers. These cryogenic detectors are promising devices to investigate the $0\nu2\beta$ decay for their remarkable energy resolution at the Q-value and an efficiency close to 100 %. A further description of these devices can be found in Ch. 2. Several experiments are exploiting this technology in this search field. Two main categories can be identified in this group: the experiments performing a pure calorimetric measurement and the ones that are performing active particle identification with a double read-out (see Sec. 2.6). The CUORE experiment [68] and its predecessors (MiBeta [91], CUORICINO [92] and CUORE-0 [93]) — investigating the $0\nu2\beta$ decay of ^{130}Te — belong to the first group. The CUORE experiment is now acquiring data with a detector mass of the order of the tonne scale. The TIN-TIN experiment [94] — still in a R&D phase — plans to employ bolometers containing ^{124}Sn exploiting a pure calorimetric measurement. Other experiments as LUCIFER [95] and its follow-up CUPID-0 [96], LUMINEU [97] and its follow-up CUPID-Mo [63] as well as AMoRE [98] belong to the new generation of $0\nu2\beta$ experiments with particle identification. These searches exploit scintillating bolometers coupled to light detectors to distinguish between $\beta(\gamma)$ events and α ones, reducing consequently the background. A deeper discussion of the CUORE experiment and its upgrade is postponed to Chapter 4.

Inhomogeneous detectors. These detectors use an external source. The only large-scale experiment in this field is SuperNEMO [81], that demonstrated its potentialities with NEMO 3 [99] and its predecessors. In the case of SuperNEMO, the $0\nu2\beta$ isotope is embedded in thin foils surrounded by a tracker that are then followed by a calorimeter. The tracker helps for the background rejection providing information on the decay topology and the calorimeter provides information on the

two-electron energy. All the $0\nu2\beta$ isotopes can be embedded in the source foil used. This allowed NEMO 3 experiment to measure a large number of nuclei: ^{48}Ca, ^{82}Se, ^{96}Zr, ^{100}Mo, ^{116}Cd, ^{130}Te, ^{150}Nd. A drawback of this technology is its poor energy resolution and efficiency.

A similar approach — detecting both the topology and the energy of the events — is proposed by the MOON [100] and DCBA/MTD [101] experiments. The first one proposed to use thin molybdenum foils surrounded by scintillating fibres for the detection of the event position and plastic scintillator plates for the energy measurement. The second one studied the possibility to employ a magnetic tracking detector to reconstruct the event topology.

Table 1.3 reports the state of the art for the most important limits achieved on the Majorana neutrino mass and $0\nu2\beta$ half-life. The best limit has been established by the KamLAND-Zen experiment with ^{136}Xe [69]. Table 1.4 lists the projections on the Majorana neutrino mass for future experiments. Fig. 1.7 shows the Majorana mass as a function of the lighter neutrino mass highlighting the most stringent limits obtained for four different isotopes.

2 Bolometers

In this chapter the bolometric technique is presented. We will see the basic elements that form a bolometer: its absorber and its thermal sensor, respectively in Sec. 2.2 and 2.3. In this context the detector working principle is described. Then, the limits to the energy resolution, that can be introduced by detector design features and by the read-out system, are enumerated in Sec. 2.4. Later, the most common model for bolometric detectors is presented in Sec. 2.5. In this occasion the main parameters modelling the bolometers are listed and a simplified dynamic response is derived. At this point a few techniques to identify different events are investigated in Sec. 2.6. Finally Sec. 2.7 presents the Neganov-Trofimov-Luke effect that can be used to boost particle identification.

2.1 Introduction

A bolometer is a radiation detector working at low temperatures used to measure radiation flux change via a temperature variation. In this work, we will extend this definition to include in this category also calorimeters. In this conception, bolometers are used as a particle detector where the energy deposited corresponds to a temperature increase. The idea to apply these devices for rare-event searches has been proposed in Ref. [102]. In this broad definition of bolometer, we will focus on devices working at temperatures lower than 30 mK and with masses in the 1 g − 1 kg range.

The working principle of these detectors can be described by:

$$\Delta E = C\ \Delta T, \tag{2.1}$$

where ΔE is the energy that we want to measure, ΔT the temperature variation corresponding to our signal and C the detector heat capacity. The energies considered in our applications are in a range between a few tens of eV to a few MeV. To illustrate the interest of low temperatures let us suppose that an energy of 1 MeV is deposited in 10 g of TeO_2 at 300 K and at 10 mK. In the first case the temperature will rise of $\sim 1.0 \times 10^{-10}$ mK while in the second case of ~ 1 mK because of the dependence of the specific heat with the temperature. Now, if we consider the relative temperature variation in percentage, it will be of 3.4×10^{-14} % at 300 K and 10 % at 10 mK. Obviously it is possible to detect the temperature variation only in the second case.

As will be seen later an interacting particle is measured thanks to the mediation of phonons. The high performance in terms of threshold and resolution obtained by these devices are due to the very small value of the low temperature phonon energy used in the mediation, that is of the order of 10^{-5} eV at 100 mK [103] and scales with the temperature.

Fig. 2.1 (*left*) shows a representation of a bolometer: its absorber — where the energy is released — is coupled to a thermal sensor able to read the temperature variation induced by the deposited energy. In this configuration an energy release increases the absorber temperature by steps causing a continuous warm up of the bolometer. It is required to connect the detector to the thermal bath through a controlled link to evacuate the heat released by energy depositions. In this case, the heat is transferred to the bath and the bolometer recovers its original temperature after each event. Each event acquires the shape of a

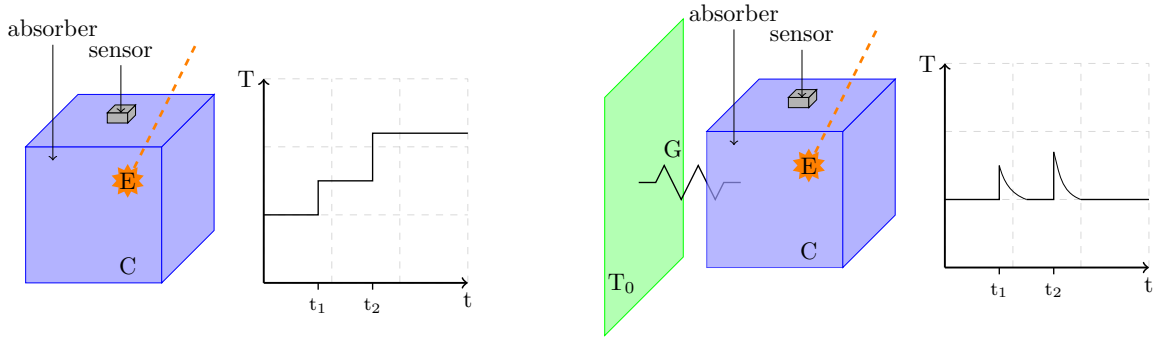

Fig. 2.1: *Left panel*: simplified scheme of a bolometer without a thermal link, the plot on the right shows the thermal response of this device after energy depositions. *Right panel*: simplified scheme of a bolometer connected to the heat bath by a thermal link. The left plot shows the temperature evolution of this device. The base temperature is recovered after each energy deposition.

pulse as shown in Fig 2.1 (*right*). The time required to return to the bath temperature — decay time — depends on the link conductance, as it will be shown later, and on the total heat capacity of the detector. Most detectors used in this work are quite slow, the rise time can be of the order of $5 - 30$ ms and consequently the decay time must be kept of the order of $10 - 300$ ms. In presence of a high event rate, two events with a short time delay with respect to the detector response can sum up. We will refer to this phenomena as pile-up from now on. Faster pulses — deriving from an improved thermal connection — can reduce the influence of this issue on the measurement, but in this case we have to pay attention not to evacuate the heat before it is transferred to the sensor, which would imply a signal loss.

2.2 Absorber

The energy of an event is deposited in the bolometer absorber that is usually made out of a crystal, as we will see. One of the main advantages of bolometers is the wide choice of the absorber material. This freedom allows us to embed the $0\nu2\beta$-candidate isotope inside the crystal increasing the detection efficiency close to 100 %. Despite the high flexibility in the material choice, the absorber has to meet a few conditions: a monocrystalline structure is required to ensure a homogeneous phonon response and it must have a low heat capacity at low temperatures. The demand for a low heat capacity derives from Eq. (2.1): for the same energy deposition, a lower heat capacity increases the temperature variation. The heat capacity is defined according to equation $C(T) = M\ c(T)$, where M is the number of moles and c the specific molar heat. In case of a generic crystal, the specific molar heat is composed by a lattice component c_l — proportional to the cube of the temperature — and an electron one c_e proportional to the temperature. Dielectric and diamagnetic crystals are preferred as absorbers because their specific molar heat has only the lattice contribution:

$$c_l(T) = \frac{12\pi^4}{5} N_A k_B \left(\frac{T}{T_D}\right)^3, \tag{2.2}$$

where N_A is the Avogadro number[1], k_B the Boltzmann constant[2] and T_D the Debye temperature. On the contrary metals specific molar heat can be approximated at low temperatures by the electron contribution

[1] $N_A = 6.022 \times 10^{23}$ mol^{-1}
[2] $k_B = 1.38 \times 10^{-23}$ J/K

according to:

$$c_e(T) = \frac{\pi^2}{2} N N_A k_B \frac{T}{T_F} = \gamma T, \tag{2.3}$$

where N is the number of conducting electrons in each atom and T_F is the Fermi temperature defined as the ratio between the Fermi energy and the Boltzmann constant.

The absorber is a key element of our system because the energy-heat conversion takes place in it thanks to phonon mediation. An absorber — working at 20 mK — has a distribution of thermal phonons at equilibrium with average energies of the order of 1 μeV. When some radiation interacts with the absorber, the energy deposited generates a hot area close to the impact zone, where athermal phonons — out of thermal equilibrium — are created with energies of the order of $10 - 50$ meV. The phonons, thus produced, have optical or longitudinal acoustical modes characterised by very high frequencies of the order of the Debye frequency ($\sim$ THz) corresponding to the aforementioned energy range. These phonons have a very short mean free path and will decay in less energetic phonons with a life time which varies as $1/f^5$, where f is the phonon frequency. These initial phonons travel at the speed of sound and their short life time allows them to travel only for about 100 crystal cells. Their inelastic interaction will divide their frequency increasing their life time and mean free path. This process of energy degradation continues till when the phonon energy is of the order of $\sim$ 1 meV — after a time of $10 - 100$ ps — causing the progressive extension of the mean free path. At this point we can start to speak of ballistic propagation in the case of pure crystals. The phonons are able to reach the crystal surfaces accelerating the thermalisation process. The speed of this process depends on the crystal surface quality: it will require a longer time for surface of higher quality. Finally a new equilibrium is reached: the system has a temperature higher than the initial one, which will be measured by the thermal sensor. In actual bolometers this process contributes to define the detector rise time. It may happen that only a part of the energy contained in the initial athermal phonon family can reach the sensor. In this case the bolometer cannot be considered any more a perfect calorimeter. Finally the heat will be evacuated by the thermal link, connecting the detector to the bath. In reality the situation is not so simple because a part of the energy can be lost before the complete thermalisation in the absorber through the thermal link. For more information and details about the evolution of the phonon population generated by the impinging particle, consult Ref. [104, 105].

2.3 Thermal sensors

The thermal sensor can be made according to different technologies requiring different read-out approaches. An overview on the main sensor typologies follows below with more details about their read-out system in Fig. 2.2.

Doped semiconductors can be used as temperature-to-resistance converters working close to the metal-insulator transition. Several devices belong to this category, but we will concentrate on NTD (*Neutron Transmutation Doped*) germanium thermistors since they were largely employed in the realisation of this work. These devices were biased with a constant current, therefore a temperature variation — translated in a resistance variation — is measured as a voltage change. More details about NTDs are presented later in this section.

TES (Transition Edge Sensor) are sensors based on a superconductive transition: a temperature variation corresponds to a resistance variation. These devices are characterised by a high sensitivity in a small range of temperatures where the superconducting transition takes place. We can divide these sensors in two groups based on their normal-state resistance: low-resistivity TES and high-resistivity TES. The first ones have resistance of the order of a few $10 - 100$ mΩ and require a read-out system based on SQUID (*Superconducting Quantum Interference Device*), a sensitive

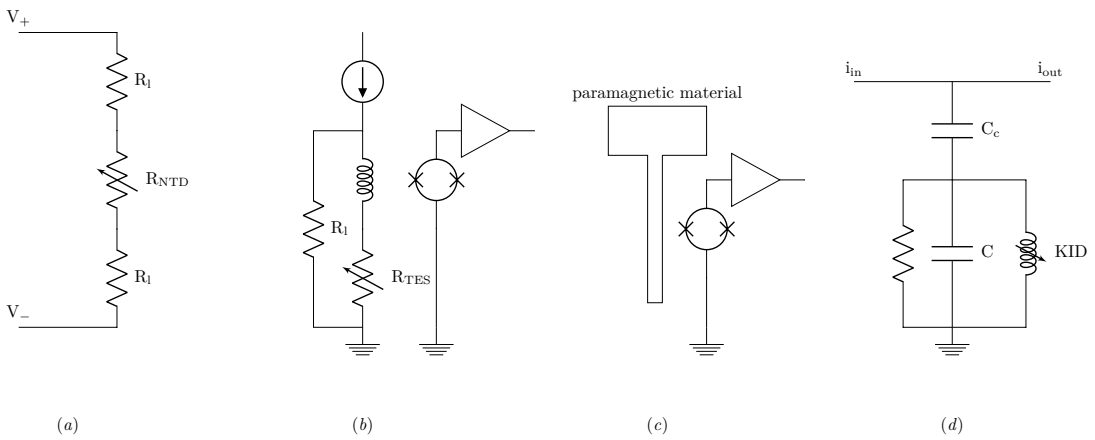

Fig. 2.2: *From left*: (a) A common bias circuit for NTDs is constituted by a differential circuit formed by only two load resistors (R_l) crossed by a constant current. (b) TES bias circuit. The TES induces a variation in the inductance magnetic field that is read by a SQUID. (c) The magnetic field variation is read by a SQUID also in this case. (d) KID bias circuit is formed by a resonant circuit. Many circuits like this can be put in parallel on the same read-out line creating a multiplexed measurement.

magnetometer. The second ones can have resistances of the order of the 100 kΩ − 10 MΩ at the normal state and can be read with a NTD-like read-out system. This second kind of devices is not so common, in fact it has been developed only by the group where this work was carried out so far.

MMC (Metallic Magnetic Calorimeter) are temperature sensors whose detection principle is based on a measurement of magnetisation, that is inversely proportional to the temperature. They are constituted by a paramagnetic metal placed inside a SQUID loop. The latter is able to convert a magnetisation variation into a voltage signal. This technology is characterised by a good time resolution able to reduce significantly the pile-up.

KID (Kinetic Inductance Detector) are superconducting devices that are mainly used for photon detection but they can be used also for phonon measurement. An energy released in these devices breaks Cooper pairs and increases the inductance, that is inversely proportional to the Cooper pair number. The combination of this system with a capacitor forms a resonant circuit with a characteristic frequency. This is a convenient system because permits the multiplexing of different channels that are read by a single read-out line. This can be done by assigning a different resonant frequency for each circuit.

The logarithmic sensitivity α — defined in Eq. (2.4) — quantifies the sensor response as a function of a temperature variation and can be used to compare two resistive sensors like the NTD and TES:

$$\alpha = \frac{d\ lnR}{d\ lnT} \sim \frac{\Delta R}{R}\frac{T}{\Delta T}. \tag{2.4}$$

We can divide resistive sensors in two categories: the ones characterised by a positive α as the TES and the ones with a negative α as the NTD. In general, TES are characterised by a higher sensitivity on a small range of temperatures and NTDs have a smaller sensitivity ($|\alpha|$) but on a larger temperature range. The choice between them depends on the experiment requirements. The detectors studied in this work have been equipped with NTD germanium and/or high-resistance TES because of their easier operability and scalability. These two technologies will be presented in more details below.

NTD germanium thermistors are constituted by a small parallelepiped cut out of a germanium crystal doped with neutrons at a nuclear reactor in our case. These devices are then annealed to improve the crystal uniformity. The two main processes — occurring after the neutron capture — are the β decay of ^{75}Ge in ^{75}As and the electronic capture of ^{71}Ge that produces ^{71}Ga. The first one produces a n-doping and the second a p-doping, both are activated during the annealing. The doping of germanium is a delicate process: a too high concentration of n-type impurities will decrease the resistivity of the sensor by the increase of the energy levels close to the conduction band. For even higher impurity concentration the material will assume a metallic behaviour. On the contrary, a low level of concentration will trap the carriers in the valence band and the resistivity will increase: the material will behave as an insulator. The material with a not-too-high and not-too-low donor concentration — hence with properties of a "bad" insulator or a "bad" metal — is close to the metal-insulator transition. There is a very well defined impurity concentration that characterises the metal-insulator transition: it is of the order of $5 - 8{\times}10^{16}$ cm^{-3} net dopant concentration for germanium. A material in this transition is interesting because of its ability to change properties as a function of its temperature and magnetic field. The optimum doping concentration for a NTD germanium is slightly lower than the one corresponding to the metal-insulator transition. NTD germanium enters the category of Anderson insulators because the n-type doping introduces disorder in the lattice. Their resistance R varies as a function of the temperature T according to:

$$R = R_0 exp\left(\frac{T_0}{T}\right)^n, \tag{2.5}$$

where R_0 and T_0 are two parameters determined by the doping concentration. R_0 depends also on the geometry of the sensor. T_0 values are only a function of the doping and decrease for higher concentrations. The exponent n reflects three different types of conduction:

$n = 1$ the insulator behaves as a semiconductor where the conduction is made through the gap. When the electrons in the valence band receive enough energy, they can move to the conduction band decreasing the material resistivity. In this case the Eq. (2.5) is named after Arrhenius.

$n = 1/4$ the insulator resistivity can be described according the Variable Range Hopping (VRH) model, theorised for the first time by Mott [106]. The VRH model has been designed in case of glass-based materials working at low temperatures. The model assumes that the charge carriers are trapped in three-dimensional potential minima. The conductance of the material is done through the movement of the electrons from a minimum to another one by tunnel effect. The movement direction is determined balancing between the energy variation $\Delta\varepsilon = \varepsilon_j - \varepsilon_i$ of the two sites and their distance $r_{ij} = r_j - r_i$. In fact an electron will move to a site even if it is farther apart in the case in which the energy difference is smaller. This is contrary to the result obtained by a simple tunnelling effect when an electron will jump to the closest minimum whatever will be the energy difference. The transport is usually induced by the phonon interactions that provides energy to the electron.

$n = 1/2$ Efros and Shklovskii improved Mott model including the Coulomb interaction. In fact an electron tends to avoid movement towards potential minima already occupied by another electron because it would be repulsed. The arrival site depends on a combination of electric repulsion, minimum distance and energy variation.

In practice, the exponent value may be different from the three values (n = 1, 0.5, 0.25) due to various phenomena taking place in the same temperature range [107]. Anderson insulators can undergo one of these models or a combination of the three depending on the temperature range. In our temperature range, the NTDs follow the Efros-Shklovsii model, for this reason we fix the exponent to 0.5 in the analysis of resistance-temperature characteristics.

The electrical contacts of the NTD are made with two opposite gold pads implanted in the germanium wafer. There are two geometries: either the contacts are placed only on two opposite faces of the sensor or wrapped around (i.e. they present a small prolongation of the contacts on the sensor top surface).

The thermistor gluing is a critical point in the detector mounting. In fact different thermal contractions between the absorber crystal and the NTD at low temperatures can stress the sensor, raising its resistivity. The lattice contraction can modify the band structure changing the resistance-temperature dependence. In order to reduce the effects of the thermal contractions — that on the one hand stresses the thermistor, but on the other hand may also induce cracks in the absorber — the NTD is glued with a matrix of spots.

High-resistance TES are made with films of Nb_xSi_{1-x}, a compound composed of a superconductor (niobium) and a semiconductor (silicon). This material is a superconductor when its two constituting elements are in a precise relation regulated by the niobium concentration (x) that is usually higher than 12 %. NbSi is an amorphous material that ensures its high resistance in the normal state and makes it an interesting sensor for our read-out system. The main characteristics of this kind of sensors are here listed:

the niobium concentration gives us information about the material resistivity and its critical temperature, where the transition between the normal state and the superconducting one takes place. A low niobium concentration will increase the resistance and lower the critical temperature of the material.

the thickness of the film increases the possible paths accessible to the electrons, lowering the sensor resistance and increasing the transition temperature. A thin film is preferred for its low heat capacity to work at temperatures of the order of 10 mK, but its fabrication can be complicated. Indeed extra care has to be taken during the fabrication process to prevent any dust or defect to break the film continuity.

the sensor annealing allows us to increase the disorder inside of the sensor, the opposite behaviour with respect to NTDs. The sensor annealing increases its resistance and lowers the transition temperature.

The transition temperature depends on the niobium composition, the annealing and also the film thickness.

This kind of sensors requires to be formed by long and thin strips of NbSi that are usually shaped in a meander or spiral to achieve high-resistance TES. The NbSi sensors can be fabricated according to these two processes:

- the film is deposited via ultra high vacuum co-deposition of niobium and silicon film and then patterned by lithography and etching techniques.
- the film is deposited on an already patterned substrate and then it is lifted off.

In both cases, edge effects can appear modifying the behaviour of the sensor.

These sensors can be biased either with a constant voltage or a constant current. The choice between one of the two methods depends on the geometry of the sensor:

- when the sample has a short distance between the contacts, a voltage bias is employed as in the case of low-resistance TES. This is preferred because otherwise an event increases the TES resistance and dissipates a Joule power $P = IR^2$, that can heat up the sensor increasing its temperature and establishing a positive feedback. This process of heating can lead the sensor to the normal state preventing its cooling down as a consequence of an energy deposition. In case of a voltage-based bias, the power dissipation $P = V^2/R$ decreases after an energy deposition.

- a TES constituted by a long film can present inhomogeneities that can cause the partial transition of the sensor when it is biased with a constant voltage. If a part of the sensor is in the normal state and a part in a superconductive one, the sensor presents a lower sensitivity and an unstable behaviour.

The TES employed in this work belonged to the second group, therefore they were biased by a constant current. Obviously the electro-thermal feedback is positive, but by limiting the current bias we can work in a regime with a small positive feedback that does not cause detector instabilities [108].

For a more detailed description of this kind of devices, consult Ref. [108, 109].

We have seen two kinds of resistive sensors biased with a constant current. They have a voltage signal ΔV produced by a resistance variation ΔR, as we have seen, depending on the bolometer temperature:

$$\Delta V = I\Delta R = -\frac{\partial R}{\partial T} I \Delta T. \tag{2.6}$$

Considering the definition of logarithmic sensitivity α in Eq. (2.4), we can rewrite the last formula as:

$$\Delta V = \alpha \frac{R}{T} I \Delta T = \alpha V \frac{\Delta T}{T}, \tag{2.7}$$

where V is the sensor voltage in absence of energy deposition and $\Delta T/T$ is the sensor relative temperature variation. This equation presents the key parameters that have to be kept under control in order to maximise the detector response. The sensitivity and the voltage are characteristics of the sensor. A resistive sensor — with a high voltage — seems preferable, but in practice a compromise between the signal amplitude and the noise is needed as we will see in the following section. The maximisation of the relative temperature variation can be achieve with a good heat collection from the crystal, that as we will see later depends on the glue coupling and the thermal link.

2.4 Energy resolution

Bolometers are extraordinary detectors that can reach record resolutions, for example the CUORE-0 experiment reached a resolution of the order of 0.2 % FWHM at the 2615-keV γ-quanta of ^{208}Tl [110] with NTD sensors. Multiple factors contribute to enlargement of bolometers resolution, they are discussed below. The condition necessary but not sufficient to have a good energy resolution is to have a high signal-to-noise ratio.

This can be achieved maximising the signal on one side and minimising the noise on the other side. In the first case, we have to act on the detector design to optimise the thermal coupling. In particular we want to be sure that all the heat generated in the crystal moves to the thermal sensor. This can be obtained with a good contact between the absorber and the sensor through the glue. Also the thermal link has to be tuned to avoid energy evacuation before its complete transfer to the sensor that would reduce the detectable energy fraction. In our detectors the main thermal link passes through the sensor bonding wires, obliging the heat to pass in the sensor before being evacuated. However a part of heat can escape also from the crystal clamping system. This effect has to be negligible to avoid energy losses.

In the case of the noise, the causes can be divided in two main groups: noise sources intrinsic to the sensor and the ones independent from the thermistor. The first typology includes:

Johnson Noise. The Johnson noise $n_J$is due to the thermal agitation of electrons inside the conductors. The produced noise is a white noise. In first approximation it can be defined according to the formula:

$$\sqrt{n_J^2} = \sqrt{4k_B T R} \quad [V/\sqrt{Hz}], \tag{2.8}$$

where k_B is the Boltzmann constant, T the temperature and R the sensor resistance. In the sensor design, we can reduce the Johnson noise by lowering the thermistor resistance and acting on the working temperature.

Flicker noise. The flicker noise is also known as 1/f noise for the shape of its power spectral density. It becomes dominant for low frequencies and is particularly troublesome in bolometric measurements because it populates the signal region. The flicker noise occurs in almost all electronic devices and can have different origins.

Shot noise. The shot noise is originated by the discrete nature of the charge carriers that can introduce random fluctuations of the electric direct current.

On the contrary the noises independent from the sensor physics are:

Electronic noise. The electronic read-out contributes to the introduction of noise in the bolometric signal. A low noise electronics is therefore indispensable to preserve a good resolution.

Photon noise. This kind of noise concerns only photo-detectors. It is generated by the blackbody radiation. Let us imagine to have an ideal light detector perfectly sealed in its holder at the bath temperature. In this case the detector sees the black body radiation of materials at a temperature of the order of 10 mK, the signal-to-noise ratio of the detector does not allow us to discriminate single events. When the detector is not completely sealed and is able to see the black body radiation from warmer stages, the photons flux contains events belonging to the tail of the distribution with higher energy. These events can be detected with an improved signal-to-noise ratio. For more detail see Ref. [111, 112].

But not all noise sources can be controlled with the bolometer and electronic optimisation. The thermodynamic noise belongs to this group and originates from the connection to the heat sink through the thermal link. The heat exchange between the bolometer and the thermal bath is continuous. This constant heat movement contributes to the detector internal energy fluctuation, that can be expressed with the following equation:

$$\Delta U_{RMS} = \sqrt{k_B T^2 C}, \tag{2.9}$$

where k_B is the Boltzmann constant, T the detector temperature and C its heat capacity. This energy is called the *ultimate energy resolution* and is directly translated in a signal noise. It can be reduced in a detector-design phase choosing materials with a small heat capacity and after in a detector-operation phase by working at low temperatures. It is interesting to notice that the internal energy fluctuations do not depend on the energy released in the crystal.

Also energy losses and fluctuations belong to this category. Fig. 2.3 shows a scheme of the possible energy losses during the interaction with the absorber. An incoming event can interact with the nuclei or with the electrons that compose the absorber crystal. We will have a nuclear interaction in the first case that can result in creation of structural defects or in a heat deposition in the absorber. In the second case, the incident radiation can react with absorber electrons, producing electrons or photons. A part of their energy will end up in heat, but a fraction can be emitted as light and/or be lost by the formation of secondary electrons that can escape from the crystal. The energy fluctuations can be caused by crystal lattice defects that can trap a part of the energy. Also position effects belong to this category, a part of athermal phonon energy can move to the sensor before its complete thermalisation depending on the interaction point. In addition, amplitude drifts depending on the time can worsen the energy resolution when they are not well corrected.

Also vibrations are a dangerous issue for the energy resolution. They act both on the read-out noise through the cabling and on the thermal noise. Wire vibrations cause friction between the conductor and the insulator of the wire. This friction can generate an accumulation of charges that introduces noise in

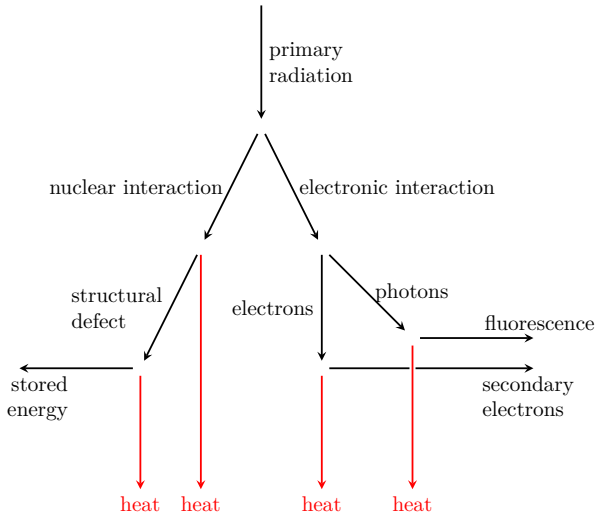

Fig. 2.3: Scheme summarising the possible energetic interactions that can occur in a bolometric detector. It has been adapted from Ref. [113].

the conductor when freed, this is also known as tribo-electric effect [114, 115]. Wire vibrations can also induce electrical capacitance variations which translate into noise. Moreover the vibrations introduce frictions between the main absorber and its support. This friction generates heat that contributes to the measurement as an extra noise. A few techniques employed to control this issue are presented in Sec. 3.1.2.

2.5 Thermal model, a brief introduction

Bolometers have a quite simple structure: a thermal sensor glued on an absorber — kept by supports in a holder at cryogenic temperatures — with a thermal link. The behaviour of a bolometer can be sketched with a thermal circuit. There is a direct analogy between a thermal circuit and an electronic one. Each node of the circuit is defined by a temperature that can be seen as an equivalent of a voltage. In our case, the nodes of the system are the sensor, the absorber and the thermal bath. The connection between the nodes is implemented with glue, bonding wires and PTFE clamps. In our model, these elements are characterised by their ability to transmit the heat between two nodes, that is measured through their conductance. That is equivalent to a resistor that expresses the ability to resist to the passage of a current in an electronic circuit. The thermal conductance is described with a temperature power law, defined by:

$$G(T) = g_0 T^{\alpha} \quad [W/K], \tag{2.10}$$

where g_0 and α are two parameters: the dimension of g_0 are $\mathrm{W/K^{\alpha+1}}$ and α is dimensionless. An energy deposition in a node of the system increases its temperature at first. The generated heat will be evacuated to the close nodes through the conductances. The energy transport from a node at a temperature $\mathrm{T_1}$ to a second node at $\mathrm{T_2}$ through a conductance $G(T)$ is described by:

$$P = \int_{T_2}^{T_1} G(T) dT. \tag{2.11}$$

Fig. 2.4 shows a sketch of a bolometer model, a few considerations about it follow below.

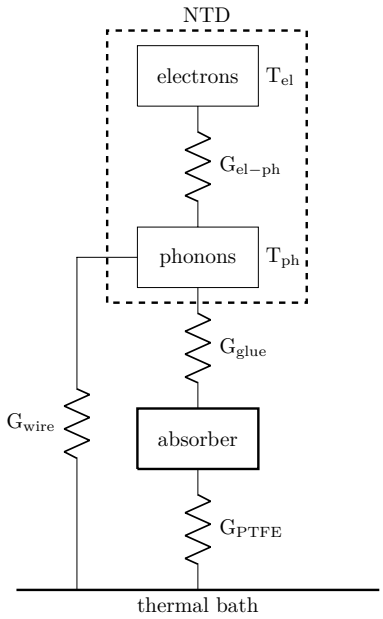

Fig. 2.4: Thermal scheme of a bolometer.

Hot-electron model In this scheme the thermal sensor is composed by two different stages, one constituted by the lattice and one by the electrons, at different temperatures. The two stages are connected by a conductance, defined as the electron-phonon conductance. This representation well describes the results of the introduction of a bias system in the detector structure. The sensor read-out is done by biasing it with a constant current and reading the voltage developed at the resistor extremities. The current flow introduces a power $P = R\ I^2$ in the sensor that heats up the electrons to a temperature T_{el}, while the lattice of the sensor stays at a lower temperature T_{ph} because of the thermal decoupling between electrons and phonons.

Heat capacities Each node of the system is characterised by a heat capacity. The crystal — usually diamagnetic and dielectric — has a heat capacity dominated by its lattice and described by the product of the crystal mole number with the lattice specific molar heat in Eq. (2.2). The thermal sensor, that is composed by two stages constituted by the phonons and the electrons, has two different heat capacities. The heat capacity of the phonon stage is dominated by the lattice as the absorber and is controlled by the same equation. The heat capacity of the electron stage is usually taken as proportional to the temperature. In this model, we will consider the heat capacity of the thermal bath as infinite.

G_{glue} The glue conductance considers the link between the sensor and the absorber. It is a delicate point because of the reproducibility of the gluing: this value strongly depends on the surface and the thickness of the glue deposition. The glue conductance is mainly related to the resistance opposed to the heat flow by the contact between dissimilar surface. As boundary conductances, this one has an approximate cubic temperature behaviour. Since the glue conductance belongs to the boundary conductance, it is commonly called Kapitza. This name originates from an experiment carried out in 1941 by Kapitza that discovered a low thermal conductance between liquid helium and copper [116]. This result was unexpected because both materials are good conductors. As an extension all the conductance surface phenomena are incorrectly named after Kapitza. The

Tab. 2.1: Electron-phonon conductances. The exponents highlighted in bold have been fixed in the analysis. Note that the conductance definition is $(\alpha+1)g_0T^\alpha$ in Ref. [118, 120, 121, 119, 122, 123] that is different from the convention in Eq. (2.10) used in this work. The conductance values corresponding to a temperature of 30 mK have been renormalised according to the sensor volume.

	Ref.	n_A-n_D [cm^{-3}]	NTD type	volume [mm^3]	g_0 [$W/K^{\alpha+1}$]	α	G_{el-ph} @ 30 mK [nW/(K mm^3)]
Wang	[118]	6.6×10^{16}	12	0.6	0.8×10^{-2}	5	1.9
Wang	[118]	6.6×10^{16}	12	0.6	0.13×10^{-2}	4.5	1.7
Alessandrello	[120]	7.2×10^{16}	23	6.0	70×10^{-2}	4.6	65
Aubourg	[121]	6.3×10^{16}	28	1.5	2×10^{-2}	**5**	1.9
Aubourg	[121]	6.6×10^{16}	12	1.5	6×10^{-2}	**5**	5.8
Aubourg	[121]	7.2×10^{16}	23	1.5	9×10^{-2}	**5**	8.7
Soudée	[119]	7.2×10^{16}	23	2.1	0.24×10^{-2}	**4**	4.6
Pasca	[122]	6.6×10^{16}	31	30	7×10^{-2}	4.5	1.9
Pasca	[123]	6.4×10^{16}	34B	9.0	88×10^{-2}	5.4	3.4
Pasca	[123]	6.0×10^{16}	38	33	8.7×10^{-2}	4.4	2.5
Pasca	[123]	5.9×10^{16}	36	33	5.8×10^{-2}	4.5	1.2

single-spot glue conductance has been measured in Ref. [117]:

$$G_{glue} = 2.6\times10^{-3}\ T[K]^{3.0845}[W/(K spot)], \tag{2.12}$$

where the spot has a cylindrical shape (Ø1×0.05 mm). Other measurements [118, 119] of the glue conductance have been carried out, but usually the sensors were glued with film on copper.

G_{el-ph} The electron-phonon conductance is taken into account by the hot-electron model and expresses the conductivity between the electron and phonon stage in the sensor. An exponent α of around 5 has been experimentally measured for the electron-phonon conductance. Table 2.1 reports the main results obtained in the electron-phonon measurements for NTD-germanium thermistors.

G_{wire} The bonding-wire conductance connects the sensor to the thermal bath in our model. First of all we have to notice that the connection between the thermal bath and the NTD does not pass through the electron stage of the sensor, but through its lattice. This effect is counter intuitive since the heat conductance of the wire is due to the electrons in the conductance band and there is of course electrical contact between the wire and the sensor. But real results can be justified only with a thermal link placed in this way [124]. The bonding-wire conductance can be described by Eq. (2.10), where the exponent α is shaped by: a boundary conductance due to the contact of two different surfaces — implemented between the NTD and the gold pad — and a metallic one done by the wire itself. The boundary component has a cubic behaviour with the temperature and the metal conductance is proportional to the temperature. The resulting exponent has an intermediate value between the two, but usually the boundary conductance has a dominant effect. The bonding wire conductance has been measured experimentally in Ref. [117] and its value is here reported:

$$G_{wire} = 3.6\times10^{-5}\ T[K]^{2.419}[W/K mm^2]. \tag{2.13}$$

This value is renormalised by the section of the pad area.

G_{PTFE} The conductance provided by PTFE between the absorber and the bath is small with respect to the bonding-wire one. The conductance is provided by the contact between two different materials

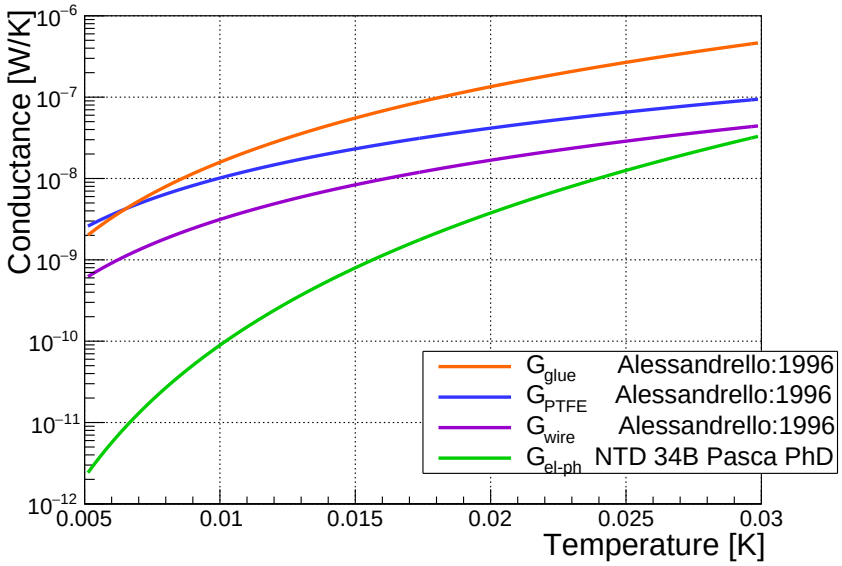

Fig. 2.5: Conductance of the various bolometer elements as a function of the temperature in the $5 - 30$ mK range.

— the crystal and the support — and the conductance of the PTFE itself. An example of a PTFE conductance measured experimentally is reported in Ref. [117] for 10 g of material:

$$G_{PTFE} = 1.2 \times 10^{-4}\ T[K]^{2.0366}[W/K]. \tag{2.14}$$

In absence of more precise measurements, this value gives the order of magnitude of the PTFE contribution.

Fig. 2.5 shows the conductances here discussed (from Ref. [117, 123]) giving an idea of their values in the case of a NTD belonging to the 34B batch, glued with nine Ø1 × 0.05-mm spots and characterised by a contact area of 6 mm^2. In Chapter 5, the measurement of the glue and electron-phonon conductances performed in this work are reported.

The dynamic response of a bolometer represents the temporal evolution of the temperature signal after an instantaneous energy deposition in the absorber. In this case we will refer to a simplified model for the dynamic response, as the one reported in Fig. 2.1. The absorber is defined by a heat capacity C and is connected to the thermal bath — at a constant temperature T_0 — by a conductance G. An energy, $E = C\Delta T$ deposited in the absorber, is evacuated through the conductance G and its time variation is described by:

$$P = \frac{dE}{dt} = C\frac{\Delta T}{dt}. \tag{2.15}$$

In case of a temperature difference between the bolometer and the bath, the conductance, the heat capacity and the temperature variation are linked by the formula:

$$-\,C\frac{\Delta T}{dt} = G\ \Delta T, \tag{2.16}$$

where the minus sign takes into account the fact that the temperatures decrease with the time. If now we add an instantaneous energy deposition due to a particle, the corresponding power can be described with

a Dirac delta function $P = E\ \delta(T)$. As, this energy is progressively absorbed by the bath, the energetic budget becomes:

$$E\ \delta(T) - C\frac{\Delta T}{dt} = G\ \Delta T. \tag{2.17}$$

Solving this differential equation, the pulse shape can be described by:

$$\Delta T(t) = \frac{E}{C} e^{-\frac{G}{C}t}. \tag{2.18}$$

This is a rough evaluation, that does not consider the pulse rise time, but it provides a few interesting concepts. First of all, the pulse amplitude is equal to the ratio between the energy and the heat capacity. The amplitude linearity in the energy assures us the possibility to reconstruct an energy spectrum and the inverse proportionality with the heat capacity reminds us to control this parameter in the absorber choice. The second key information is the pulse decay time C/G that depends on the heat capacity and the conductance to the bath. This information suggests us to act on these two parameters in the detector design phase to control the pile-up issue. In first approximation these considerations are true, but the bath coupling has to be designed also considering the rise time to avoid the heat evacuation before its complete thermalisation.

The sensor bias can provide us with a small help in the detector time-response issue thanks to the electro-thermal feedback. This is valid only for sensors characterised by a negative logarithmic sensitivity α, defined in Eq. (2.4), as the NTDs. This effect is produced by the introduction of a joule power $P = \Delta R\ I^2$ — due to the current flowing in the sensor — in the Eq. (2.17). Exploiting the definition of logarithmic sensitivity in Eq. (2.4), this power can be redefined as:

$$\Delta R\ I^2 = \alpha\frac{\Delta T}{T} R\ I^2 = \alpha\frac{\Delta T}{T} P. \tag{2.19}$$

The resulting energy budget becomes:

$$C\frac{\Delta T}{dt} + \left(G - \frac{\alpha P}{T}\right)\Delta T = E\delta(t). \tag{2.20}$$

Solving the differential equation, we obtain a pulse shape similar to the one of Eq. (2.18):

$$t_{decay} = \frac{C}{G - \frac{\alpha P}{T}}. \tag{2.21}$$

The decay time is shortened for sensor with a negative α, as the NTDs, and extended for sensors with a positive α, like the TES. In the first case this effect is referred as negative electro-thermal feedback, while in the second case as positive electro-thermal feedback.

Considering a more complete thermal model, like the one in Fig. 2.4, the dynamic response would be more complicated. The time response does not depend on a single decay time, but they will be constituted by a sum of exponentials with different time constants. These will depend on the combination of the various parameters of the model. The full solution can be found in Ref. [125].

2.6 Particle identification

The calorimetric response of bolometers is not sensitive to the charge and the position of the energy deposited. This lack of particle identification can be an issue for the background control. But the freedom in the absorber choice could allow us to use scintillation and/or ionisation to provide a secondary

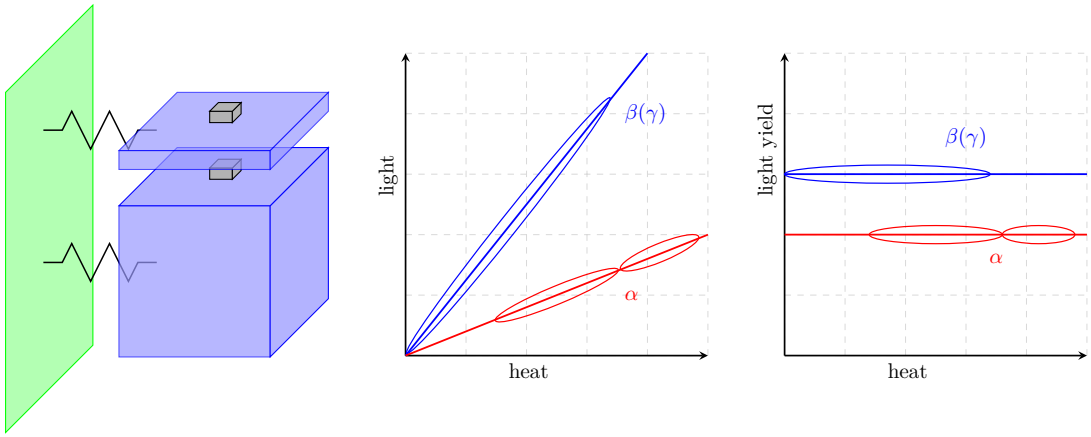

Fig. 2.6: *Left panel*: scheme of a bolometric light detector coupled to a heat detector. *Middle panel*: example of a heat-light scatter plot obtained with a composite bolometer. *Right panel*: example of the light yield as a function of the energy. In both plots the crystal has an α quenching factor lower than 1.

information on the occurred event topology. A double read out has to be implemented: an ionisation signal can be measured directly from electrodes deposited on the bolometer surface and a light emission can be detected by a secondary detector. The choice of the latter one is restricted by the request of a cryogenic and radiopure working environment: the light detection is usually implemented with a bolometer. Fig. 2.6 (*left*) shows a scheme of bolometer coupled to a light detector working according to the same principle.

The particle identification performed with a double read-out of heat and light signals is used by experiments searching for the $0\nu2\beta$ decay (as AMoRE [98], LUMINEU and its follow up CUPID-Mo, LUCIFER followed by CUPID-0) and dark matter (as CRESST [126], COSINUS [127] and ROSEBUD [128]). The particle identification obtained with the ionisation channel is implemented by the EDELWEISS [129] experiment and CDMS [130].

A double read-out exploits the fact that different particles will produce a different ionisation/light outputs: particles which interact mainly with the electrons will produce more ionisation than those interacting with the nuclei; with respect to light emission, it is difficult to make generalisation. In most of the cases, the light emitted by α particles will be lower than for β and γ. The α interaction is more localised and the particle has access to a smaller number of impurity centres that contribute to the light emission [131]. The light centres absorb all the possible α's energy till their saturation and the remaining energy is deposited as heat. This is the reason why there is a quenching between energy of α's and $\beta(\gamma)$ events. In most of the cases, crystals have an α light quenching factor lower than 1, that produces a scatter plot as the one in Fig. 2.6 (*middle*). According to literature, only ZnSe crystal presents an α quenching factor higher than 1. A conclusive physical explanation of this effect has not been found yet, presently it is thought that it is related to special defects in the crystalline structure [132]. Really good scintillators — as $CdWO_4$ and $Bi_4Ge_3O_{12}$ used in dark matter experiments — are able to distinguish α, $\beta(\gamma)$ and nuclear recoils.

Till now, we have spoken about the light output but its value depends on the energy deposition that generated it, as it is clear from Fig. 2.6 (*middle*). The light yield — defined according Eq. (2.22) — is independent of the original energy deposition in our energy region and is more useful to compare different results. This quantity is defined as the ratio between the light L collected by the light detector and the heat E measured in the main bolometer absorber:

$$LY = \frac{L}{E}. \tag{2.22}$$

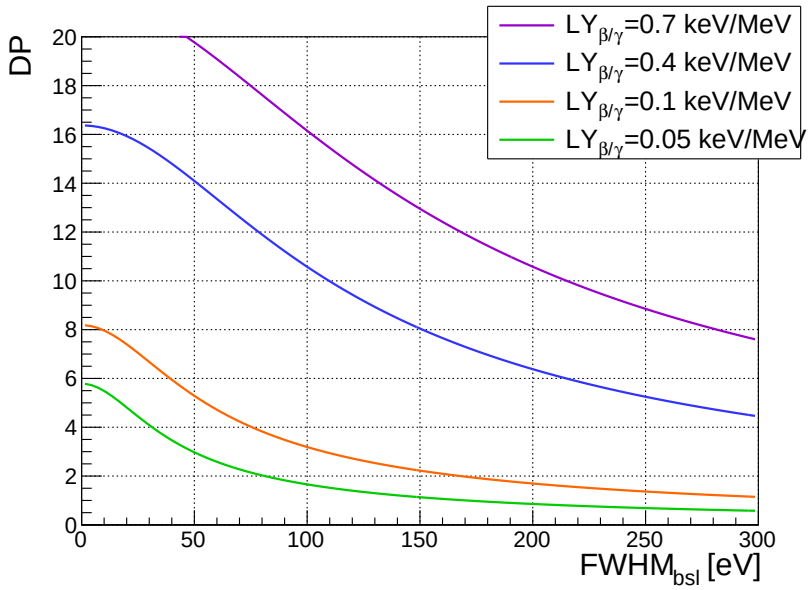

Fig. 2.7: Discrimination power at 2.6 MeV as a function of the light-detector FWHM baseline for different light yield.

Fig. 2.6 (*right*) shows a sketch of the light yield as a function of the energy deposited in the main crystal. In order to compare the separation between the $\beta(\gamma)$ band and the α one in different experiments, one can define the discrimination power DP as:

$$DP = \frac{\left|LY_{\beta/\gamma} - LY_{\alpha}\right|}{\sqrt{\sigma^2_{\beta/\gamma} + \sigma^2_{\alpha}}}. \tag{2.23}$$

The meaning of this formula is quite intuitive, we have a better $\beta(\gamma)$ and α separation for a large distance between the two bands and small widths. Fig. 2.7 shows the relationship between these parameters: the discrimination power for 2.6-MeV energy deposited in the main bolometer is represented as a function of the baseline FWHM in case of four different $\beta(\gamma)$ light yields. It has been calculated with a few assumptions: the quenching factor of the α light with respect to the $\beta(\gamma)$ is 0.2; the band width (both in the case of α and $\beta(\gamma)$ events) is composed by the sum of the baseline width and the enlargement generated by photon statistics; the light derives from photons of 2 eV that corresponds approximatively to the maximum of emission wavelength for scintillating crystals. The request of low-noise light detectors becomes essential for crystals characterised by a low light yield.

The crystal volume is an important factor in detector construction: a large crystal is logically preferable for its larger mass — that in view of a tonne-scale experiment means a lower number of channels — but on the other hand it is problematic for the light yield. In fact the light produced by a large-mass crystal will be more probably self absorbed before reaching the light detector, reducing significantly the light output.

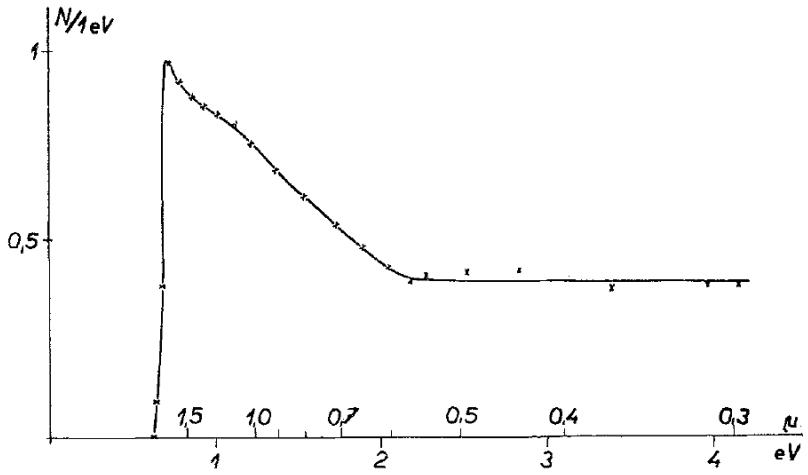

Fig. 2.8: Number of electron-hole pairs produced in a germanium absorber after the deposition of 1 eV as a function of the wavelength and energy of the incident photons. All the information about this measurement are in Ref. [133].

2.7 Neganov-Trofimov-Luke effect: boosted light detectors

The Neganov-Trofimov-Luke (NTL) effect has been named after B. S. Neganov and V. N. Trofimov, who proposed this technique in 1985 [134], and P. N. Luke, who applied this concept for the first time [135] in 1988. B. S. Neganov and V. N. Trofimov suggested a method to improve calorimetric measurements of ionising radiation performed at low temperatures by placing a semiconductors — behaving as an insulator — or a dielectric crystal — characterised by a narrow band gap — in a stationary electric field. The result of a ionising event is the transfer of one or more electrons from the valence band to the conductance band and the creation of a hole in the valence band. The electron and the hole are then drifted in the electric field in opposite directions, transforming the particles energy into heat as the result of various dissipative processes.

P. N. Luke applies this effect to a high-purity germanium p-i-n diode with a shape of a 5-mm-side cube coupled to a NTD, testing the detector performance with an α source. He showed the possibility to lower the detection threshold for ionising detectors thanks to an improved signal-to-noise ratio obtained by the amplification of signals. The higher signal-to-noise ratio provides also a better energy resolution when it is not limited by the Poissonian fluctuations of the generated electron-hole number.

This effect can be summarised by the formula (2.24). A given energy E_0 deposited in a semiconductor substrate creates electron-hole pairs, that are drifted by the electric field generated by the voltage bias V_{el} applied on the detector electrodes. The total heat deposited in the absorber is E, thus defined:

$$E = E_0 + \eta \frac{q\ V_{el}}{\epsilon} E_0, \tag{2.24}$$

where q is the electron charge and ϵ the energy required for the creation of an electron-hole pair, also called quantum efficiency in the semiconductor physics [133]. The value of ϵ depends on the energy of the incident radiation, as shown by S. Koc in the case of a germanium absorber [133]. Fig. 2.8 shows the pair number produced as a consequence of the deposition of 1 eV for different wavelength photons. Photons with an energy closer to the gap produce a higher number of electron-hole pairs, so they are characterised by a better gain. For this reason the calibration in presence of the electrode bias is complicated: the

detector gain depends on the event energy. In Eq. (2.24), we consider also η, a coefficient taking into account losses due to charge recombination and trapping. This parameter — that can vary between 0 and 1 — tends to 1 when the absorber is highly pure (lower trapping), the electrodes bias is high, the drift length are short and the semiconductor is neutralised [136]. The gain provided by this effect is reported below:

$$G = 1 + \eta \frac{q\ V_{el}}{\epsilon}. \tag{2.25}$$

If $V_{el} \gg \epsilon/q$ we can consider that the total heat is mainly provided by the NTL effect.

3 This is how we do it

This chapter gives an overview of the instruments and methods employed in this work. In particular the cryogenic facilities are introduced in Sec. 3.1. The cryostat working principles, the techniques used to carry out low-radioactivity and low-noise measurements and the electronic read-out systems employed for the data acquisition are here described. Once that the terminology is defined, a quick overview of the facilities used in this work is presented. Then Sec. 3.2 explains the procedures used for bolometer assembly. Finally the detector characterisation and analysis processes are described in Sec. 3.3, with a particular focus on the calibration sources in the subsequent section.

3.1 Cryostat

We have seen that bolometers require working temperatures of the order of 10 mK in our case (see Sec. 2.2). This demand is satisfied by the employment of cryostats, in our case dilution refrigerators. In this sector different technologies are available, we can distinguish two main families: wet-cryostats that use cryogenic liquids to cool down and dry-cryostats that do not.

Now we will have a look at the principles used to reach these temperatures, starting from the warmest stage of a cryostat. The first part that we encounter is the Outer Vacuum Chamber (OVC), a vessel that provides the first heat insulation. It exploits vacuum to ensure a protection against conduction and convection of heat from the room-temperature environment. But it does not protect against the 300-K radiation, that can be rejected in two different ways. Dry-cryostats use a super-insulation system, composed by about seven layers of reflecting material separated by thin nets that fix a gap between the foils. The super-insulation system is under vacuum inside the OVC, for this reason there are some holes in the reflector to facilitate the pumping procedure. This technique can be assisted by a liquid-nitrogen bath in wet-cryostats. The liquid nitrogen is a not-too-expensive cryogenic liquid with a boiling temperature of 77 K and a high latent heat of evaporation. This quality is the key point for the protection against the 300-K radiation.

The Inner Vacuum Chamber (IVC) is placed inside the OVC; as the name tells us, it consists of a second vacuum room. This stage is kept at a temperature of around 4 K, that can be reached with two different techniques: a dry-cryostat will have a pulse tube and a wet-cryostat will use a ^{4}He bath. The last one is accomplished with a bath containing ^{4}He, a cryogenic liquid with a boiling temperature of 4.2 K. Sometimes it is assisted by a thermal machine to cool down the helium vapours reducing its evaporation. The difference between a wet and a dry cryostat consists in the reference temperature. A ^{4}He bath will be always at 4 K regardless of the heating power that it has to contrast: a higher power will accelerate the helium evaporation but the bath will remain at 4 K. On the contrary, the cooling power provided by a pulse tube is limited and the final reference temperature depends on the heating power. A higher temperature of the 4-K stage can influence the helium-condensation speed and consequently the cryostat performance. The use of pulse tubes can introduce additional vibrations in the experiment that are not present in a set-up based only on a ^{4}He bath. However, the introduction of a thermal machine in a wet cryostat will also introduce vibrations. Pulse tubes do not need moving parts at cold temperatures

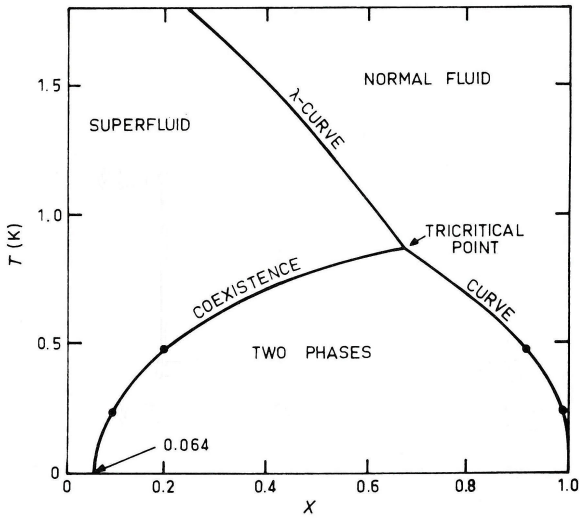

Fig. 3.1: Phase diagram with the temperature as a function of the ^{3}He content in the ^{3}He-^{4}He mixture [137]. x is defined as ^{3}He/(^{3}He+^{4}He). The line is named λ-curve because of its shape, it separates three possibles states: normal fluid, superfluid and the presence of two simultaneous phases (liquid and gaseous). The three states coexist at the tricritical point at 860 mK.

— in contrast to the thermal machines — and are known to introduce less vibrations on the experiment. Nevertheless the noise generated by their vibrations is non-negligible, the effects are especially critical for non-massive bolometers like light detectors. Several strategies have been studied to minimise the vibrations, Sec. 3.1.2 reports some considerations on this topic. However, a pure helium bath — even if it has less problems in terms of vibrations — requires at least bi-weekly refill, that obliges the interruption in the data acquisition affecting the dead time of the experiment, and a non-negligible cost in terms of helium.

The IVC contains the dilution unit circuit that ends in the mixing chamber to which detectors are connected. The cryostats — used in the realisation of this work — exploit a ^{3}He-^{4}He mixture to cool down. ^{3}He and ^{4}He are two stable isotopes of helium, the first one is produced by the tritium disintegration — we can see it as a sub-product of the hydrogen bomb — and the second is a by-product of the petrol extraction. Fig. 3.1 shows a phase diagram depending on the temperature and the ^{3}He concentration in a ^{3}He-^{4}He mixture. The two-phase state is exploited in the cooling process: one phase is mainly formed by ^{4}He with a small concentration of ^{3}He, named ^{3}He-diluted phase, and the other one is highly concentrated in ^{3}He with a small part of ^{4}He, it is therefore called ^{3}He-concentrated phase and stays above the previous one. This unusual equilibrium state is achieved because of the different quantum properties of helium nuclei: ^{3}He is a fermion and ^{4}He a boson. The ratio between ^{3}He and ^{4}He in the ^{3}He-diluted phase is well defined and tends to stay constant. When a part of ^{3}He is removed, the ^{3}He-diluted phase tries to re-establish the equilibrium absorbing some ^{3}He from the ^{3}He-concentrated phase. The cooling effect is produced during the ^{3}He absorption that generates an endothermic reaction at the interface between the two phases.

Now we have to distinguish two different conditions: the initial cooling down and the steady operation condition. The first one is a complicated process obtained by a progressive liquefaction of ^{4}He and ^{3}He,

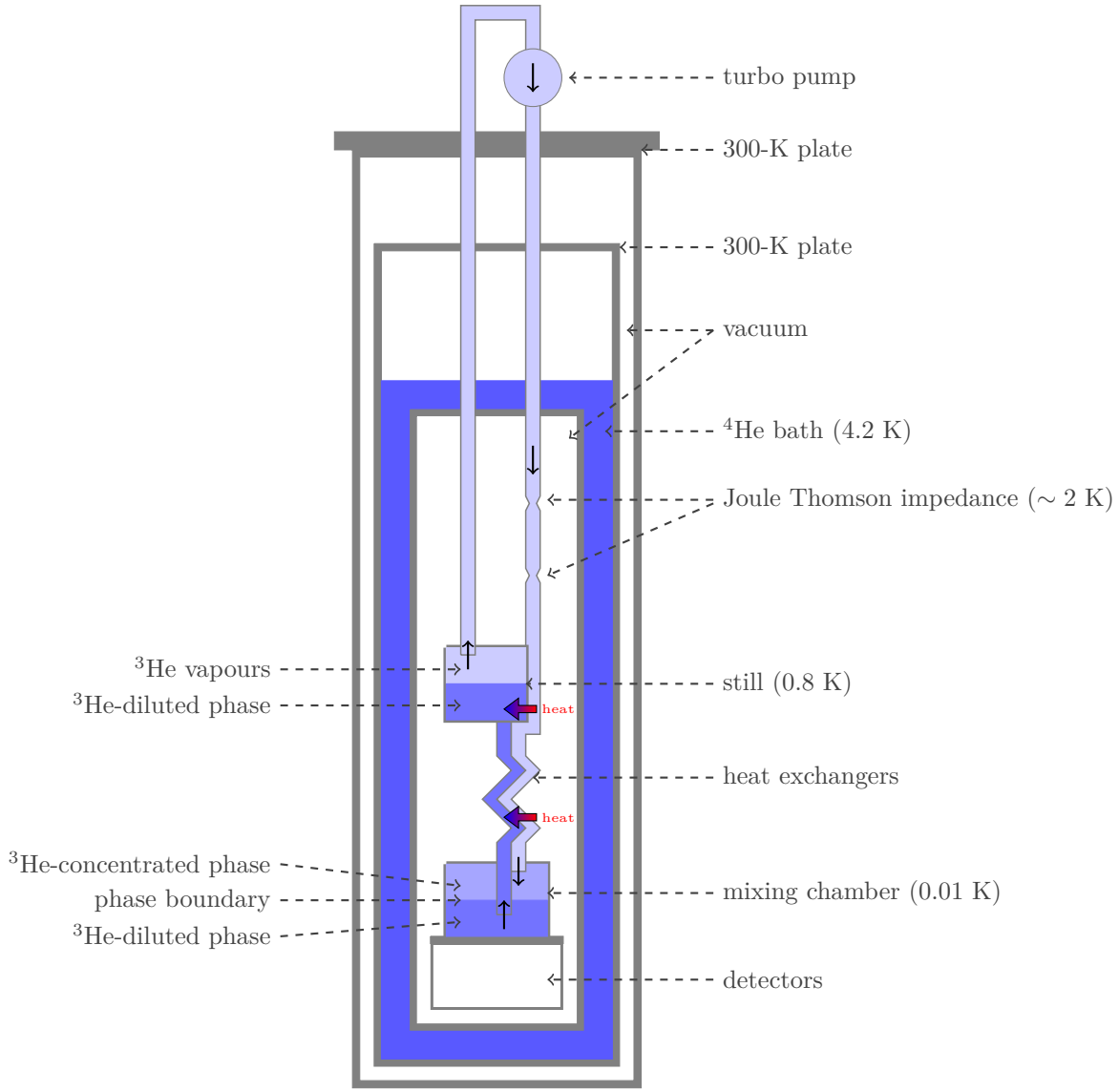

Fig. 3.2: Scheme of a wet-cryostat where the ∼ 1 K stage temperature is achieved through a Joule-Thompson impedance. Real proportions are not respected in favour of a clearer representation of key elements.

and then their progressive cool down. We decided to avoid a detailed discussion because it goes beyond the purpose of this manuscript. Concerning the normal-circulation description we will refer to Fig. 3.2. During regular operation, we will have already two phases in the mixing chamber: one diluted in ^{3}He (on the bottom) with a proportion of around 6:94 and one concentrated in ^{3}He (on top). Also the still will contain a mixture of ^{3}He-^{4}He with an approximate proportion of 1:99 of ^{3}He. The still and the mixing chamber are connected by a pipe plunged in the ^{3}He-diluted phase. The lower concentration of ^{3}He in the still attracts the ^{3}He atoms from the mixing chamber thanks to the action of osmotic pressure. The ^{3}He reduction in the ^{3}He-diluted phase causes its absorption from the ^{3}He-concentrated phase to return to an equilibrium. In order to keep a lower ^{3}He concentration in the still than in the mixing chamber to permit the effect of the osmotic pressure, the liquid in the still is continuously pumped. The ^{3}He is the only isotope extracted from the still thanks to its lower vapour pressure. The ^{3}He is pumped outside the cryostat with a turbo pump, cleaned in a nitrogen trap and a non-reactive gas purifier, and then re-injected in the cryostat. The room-temperature gas entering the cryostat is cooled down to 4 K at the pulse tube (or helium bath) stage. Then it encounters a 1-K pot or Joule-Thomson flow impedances in its path toward the mixing chamber. Two different means to cool down the mixture to a temperature of the order of 1 K in the first case and roughly 2 K in the second. The impedances exploit the Joule-Thomson effect: the gas has to pass through a neck in the circulation pipe that provokes a pressure decrease in the gas and its consequent cooling-down. The Joule-Thomson impedances are a quite recent technique, previously the 1-K pot was used and it consisted in a pumped ^{4}He bath. The pumping on the gas enables to lower its temperature from 4.2 K to $1 - 1.2$ K. The 1-K pot technique is used in wet-cryostats and is refilled continuously from the ^{4}He bath because the pumping causes a quick helium evaporation. At this stage the mixture is at around $1 - 2$ K and arrives at the still where it is thermalised reaching temperatures of the order of 0.7 K. The ^{3}He is progressively cooled down and liquefied in the heat exchangers. Those devices establish a thermal contact between the entering ^{3}He and the liquid going from the mixing chamber to the still. This contact is obtained in two steps: the continuous heat exchangers and the discrete ones. The first ones consist of two coaxial tubes in which the entering and the leaving liquids flow in opposite directions. The second kind consists of a structure composed by equal sub-modules with a large contact surface — made by pressed metal powders — between the incoming and outgoing liquid [138]. Finally, the ^{3}He is injected in the ^{3}He-concentrated phase.

3.1.1 Low radioactivity measurement

A low-radioactivity background is a must in rare-event searches because it is a strong limiting factor to the discovery potential. It is also a non-negligible point during a R&D phase because slow-device performance can be strongly affected by a high event rate. Depending on the cryostat purpose, physics or R&D, it will have different requirements:

Material radiopurity. Rare-event searches require an extreme care devoted to the background control. On one side this is translated in the choice of radiopure materials for the detector assembly including the detector itself (the crystal, its thermal sensor and heater), the detector holder and the smaller details (the tin for the soldering, the glue, the wires and so on). This attention has to be extended also to the materials used in the cryostat construction. In fact the cryostat parts close to detectors — as internal shields, cabling and connectors — require a high radiopurity to minimise Th/U and other radio-isotope content close to the detector.

Passive shields. Two types of passive shields can be equipped depending on the background type to reduce. A lead shield reduces the natural radioactivity coming from the Th/U chains thanks to his high density. Lead with a low content of ^{210}Pb is required. This isotope — belonging to the ^{238}U series and incorporated during the lead production — undergoes a β-decay ($Q_\beta = 63.5$ keV) with a half life of 22.3 years. Given its β-decay energy and the decay energy of its daughters, it is

not dangerous in the $0\nu2\beta$ region but it contributes to the background as pile up. This isotope is absent in ancient lead because of its 22.3-yr lifetime.

A polyethylene shield, thanks to its high hydrogen content, can be employed to limit the neutron flux. This is particularly important in case of dark matter bolometric experiments where the goal is to detect nuclear recoils that can be produced by both dark matter and fast neutrons.

Cosmic-ray muons Muons, originated in the cosmic ray radiation, can deposit energies that can mimic events in the $0\nu2\beta$ region or activate material close to the detector. This kind of background can be reduced by operating the detectors in underground facilities exploiting the flux attenuation done by the mountain rocks. The flux reduction depends on the height and rock-type of the mountain present above the facility. The reduction can be translated in the water-equivalent depth expressed in km (km w. e.) necessary to get the same flux attenuation. This conversion is useful to compare different experimental locations, for example Ref. [139] reviews the muon fluxes measured in different laboratories.

Radon-free environment ^{222}Rn is a dangerous contaminant for low-radioactivity measurements because it is in a gaseous state and its radioactive daughters can be deposited on surfaces by air contact. For this reason, cryostats sometimes are installed in radon-free chambers to avoid contaminations during the detector installation.

3.1.2 Noise reduction

Bolometer signals develop in a low-frequency region of the order of a few tens of Hz for massive bolometers and a few hundreds of Hz for light detectors. Therefore low-frequency noise sources — like the ones generated by vibrations — are a critical issue. The pumps and the pulse tube can contribute significantly to low-frequency noise, but the vibrations can also be due to acoustic disturbances or be originated outside of the laboratory. Multiple techniques are adopted to minimise the vibration influence on the detectors, a short list follows below:

Cryostat damping system. Cryostats are usually sustained by damping systems to reduce the effects produced by vibrations. The damping system is done by sitting the cryostat on three or four pillars decoupled from the cryostat thanks to a laminar flow provided by compress air.

Decoupling system. One of the most effective techniques to reduce the vibration effects is based on the detector decoupling from the mixing chamber with a suspension mechanism [140, 114, 115]. The suspension can be made by connecting the detector to the mixing chamber with one or more springs. The spring elastic constant and their elongation have to be chosen as a function of the detector mass and the available space to avoid possible thermal shorts. It is important not to forget the thermalisation between the detector and the mixing chamber. This link has to be soft because a rigid connection between the two elements would cancel the purpose of the suspension. In our case we used narrow copper bands softened by heating and copper braids.

Clamping. Also the detector clamping has been studied to reduce the detector vibrations. We tried to change the PTFE clamping with a more rigid system based on sapphire balls to anchor better the detector avoiding unwanted vibrations. But it did not produce a clear difference on the noise.

Cabling. Another key point on the vibration problem are the cables as we have seen in Sec. 2.4. In fact cable vibrations induce a friction between the insulating materials (especially in presence of plastics) and the conductor. The friction produces random charges that contribute to the noise. This effect can be limited with the use of anti-triboelectric cables. These are made by two insulated twisted-pair wires surrounded by a conductor (for example a carbon layer), the mass shielding and

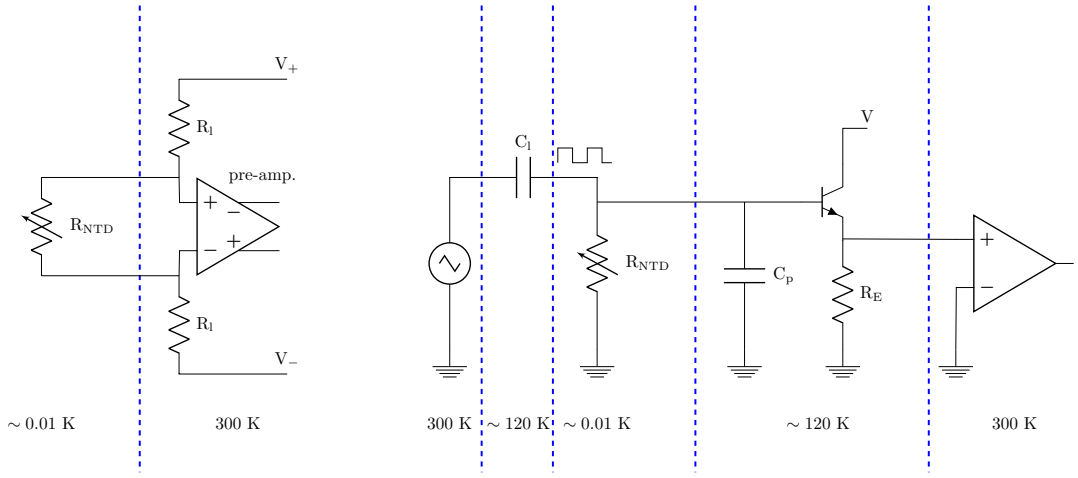

Fig. 3.3: *Left panel*: scheme of a DC bias circuit. Only the sensor is at low temperatures, while bias and amplification stages are at room temperature. *Right panel*: scheme of an AC bias circuit constituted by a first amplification stage at low temperatures.

the insulator. The conductor has to be tight to the wire insulator to evacuate charges. This should be the duty of the mass shielding, but often it does not work properly because it is not tight enough. The generation of noise in the cables can also be introduced by a capacitance variation due to their vibration.

Also the photons can contribute to the noise budget, as we have seen in Sec. 2.4. This problem is non-negligible for high-performance light detectors. We try to seal the detector holders as much as possible in order to minimise the radiation in contact with the device. At the cryostat level, it is possible to coat the inner screen with a infra-red-absorbing black paint to absorb the radiation reflections.

3.1.3 Electronic read-out

The detector read-out has been carried out with different electronics. We can divide these systems in two main categories: warm and cold electronics. In the first case all the electronic apparatus is placed at room temperature while in the second a first amplification stage is installed inside the cryostat. A cold electronics, having the first amplification stage closer to the detector, is characterised by lower noise that otherwise would have been picked up in the long wires running from base to room temperature. This characteristic is not essential for macrobolometers used in the $0\nu2\beta$ search given their big signals expected for this process. The drawback of a cold electronic stage is the installation of devices that need to work at temperatures of the order of 100 K in a cold environment. Their thermalisation and positioning are not always an easy issue. On the other hand, a warm electronics is more manoeuvrable: interventions are easier in case of failure.

We can also distinguish two different bias and read-out philosophies: one is based on a direct current (DC) flowing through the sensor and the other one based on an alternated current (AC) bias.

The DC bias is constituted by a symmetric high-precision voltage supplier (V_+ and V_-) applied to two load resistors R_l, as in Fig. 3.3 (*left*). The current flowing through the sensor R_{NTD} is defined according to the formula:

$$I_{NTD} = \frac{V^+ - V^-}{2\ R_l + R_{NTD}} \sim \frac{V^+ - V^-}{2\ R_l}. \tag{3.1}$$

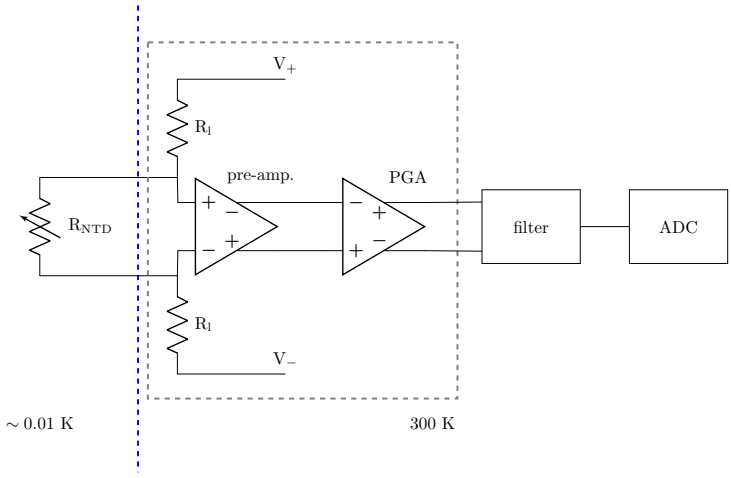

Fig. 3.4: Read-out chain in the case of DC warm electronics. The sensor operates inside the cryostat while all the electronics is at 300 K. In our case the bias block, the pre-amplifier and the PGA are hosted in a single front-end board followed by a Bessel filter and an ADC.

The approximation is true if the sensor resistance is negligible with respect to the one of the load resistors. The resistance of a single load resistor can vary in the range 100 MΩ − 30 GΩ depending on the sensor resistance. This system is simple and easy to build and operate.

The AC bias requires a more complicated circuit, shown in Fig. 3.3 (*right*). In this case, the two resistors are substituted by a load capacitor C_l. It has to differentiate the triangular waveform used to bias the detectors, that is transformed in a squared wave at one of the sensor extremities. The frequency of the square waveform is named modulation frequency and can be of the order of 1 kHz. The sampling frequency has to be higher than the modulation frequency. The signal is added to the square waveform and has to be demodulated before being analysed.

The signal is amplified in the first stage by a cold JFET and then at room-temperature by a programmable-gain amplifier (PGA). This system is not differential — unlike the previous one — and is more sensitive to the common-mode noise. The first stage of amplification presents a parasitic capacitance at the gate contact of the JFET. Its value is around 60 pF and when combined with the sensor resistance modifies the shape of the square function at JFET entrance by extending its rise time. This effect is compensated by adding a current peak in correspondence of the rise time, that has to charge the parasitic capacitance.

The main advantage of the AC bias system is its ability to eliminate the low-frequency noise (see Sec. 2.4) like the 1/f noise generated by the JFET. This is possible because the bolometer signal is convoluted with the squared waveform and the signal frequency spectrum is translated to the waveform modulation frequency while the low-frequency noise is not influenced by the modulation. Therefore the low-frequency noise is easily removable by a pass-band filter around the modulation frequency.

Fig. 3.4 shows the read-out chain in presence of a warm DC electronics. The temperature sensor — placed inside the cryostat — is biased with a constant current generated by a differential high-precision voltage applied to two load resistors. A pre-amplifier is connected at the sensor nodes and provides a constant amplification. This first amplification stage is done by JFETs (*Junction gate Field-Effect Transistors*) characterised by a low noise and a huge impedance at the input to avoid perturbation in the bias circuit.

The pre-amplifier is then followed by a PGA. It is worth noticing that the read-out is fully differential to eliminate the common-mode noise sources. Signals are then filtered to cut high-frequency noise, usually a Bessel filter is used. At the end, the signals are digitalised with an analog-to-digital (ADC) converter — whose resolution is defined by its bit number — and sent to the data-acquisition program.

In the configuration here described, each detector has to be connected to the electronics by two wires. Each couple of wires is twisted to minimise the effects that can be produced by magnetic fields. The twisted pair can be inserted in a coaxial configuration to reduce external interference like cross-talk, the drawback of this solution is the large space occupancy especially for a large number of channels.

3.1.4 Cryostat overview

The results here presented have been obtained using four different ^{3}He/^{4}He dilution refrigerators: Ulisse, CRYOFREE, CUPID R&D and EDELWEISS. An essential description of these cryostats is reported in Table 3.1. A few comments will follow on the table entries that are not self-explained. The EDELWEISS cryostat is a quite unusual cryostat since it is not completely wet nor dry. In fact there is the coexistence of a ^{4}He bath and a Gifford-Mac Mahon thermal machine to limit its helium consumption. Another peculiarity of this set-up is the geometry. Normally cryostats have a vertical structure with the coldest point at the bottom. The EDELWEISS-cryostat structure is upside-down with the mixing chamber on top. Fig. 3.5 shows a few photographs of the cryogenic facilities employed in this work.

We can divide these cryostats in two main categories: the ones dedicated to R&D like Ulisse and CRYOFREE and the ones dedicated to physics measurements. R&D measurements are mainly used to quickly test detectors and do not need extremely low-background environment. Therefore they are usually set in aboveground laboratories, they have a minimal shield and the cleanliness requirements are less stringent. The situation is opposite for cryostats dedicated to low-background measurements, like the CUPID R&D and the EDELWEISS facilities.

3.2 Detector assembly

First of all the absorber material has to be chosen depending on the physics investigated. The crystal constraints are not many: a low heat capacity, a mono-crystalline structure and a high Debye temperature, as it has been discussed in Sec. 2.2. Concerning light detectors we use semiconductor absorbers made of germanium or silicon.

In this work, we have used NTD germanium thermistors developed in the Lawrence Berkeley National Laboratory by J. W. Beeman. The ones described here have a size of $3 \times 3 \times 1$ mm and come from the batches 39C, 41B, 34B[1]. Table 3.2 lists some examples of R_0 and T_0 values for the NTDs belonging to these batches. Low-mass bolometers were equipped with NTDs smaller than the ones used for standard bolometers in order to lower their heat capacity. In fact the heat capacity of small crystals can be comparable to the one of NTDs. In this case a smaller NTD is required to optimise the detector performance. These devices derived from a standard NTD cut in three parts along the direction perpendicular to contacts. The cut was performed with a wire saw, therefore a part of the NTD was lost: if a $3 \times 3 \times 1$-mm NTD is characterised by a mass of 48 mg, a reduced NTD has a mass in the range of $6 - 10$ mg. One of these reduced sensors has been characterised: it had $R_0 = 6.3(2)$ Ω and $T_0 = 3.50(5)$ K. In order to further boost the bolometric performance, some of the reduced NTDs were sanded down to decrease their thickness and consequently their heat capacity. In this work we mainly used sensors with a wrapped around geometry to simplify the bonding procedure.

The sensors were glued with an epoxy on the top of the absorber, close to the edge to facilitate the bonding. In particular we used Araldite — a bi-component glue composed by a hardener and a resin —

[1] The nomenclature is preserved from the Lawrence Berkeley National Laboratory and indicates the germanium wafer doping.

Fig. 3.5: *Top-left panel*: photograph of the EDELWEISS cryostat, the electronics is visible in the bottom part and the cryostat in the upper one. *Top-right panel*: photograph of the cryostat upper part with the galette system used to host the detectors. Galette is an internal nickname used by the EDELWEISS collaboration to refer to a set of round copper plates used to hold the detectors. As it is visible by some EDELWEISS detectors mounted, this system does not have bolometer suspension. *Center-left panel*: photograph of the decoupling system mounted in the EDELWEISS set-up. It is constituted by three springs to reduce the vibration effects. *Center-right panel*: the Ulisse cryostat test facility. *Bottom-left panel*: the CRYOFREE dilution unit. *Bottom-middle-and-right panel*: detectors mounted on the CRYOFREE and Ulisse cryostats with a spring decoupling system.

Tab. 3.1: The cryogenic facilities employed in the execution of this work are here compared according to their location, hardware structure, shields and electronic systems.

	Ulisse [141]	CRYOFREE	CUPID R&D [140, 142, 143, 97]	EDELWEISS [144, 145, 129]
Location				
Laboratory	CSNSM (France)	CSNSM (France)	LNGS (Italy)	LSM (France)
Underground [Rock overburden (km w.e.)]	No	No	Yes [3.6]	Yes [4.8]
Cryostat				
Type	Dry	Dry	Wet	Wet
Geometry	Standard	Standard	Standard	Reversed
Experimental volume (L)	~ 5	~ 19	~ 8	~ 50
Damping system	Yes	Yes	No	Yes
Inside mechanical decoupling	Yes	Yes	Yes	Yes
Base temperature (mK)	<10	$11-12$	7	10
Shield (external)				
Low activity lead (cm)	10	Yes	20	18
Roman lead (cm)	No	No	No	2
Polyethylene (cm)	No	No	8	55
Boron carbide (cm)	No	No	1	No
Anti-radon box	No	No	Yes	No
Muon veto	No	No	No	Yes
Shield (internal)				
Roman lead (cm)	No	No	5.5	14
Polyethylene (cm)	No	No	No	10
Readout and DAQ				
Electronics	warm	warm	cold and warm	cold
Dual readout channels	18	20	10 + 8	48
Bias	DC	DC	DC	AC
ADC digitization (bit)	16	16	18	16 or 14
Sampling rate (kSPS)	Up to 250/channels	Up to 250/channels	Up to 250/channels	Up to 1

Tab. 3.2: Typical values of R_0 and T_0 measured for the three different NTD batches used in this work.

Batch	T_0 [K]	R_0 [Ω]	fixing technique	Ref.
39C	4.26	1.07	vacuum grease	[146]
34B	3.87(4)	0.835(1)	glue film - Mylar - glue film	[123]
41B	3.8	1.5	glued with 6 spots	

that was introduced in bolometer manufacture because of its low radioactivity. The two components of the glue were mixed in an equal amount — checked by eye — for thirty seconds just before the gluing. After the gluing, the glue was left to harden for two hours.

The gluing of light detectors consists in the deposition of three glue spots with a needle on the edge of the absorber surface followed by the seating of the NTD over them. The thermal sensor was pressed with a constant pressure provided by the bonding machine. The bonding-machine needle applied a 30-g weight over the sensor preventing its movement during the glue drying. A glue film was formed between the NTD and the wafer.

Bolometers equipped with $3 \times 3 \times 1$-mm NTD were glued with two different techniques:

The Mylar-mask method. This procedure requires the use of the instruments presented in Fig. 3.6 (*top*). First of all the NTD is fixed on the mechanical arm thanks to a pumping system. Then also the pogo-pin[2] matrix — used to deposit a matrix of glue spots — is installed in front of the chip. The crystal is positioned below the mechanical arm and an U-shaped Mylar mask is placed on its top surface surrounding the point where the NTD will be glued. The glue is then prepared and dosed in a PTFE container: the container has a fixed depth and the glue is levelled at its top to have a reference amount of glue. The pogo-pin matrix is plunged in the glue and a reproducible quantity of glue sticks to the pogo-pins. The pogo-pin matrix is then descended on the crystal surface: the glue spots are left inside the borders of the Mylar mask. At this point, the pogo-pin matrix is removed from the mechanical arm and the NTD is approached to the glue spots. After the NTD alignment with the mask, the sides of the NTD — close to the gold pads — are seated on the Mylar-mask sides.

Gluing tool. We will refer to the photographs presented in Fig. 3.6 (*bottom*) for the following description. At the beginning the NTD is seated on the gluing tool in the designated area and is blocked with a pumping system. The 50-μm spacing between the NTD surface and the gluing tool external cylinder is fixed with an especially-designed cover, as described in the caption of Fig. 3.6. At this point, the glue spots are directly deposited on the NTD. The crystal is positioned in a PTFE structure that can slide along the gluing system and seat the crystal on the external cylinder top surface. If the previous method can be applied to crystals with almost any shape, this method requires a PTFE holding structure that fits massive crystals.

Another kind of sensors — high-resistivity NbSi TES — were used in this work. The following description lists the main steps used to fabricate NbSi TES sensors:

- the germanium wafer is glued to a silicon wafer that will improve its resistance to stress during the fabrication process, at the end of the procedure they will be unglued;
- the NbSi TES is fabricated using the so called lift-off process. This process starts with the coating of the wafer, using 1.3-μm-thick S1813 resist. The resist is photo-sensitive in the visible range;

[2] Pogo-pins are spring loaded short sticks used in electronics used to establish an electronic contact between two boards. In our case we exploit these devices to deposit a uniform matrix of small glue spot compensating possible misalignments thanks to the spring system.

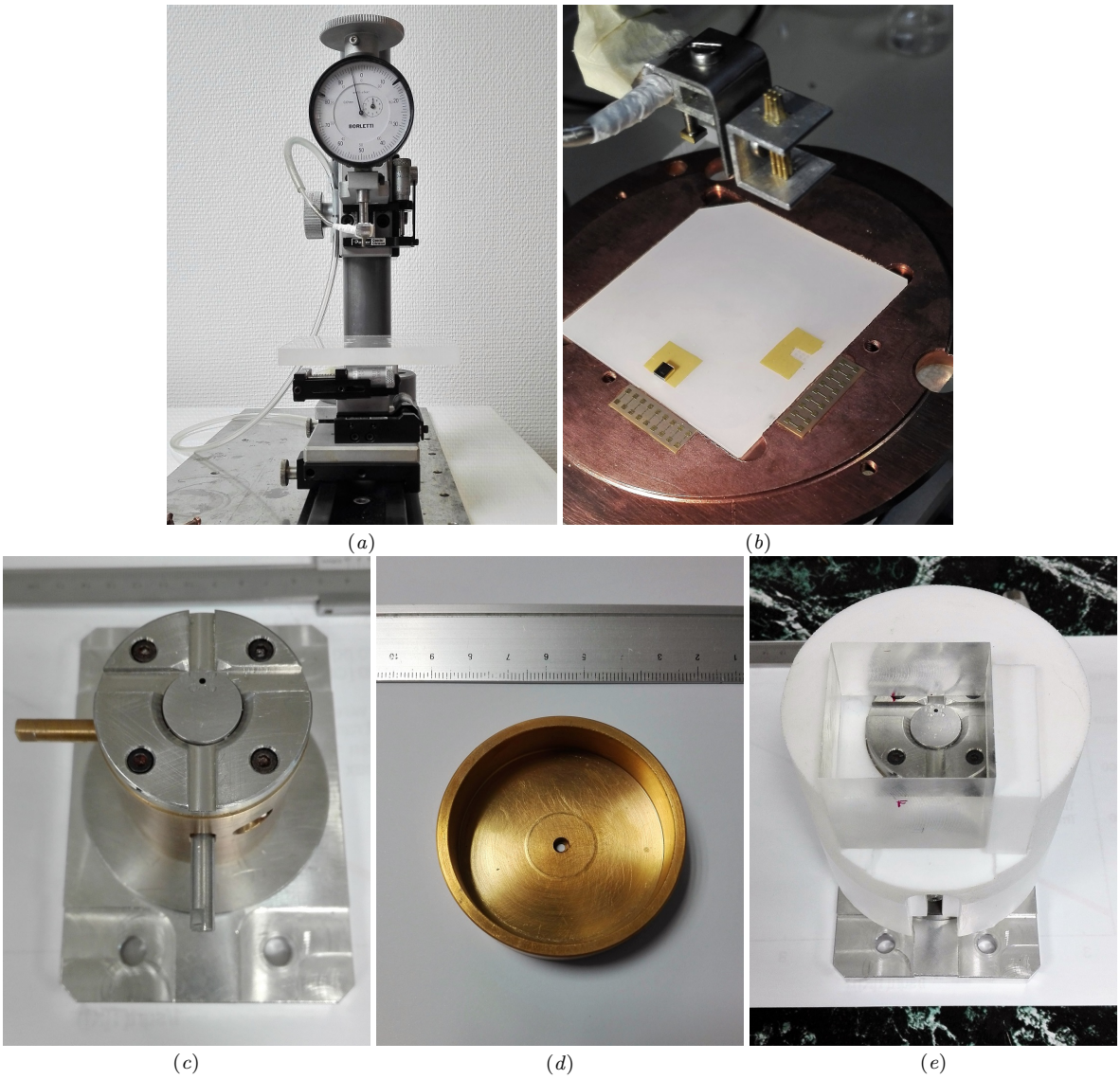

Fig. 3.6: (*a*) Mechanical arm used for the gluing. It is connected on the same structure with a moving platform. The arm keeps the NTD and the pogo-pin matrix, while the platform supports the crystal. The movements of both can be controlled at millimetre fractions thanks to position manipulators. (*b*) Photograph of a NTD gluing to a TeO_2 slab. On the bottom, there are a glued NTD seating on its Mylar mask (on the left) and a Mylar mask surrounding six glue spots just before the NTD deposition (on the right). On the top, there are the pogo-pins matrix and (just behind) the NTD sucked are visible. (*c*) Photograph of the gluing system. It is constituted by two concentric cylindrical structures: the external one is fixed while the inner one can slide in the vertical direction. The NTD is placed in its squared seat over the inner cylinder and it is fixed thanks to a pumping system connected to the frontal pipe. (*d*) Photograph of the cap used to fix the 50-μm space thanks to the step in its inner part. It is pressed over the gluing system, the lower part of the step seats over the external cylinder, while the inner part lowers NTD seated in the gluing-system inner cylinder of 50-μm. (*e*) Photograph of the PTFE structure used to hold and deposit the crystal on the gluing-system. In this image, the structure is holding a cubic plexiglas used for test as a fake crystal.

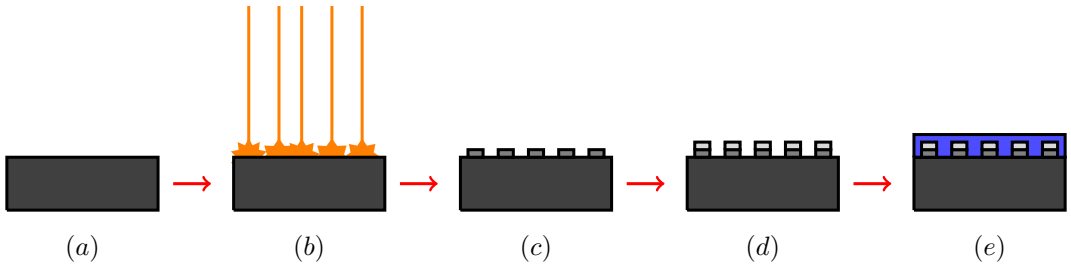

Fig. 3.7: Treatment summary scheme for the production of NTL-assisted light detectors: (a) bare germanium wafer. (b) argon ions bombardment. (c) amorphous aluminium deposition. (d) aluminium electrodes deposition. (e) SiO coating.

- we used a direct laser beam light to pattern a meander or a spiral on the resist. The laser beam removes the resist below the future sensor and fixes the resist that will no longer be soluble in to the developer chemicals;
- after its development, the sample is ready for the deposition of a uniform layer of NbSi;
- finally the sample is immersed in acetone to remove the resist residuals;
- the sample is now ready to be tested. We can fine-tune the critical temperature of the TES by annealing the samples at temperatures in the range $50 - 200$ °C.

These TES sensors have been deposited both on silicon and germanium absorbers.

The bonding has been made by Ø25-μm gold or aluminium bonding wires. Gold is a good thermal conductor at low temperatures while aluminium is a superconductor. The bonding has been performed with a West Bond 7400 B bonding machine. The bonding process used is wedge type where the link between the material and the wire is carried out with a defined ultrasonic power applied for a fixed amount of time. The gold bonding wire was favoured for NTD sensors to establish the thermal link. The aluminium one was used for the TES because of its better adherence to NbSi with respect to gold. In absence of the gold bonding wire, the thermal link has to be done otherwise. The heaters can be bonded with both aluminium and gold wires depending on the requirements: the first one could be useful to improve the thermal link while the second one is preferred to avoid a heater power loss through the bonding wire.

In the most of the cases, the NTDs were bonded to Kapton-insulated gold-coated copper contacts. Those were glued with a film of Araldite glue to the copper holders. A few detectors have been equipped with pins instead of this kind of contacts. The pins are small copper tubes that establish an electrical contact between the inside and the outside of the detector casing. Special holes are fabricated in the holders to host the pins. These are glued in the holes with Araldite glue in order to avoid the electrical contact between the pin and the holder.

The bolometers were fixed in copper holders by PTFE clamps. This material was chosen for its intrinsic low radioactivity, low thermal conductivity and high contraction at low temperatures. In one case the clamping has been done with sapphire balls to check the influence of a different clamping system on the detector noise performance. The copper used for the holders was chosen for its low content of hydrogen [147] to lower the detector assembly cooling time.

3.2.1 GeCo light detector

The main results of this work have been obtained with a series of NTL-assisted light detectors, that have been developed and produced at CSNSM. The necessity of applying a voltage bias across the absorber

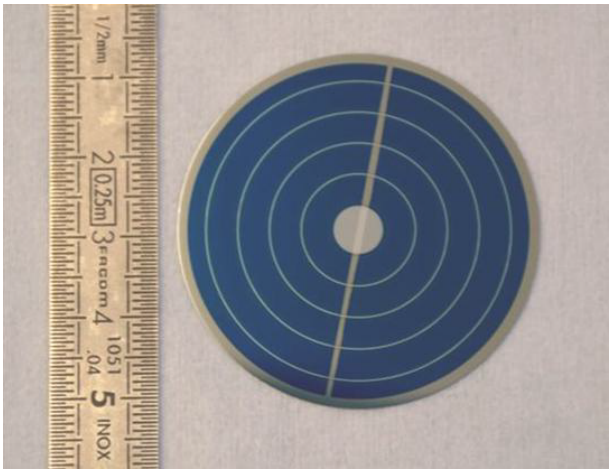

Fig. 3.8: Photograph of the absorber used to make a NTL-boosted light detector.

requests a particular surface treatment that will be here summarised. We choose electronic-grade-purity Ø44 × 0.17-mm germanium wafers as absorbers for NTL-based light detector because they are high-purity semiconductors. Our wafers are grown along the <100> axis by UMICORE. The crystal treatments — summarised in Fig. 3.7 — start with a surface bombardment with argon ions. The first layer of oxidised germanium is removed to increase the adherence of the following depositions. The surface that will be occupied by the electrodes is covered by an amorphous layer of germanium and hydrogen, the last one is used to saturate the germanium dandling bonds. This 50-nm-thick layer forms an insulation between the absorber and the electrodes that reduces the risk of development of leakage currents and improves the charge collection [148]. Then 100-nm-thick aluminium electrodes are deposited on the last layer. As it is visible from Fig. 3.8, five concentric electrodes are deposited with a pitch of 3.8 mm. This geometry was chosen to reduce the drift length and consequently improve the charge collection [149]. At the end, the absorber is coated by a 70-nm-thick SiO layer to improve the light collection [150]. A vertical strip is left uncovered by the last treatment to allow us to bond the electrodes. The bonding is made with aluminium wire creating two sets of alternated electrodes. We will refer as *outer* to the electrode set including the center, the third and the fifth rings from the center, while the remaining two will belong to the *inner* set. The wafer edge is used to keep the wafer during the treatments and is constituted by bare germanium. Fig. 3.8 presents a complete absorber ready to be mounted. At this point the device can be supplied with a small NTD that is glued on the outer bare germanium edge.

3.3 Detector characterisation

Before starting a measurement, the cryostat working temperature is decided. At this point detectors best operational point has to be chosen. It corresponds to the working point with the highest signal-to-noise ratio. This can be identified in two different ways depending on the detector type. Light detectors are shone by a LED that produces events with the same energy. The light of a room-temperature LED is delivered at low temperatures thanks to an optical fibre. This solution was preferred to cold LED because of its more stable output [151]. In this work two different types of LED were used: a Honeywell HFE4050 with a wavelength of 850 nm and an Agilent HFBR-1404 of 820 nm. These two LEDs share the same AlGaAs diode technology and were chosen because of their fast response. In fact they can be controlled with square excitations with a width of the order of tens and hundreds of nanoseconds that does not

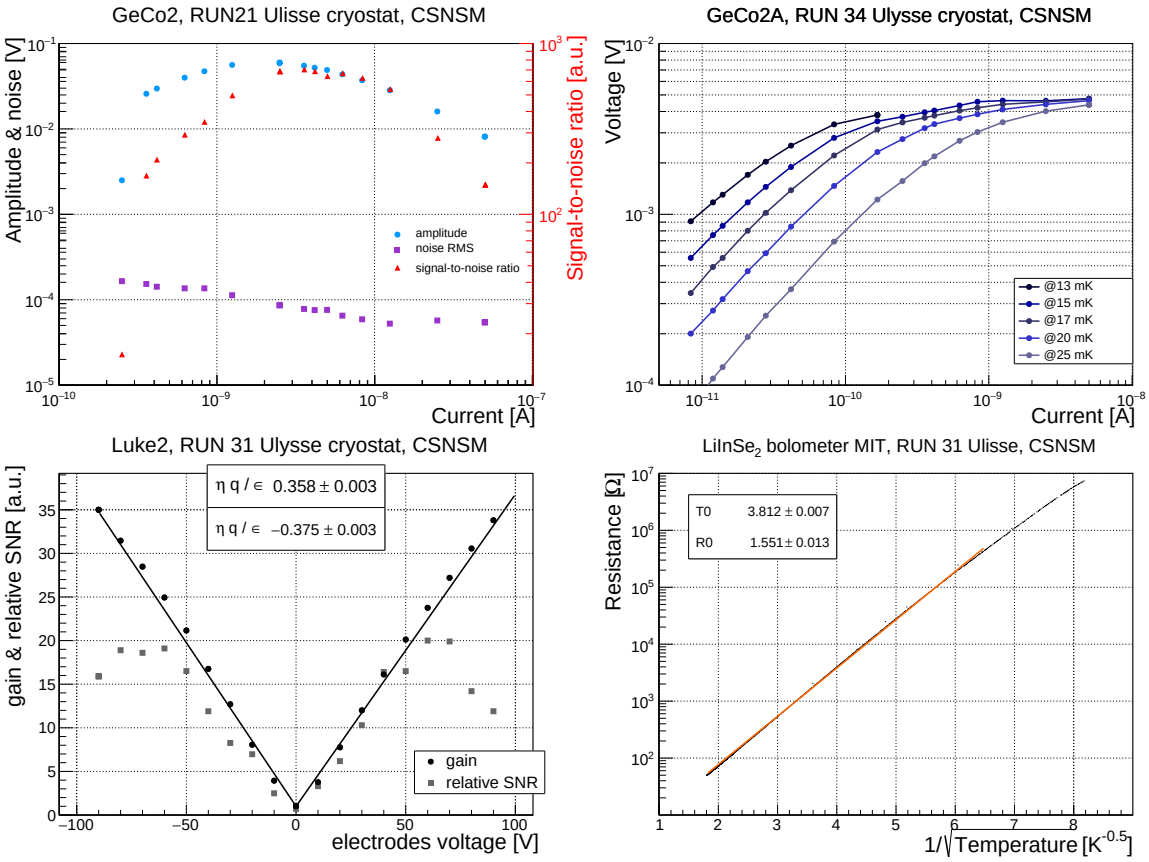

Fig. 3.9: *Top-left panel*: signal-to-noise ratio as a function of the current bias. On the same plot the corresponding amplitude and the RMS noise are presented. *Top-right panel*: example of load curves measured at different temperatures. *Bottom-left panel*: gain and signal-to-noise ratio of a NTL-enhanced light detector as a function of the voltage bias applied on the grids. *Bottom-right panel*: example of resistance-temperature characterisation for a 41B germanium thermistor mounted on a $LiInSe_2$ crystal. The points are fit by Eq. (2.5).

alter the rise time of bolometers. The signal-to-noise ratio is calculated as the ratio between the LED pulse amplitude and the RMS baseline noise in absence of events. All the current bias allowed by the electronics are tested with this method. Fig. 3.9 (*top-left*) shows an example of signal-to-noise ratio as a function of the current bias. It is worth noticing that the best signal-to-noise ratio does not correspond to the highest amplitude because the noise has the tendency to lower for high bias. During this procedure the detector resistance is measured as the ratio between the voltage developed across the sensor and the current used to bias it. Fig. 3.9 (*top-right*) shows an example of voltage-current curves, also called load curves, measured at different bath temperatures. This kind of plots has some common characteristics: the highest voltages are developed at low temperatures; the sensor resistance is constant for sufficiently low bias and this region is said to be linear; all the curves reunite for highest biases. The linear area has the higher resistance when the current flowing in the sensor is not able yet to heat it up.

This same procedure has been used a few times also on the main bolometer when it was not transparent to the LED wavelength. But usually the events in the main bolometer were induced by a heater. These devices can be seen as resistors characterised by a stable and constant resistance at low temperatures. These devices release a controlled amount of heat in the bolometer by Joule effect when they are excited by voltage square pulses for a limited amount of time. In our case we used heaters made of silicon heavily-doped with arsenic [152] produced in the frame of the CUORE experiment.

In case of NTL-enhanced devices, the voltage bias to apply on the electrodes was selected maximising the signal-to-noise ratio. This procedure was also carried out with the same technique used for identification of the best working point with the assistance of the LED pulses. Fig. 3.9 (*bottom-left*) presents an example plot of the gain and signal-to-noise ratio as a function of the grids bias obtained by a NTL-assisted light detector. The gain is fitted with the Eq. (2.24) where the free parameter is the slope. The electrodes can be supplied in different configurations: the inner or outer set can be grounded and the entire voltage bias applied on the other set, or a symmetric bias can be applied to both sets of electrodes. All configurations are not equivalent because the detector design is not completely symmetrical: the detector edge is left without electrode and is connected to the cryostat ground through the mounting. So, the outer part of the detector — corresponding to ~ 28 % of the total surface — receives a partial amplification depending on the bias configuration. The voltage bias used to supply the electrodes was produced with a separate box containing a series of 9-V batteries to minimise the noise that a generator can introduce.

In a few cases NTD sensors — already glued to the crystal — have been characterised to reconstruct the behaviour of their resistance as a function of their temperature. This kind of measurements was carried out with the help of the TRMC2, a temperature bridge developed in Grenoble (France) that is commonly used in dilution refrigerators for voltage-current sensor and thermometry characterisations and temperature stabilisations. This bridge can also perform temperature ramps and plateaux with a controlled speed, that are used for the sensor characterisations. At the same time, the TRMC2 takes care of the measurement of the sensors. This device is able to provide a low voltage bias to the thermistors in order to prevent their overheating that would affect their resistance-temperature characteristic. An example of a detector resistance as a function of the temperature is reported in Fig. 3.9 (*bottom-right*). The representation of the data with the resistance in a logarithmic scale and the inverse of the square-root of the temperature allows us to linearise the Efros-Shklovskii relation.

At this point the data acquisition can start. Parameters like dynamic range, sampling frequency, gain and Bessel frequency are chosen depending on the typology of the detector. Faster bolometers — as the light detectors — require a faster sampling frequency and a higher cut-off frequency for the filter to correctly reconstruct the events. The choice of the gain and the dynamic range depends on the signal amplitude. Often the LED and the heater have been employed during the measurement to deliver pulses with constant amplitude to the detectors. These events are useful to correct possible temperature instabilities with the consequent improvement of the energy resolution [153].

All the data used in this work have been acquired in stream mode and analysed with an off-line

program named *ithaca* developed at CSNSM in the framework of LUMINEU collaboration. This program uses a triggering system based on the optimum filter theorised by Gatti and Manfredi [154]. This filter is an adaptive filter whose objective is the optimisation of the signal-to-noise ratio. The signal, collected as a mean pulse, and the noise, represented by a differential noise spectra, are analysed in the frequency domain. The transfer function that maximises the signal-to-noise ratio is defined by:

$$H(\omega) = \frac{s_m(\omega)}{\left|N(\omega)^2\right|} e^{-i\omega\tau_m}, \tag{3.2}$$

where $s_m(\omega)$ is the mean pulse, $\left|N(\omega)^2\right|$ the noise power spectra and τ_m gives information about the position of the maximum amplitude of the pulse. The optimum filter does not preserve the signal shape but provides a good reconstruction of the amplitude parameter, the energy estimator in the bolometric technology. After the analysis, the program provides a ntple-file where each event is described according parameters like amplitude, baseline level, decay time, correlation with respect to the mean pulse and so on. Once the energy spectrum is produced, the main information that we extract to define the detector behaviour are:

Sensitivity. This quantity provides the conversion between an energy deposition and the corresponding sensor voltage variation. The sensitivity S is calculated according to:

$$S = \frac{A\ DR}{E\ 2^n\ G}, \tag{3.3}$$

where A is the amplitude of the peak measured in digit and E its energy, G is the gain while DR and n are respectively the dynamic range and ADC digitalisation.

Peak resolution. Depending on the type of detector, the energy resolution can be referred to different energies. Light detectors — mainly interested in the low energy region — have resolution evaluated at characteristic X-ray lines, while massive bolometers — dedicated to $0\nu2\beta$ decay — are characterised by the resolution of the high-energy γ-quanta like the 2615-keV ^{208}Tl line. A good resolution is one of the key parameters for a good sensitivity to the $0\nu2\beta$ decay.

Baseline resolution. This parameter expresses the width of the baseline. It contributes to the detector resolution and to the definition of the energy threshold. The last one is mainly important for low energy application, as in the case of the light detection.

3.4 Calibration

The detector energy calibration has been performed with different sources depending on the energy range considered. Their decay rate needs to be low ($< \sim 1$ Hz) because otherwise the pile up would start to worsen the detector performance. A short overview of the used methods follows.

^{55}Fe source was used for the light detector calibration. It is an iron isotope that decays to an excited state of manganese by electron capture:

$$^{55}Fe + e^- \rightarrow ^{55}\ Mn^* + \nu_e \rightarrow ^{55}\ Mn + \nu_e + \gamma. \tag{3.4}$$

The de-excitation of the manganese occurs with the emission of X-ray lines, the two dominant ones are at 5.9 keV and 6.4 keV. This is an interesting source for light detector due to its energy region. The ^{55}Fe source consisted of a drop of a solution containing this isotope deposited on a copper tape, dried and then covered by tape as a protection and to stop Auger electrons. The source was not collimated and a minimum 4-hour run was needed to calibrate in case of the most intense sources.

The source was always mounted on the light detector cover, on the side opposite to the NTD to avoid spurious events. The use of this kind of source is not allowed in the EDELWEISS cryostat since the possible dispersion of the dried source could be a dangerous contaminant in the low energy region that is investigated by the EDELWEISS experiment. In any case, we found an alternative calibration technique by the exploitation of a ^{60}Co intense source in that cryostat.

^{60}Co source — characterised by a high decay rate — is used by the EDELWEISS collaboration for the regeneration of their hybrid charge-heat detectors. ^{60}Co decay produces γ rays with an energy of 1460 keV that reach the detectors ionising the atoms of the nearby materials. The de-excitation generates the emission of X-rays that can be used for the calibration of light detectors. This effect can be exploited with any kind of high-energy and high-rate source.

Muons can also be used for an alternative rough calibration technique in aboveground set-ups. The muon energy in first approximation can be described by a Landau distribution:

$$L(x) = A_0 exp\left[-\frac{1}{2}\left(\frac{x - x_{max}}{\sigma} + exp\left(\frac{x - x_{max}}{\sigma}\right)\right)\right], \tag{3.5}$$

where A_0 is the distribution amplitude, x_{max} the maximum position and σ its width. A muon average energy released in a material can be calculated with its stopping power, the material density and thickness. In case of a germanium slab of 175 μm, the energy deposited is around 128 keV but it corresponds to the average of the distribution and not to its maximum x_{max}. The energy at the distribution maximum can be calibrated with a ^{55}Fe source, but the presence of eventual non-linearities in the detector response can spoil the calibration. We solved this problem with a Monte Carlo simulation of the muon flux on a 175-μm-thick germanium slab: the maximum energy was around 100 keV. In any case, we have to notice that a calibration performed with the muons is not completely reliable at low energies in the NTL regime. In fact the effect of non-linearities, the different interaction mode — a localised ionisation caused by one particle versus a diffuse interaction of several low-energy photons — and a different efficiency in the electron-hole-pair production can affect the energy evaluation. However this technique has been practical and indispensable when other methods were unavailable.

^{232}Th source is used for the calibration of massive bolometers. The γ-quanta — emitted by the ^{208}Tl line at 2615 keV — is the most common calibration method in $0\nu2\beta$ experiments because the γ-peak is close to the region of interest. The resolution of this peak can provide information about resolution achievable at the the $0\nu2\beta$-peak. A thoriated wire with ~ 1 % of ^{232}Th was used as source. It was placed outside of the cryostat between the 300-K screen and the lead shield.

^{210}Po source has been used for its α decay at 5.3 MeV. It has been obtained by the implantation of ^{218}Po atoms in copper tape. This source has been used for the calibration exploiting its monochromatic peak but also as a smeared source to investigate the $\beta(\gamma)$ and α separation. A few construction details and its test are reported in Appendix 9.1.

U was employed as an alternative of the ^{210}Po. This source contributes to the background also with a β spectrum of ^{234}Pa^m [97], a ^{238}U daughter, that the ^{210}Po does not present. This source is made by the deposition of an uranium-based salt on a copper band. The source emits α particles at two different energies: 4270 and 4679 keV. α sources like this one and the ^{210}Po are interesting for small crystals where the ^{208}Tl γ-quanta are not contained.

4 The CUORE experiment and beyond

The CUORE experiment is introduced in Sec. 4.1: where its current performance and future sensitivity are presented. An overview of the CUORE background budget is also illustrated with all the techniques employed to minimise its various components. The main background in our region of interest (2.5 MeV) stems from degraded-energy α events coming from surfaces adjacent to the CUORE detector. Current R&D efforts are focused on rejecting this background and are further discussed in Sec. 4.2. These R&D efforts fall under the umbrella of the CUPID experiment, the follow-up experiment to CUORE, which currently seeks to determine the viability of using the same $0\nu2\beta$-decay isotope as CUORE or switching to other isotopes.

4.1 The CUORE experiment

The CUORE (*Cryogenic Underground Observatory for Rare Events*) experiment [155] is the first bolometric tonne-scale experiment, searching for both $0\nu2\beta$ and $2\nu2\beta$ decays in ^{130}Te employing TeO_2 bolometers. This experiment is hosted at Laboratori Nazionali del Gran Sasso (Italy) in hall A, that provides an average rock burden equivalent to ~ 3.6 km w. e. [139].

The choice of ^{130}Te was supported by its high isotopic abundance corresponding to 34.2 % [156]. Such a high natural abundance of the $0\nu2\beta$ decay isotope did not require crystal enrichment for the construction of the CUORE experiment. The TeO_2 absorbers are dielectric and diamagnetic crystals [157] with a reasonably high Debye temperature of 232(7) K [158]. TeO_2-based bolometers have been deeply investigated and they demonstrated good performance first with CUORICINO [159] and then with the CUORE-0 [93] experiment. ^{130}Te has a $Q_{\beta\beta}$ of 2527 keV [160], slightly below the limit of the natural γ radioactivity given by the γ-quanta at 2615 keV of ^{208}Tl.

The CUORE detector is made up of 988 bolometers that are made of 0.75-kg $5 \times 5 \times 5$-cm-cubic TeO_2 crystals [157]. Each of them is coupled to a NTD germanium thermistor [161] for the read-out and a heater made of heavily-doped silicon [152] used to stabilise the detector output in time [153]. The connection between the sensor and the thermistor has been done by a 9-spot matrix of Araldite glue positioned by a robot specifically designed to ensure the reproducibility of this procedure [162]. The chip bonding is done with gold bonding wire and their connection to the read-out is performed with PEN-Cu cables [163]. The total deployed mass of TeO_2 is 742 kg of which 206 kg are ^{130}Te, corresponding to 9.6×10^{26} candidate nuclei. The detectors are held by PTFE clamps in a minimalistic copper structure to reduce the copper amount close to the detector. The bolometers are arranged in 19 towers of 13 floors each, where groups of four detectors are hosted. Fig. 4.1 presents a frontal and a bottom views of the CUORE detector.

The CUORE detector is operated in a custom made ^{3}He/^{4}He dilution cryostat, that can reach a temperatures down to 6 mK [164]. It is surrounded by six screens: 10 mK (mixing chamber), 50 mK, 600 mK (still), 4 K (pulse tubes), 40 K and 300 K (room temperature). Except the outer screen that is made of stainless steel, all the others are made of copper. In particular, the 10 mK shield is made of NOSV copper while all other copper shields use OFE copper. The NOSV copper can reach higher level

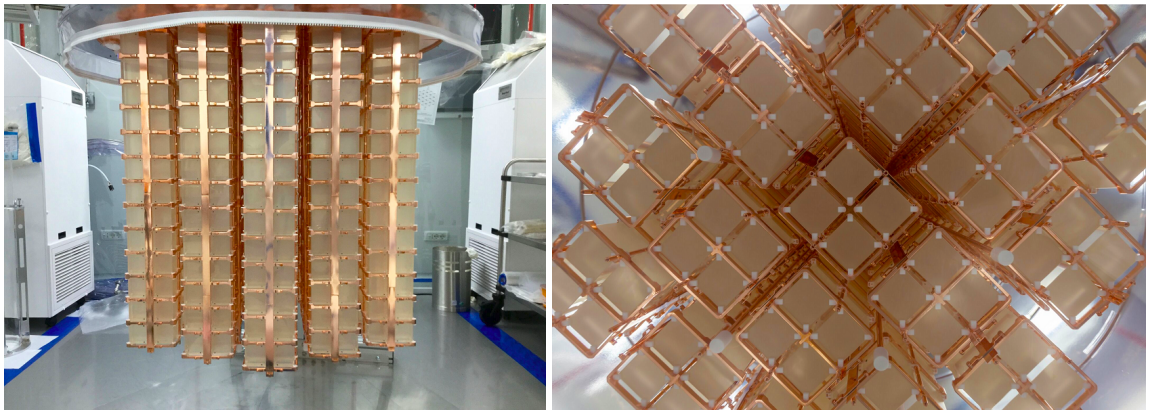

Fig. 4.1: Photographs of the CUORE detector: front (*left*) and bottom (*right*) view.

of radiopurity and for this reason it has been employed also in all the mounting structures close to the detector. Both the 4 K and the 40 K stages are wrapped in super-insulation foils to limit the effects of radiation. The facility does not employ cryogenic liquids: the 4-K stage is cooled by five pulse tubes of which four are operated and the 1-K stage is implemented by Joule-Thompson impedances.

The tower support plate — also made of NOSV copper — holds the CUORE detector and is decoupled from the cryostat structure to minimise the vibration noise. This plate is thermally linked to the mixing chamber.

Two shields protect the CUORE detector from the natural γ-radioactivity: one internal and one external. The inner shield is constituted by 30-cm-thick modern lead followed by 6.4-cm NOSV copper placed at the 50-mK stage above the detector and by 6-cm-thick ancient Roman lead [165] at the 4-K stage surrounding the detector below and on the sides. The outer shield is formed by a 25-cm-thick modern lead shield and by a 20-cm-thick polyethylene shield to moderate neutrons of which 2 cm are charged with boron to capture them.

The detector calibration is usually performed at the beginning and at the end of a physics run with a ^{232}Th source. In order to shine all the detectors with an uniform rate of events, a detector calibration system has been specifically designed [166], consisting of 12 NOSV copper tubes — inserted between the towers — where thoriated capsules arranged in wires can be slide down.

4.1.1 Background

The $0\nu2\beta$-decay detection occurs when the two electrons are stopped and deposit all their energy (2527 keV for ^{130}Te) in the bolometer. In the case of the CUORE experiment, the region of interest is constituted by 100 keV around the $0\nu2\beta$-decay between 2470 and 2570 keV. This region has been chosen to exclude the 2448-keV γ-quanta of ^{214}Bi and the 2587-keV line produced by the tellurium X-ray escape after a 2615-keV ^{208}Tl γ-quanta energy deposition. However, the region of interest includes a peak produced by the simultaneous absorption of the two γ-quanta (1173 and 1332 keV) generated by the ^{60}Co. A short description of the main events that can mimic the $0\nu2\beta$ decay is here summarised.

Natural and artificial environmental radioactivity. This category includes ^{238}U, ^{232}Th and ^{40}K events — generated by isotopes present in nature with a long half life — and by ^{60}Co, ^{134}Cs and ^{137}Cs isotopes with an anthropogenic origin. The main sources of background in the region of interest are constituted by: multi-Compton events produced by the 2615-keV γ-quanta originated in the cryostat and surface contamination close to the detector produced by ^{238}U and ^{232}Th. The surface events can also be produced by the ^{222}Rn daughters of the ^{238}U-broken chain. During the design and

construction of the CUORE experiment [110], a strong emphasis was placed on the minimization of these backgrounds. All the materials employed in the experiment — both at the detector and the cryostat level — have been carefully measured and selected to ensure minimum levels of bulk and surface contaminations [167]. Production and construction procedures have been optimised to avoid the introduction of further contaminants. Since the most challenging background comes from the surfaces, all the materials constituting the detector, the cryostat and the instruments used in the construction have been carefully cleaned. Particular care has been devoted to the copper surface cleaning procedure [168], this included the copper structures holding the detectors but also the cryostat screens. For the same purpose, the crystal surfaces have been polished. In order to avoid the contamination of ^{222}Rn daughters, all the parts constituting and surrounding the detector have never seen air. They have been manipulated and stored under nitrogen and during the mounting on the cryostat they have been kept in a radon depleted atmosphere which was constantly monitored [169, 170].

Cosmic rays. Only very high energy cosmic rays reach the CUORE detector and contribute to the overall background budget thanks to the 3600 m. w. e. rock overburden provided by the Gran Sasso mountain. The primary method of selecting (and then rejecting) these events comes from finding events that interact with more than a single detector within a specific time window.

Cosmogenic activation of materials. This phenomenon is produced by highly energetic neutrons produced by cosmic radiation. However the materials are also activated in the time that elapses between their production and their underground storage. The main isotopes produced by cosmogenic activation are ^{60}Co, ^{110}Ag and ^{110m}Ag. The first one concerns both copper and tellurium of the crystals. ^{60}Co β decays ($Q_\beta = 2824$ keV) with a γ emission of 1173 keV or 1332 keV. The so-called sum peak involves events where both gammas are absorbed in the same detector resulting in total energy deposition very close the $0\nu2\beta$ signal peak. ^{110}Ag and ^{110m}Ag concern only tellurium and β decay ($Q_\beta = 2892$ keV). In order to avoid this kind of background, crystals stayed aboveground only for around 3 months and then they have been stored underground for at least 4 years.

This list should also include neutrons, muons and γ-rays originated in the laboratory, but their contribution is negligible because they are stopped by the shields and can be rejected neglecting events in coincidence in more than one bolometer.

The background of the CUORE experiment has been simulated with Geant-4 considering the detector response, post-analysis cuts including multiplicity and pile-up. The results of the simulations produced a background index of $1.02 \pm 0.03(\text{stat})^{+0.23}_{-0.10}(\text{syst}) \times 10^{-2}$ counts/(keV yr kg) [167]. Fig. 4.2 shows a histogram with the CUORE background budget (*left*) and a background simulation in the region of interest (*right*). The dominant components are due to the natural radioactivity present on the material surfaces close to the detector that are included in the entry *CuNOSV: natural radioactivity*.

4.1.2 First result and sensitivity

After the detector installation in August 2016, cool down in December 2016 and its following commissioning, the CUORE experiment started to acquire data in May of 2017. Concerning the bolometers, 984 channels are working over the total 988 installed. The first results — presented in Ref. [68] — are reported in this section. The average energy resolution FWHM is 7.7(5) keV in the $Q_{\beta\beta}$ region of interest during physics run. For this first result a total exposure of 86.3 kg yr for the TeO_2 — that corresponds to 24.0 kg yr for ^{130}Te — has been acquired. These data — divided in two data sets — have been measured maintaining the detector at a temperature of around 15 mK. The CUORE limit on the $0\nu2\beta$ half life of ^{130}Te is 1.3×10^{25} yr (90 % C.L.). When this result is combined with the results from Cuoricino and CUORE-0, the limits becomes 1.5×10^{25} yr (90 % C.L.). The corresponding background in absence of signals is 0.014(2) counts/(keV kg yr).

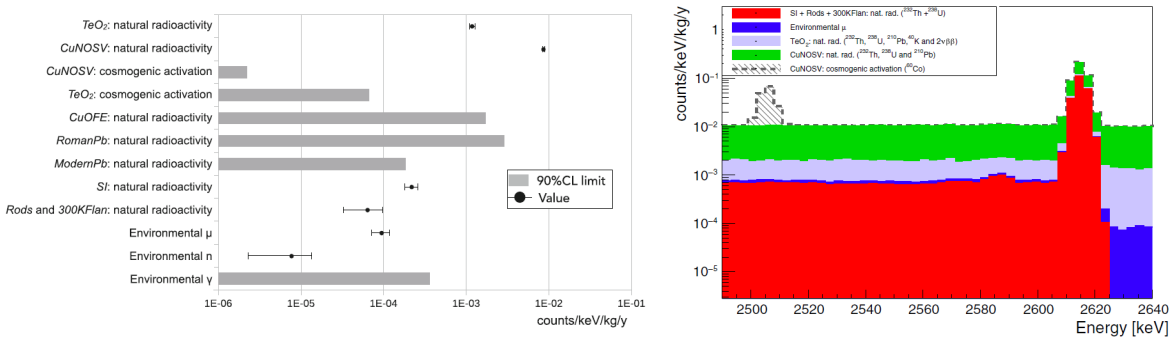

Fig. 4.2: *Left panel*: main CUORE background budget. The bands represent a limit at 90 % confidence level and the points show the value with 1σ statistical error. The acronym SI stands for superinsulation. *Right panel*: simulation of the background in the region of interest. Only the contribution from sources with an activity incompatible with zero are illustrated. The only exceptions are the ^{60}Co of NOSV copper, the ^{40}K present both in the detector and the surrounding copper and the $2\nu2\beta$ decay of ^{130}Te. For more detailed information concerning these figures consult Ref. [167].

The CUORE sensitivity to the $0\nu2\beta$ decay in 5-yr life time has been calculated with a Bayesian analysis in Ref. [171]. This value has been evaluated in an energy interval between 2470 and 2570 keV for a background index of 1.02×10^{-2} counts/(keV kg yr) and two different FWHM energy resolutions: 5 and 10 keV. When the detectors are divided in four subgroups, characterised by different background indexes, the resulting sensitivity is 9.1×10^{25} yr in case of a 5-keV-FWHM energy resolution and 6.2×10^{25} yr in case of a 10-keV-FWHM energy resolution.

4.2 The CUPID experiment

A follow-up of the CUORE experiment is proposed: CUPID (*CUORE Upgrade with Particle IDentification*) [82]. This experiment seeks to reach a sensitivity to the effective Majorana mass of 20 meV for the less favourable nuclear matrix elements to investigate completely the inverted hierarchy. This objective will be achieved acting on two fronts: via isotope enrichment and background identification/rejection. The first requirement is needed to increase the candidate mass without increasing the experimental volume, since CUPID will be hosted in the CUORE facility.

A summary of the present status of the R&D pertaining to the background rejection is presented here. Fig. 4.3 shows a summary of the possible technologies envisaged by the CUPID experiment. In particular two main possibilities are under investigation: keeping the same $0\nu2\beta$ isotope used in the CUORE experiment or to change it.

The advantage of maintaining ^{130}Te is its high isotopic abundance and its consequent low enrichment cost. Moreover TeO_2 is a well-known compound that has been extensively studied in these years. On the other hand, ^{130}Te Q-value is lower than the highest peaks present in the natural γ radioactive background. The selection of $^{130}TeO_2$-based bolometers for the CUPID experiment will require a dedicated crystal enrichment in ^{130}Te. This option have been investigated in Ref. [173]: two enriched $^{130}TeO_2$ have been tested in a bolometric measurement. The bolometric performance and radioactive content are listed in Tables 4.2 and 4.3. As we have seen in Sec. 4.1.1, the dominant background in the CUORE experiment is due to α particles coming from the surfaces close to the detector. An α-particle tagging technique is needed and two different approaches are considered: the α-tag accomplished with a heat-light dual read out or the achievement of a surface sensitivity. The next two sections will present possible solutions studied for both approaches.

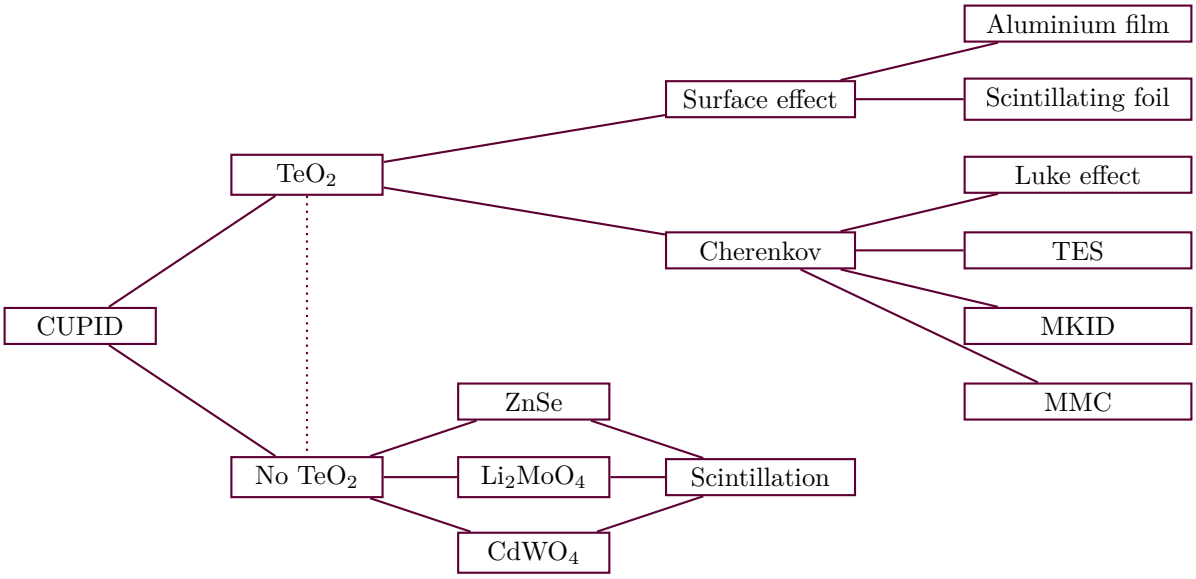

Fig. 4.3: Scheme of the ongoing R&D for the CUPID experiment adapted from Ref. [172].

4.2.1 Cherenkov light detection

This solution exploits the light emitted by TeO_2 crystals to separate $\beta(\gamma)$ events from the α background coming from the absorber bulk and surface. The main light output of TeO_2 crystals is due to the Cherenkov light [174] produced by particles travelling faster than the speed of light in the material. These photons are characterised by wavelengths in the interval $300 - 600$ nm with a dominant component for lower wavelengths [174, 175]. In the energy region concerning the ^{130}Te $0\nu2\beta$ decay (around 2.5 MeV), only $\beta(\gamma)$ events pass the energy threshold for the Cherenkov light production. In fact $\beta(\gamma)$ require energies higher than 50 keV to produce Cherenkov light while α's have a threshold of 400 MeV [174].

A $0\nu2\beta$ event produces two electrons sharing a total energy of 2.5 MeV in the case of ^{130}Te, the corresponding Cherenkov photons energy is of the order of 780 eV [175]. The light is easily auto-absorbed in TeO_2 crystals because of the high reflective index of this material, 2.4 for a 405-nm wavelength [176]. Moreover the auto-absortion effect increases for larger mass detectors [175]. According to simulations in Ref. [175], we are able to detect only around 18 % of the total Cherenkov photons emitted (this value considers also collection issues). This is confirmed experimentally: only 100-eV signals are collected by a CUORE-size crystal from an event of 2527 keV [177]. Such a tiny energy cannot be detected by a NTD-based light detectors used in double-β-decay search with scintillating bolometers [178] because their baseline noise width are usually of the order of 100 eV (50 eV in the best cases). The performance of these detectors has been investigated in Ref. [179, 177] respectively with a 117-g and a 750-g TeO_2 bolometers and has shown an insufficient $\beta(\gamma)$ and α separation. Optimised photo-bolometers — as the ones described in Ref. [180] — can reach thresholds of the order of 20 eV that would be interesting for the Cherenkov light detection [172]. But their complex fabrication makes them a non-viable candidate for a tonne-scale experiment. Other technologies have been investigated for the detection of this tiny light, a brief overview follows.

NTL-based light detectors equipped with a NTD germanium sensor. The low-energy threshold and high signal-to-noise ratio of NTL-assisted devices — whose working principle is explained in Sec. 2.7 — can be exploited to detect the Cherenkov light. Two different kinds of absorber materials have been investigated in this context: germanium — presented in this work — and silicon. The

germanium technology has been developed and produced in CSNSM as described in Sec. 3.2.1, all the information about their performance, test and other possible applications can be found in Chapter 6. Further information about a first test with one of these detectors coupled to a CUORE-size crystal can be found in Ref. [181].

Silicon-absorber detectors have been developed by the Bruno-Kessler Fondation and tested in Milano-Bicocca University. The geometry chosen consists of a central point and a border electrode that can stand biases up to 300 V. The main result obtained by these devices coupled to a 1-cm-side cubic TeO_2 bolometer are in Ref. [182].

NTL-enhanced light detectors have been studied for the first time in the framework of the CRESST experiment [126] to lower the energy threshold and to investigate less energetic nuclear recoils [183, 184, 185, 186]. One of these devices has been tested with a TeO_2 bolometer, its description follows in the next paragraph dedicated to low-impedance-TES detectors.

Low-impedance TES. This kind of sensors has been developed in the framework of the CRESST experiment and they have been applied to the TeO_2 Cherenkov light detection. The light detectors equipped with TES are characterised by fast responses and a very low threshold, indispensable for low-mass dark matter searches. The TES performance applied to the TeO_2 Cherenkov light detection has been tested in two different configurations. The first test [187] was carried out with a light detector developed in the framework of CRESST-II and EURECA [188]. This device consisted of an iridium-gold TES deposited on a silicon carrier then glued to a silicon substrate. The light detector was also provided with aluminium electrodes to exploit the NTL effect for the amplification of thermal signals. The second measurement [189] was performed with a CRESST-II type light detector: a thin tungsten film with a transition at 17.5 mK was deposited on a sapphire absorber where a silicon layer was grown. This photo-bolometer was coupled to a 285-g TeO_2 bolometer also equipped with a deported-TES. The TES-based devices are interesting but their employment would require a non-negligible effort in terms of detector production and read-out. In fact the fabrication and operation of a one-thousand TES with a consistent and low-transition temperature can be a challenge.

A TES-based light detector R&D is ongoing at Berkeley University in collaboration with Argonne National Laboratory in view of a ^{130}Te-based CUPID experiment. They are studying Au/Ir/Au trilayers and Ir/Pt bilayers TES deposited on silicon substrates [190]. The sensors have a critical temperature between 20 and 110 mK. These devices are still in a prototype stage and have not been tested with a TeO_2 bolometer yet.

High-impedance TES. These thermistors have been developed and fabricated in CSNSM, but a measurement with a TeO_2 bolometer has never been performed. Some considerations about their fabrication can be found in Sec. 2.3 and 3.2, while the tests performed during this work are in Chapter 7.

MMC sensors. This kind of sensors — introduced in Sec. 2.3 — was promising for the light read-out thanks to their low threshold [191]. MMC-equipped light detector with a silicon absorber have been developed and tested [192] in the framework of LUMINEU collaboration by the KIP Heidelberg group but these devices have never been tested with a TeO_2 crystal.

MKID-equipped light detectors. A short explanation of their working principle is reported in Sec. 2.3. MKID sensors have never been applied before to $0\nu2\beta$ experiments but they have been employed in astrophysics. They have been investigated because of the possibility of multiplexing multiple channels on a single read-out line. In fact it was thought that the doubling of the read-out channels could have negatively impacted the CUORE cryostat base temperature. MKID-based light-detectors have been studied in the framework of the CALDER project [193]. They are studying

a trilayer aluminium/titanium/aluminium KID sensor that achieved a baseline RMS resolution of 26 eV. Presently a test with TeO_2 bolometers is foreseen by the end of 2018.

The main results obtained in the measurement of the Cherenkov light emitted by TeO_2 bolometers are reported in Table 4.1.

4.2.2 Surface sensitivity

The identification of surface events, including α's and β's, can be the solution to the two most challenging backgrounds of the CUORE experiment. Two different approaches are investigated: aluminium film deposition and scintillating foil.

In the first case, bolometers are coated by an aluminium layer, a superconductive material at the normal CUORE operating temperatures. All events — occurring close to the coated surface — deposit a part of the energy in the aluminium film breaking Cooper pairs. These quasi-particles recombine after a few milliseconds producing a second athermal phonon population. The second heat injection produces a delayed signal that changes the pulse shape of the events by increasing the rise time. Bulk events are practically not affected by this effect because their energy fraction reaching the crystal surface is smaller. A complete aluminium coating of the crystal would produce a dead-layer with a thickness of $1 - 2$ mm solving the issue of the surface background. This principle has been demonstrated with a 12-g TeO_2 bolometer with one face covered by an aluminium deposition [197]. The read-out was done by a NbSi sensor because of its fast response. New measurements are foreseen in the framework of the CROSS project. This technique does not need a second read-out channel and is supposed to reject all surface events.

The second approach suggests to reject surface events exploiting a plastic scintillator foil that surrounds the TeO_2 bolometer. When a surface event occurs a part of the energy is released in the scintillator. At this point the scintillator foil emits some light that is collected by a light detector placed in the same cavity. The light collection is improved with the use of a reflecting foil surrounding the scintillator. A first prototype has been made with a $3 \times 3 \times 6$-cm TeO_2 crystal and a ^{147}Sm source in the framework of ABSuRD [198].

The above discussion explored the benefits of keeping the same $0\nu2\beta$ compound used by the CUORE experiment. However, switching isotopes can also provide certain advantages. Some isotopes possess a Q-value higher than the γ natural radioactivity end point at the 2615-keV line of ^{208}Tl. Additionally at these higher energies, more favourable space phase factors increase the sensitivity to the decay and scintillating properties can be employed in the α background suppression. The drawback is a lower isotopic abundance but it can be overcome with isotopic enrichment. ^{82}Se, ^{100}Mo and ^{116}Cd are considered by the CUPID group of interest as the most promising candiates for next-generation searches. Refer to Sec. 1.3 for an overview and comparison between the $0\nu2\beta$ isotopes. A succinct overview on the present status is here presented.

4.2.3 ^{82}Se-based crystals

The LUCIFER experiment was dedicated to the investigation of the ^{82}Se isotope embedded in ZnSe crystal. This $0\nu2\beta$ candidate has a Q-value of 2997.9(3) keV [199] and a natural isotopic abundance of 8.82 % [200].

After the initial tests that demonstrated the potential of this compound [201, 202], the LUCIFER experiment (later renamed CUPID-0 as it was considered the first CUPID demonstrator) started in March 2017. It is currently acquiring data in Hall C of Laboratori Nazionali del Gran Sasso. The final configuration is constituted by 26 ZnSe bolometers operated in the CUPID-0 cryostat, that previously hosted the Cuoricino and the CUORE-0 experiments. Over 26 crystals, 24 are enriched in ^{82}Se at 95 %,

Tab. 4.1: Summary of the test performed with light detectors coupled to TeO_2 bolometers. This table is divided in two parts: the devices without and with the NTL amplification. In both cases, the results are ordered according to the crystal mass. It has to be considered that smaller crystals have a higher light yield due to a lower light trapping. An eventual coating of the light detector surface is reported in parenthesis after the absorber material.

TeO_2 bolometer		Light detector		Light detector performance				
crystal	mass [g]	material	surface [cm^2]	sensor	NTL bias [V]	baseline RMS [eV]	DP	$\beta(\gamma)$ acceptance at 99.9 % α rejection	Ref.
TeO_2	25	Ge	5	NTD Ge	-	16	2.4	85.4	[194, 195]
TeO_2	117	Ge (SiO_2)	34	NTD Ge	-	97	1.4	21.4	[179]
TeO_2	285	Si on Al_2O_3	13	TES W	-	23	3.7	98.0	[189]
TeO_2	750	Ge (SiO_2)	20	NTD Ge	-	72	1.5	n.a.	[177, 189]
TeO_2	6	Si	4	NTD Ge	300	n.a.	4.7	n.a.	[182]
TeO_2	23	Si	4	TES IrAu	70	7.8	3.6	99.5	[187]
$^{130}TeO_2$	435	Ge	15	NTD Ge	25	35	2.7	78.8	[173]
$^{130}TeO_2$	435	Ge (SiO)	15	NTD Ge	55	25	3.5	98.3	[173]
TeO_2	750	Ge	15	NTD Ge	90	19	2.7	86.4	[181]
TeO_2	784	Ge (SiO)	15	NTD Ge	60	10	3.2	96.3	[196]

for a total mass of 9.65 kg of $Zn^{82}Se$ and 5.28 kg of ^{82}Se, and the remaining 2 are natural, contributing an additional 40 g of ^{82}Se [203]. The light read-out is done with bolometric SiO-coated germanium light detectors, that are equipped with a NTD germanium thermistor and a heater.

The detectors present good performance and rejection of the α background, reported in Table 4.2. The selenium percentage corresponds to 56 % of the total mass ensuring an advantageous fraction of candidate nuclei. The radioactive impurity concentrations of the crystals are listed in Table 4.3. The weak points of this technology are: the complex crystallization process [204] and its lower energy resolution compared to the other bolometers.

4.2.4 ^{100}Mo-based crystals

The ^{100}Mo isotope is another next-generation $0\nu2\beta$ candidate thanks to its high Q-value ($Q_{\beta\beta} = 3034$ keV [88]). It has an isotopic abundance of 9.7 % [205] and it can be enriched by centrifugation above 95 %. This isotope has been investigated embedded in different crystals: the two main compounds considered by CUPID are $Zn^{100}MoO_4$ and $Li_2{}^{100}MoO_4$. Other compounds as $PbMoO_4$ [206] and $Na_2(MoO_3)_4O$ — presented in Sec. 6.6 — have been tested but their study is still at an initial stage. Also the $Ca^{100}MoO_4$ belongs to the Mo-based compounds but it is not investigated in CUPID R&D: it is employed by the AMoRE experiment [98].

Therefore we will report only the results obtained with $Zn^{100}MoO_4$ and $Li_2{}^{100}MoO_4$ bolometers. The $Zn^{100}MoO_4$ compound has been tested recently as a bolometer [207] and the first R&D followed in the framework of the LUCIFER experiment [208]. A more systematic investigation has been carried out by the LUMINEU experiment that considered the opportunity to employ it in a $0\nu2\beta$ demonstrator. But this compound has been rejected by the LUMINEU collaboration in favour of $Li_2{}^{100}MoO_4$ because the latter presents uniform and better bolometric performance and a higher radiopurity. A comparison between the two compounds can be found in Tables 4.2 and 4.3. $Li_2{}^{100}MoO_4$ detectors have a high energy resolution and are characterised by good separation between $\beta(\gamma)$ and α. There are two drawbacks related to this technology. The former, of technical nature, is due to the weak hygroscopicity of Li_2MoO_4. The latter comes from an intrinsic feature of ^{100}Mo: its relative short $2\nu2\beta$ half life (6.9×10^{18} yr) generates background because of random coincidences of two $2\nu2\beta$ events. The first point tends to make the crystal surface more opaque without changing the bolometric performance. This feature is positive for the light collection, that is enhanced thanks to the reduction of light trapping at the surfaces. Therefore, even if hygroscopicity is not welcome, it has shown no negative consequence so far. The $2\nu2\beta$ pile-up contribution to the background has been studied and this issue can be reduced to a negligible level employing performant light detectors [209]. In particular, as we will seen in Sec. 6.5, a NTL-enhanced light detector — thanks to its higher signal-to-noise ratio — can permit a better pile up rejection.

The first demonstrator of the $Li_2{}^{100}MoO_4$ technology — CUPID-Mo — is hosted in the EDELWEISS cryostat in the Laboratoire Souterrain de Modane (France). It consists of 20 0.2-kg $Li_2{}^{100}MoO_4$ crystals for a 5-kg total mass of ^{100}Mo. Each $Li_2{}^{100}MoO_4$ bolometer is equipped with one NTD and one heater and it is coupled to a SiO-coated germanium light detector.

4.2.5 ^{116}Cd-based crystals

Also ^{116}Cd is an interesting isotope for the $0\nu2\beta$ search thanks to its high Q-value ($Q_{\beta\beta} = 2813.5$ keV [210]) and its reasonably high isotopic aboundance (i.a. = 7.49 % [200] with further enrichment possible). This material is a good scintillator and is commercially produced for a wide range of applications. Cadmium has been enriched in ^{116}Cd and used for the $0\nu2\beta$ search embedded in a $CdWO_4$ scintillator with the Solotvina [211, 67] and the AURORA [212] experiments. The first bolometric test done with an enriched $^{116}CdWO_4$ showed good performance [213] reported in Table 4.2. The CYGNUS project [214] is going to investigate the $0\nu2\beta$ decay of ^{116}Cd with 1.16 kg of $^{116}CdWO_4$ in the EDELWEISS cryostat.

Tab. 4.2: Main performance obtained by the compounds studied in view of the CUPID experiment.

	$Zn^{82}Se$ [178, 203, 96]	$Zn^{100}MoO_4$ [97]	$Li_2{}^{100}MoO_4$ [97, 63]	$^{130}TeO_2$ [173]	$^{116}CdWO_4$ [213]
mass [kg]	0.45	0.38	0.2	0.44	0.034
FWHM $Q_{\beta\beta}$ [keV]	23	9.7	$5-6$	$4.3-6.5$[1]	7.5
LY [keV/MeV] (β/γ)	3.3 to 5.2	$1.2-1.3$	0.7	-	31
LY [keV/MeV] (α)	9.1 to 14.1	$0.1-0.2$	0.2	-	5
DP $\beta(\gamma)$ - α [σ]	$10-12$[2]	$8-11$	9	$2.7-3.5$	17

Tab. 4.3: Main radiopurity limits measured for the principal enriched bolometers and considered by the CUPID group of interest.

	$Zn^{82}Se$ [203]	$Zn^{100}MoO_4$ [97]	$Li_2{}^{100}MoO_4$ [97, 63]	$^{130}TeO_2$ [173]	$^{116}CdWO_4$ [215, 216]	$^{116}CdWO_4$ [213]
crystallization	single	single	double	single	single	double
^{232}Th [μBq/kg]	2.5(2)	≤ 8	≤ 3	≤ 4	≤ 80	3(2)
^{228}Th [μBq/kg]	13.6(4)	≤ 8	≤ 8	≤ 2	57(7)	10(3)
^{238}U [μBq/kg]	5.1(2)	10(4)	≤ 5	8(3)	500(200)	800(200)
^{226}Ra [μBq/kg]	17.0(4)	14(3)	≤ 7	≤ 2	≤ 5	≤ 15

4.2.6 Multi-isotope option

An interesting alternative to the choice of a single isotope for the future of the CUPID experiment is the use of all the discussed isotopes in the same experiment. Ref. [217] reports the estimation of effective Majorana mass limits obtainable by an experiment in a single or multi isotope configuration. In particular, it considers $Zn^{82}Se$, $Li_2{}^{100}MoO_4$, $^{130}TeO_2$ and $^{116}CdWO_4$ crystals. Two different background rates are there envisaged: one of the order of 10^{-4} counts/(keV kg yr) and one of 4×10^{-6} counts/(keV kg yr) (corresponding to the zero-background case). In the former case[3], the combined result of a multi isotope measurement can provide a limit on the neutrino mass scale as good as the ones established by a single-isotope measurement based on $Li_2{}^{100}MoO_4$ or $^{130}TeO_2$ and providing a limit on the Majorana neutrino mass on the order of $0.018-0.021$ meV.

[1] At the 2615-keV γ quanta of ^{208}Tl.
[2] On a pulse shape parameter of the light.
[3] That looks viable according to the results achieved so far.

5 Thermal model measurements in a CUORE-like set-up

A better determination of the parameters describing the bolometer thermal model would improve the detector understanding and consequently could allow us to build higher-performance detectors. This chapter describes two measurements aiming at the evaluation of two thermal parameters: the glue conductance and the electron-phonon conductance, both introduced in Sec. 2.5. We decided to measure these parameters in a CUORE-like set-up in order to reproduce the same behaviour of a CUORE detector. A general description of the set-up is presented in Sec. 5.1 and a presentation of the three phases constituting each of the two measurements is given in Sec. 5.2. The details and the results of each run are presented in Sec. 5.3 and 5.4.

5.1 General set-up description

We wanted to reproduce as much as possible the conductances present in a CUORE bolometer for these reasons:

- the absorber employed was a TeO_2 mono-crystalline slab of the size $50 \times 50 \times 0.92$ mm with the crystal orientation <110>. We wanted to reproduce as much as possible the working conditions of a CUORE detector including the thermal contractions, that influence the stress applied to the thermistor and change its resistance-temperature response. The absorber was coupled to a copper holder — representing the thermal bath — with Dow Corning vacuum grease deposited in spots. We chose to use spots and not a complete grease film because air bubbles between the slab and the film or between the film and the holder could cause the detachment of the slab from the support during the cool-down. Furthermore, we tried to thermalise the slab to the holder with a few bands of copper tape, however not all of them remained adequately attached to the surfaces. The purpose was to get an absorber-bath thermal conductance dominating all the other conductances of the set-up.

- Four CUORE NTDs from the batch 39C — Table 5.1 reports their dimensions — were glued on the slab with Araldite glue. Unfortunately, the CUORE gluing system was not available for the present study. Two different gluing techniques were employed in the two measurements, more details will follow.

- On top of each NTD a CUORE heater was glued with Araldite. The details of the gluing differ in the two measurements: their description is postponed. In both cases, the heaters were projected off the NTD border by about 1 mm in order to facilitate the NTD bonding.

- The link between the chips and the Kapton connectors was done with 25-μm aluminium bonding wires, because this material is a poor thermal conductor after its transition to the superconductive

Tab. 5.1: NTD dimensions summary.

	dimensions [mm]
NTD1	$2.95 \times 2.86 \times 1$
NTD2	$2.97 \times 2.86 \times 1$
NTD3	$2.95 \times 2.86 \times 1$
NTD4	$2.97 \times 2.86 \times 1$

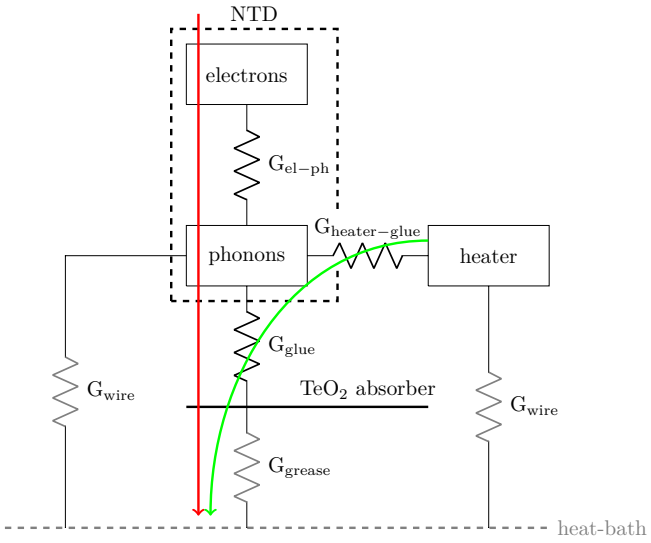

Fig. 5.1: Thermal scheme of our set-up.

state. We want to avoid that the injected thermal power flows back to the heat sink through the bonding wires. Each pad is bonded with two wires in order to have sufficient redundancy. The CUORE heaters have four contacts that are connected in different points of the meander. Therefore, a different resistance value corresponds to each couples of pads. When possible the heaters were contacted to the two external pads in order to have the highest resistance.

Both measurements have been carried out in Ulisse cryostat, refer to Sec. 3.1.4 for its description.

5.2 Measurement description

The thermal scheme corresponding to one NTD-heater system of our set-up is represented in Fig. 5.1. In this scheme, the dashed box represents the NTD: it can be imagined as being composed of an electron and a phonon systems connected by the electron-phonon conductance (G_{el-ph}). The NTD is glued to the TeO_2 slab and this connection is represented by the glue conductance (G_{glue}). The heater is glued to the NTD, represented by the heater-glue conductance ($G_{heater-glue}$), which of course contacts the lattice stage. The bonding wire conductance of the NTD is also connected to the lattice of the NTD and it is represented by (G_{wire}). Also the heater is bonded with aluminium wires, represented by a wire conductance (G_{wire}) as well. The wire conductances — represented in gray on the scheme — are negligible because the aluminium wire is a superconductor at our working temperatures. The TeO_2 slab is coupled to the heat sink with vacuum grease, providing a conductance to the heat sink (G_{grease}). It is

represented by a dashed gray line because it has to be ignored in the following measurements since all the temperatures are referred to the slab temperature, allowing us to neglect the grease conductance.

The purpose of these runs was to measure the glue and the electron-phonon conductances. These measurements were organized in three phases which are described in the following sub-sections.

5.2.1 Phase 0 - NTD characterization

We characterized the NTDs in order to determine the dependence of the NTD resistance on its temperature. The Efros-Shklovskii's law in Eq. (2.5) gives the relationship between these two quantities through the parameters R_0 and T_0. In this equation we fixed the exponent to 0.5, as it is commonly done for NTDs. We characterized the NTDs in the set-up itself, because the stress of the glue can modify the values of R_0 and T_0. In order to evaluate the parameters R_0 and T_0, we measured the NTD resistance and the cryostat base temperature with a TRMC2 bridge described in Sec. 3.3.

5.2.2 Phase I - Glue conductance

The purpose of *Phase I* was to measure the glue conductance (G_{glue}): we injected a power through G_{glue} and we measured the slab temperature and the NTD lattice (phonon) temperature. We define the injected powers P as in Eq. (5.1) and we parametrize the conductances as in Eq. (2.10). So we have to measure the coefficient g_0 and the exponent α in order to completely define the glue conductance as a function of the temperature. We fit the phonon temperature T_{ph} as a function of the injected power with Eq. (5.2), in order to evaluate g_0 and α.

$$P = \int_{T_{slab}}^{T_{ph}} G(T)dT \tag{5.1}$$

$$T_{ph} = \left(P\frac{\alpha+1}{g_0} + T_{slab}^{\alpha+1} \right)^{\frac{1}{\alpha+1}} \tag{5.2}$$

The power is injected in the NTD lattice through the heater. The power path is represented by the green arrow in Fig. 5.1. All the power passes through the heater-glue conductance $G_{heater-glue}$ and then the glue conductance G_{glue}, because the aluminium wires are in a superconductive state and prevent the power from flowing back. In fact, the conductance of a Ø25-μm aluminium bonding wire with a length of around 7 mm corresponds to 15 pW/K [218] at 25 mK, that is negligible with respect to the conductance of our system. We neglected the heater-glue conductance because it dominates the wire conductance and the power cannot flow to other directions.

The power injected is well known because we put a known constant current with a "semi-vintage electronics"[1] through the heater and we measured the voltage between the heater pads with the same electronics. At this point, we measured the temperature of the NTD lattice: we put the minimum current allowed by the semi-vintage electronics (250 pA with 1-GΩ load resistor) in the NTD and we measured its voltage. From this information we were able to calculate the lattice temperature from the values of R_0 and T_0 measured in the *Phase 0*. The slab temperature was measured with the same procedure with one of the other NTDs.

5.2.3 Phase II - Electron-phonon conductance

The purpose of *Phase II* was to measure the electron-phonon conductance (G_{el-ph}). In this case, we injected the power through the NTD, so the power path is represented by the red arrow in Fig. 5.1. The

[1] The semi-vintage electronics consists of six refurbished electronic modules used in the 20 detector array measurement of the MiBETA experiment. The read-out has a DC coupling (see Sec. 3.1.3) as the one of the Cuoricino and the CUORE experiment.

Tab. 5.2: Correspondence between the NTD sensors and the corresponding glue spot number.

NTD1	NTD2	NTD3	NTD4
6 spots	3 spots	1 spot	6 spots

Tab. 5.3: Glue spot mean diameter for each spot matrix.

spot number	mean diameter [mm]
1 spot	0.6(1)
3 spots	0.64(9)
6 spots	0.60(5)
mean	0.61(4)

current was put by the semi-vintage electronics and the voltage was read by the same system. All the power flows through the electron-phonon conductance first and then through the glue conductance, so we can equate the two power values:

$$\frac{g_{el-ph}}{\alpha_{el-ph}+1}\left[T_{el}^{\alpha_{el-ph}+1}-T_{ph}^{\alpha_{el-ph}+1}\right]=\frac{g_{glue}}{\alpha_{glue}+1}\left[T_{ph}^{\alpha_{glue}+1}-T_{slab}^{\alpha_{glue}+1}\right]. \tag{5.3}$$

We know g_{glue} and α_{glue} from the measurement of *Phase I* and we want to measure g_{el-ph} and α_{el-ph}. We measure directly T_{el} with the NTD and we obtain T_{ph} knowing the power injected in the NTD and the parameters from the *Phase I*. We can rewrite the Eq. (5.3) expressing T_{el} as a function of T_{ph}:

$$T_{el}=\left[T_{ph}^{\alpha_{el-ph}+1}+\frac{\alpha_{el-ph}+1}{g_{el-ph}}\frac{g_{glue}}{\alpha_{glue}+1}\left[T_{ph}^{\alpha_{glue}+1}-T_{slab}^{\alpha_{glue}+1}\right]\right]^{\frac{1}{\alpha_{el-ph}+1}}. \tag{5.4}$$

5.3 Conductance measurement I

5.3.1 Set-up description

In this section we will try to add a few clarifications about the set-up used in this first measurement:

NTD gluing. one purpose was the measurement of the glue conductance and to show its dependence on the glue-spot number: a larger number of glue spots is supposed to increase the conductance. Therefore we decided to glue two NTDs with 6 glue spots — increasing the statistic for our standard number of glue spots — and the remaining two with 3 and 1 glue spots. The correspondence between the NTDs identification number and their glue spot number is summarised in Table 5.2.

We first tested the quality of our glue spots by gluing and ungluing a test NTD on a Plexiglass square for each type of spot matrix in Fig. 5.2. Considering a NTD size of $3\times3\times1$ mm, we estimated the spot dimensions of the spots from those photographs. We obtained a mean spot diameter of 0.61(4) mm. All the results are reported in the Table 5.3 with their statistical uncertainty. Our spots are smaller than the CUORE-0 and the CUORE spots, whose estimated diameter was in the range $0.8-0.9$ mm [110], but in any case we will rescale our results for the spot surface.

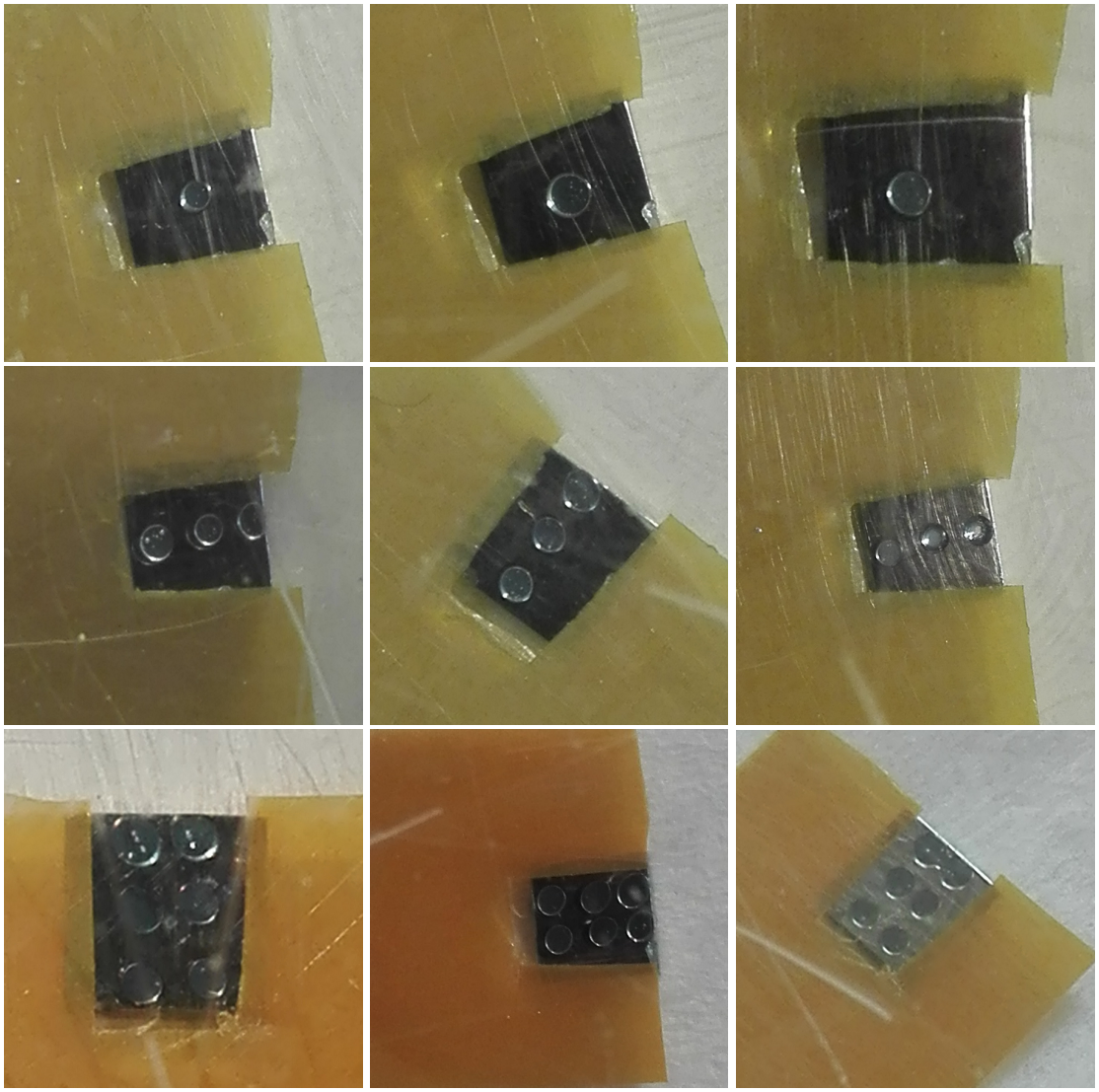

Fig. 5.2: Photographs of gluing tests on Plexiglas with 1 (*top*), 3 (*centre*) and 6 (*bottom*) glue spots.

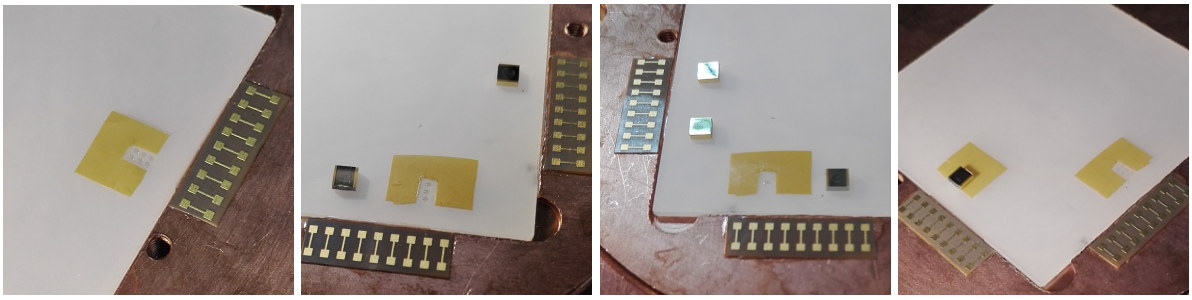

Fig. 5.3: Photograph of the glue spot deposition for NTD1, NTD2, NTD3 and NTD4 (*left to right*) surrounded by the Mylar mask.

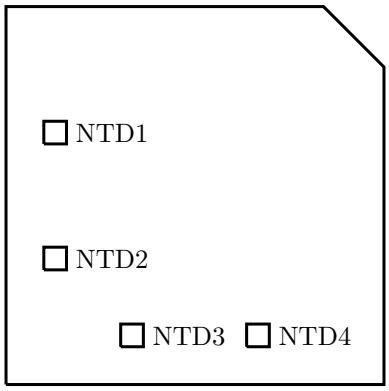

Fig. 5.4: Scheme of NTD position on the slab.

The glue spots were deposited with the Mylar-mask method described in Sec. 3.2. The glue spot deposition is shown for all the NTDs in Fig. 5.3. It has to be noticed that NTD1 was glued with a different mask (not perfectly flat) and the distance between the chip and the TeO_2 slab was larger. It was also evident by visual inspection that the NTD1 was not parallel to the TeO_2 slab. We attribute its different result with respect to NTD4 to this fact even if the number of glue spots is the same for the two sensors. The correspondence between the NTD numbering and their position on the slab is shown in Fig. 5.4.

Heater gluing. At this point we glued the heaters on top of the NTDs with a thin layer of Araldite, whose total quantity corresponds to about one glue spot (corresponding to ~ 0.014 mm^3 according to our mean diameter). Fig. 5.5 (*left*) shows the gluing of the last heater. In order to facilitate the NTD bonding, the glue spot was 1-mm distant from a NTD side and centred with respect to the gold pads; so the heater was projected off the NTD border by about 1 mm as one can see from Fig. 5.5 (*right*).

Thermal coupling to the heat sink. We used four symmetric big spots of Dow Corning vacuum grease to couple the slab to the heat sink.

In Fig. 5.6 presents three photographs of the final mounting including the bonding and phosphor-bronze wires connected. The four shadows below the TeO_2 slab are due to the vacuum grease.

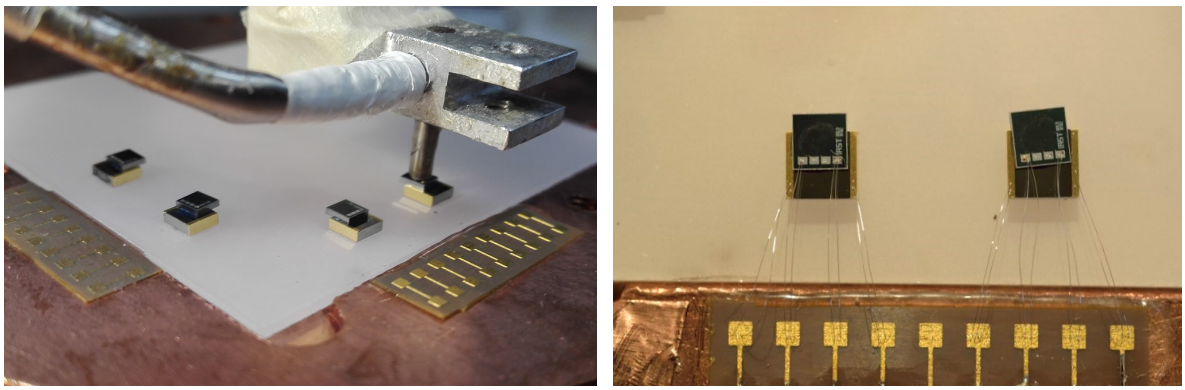

Fig. 5.5: *Left panel*: photograph of the last heater gluing on NTD4. *Right panel*: photograph of NTD3 and NTD4. The heaters are projected out of the corresponding NTDs. The chips are bonded with two aluminium wires for each pad. The external contacts have been selected for all the heaters of the mounting.

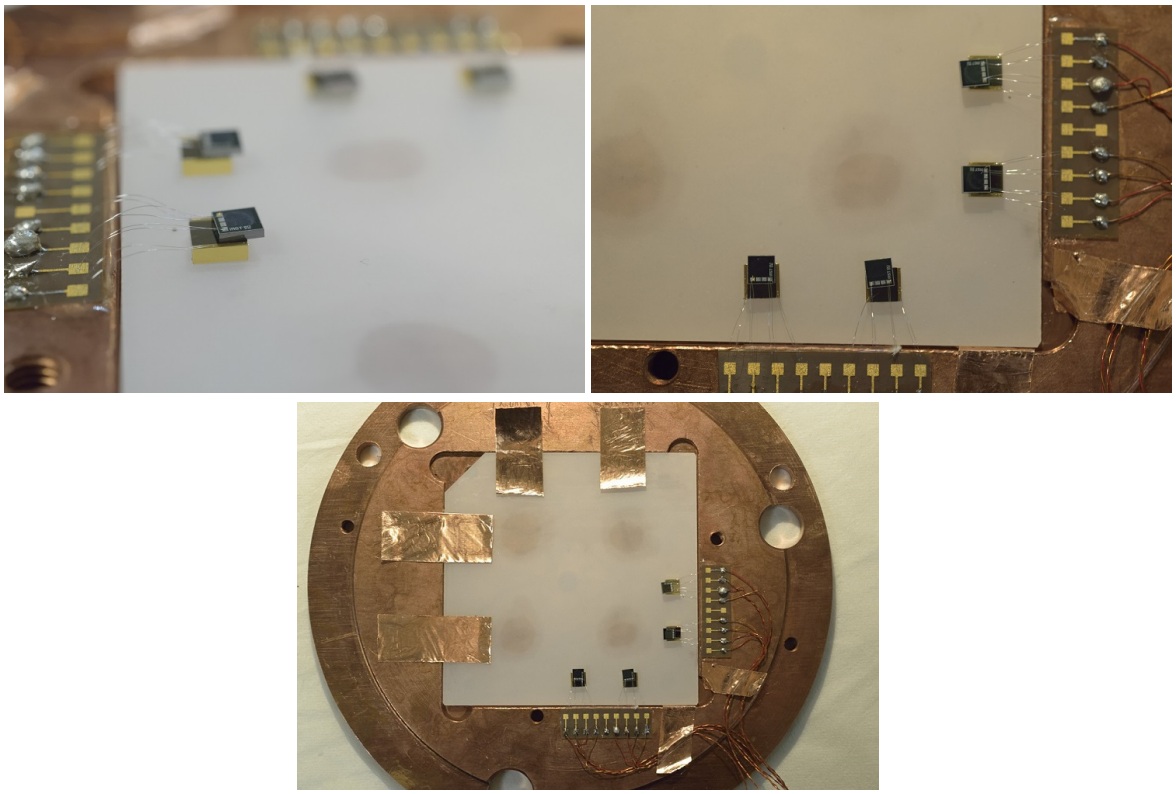

Fig. 5.6: Photographs of the completed set-up. The four shadows are due to the vacuum grease used to thermalise the slab to the copper holder.

Tab. 5.4: Summary of R_0 and T_0 values measured in-situ.

	R_0 [Ω]	T_0 [K]
NTD1	1.6(2)	4.53(8)
NTD2	1.9(2)	5.00(8)
NTD3	1.9(2)	4.83(7)
NTD4	1.8(2)	4.95(7)

5.3.2 Selection of the working temperatures

We decided to perform the first set of measurements at 25 mK because we wanted to stabilize the temperature of the slab using one NTD as temperature sensor, the TRMC2 bridge and a heater thermally anchored at the copper holder. The TRMC2 has a precision power output and can work also as an accurate PID controller. We wanted to be sure that the slab temperature did not increase for the highest powers injected in the heater, in order to simplify the data analysis. The NTDs had a high resistance and the TRMC2 was not able to measure them for temperatures lower than 22 mK, so we have chosen 25 mK as a safe temperature value for this type of measurement. Afterwards, we performed measurements at 14 mK stabilising on the copper holder instead of the slab and we discovered that our attempt to make an excellent thermal coupling between the holder and the slab was extremely successful: the temperature of the slab was stable also without TRMC2 stabilization, exhibiting small increases only for the highest injected powers.

5.3.3 Phase 0 - NTD characterization and systematic uncertainties

As pointed out above, we characterized the NTDs on the slab before starting the measurement. We used the TRMC2 bridge to perform this measurement. The bridge measured the resistance of the NTDs during a slow cool-down of the cryostat, controlled by the TRMC2 itself, from a temperature of 120 mK to 12 mK. We subtracted the cryostat wiring contribution from the measured resistances. The calibrated reference thermometer, used to measure the temperature, was placed on the copper holder.

Some NTDs of the same batch had already been characterized in CSNSM in a not-glued configuration. The glued thermistors show T_0 values compatible with these previous characterizations, while R_0 is a factor about 2 higher. This is not surprising. In measurements performed at CSNSM in 2011 studying the glue effect in CUORE thermistors, it was observed that the resistance is globally increasing without an appreciable change in sensitivity. The data points are reported in Fig. 5.7. We fitted the data with Eq. (2.5) between 24 mK and 64 mK for all the measurements. Despite the good linearity of the curves in a $\ln(R)$ - $1/\sqrt{T}$ space, we are clearly dominated by the systematic errors. The statistical error contribution is less than 0.1 % on the temperature in the worst case, corresponding to a temperature variation of 20 μK at 20 mK. This statistical error was estimated by a repeated measurement of the resistance at the same temperature. The systematic error on the temperature derived by the resistance-temperature curve fit is estimated to be of the order of $1 - 2$ mK, as discussed below. Therefore, in the following analysis we decided to neglect the statistical errors.

Many reasons can lead to systematic errors in the characterisation of the NTDs, for example a miscalibration of the reference thermometer, a deviation from the Efros-Shklovskii's law due to unknown physical effects, a thermal decoupling between the thermometer and the NTD to be characterized, parasitic powers in the thermometer and/or in the NTD, and other spurious effects. In order to estimate our systematic errors, we fitted the resistance-temperature data many times changing each time the fitting range. We have then considered the distribution of the R_0 and T_0 parameters: Table 5.4 shows the average of R_0 and T_0 parameters and their corresponding systematic uncertainties given by their standard

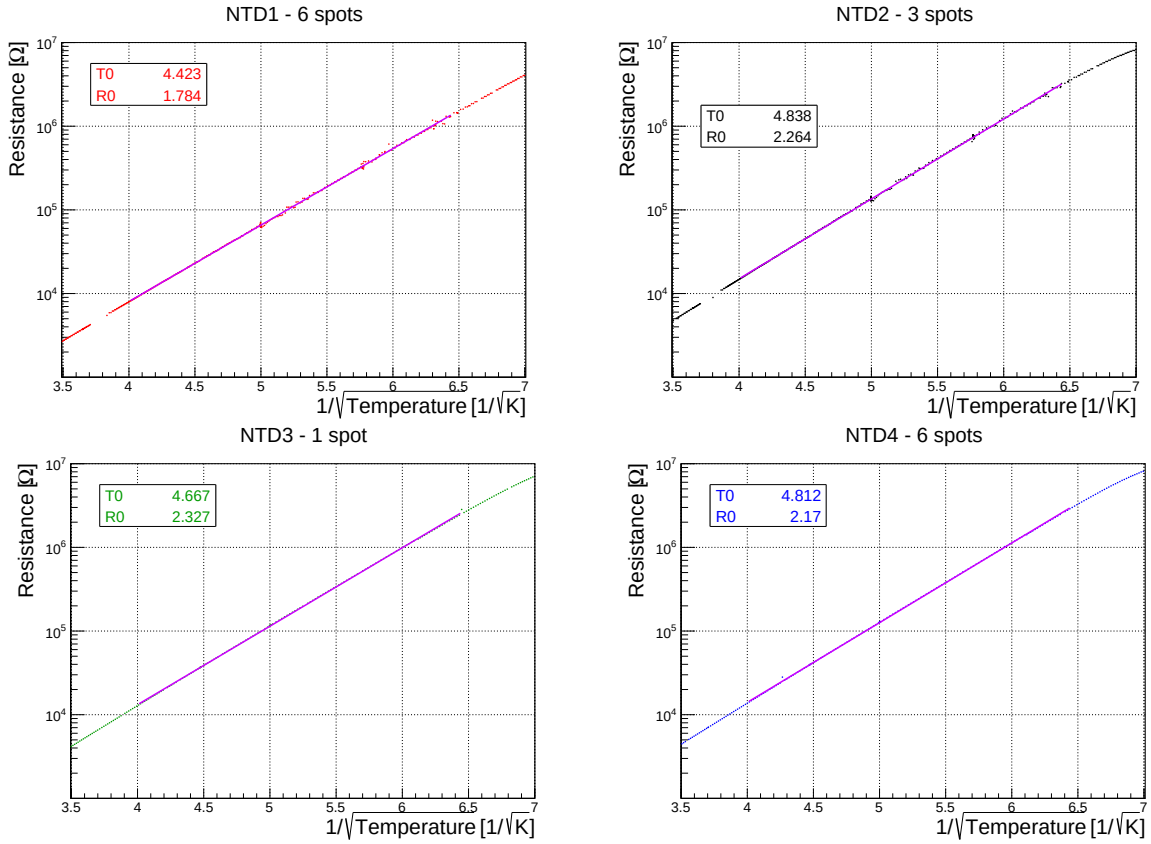

Fig. 5.7: Resistance as a function of the temperature for the four NTDs.

deviation.

The two parameters R_0 and T_0 are strongly correlated: this has to be taken into account in the derivation of the temperature from a measured resistance value. We cannot therefore simply use the errors on R_0 and T_0 as in Table 5.4 to extract the temperature and the related uncertainties from a given resistance with the Efros-Shklovskii's law of Eq. (2.5). Rather, we have proceeded as follows. For a given value of resistance, supposed to be exactly known given the smallness of the statistical error, we have extracted a distribution of values for temperatures using the families of R_0 and T_0 pairs derived in the previous fits performed with variable ranges. We have taken the mean of the temperature distribution $\overline{T}$ as a central value for the temperature and the standard deviation σ_T of the T distribution as a measure of the systematic error. For the analysis, we have associated each measured NTD resistance $\overline{R}$ to three temperature values: $\overline{T}$, $\overline{T}-\sigma_T$ and $\overline{T}+\sigma_T$, and we have repeated the analysis for these three temperature scales, using consistently the central value, the upper value or the lower value for all the data points. The systematic uncertainties on the temperature are appreciable in Fig. 5.8, where curves reporting $\overline{T}$, $\overline{T}-\sigma_T$ and $\overline{T}+\sigma_T$ as a function of $\overline{R}$ are shown.

5.3.4 Comparison between the measurements at 14 mK and 25 mK

The phonon and the electron temperatures as a function of the power injected with the heater at 14 mK and 25 mK are shown in Fig. 5.9. The data at 14 mK and 25 mK overlaps for large powers on the heater. Let's consider the triangular points at 14 mK (that correspond to the electron temperatures).

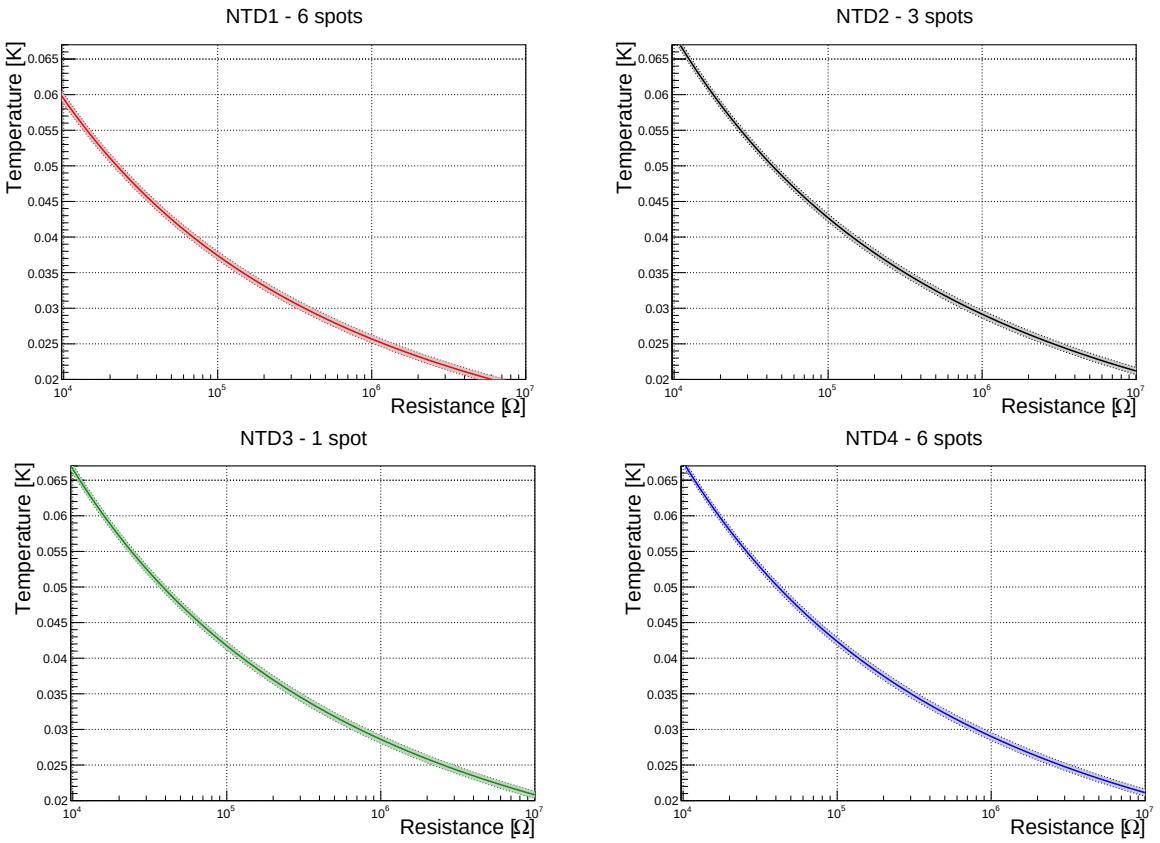

Fig. 5.8: The temperature as a function of the resistance showing its systematic uncertainty represented by a gray band.

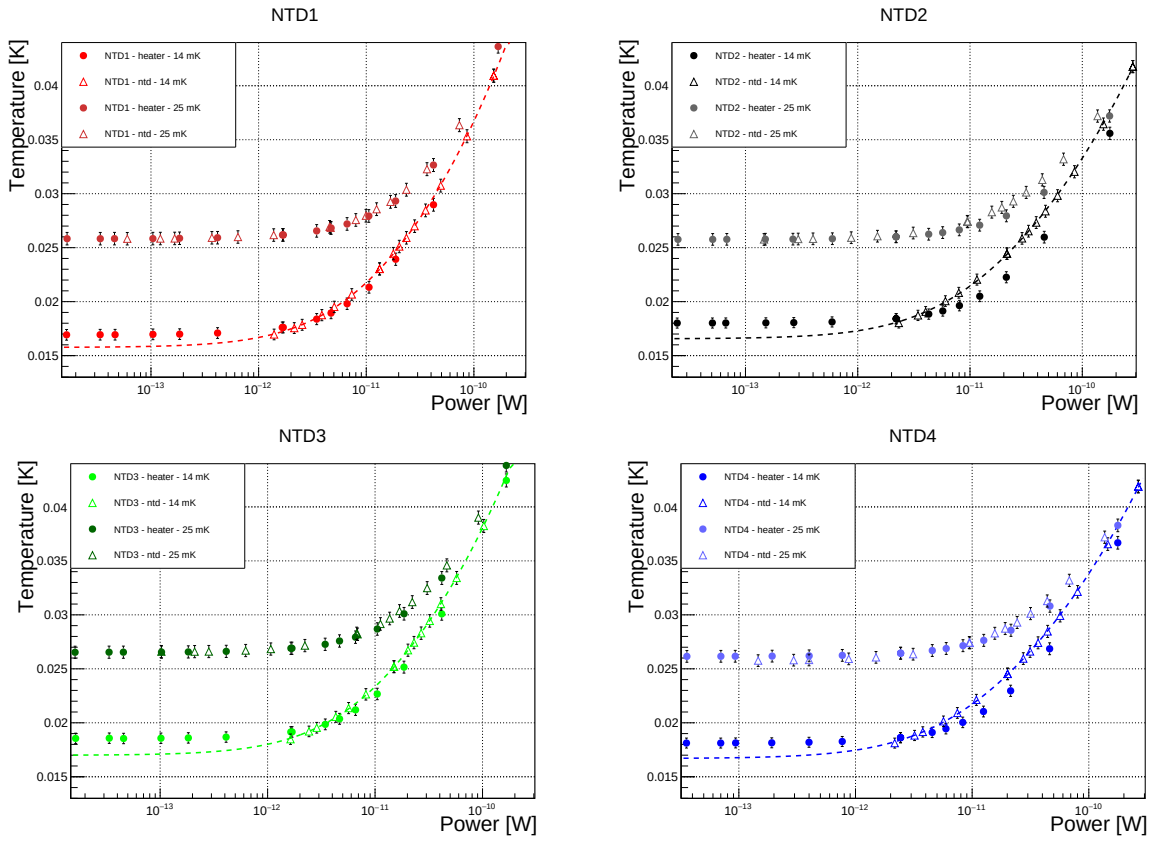

Fig. 5.9: Plot of the electron temperature (*triangular marker*) and of the phonons temperature (*round marker*) as a function of the power injected, in the case of 14 mK and 25 mK. The systematic error on the temperature, calculated as described in the text, is reported.

Their fit shows clearly that the extrapolated base temperature of the NTD electrons in the limit of zero power is below the one that we find with the heater measurement. This fact highlights a problem in the measurement at 14 mK: the minimum bias current applied (250 pA) heats up the NTDs appreciably, and therefore we are not able to meet the condition of zero-power measurement of the NTD electrons during power injection in the heater. We can conclude that the 25-mK measurement is more reliable than the one at 14 mK, where this condition is met thanks to the much lower NTD resistances, so we report the analysis only for those data. In any case, we will use the 25 mK results on the conductance laws to reproduce the 14 mK data as a consistency cross check.

5.3.5 Phase I - Glue conductance measurement

We performed the glue conductance measurement and treated the data as described in Sec. 5.2. For each current value put by the semi-vintage electronics, we measured the power dissipated in the heater, the resistance of the NTD biased with the lowest current and the resistance of the NTD at its side to check the slab temperature. We repeated this measurement at 25 mK and 14 mK, but we used only the data at 25 mK as explained in Sec. 5.3.4.

We plotted the phonon temperature as a function of the power injected by the heater. We used Eq. (5.2) to fit the data. The measurements of voltage and current made with the semi-vintage elec-

Tab. 5.5: Summary of glue conductance parameters.

	Glue conductance: $G(T)=g_0\ T[K]^{\alpha}$	
	g_0	α
NTD1	$2.3^{+0.3}_{-0.3} \times 10^{-5}$	$2.33^{+0.04}_{-0.05}$
NTD2	$2.9^{+0.5}_{-0.5} \times 10^{-4}$	$2.85^{+0.07}_{-0.06}$
NTD3	$6.6^{+0.9}_{-1} \times 10^{-5}$	$2.65^{+0.06}_{-0.05}$
NTD4	$2.7^{+0.5}_{-0.4} \times 10^{-4}$	$2.87^{+0.06}_{-0.06}$

tronics are precise and we have neglected their uncertainties in the analysis. Power is considered as an independent variable with negligible uncertainty. The only contribution to the uncertainties is due to the temperature measurement. The statistical error is negligible with respect to the systematic one, as discussed in Sec. 5.3.3.

We fitted the 25 mK data over all the power range and left α, g_0 and T_{slab} as free parameters. In order to evaluate the systematic effects, we repeated the fit three times using the central, the upper and the lower values for the NTD temperatures (see Sec. 5.3.3). Fig. 5.10 shows the fits performed on the data; the results on the conductance law parameters are reported in Table 5.5. Of course α and g_0 are correlated and must be used in pairs: the highest (lowest) coefficient g_0 has to be used with the highest (lowest) exponent α.

5.3.6 Phase II - Electron-phonon conductance measurement

We performed this measurement and treated the data as described in Sec. 5.2. For each current value injectable with the semi-vintage electronics, we measured the power dissipated in the NTD and its resistance. We also recorded the resistance of the NTD at its side, biased with the lowest current, to check the slab temperature. At this point, we calculated the electron temperature from the NTD resistance with the Efros-Shklovskii law in Eq. (2.5). Then we derived the phonon temperature knowing the power injected and the glue parameters measured in *Phase I*. We repeated this measurement at 25 mK and 14 mK, but we considered only data at 25 mK for the reason already mentioned. We used the same procedure to estimate the systematic uncertainties as for the glue conductance.

Fig. 5.9 shows the temperature as a function of the power when the latter is injected through both the heater and the NTD. When considering powers higher than $10^{-11} - 10^{-12}$ W, we notice that the temperature is higher if the power goes in the NTD, as it should be due to the electron-phonon decoupling, but this effect is much more appreciable for NTD2 and NTD4. We can therefore conclude that we are more sensitive to the electron-phonon conductance for the NTD2 and NTD4. This effect is better visualized in Fig. 5.11 for the measurement at 25 mK, where a zoom of the temperature as a function of the power injected is presented. The triangle symbols represent the temperatures of the lattice: the fit is done on those points. The square symbols represent the temperatures of the NTD electrons. The difference between the two temperatures is highlighted with a dashed line. When the glue conductance is good, like for NTD2 and NTD4, the lattice temperature is well lower than the electron one. On the contrary, when the glue conductance is low the difference between the two temperatures is smaller because a large temperature gradient is sustained between the NTD phonon and the slab. In this case, we are much less sensitive to the electron-phonon conductance and the results will have much larger uncertainties. We, therefore, decided to use only NTD2 and NTD4 to extract the electron-phonon conductance.

We plotted the electron temperature as a function of the phonon temperature in Fig. 5.12 and we

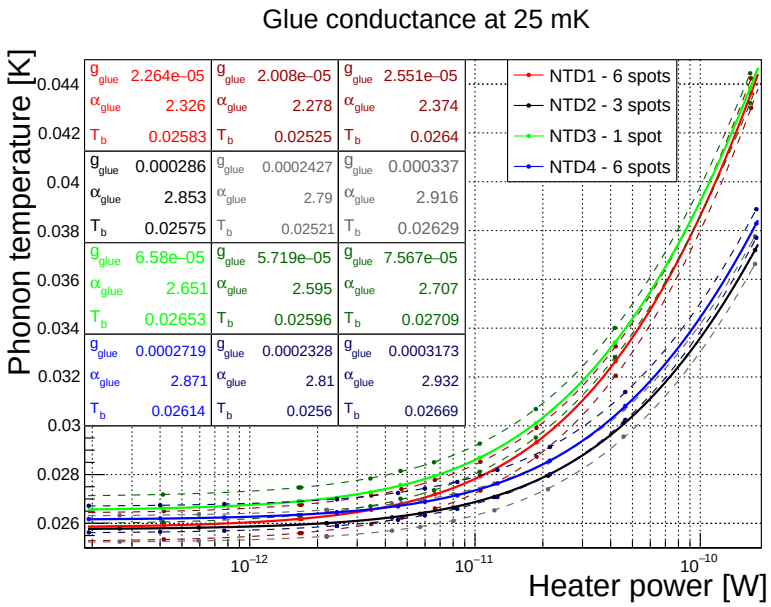

Fig. 5.10: Plot of the lattice temperature as a function of the power injected with the heater.

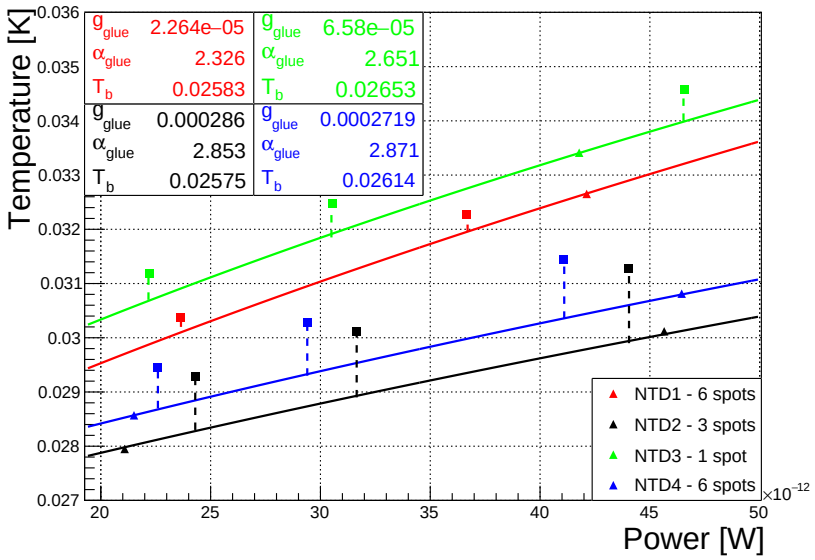

Fig. 5.11: Zoom of the temperature as a function of power injected for all the NTDs measured both injecting the power in the NTD and in the heater. The *square markers* point the electron temperatures while the *triangular ones* point the phonon temperatures. The segments highlight the difference between the two temperatures for NTD2 and NTD4 with a good glue conductance, and for NTD1 and NTD3 with a bad glue conductance.

Tab. 5.6: Sensitivity and baseline noise RMS for the four NTDs in the dynamic measurement.

	sensitivity [nV/keV]	bsl RMS [keV]
NTD1	3.4	29
NTD2	10.6	16
NTD3	1.8	65
NTD4	10.2	13

fitted it with Eq. (5.4). We considered as free parameters the temperature of the slab and the electron-phonon conductance parameters, but we fixed the glue conductance coefficient and exponent according to the measurements performed in *Phase I*. In order to take into account the systematic uncertainties on the temperature, we have repeated the analysis three times: [1] using the central value of the NTD electron temperature and the central value of the glue conductance parameters used to determine the NTD phonon temperature; [2]([3]) using the upper (lower) value of the NTD electron temperature and — consistently — the pair α and g_0 corresponding to the upper (lower) temperature scale for the glue conductance. This defines a central curve for the electron-phonon conductance and a range for this quantity due to the systematic uncertainties on the temperature. It is interesting to note that the electron-phonon conductances of the two NTDs are perfectly compatible. Their central values differ only by a few % and the differences between the two NTD glue conductance is well within the systematic uncertainties. The results obtained in *Phase II* demonstrate therefore the coherence of our measurements. The resulting electron-phonon conductance is:

$$G_{el-ph}[\text{NTD39C}] = 6.3\ T[K]^{5.5}[W/K]. \tag{5.5}$$

The electron-phonon conductance at 20 mK corresponds to 0.34 nW/(K mm^3) with an error of 30 %. It becomes 3.1 nW/(K mm^3) with 21 % of uncertainty at 30 mK, see Table 2.1 for a comparison with the electron-phonon conductance measurements reported in literature.

5.3.7 Dynamic measurements

We acquired about 3 hours of stream data from the four NTDs at the end of the run. We used the same DAQ settings for all the NTDs: gain 1072, sampling frequency 10 kHz, load resistors of 100 MΩ. We measured NTD1 and NTD2 in coincidence and subsequently NTD3 and NTD4 in coincidence, biasing them with the same current of 4.16 nA. It was not possible to acquire all the four NTDs in coincidence for technical reasons. Fig. 5.14 shows the spectra acquired. We had no kind of source but we can see the muons since the set-up was hosted in an aboveground cryostat. We fitted the muon spectrum with a Landau distribution. As it is clear from Fig. 5.14, NTD2 and NTD4 have a higher sensitivity. The peak of the distribution corresponds to a deposition of 676 keV in our 0.92-mm-thick TeO_2 slab according to Monte Carlo simulations and in agreement with the average stopping power of a TeO_2 slab corresponding to around 1 MeV. Therefore we can estimate the sensitivity and the baseline noise RMS, reported in Table 5.6.

We chose some coincident muon pulses at a fixed energy: Fig. 5.15 shows two couples of coincident pulses (*top*) at 3.38 MeV and the same pulses normalized at the maximum amplitude (*bottom*). The signal-to-noise ratio is poor because the sensitivity of the set-up is extremely low; the data have been acquired at 25 mK and the grease conductance to the bath is very high. In other terms, our set-up is in the worst possible conditions for pulse measurements, with a strong coupling of the energy absorber to the thermal bath and a weak coupling to the sensor. Of course, on the contrary, these are the best conditions to measure the glue conductance and especially the electron-phonon conductance, the main

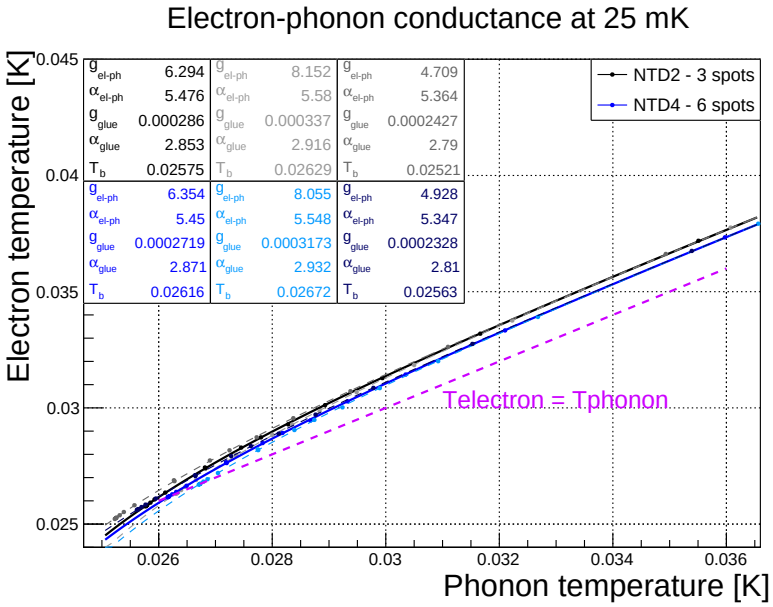

Fig. 5.12: Electron temperature as a function of lattice temperature for NTD2 and NTD4. The fit has been performed with α_{el-ph}, g_{el-ph} and T_b as free parameters. The deviation from the dashed line, where electron temperature is equal to the phonon temperature, shows our sensitivity to the G_{el-ph}.

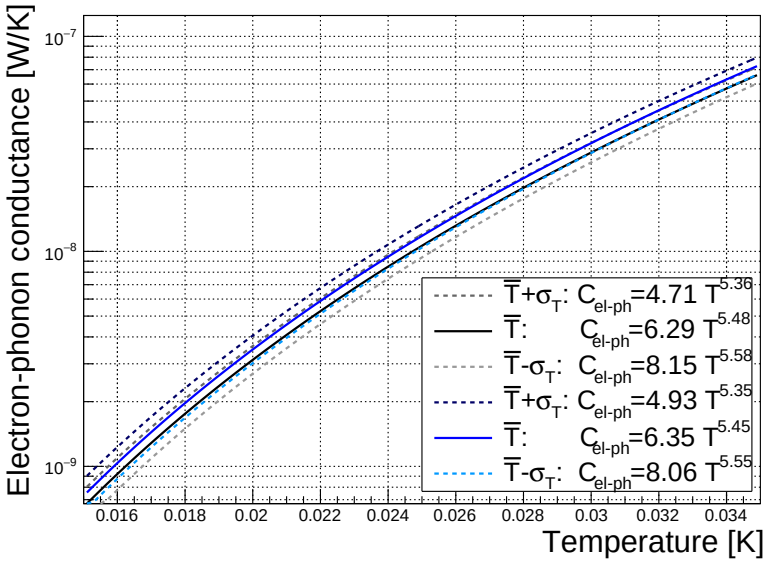

Fig. 5.13: Electron-phonon conductance as a function of the temperature for NTD2 and NTD4. For each NTD three values are considered: the one corresponding to the central temperature and two corresponding to an over and an under-estimation of the temperature. The parameters from the analysis reported in Fig. 5.12 are considered.

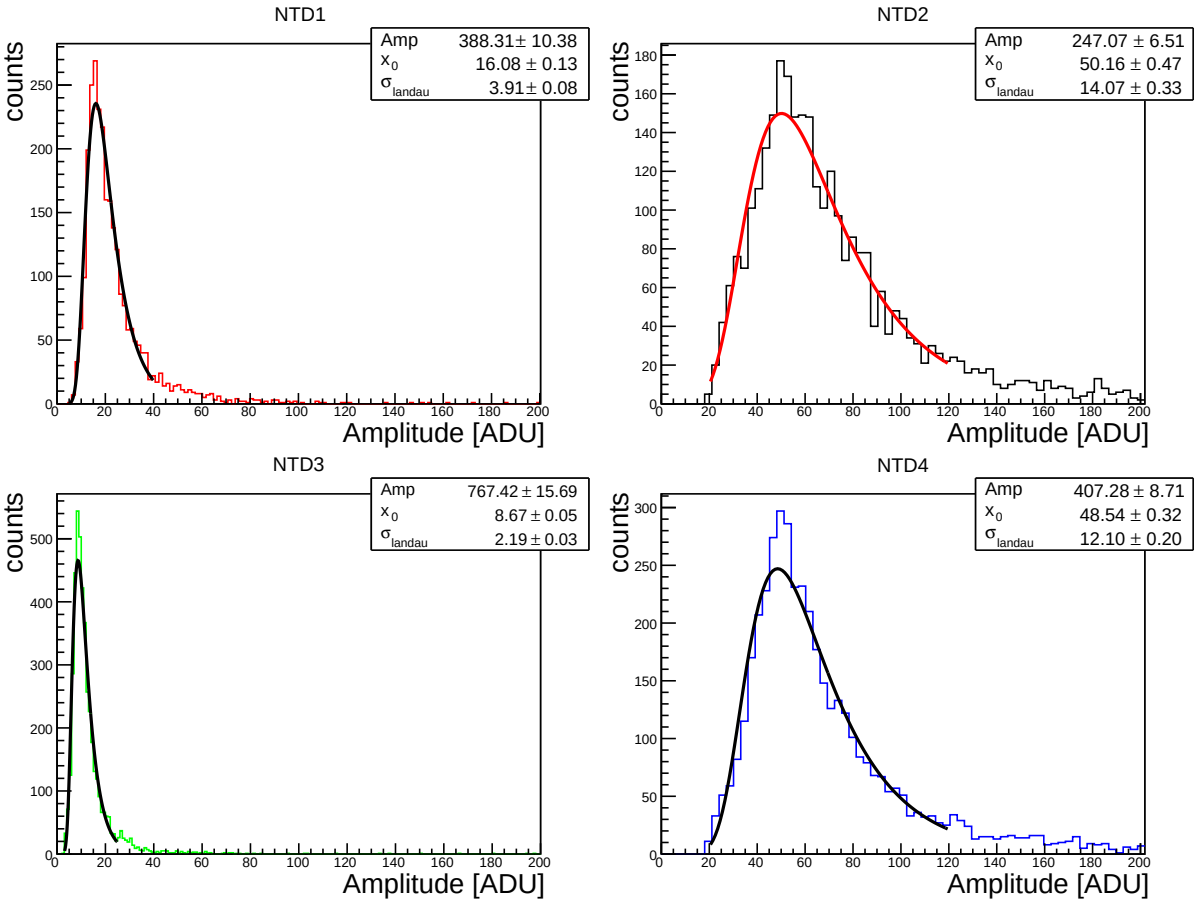

Fig. 5.14: Muons spectra fitted with the Landau distribution for the four NTDs.

Tab. 5.7: Summary of the parameters used in the simulation.

	NTD1	NTD2	NTD3	NTD4
G_{el-ph} [W/K]	$6.3\ T[K]^{5.5}$			
G_{glue} [W/K]	$2.3 \times 10^{-5}\ T[K]^{2.33}$	$2.9 \times 10^{-4}\ T[K]^{2.85}$	$6.6 \times 10^{-5}\ T[K]^{2.65}$	$2.7 \times 10^{-4}\ T[K]^{2.87}$
G_{grease} [W/K]	7×10^{-7}			
R_0 [Ω]	1.6	1.9	1.9	1.8
T_0 [K]	4.53	5.00	4.83	4.95
T_b [mK]	25.1	25.2	25.4	25.4
P_{static} [pW]	0.127	0.104	0.062	0.146
$P_{dynamic}$ [pW]	9.9	19.2	13.6	17.7
C_{TeO_2} [J/K]	$4.1 \times 10^{-5}\ T^3$			
$C_{NTD\ latt}$ [J/K]	$2.3 \times 10^{-8}\ T^3$			
$C_{NTD\ elect}$ [J/K]	$9.3 \times 10^{-9}\ T$ [220]			

aim of the run. We noticed that the NTDs (NTD2 and NTD4) with a higher glue conductance had higher pulse amplitudes and faster initial decay time (Fig. 5.15). We decided to check with simulations if a thermal model can explain this behavior.

5.3.8 Simulations

We used a simulation program following the thermal model described in Ref. [219], produced at Insubria university in 2003. The parameters used in the simulation are listed in Table 5.7. We used the common electron-phonon conductance G_{el-ph} of 6.3 $T^{5.5}$[W/K] — discussed in Sec. 5.3.6 — for all the simulations. We know all the parameters that characterise our set-up with the exception of the conductance due to the grease (G_{grease} in Fig. 5.1) between the TeO_2 slab and the heat sink. We tried to estimate its value with the static and dynamic simulations. Initially, we varied its value in the static simulations, and we noticed that it has a weak influence on the load curves: a big value of the grease conductance ($\sim 10^{-3}$ W/K-10^{-5} W/K) fits the load curves better, while a lower value tends to bend them down for high currents. Then we simulated dynamically the system, in this case we noticed that the energy deposited in the crystal flows away quickly with a high grease conductance. In conclusion, we searched for a compromise between the pulse amplitude and a good agreement with the load curves: we found 7×10^{-7} W/K. The values of R_0 and T_0 have been discussed in Sec. 5.3.3 and the glue conductance G_{glue} in Sec. 5.3.5. The heat sink temperature T_b reported in the Table 5.7 has been measured with the NTD at the side of the working NTD.

During the static measurement, we biased two NTDs at the same time: the first one was the measured NTD, while the second was biased at the lowest possible current and it was used to check the slab temperature. We simulated only the measured NTD in order to simplify the simulation, and we took into account the contribution of the second NTD as a constant power injected in the slab. This power is listed in Table 5.7 as P_{static}. During the stream data acquisition, two NTDs with the same bias were measured simultaneously. Also for the dynamic simulation, we simulated only one NTD and we considered the second NTD as a constant power injection in the slab. This power is listed in Table 5.7 as $P_{dynamic}$. We ignored the contribution of athermal phonons in this simulation.

Fig. 5.16 represents the resistances as a function of the power injected for the experimental points and their simulation: they show a good agreement.

We also simulated the pulses: we decided to reproduce a muon event that releases 3.38 MeV in the absorber. Fig. 5.17 shows a real 3.38-MeV pulse superimposed to the simulation. The long decay time and the rise time are in agreement with the data, while the real amplitude is higher than the simulated

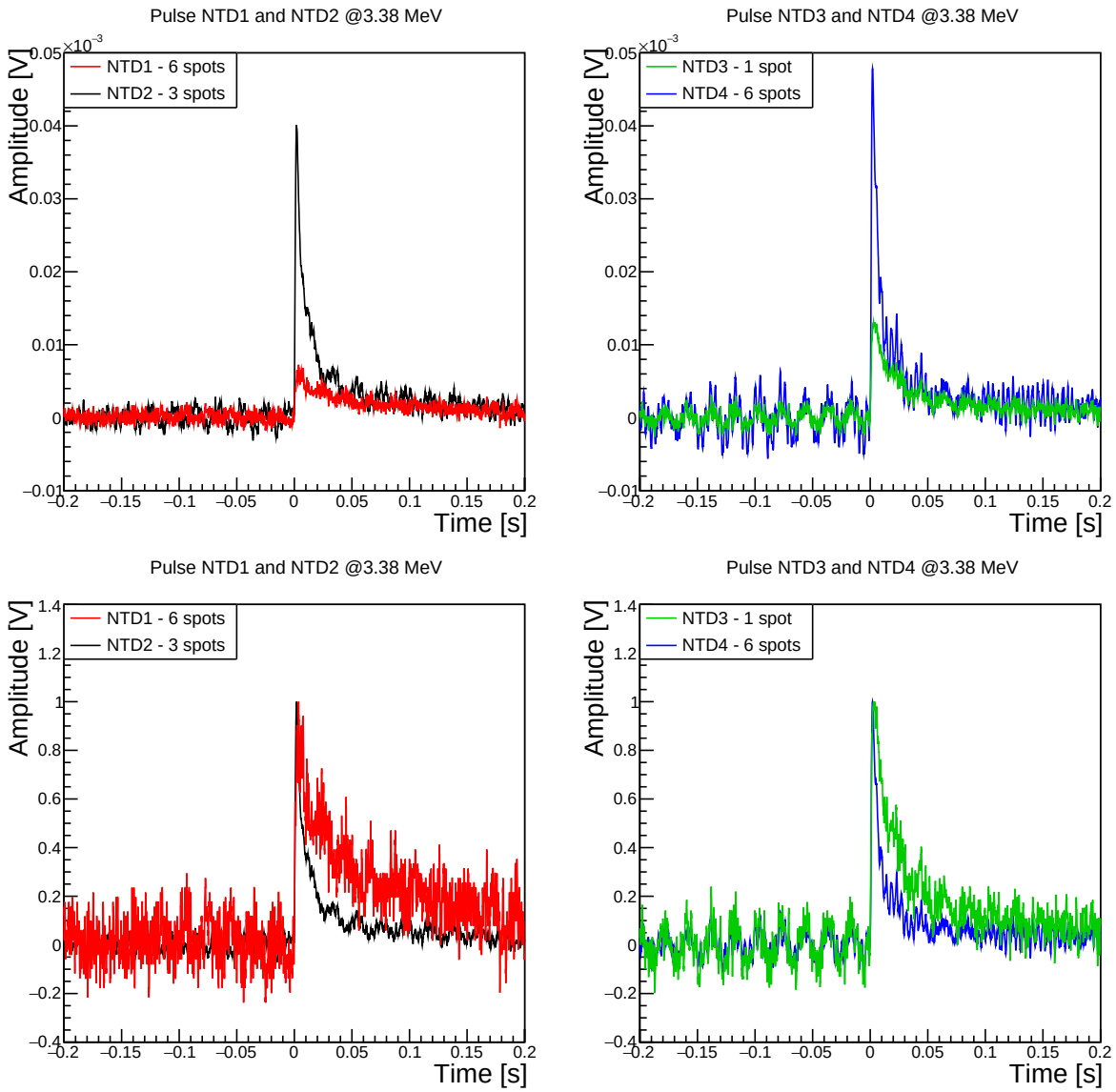

Fig. 5.15: *Top panel*: two coincident pulses at 3.38 MeV for NTD1 and NTD2 (*left*) and for NTD3 and NTD4 (*right*). *Bottom panel*: the same pulses have been renormalised to better show the behaviour of the decay time.

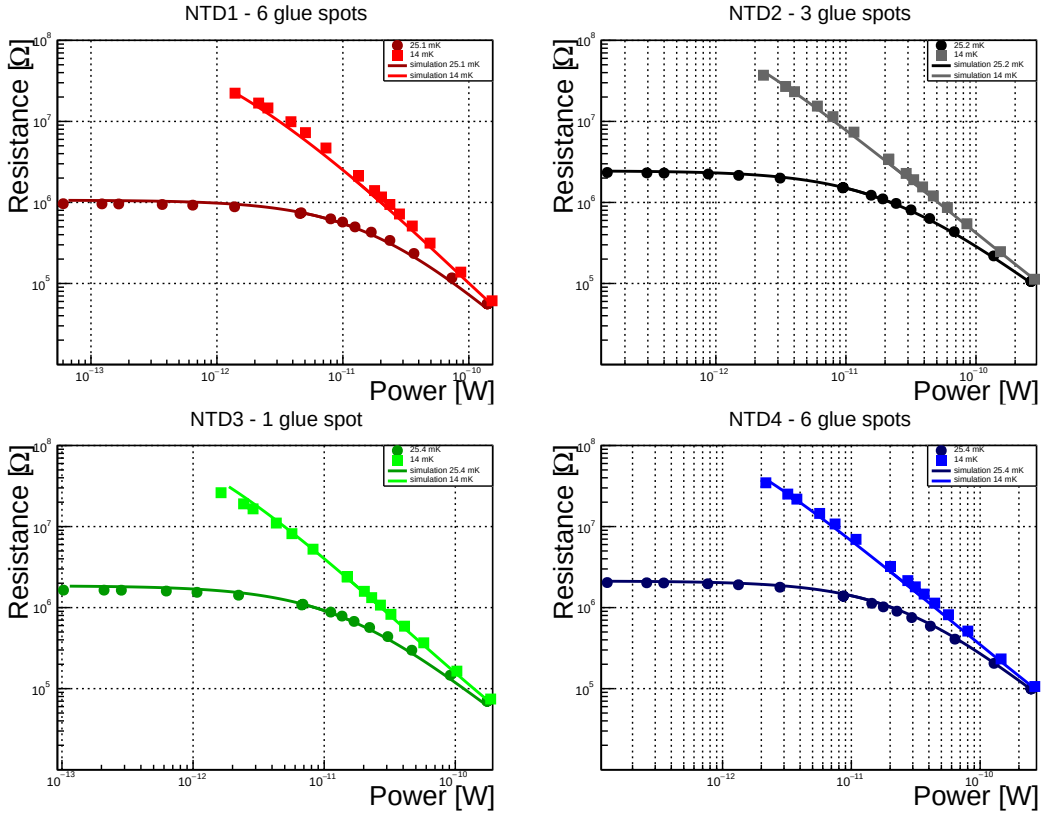

Fig. 5.16: Resistance-power curve data and their simulation, with the common electron-phonon conductance measured in our set-up.

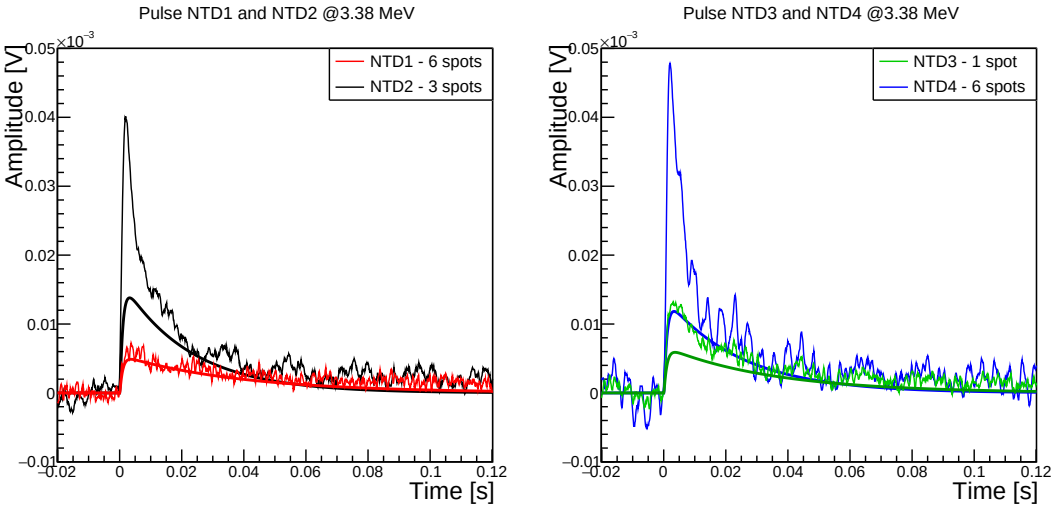

Fig. 5.17: Real 3.38-MeV pulses superimposed with their simulation. Real pulses are characterized by a higher amplitude than the simulated ones, but the rise time and the long decay time are reasonably well accounted for. We suspect that the extra amplitude in the measured pulses is due to an athermal-phonon signal that is not taken into account in the simulations. The good agreement in the case of NTD1 could be due to its worst gluing with respect to the others.

one. We suppose that it is due to athermal phonons that are not considered in the model considered. The pulses corresponding to the NTDs with a bigger glue conductance are characterized by a higher amplitude.

5.3.9 Conclusions

The coherence of the measurement performed at 25 mK is clear. The two 39C NTDs used to measure the electron-phonon conductance show a compatible electron-phonon conductance: 6.3 T[K]$^{5.5}$ [W/K]. If we renormalise the electron-phonon conductance coefficient for the NTD volume (calculated from the dimensions reported in Table 5.1), we obtain $g_0 = 0.74$ W/(K$^{6.5}$ mm^3). The electron-phonon conductance at 30 mK is 3.1 nW/(K mm^3) and can be compared with the results reported in literature (see Table 2.1). The literature values present a good spread: the average value is (3 ± 2) nW/(K mm^3) excluding Ref. [120] and (9 ± 19) nW/(K mm^3) including it. The electron-phonon conductance here measured is completely compatible with the ones reported in literature. The comparison between the measurements at different temperatures are consistent (Fig. 5.9). We cross-checked the temperatures with an adjacent NTD biased with the lowest possible current for each measurement and the result were always compatible and consistent.

As it is evident from Fig. 5.10, the glue conductances respect the following order: G_{NTD3} (1 spot) < G_{NTD1} (6 spots) < G_{NTD4} (6 spots) < G_{NTD2} (3 spots). We expected that the glue conductance would depend on the number of glue spots, but it is not the case. We can conclude that we have a problem in the glue deposition reproducibility. We do not know if this is due to our gluing technique (that has clearly shown some reproducibility problems e. g. in the case of the six-spot NTD1) or if it is a more general problem, for example due to the NTD/TeO_2 surface condition or strong sensitivity to tiny differences in temperature/mixing time/quantities during the glue preparation.

We simulated the set-up with our derived electron-phonon conductance at 25 mK and at 14 mK, finding a good agreement between the simulation and the measured data (Fig. 5.16). Therefore we are convinced that the electron-phonon conductance in Eq. (5.5) describes properly the NTD static behaviour between 14 mK and 40 mK.

As for the dynamic simulations (Fig. 5.17), the results support the observed long decay time and the rise time of the acquired pulses. The amplitude of the simulated pulses tends to be underestimated with respect to the real ones. The pulses with the lower glue conductance suffer less from this underestimation; in the case of NTD1 the amplitude is well simulated. We suspect that the underestimation is due to the presence of athermal phonons contribution, that we have not simulated so far. We can speculate that athermal phonons are transmitted more efficiently between the TeO_2 slab and the NTD when there is a higher glue conductance, and this would explain the good agreement between experiment and simulation in the NTD1 case.

5.4 Conductance measurement II

We were not completely satisfied by the result obtained on the glue-conductance measurement: it was not scaling with the spot number and the statistic was low. Therefore we decided to repeat the measurement changing the gluing method and using four sensors with the same glue-spot number. We have been obliged to unglue the previous set-up to recover the same NTD thermistors. The NTDs have been easily unglued with the dichloromethane from the slab, while the ungluing procedure between the NTD surface and the heater has been more complicated. In fact the thin glue layer between the chips prevented the infiltration of the solvent. Despite the different techniques used — including different solvents, heating of the glue and ultrasonic bath — only two NTDs have been unglued from the heater (NTD2 and NTD3). We have been obliged to break the remaining heaters to remove them. The heaters have broken in the

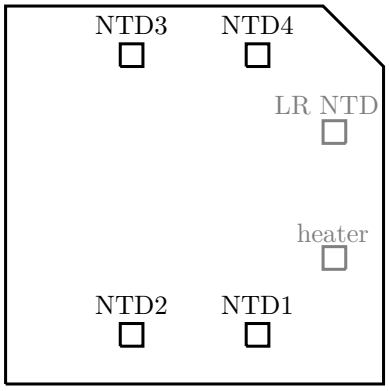

Fig. 5.18: Scheme of NTD position on the slab with the reciprocal position with respect to the heater and the low-resistivity (LR) NTD.

middle and then they have been scratched off to avoid the destruction of the NTD gold pads. The surface of NTD1 was damaged with three scratches and NTD4 with only one.

5.4.1 Set-up description

A quick discussion of the main difference of this set-up with respect to the previous is here summarised.

TeO_2 absorber. Also for this measurement a TeO_2 slab was used with the same dimensions and crystal orientation already described. But this time we decided to polish the crystal side opposite to the glued NTDs in order to see in transparency the spots deposited on the slab and to evaluate their diameter. The slab thickness after the polishing was 0.85(4) mm, while a non-polished slab has a thickness of around 0.9 mm.

NTD gluing. We decided to use the gluing tool described in Sec. 3.2 to glue the four NTDs because a more reproducible and accurate 50-μm glue-spot thickness — independent from the choice of the Mylar mask — was achievable. The absence of the Mylar mask allowed us to glue the NTDs with 9 spots instead of the 6 used in the previous measurement. This gluing tool is comfortable for massive crystals because their weight ensure an uniform and stable contact between the absorber surface and the top part of the tool. In order to compensate this, we glued the slab to a 5-cm-side plexiglas cube that was used as a fake massive crystal only during the gluing. The slab was kept in place on the plexiglas cube with tape. Fig. 5.18 shows the reciprocal position of each NTD on the slab. Fig. 5.19 shows the photographs of slab polished side in correspondence of the four NTDs, it is possible to see in transparency the glue spots. The diameter of each glue spot has been measured from these photographs. Table 5.8 lists for each NTD the weighted mean of the spot diameter, their surface and the total glue surface.

Heater gluing. Given the non-negligible problems encountered to remove the heaters glued to the NTDs with a veil of epoxy glue, we decided to use only one glue spot with a thickness of 50 μm given by a Mylar mask. The heaters have been glued with the technique presented in Fig. 5.20 (*left*).

Copper holder. We employed the same copper holder of the previous measurement increasing the number of Kapton pads. The coupling between the slab and the heat sink, represented by our copper sample

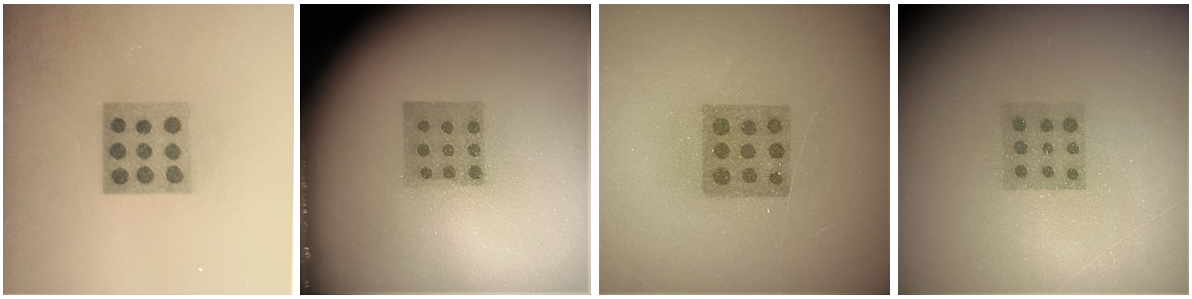

Fig. 5.19: Photographs of glue spots seen from the polished side of the slab for NTD1, NTD2, NTD3 and NTD4 (*from left to right*).

Tab. 5.8: Average glue-spot diameters for each NTD. They have been measured from the photographs of the slab side opposite to the NTDs.

	diameter [mm]	1 spot surface [mm^2]	total surface [mm^2]
NTD1	0.534(6)	0.222(5)	2.07(6)
NTD2	0.469(7)	0.171(5)	1.56(5)
NTD3	0.508(7)	0.196(6)	1.89(6)
NTD4	0.449(6)	0.154(4)	1.45(4)
mean	0.490(3)	0.181(2)	1.66(3)

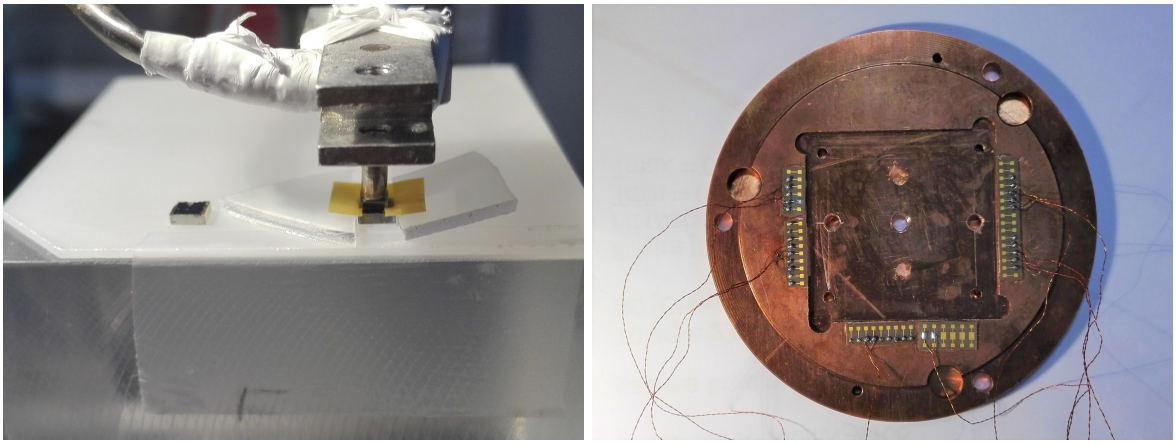

Fig. 5.20: *Left panel*: photograph of one-heater gluing. The slab, where the NTDs are already glued, is fixed to the plexiglas cube with tape. At the sides of the NTD, two small plastic pieces of the height of the NTD are placed and the Mylar mask is positioned over those. We deposited one glue spot over the NTD, in the middle of the mask. At this point the heater, sucked by the mechanical arm, is placed with the sides on the Mylar mask. *Right panel*: photograph of the set-up holder before the deposition of the slab. On the slab seat — above and below the central hole — it is possible to see the two spots of vacuum grease used to thermalize the slab. While on the right and the left of the central hole, it is possible to see two other holes close to the Kapton pads. Below this openings we placed the uranium sources.

holder, has been done with two spots of Dow Corning high vacuum grease, visible in Fig. 5.20 (*right*). We reduce the amount of vacuum grease to leave the place for two symmetric holes at the sides of the central one (in the middle of the holder). These two were used to shine the detector with two uranium sources. The presence of two sources is meant to study the set-up response as a function of the event position. In a thermal response, the same event is read with the same amplitude by a close NTD and a far one. On the contrary, in an athermal response the NTD closer to the source will see a higher-amplitude event.

Additional thermometry. We decided to glue on the slab also one heater and one NTD to stabilise the temperature of the slab. This NTD is a low-resistivity thermistor ($R_0 = 1.2\ \Omega$ and $T_0 = 1.4$ K from an old characterisation) that should have a resistance readable by the TRMC2 at 15 mK. The NTD and the heater have been glued with the Mylar mask technique, the first one with four glue spots while the second with only one.

Bonding. The link between the NTDs and the Kapton pads was done as in the previous measurement. The only difference regards the low-resistivity NTD used as thermometry. In fact it was bonded with Ø25-μm gold bonding wire. This NTD contacts do not reach the chip top surface, therefore its bonding is done soldering the wire to the NTD pads with indium. Initially we glued the low-resistivity NTD to the slab and then we tried to fix the bonding wires to its lateral pads with indium. The lateral pressures provoked the detachment of the NTD, leaving the four glue spots on the slab. We decided to invert the two processes: the wires have been soldered with indium to the pads and then the NTD has been glued again. The gold bonding wires have been soldered to the Kapton pads also with indium.

The NTDs without scratches on the surface had a mass of around 42.4 mg, while the NTD1 — that has the surface scratched because of the heater ungluing — had a mass of 41 mg; the difference in mass is of the order of 3.4 %. We measured the mass of the slab with the 4 NTD and 4 heaters glued on it, the total mass was 13.98 g. Considering a total mass of 168.27 mg for all the 4 NTDs and 27.04 mg for the four heaters (one heater is around 6.76 mg) and neglecting the mass of the glue, we can assume that the mass of our slab is 13.78 g. The slab used in the previous measurement had a mass of 14.15 g. The difference in mass between the two is due to the polishing.

Fig. 5.21 illustrates some photographs of the bonded NTDs and Fig. 5.22 shows the completed set-up.

5.4.2 Phase 0 - NTD characterization and systematic uncertainties

The resistance-temperature characterisation has been done with the TRMC2 bridge. This measurement has been repeated in different days and for different bias (in the range $100 - 200\ \mu$V) and produced always the same output. We can conclude that the NTDs were not overheated and that the data are reliable. The data were acquired in a temperature range from 150 mK to 20 mK with a controlled cool down of the cryostat with a speed of 500 μK/min with 10-minute plateau each 10 mK. The sensors were connected in a two wire configuration: the wire resistance was subtracted later during the analysis. The fit of these data was performed in a temperature interval $20 - 120$ mK with the Efros-Shklovskii's law in Eq. (2.5). Fig. 5.23 shows the resistance of the sensors as a function of the inverse of the square root of temperature: the curves have a linear behaviour. The data acquired at a constant temperature have been used to calculate the statistical error on the measurement of the resistance. The statistical uncertainty on the resistance was $1.2 - 1.6$ % at 20 mK, of the order of 0.1 % in the temperature range $30 - 60$ mK and of the order of 0.01 % at $70 - 120$ mK. The error is higher for lower temperature because it corresponds to a higher resistance values that are measured with more difficulties by the bridge. The statistical error on this measurement have been considered only on the measurement of the sensors resistance and not on

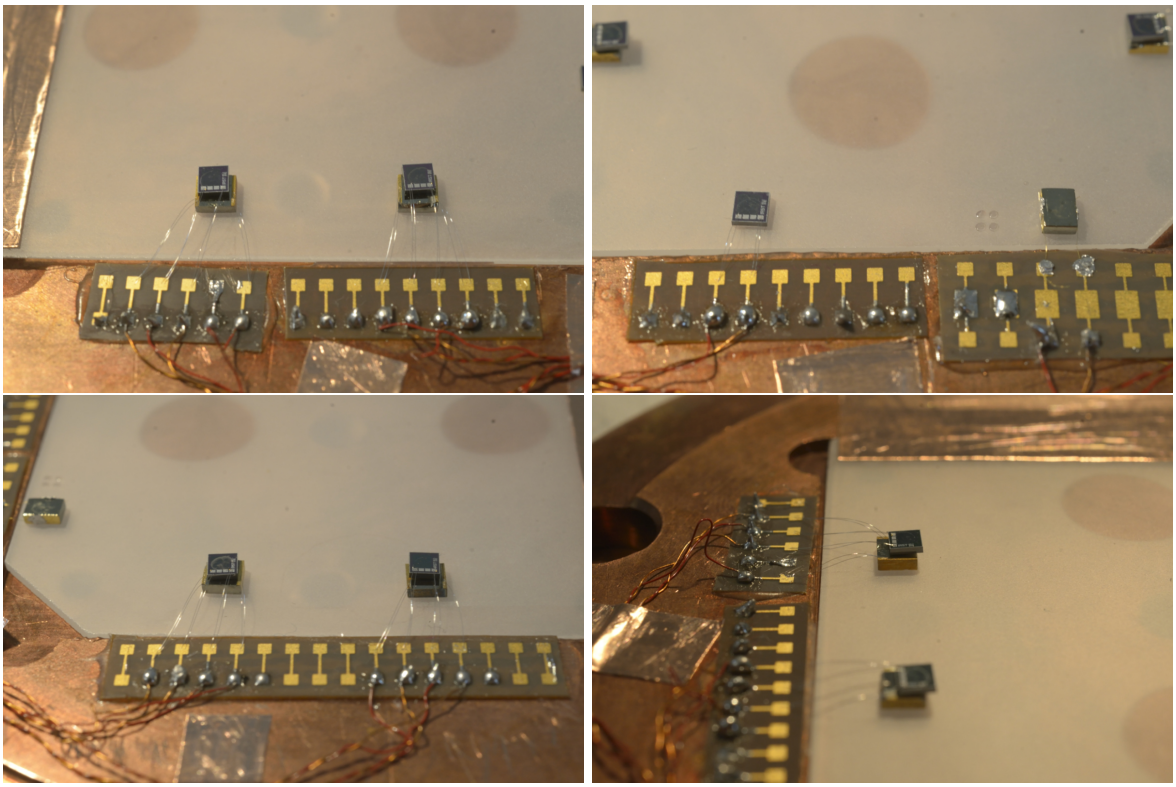

Fig. 5.21: *Top-left panel*: photograph of NTD2 and NTD1. The NTD1, on the right, has the surface slightly ruined because of a bit cruel heater ungluing from the previous set-up. *Top-right panel*: photograph of the heater and the low resistivity NTD. At the left side of the NTD there are the four glue spots of the previous low-resistivity NTD gluing. *Bottom-left panel*: photograph of NTD4 and NTD3. The right pad of NTD3 has been bonded with only one aluminium bonding wire because the pad surface was not clean enough. *Bottom-right panel*: photograph of the NTD2 and NTD1 side. The heater sticks out from the NTD in order to leave more space for the NTD bonding.

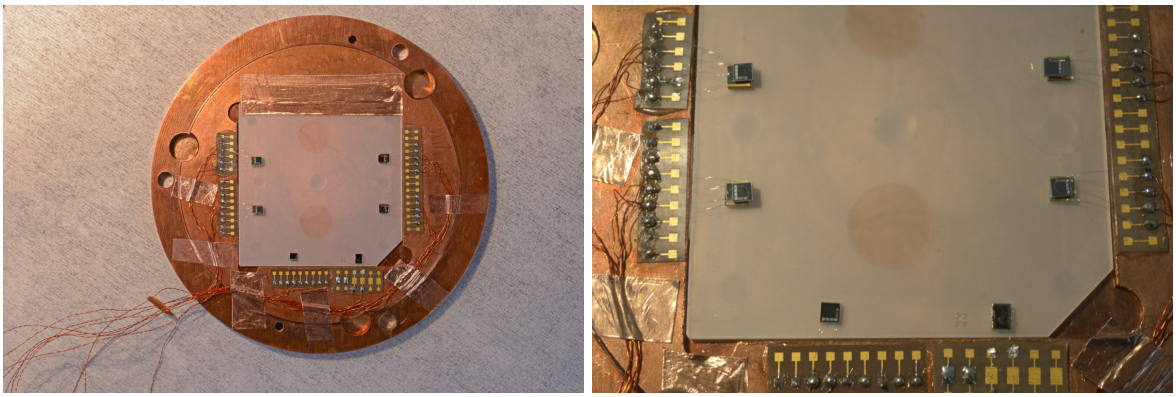

Fig. 5.22: Two photographs of the final mounting. The two round shadows below the slab are due to the vacuum grease used to couple the slab to the holder. The side of the slab without NTDs have been glued to the copper holder with a tape to improve the slab coupling and the stability of the slab during the bonding.

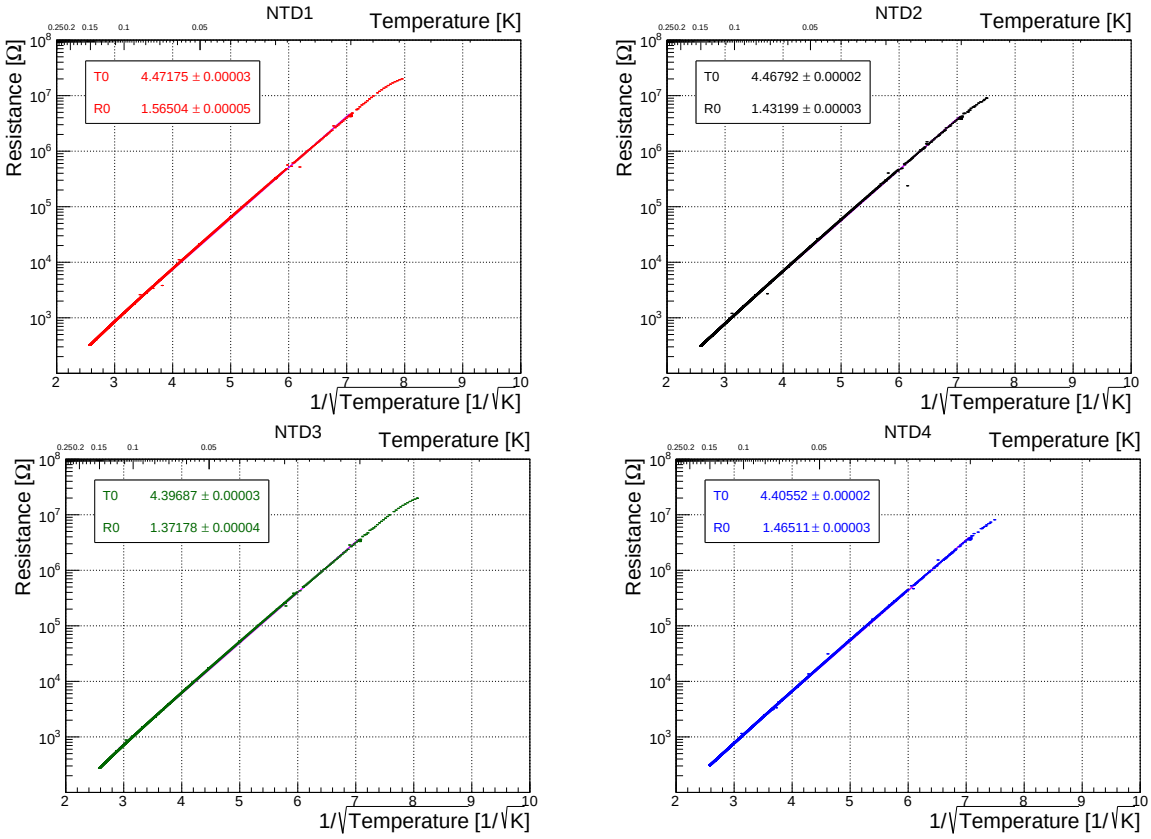

Fig. 5.23: Resistance-temperature characterisation of the four NTDs.

the temperature, because the thermometer resistances are lower with a consequent even lower error in the measurement.

The systematics dominate the uncertainty of these characterisations. They can be caused by thermal mismatches between the sensor and the copper support or by the validity of the Efros-Shklovskii only in a smaller temperature range with respect the considered one. This effect is visible by changing the fit interval range. The systematics on this measurement were treated as described in Sec. 5.3.3 and the resulting R_0 and T_0 values are reported in Table 5.9. These values and their systematic uncertainties were used to evaluate the temperature error as a function of the NTD resistance in Fig. 5.24. The values of R_0 and T_0 obtained in this measurement are lower than the ones obtained in the first measurement and listed in Table 5.4. Their lower resistance is probably due to the different gluing technique used in the second measurement.

5.4.3 Working temperatures

The data have been acquired at three temperatures during this run: 15 mK, 20 mK and 25 mK. Knowing the overheating issue that we got during the previous run in the measurement at 14 mK, we changed the load resistors for the 15-mK measurements. If we used a couple of 1-GΩ resistors and a couple of 100-MΩ ones in the previous case, this time the latter one has been substituted by two 30-GΩ resistors to reduce the power injected. Fig. 5.25 shows the electron and the phonon temperature as a function of the power injected. The sensor over-heating was solved this time and we used all the data for the analysis.

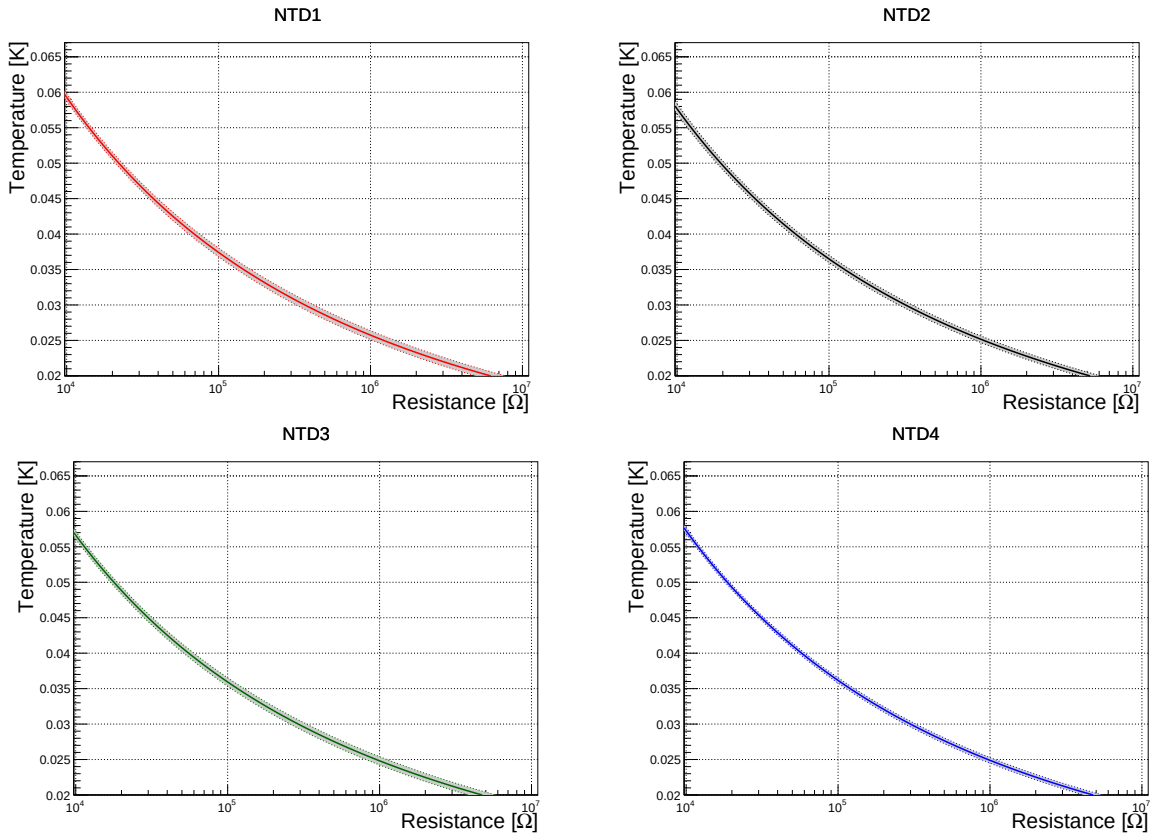

Fig. 5.24: The temperature as a function of the resistance calculated from the average R_0 and T_0 obtained with the analysis of systematic errors. Their systematic uncertainty is represented by a gray band.

Tab. 5.9: Summary of R_0 and T_0 values for the four NTDs.

	R_0 [Ω]	T_0 [K]
NTD1	1.4(2)	4.7(1)
NTD2	1.31(8)	4.64(5)
NTD3	1.3(1)	4.62(8)
NTD4	1.4(1)	4.55(4)

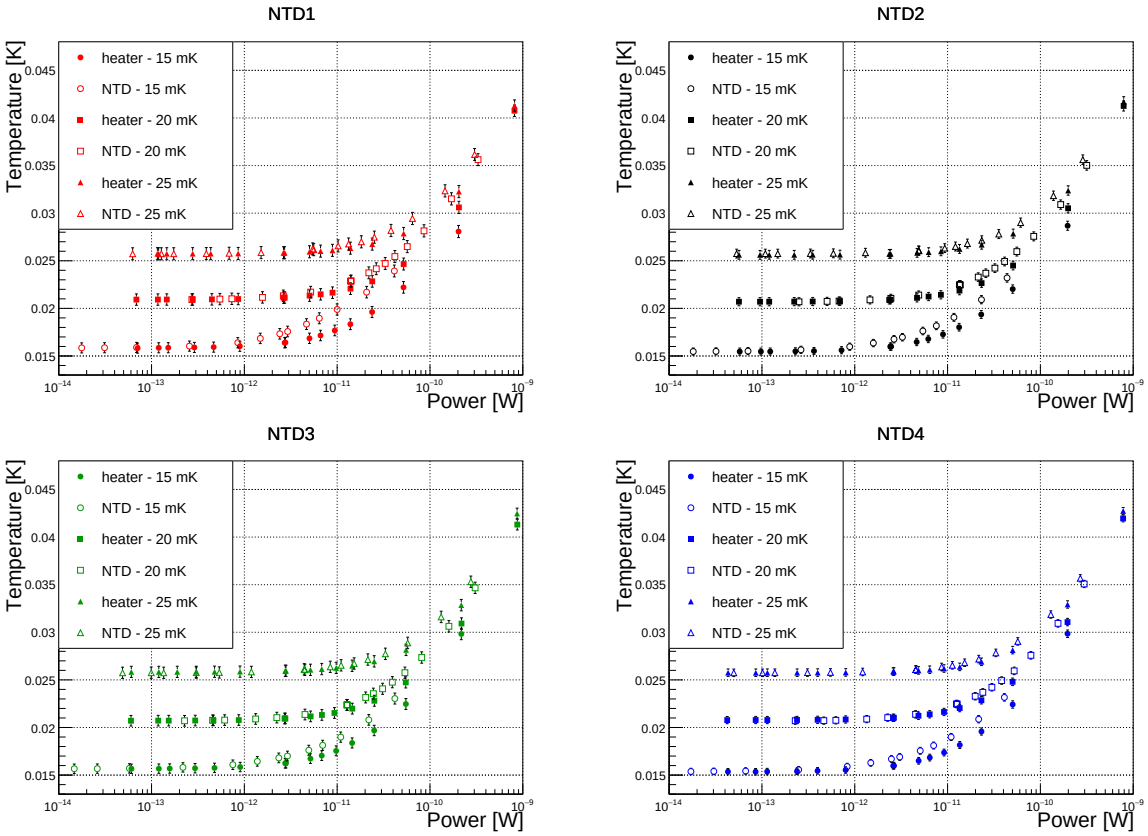

Fig. 5.25: Plot of the electron temperature (*open marker*) and of the phonons temperature (*full marker*) as a function of the power injected in the case of 15 mK, 20 mK and 25 mK. The systematic error on the temperature, calculated as described in the text, is reported in the error bar.

Tab. 5.10: Results obtained for the glue conductance correlated with the total glue surface reported in Table 5.8.

	Glue conductance: $G(T)=g_0\ T[K]^{\alpha}$			
	g_0	α	G @ 20 mK [W/K]	total surface [mm^2]
NTD1	$2.4^{+0.8}_{-0.5} \times 10^{-3}$	$3.18^{+0.09}_{-0.09}$	9.5×10^{-9}	2.07(6)
NTD2	$1.6^{+0.3}_{-0.1} \times 10^{-3}$	$3.09^{+0.04}_{-0.05}$	9.0×10^{-9}	1.56(5)
NTD3	$2.3^{+0.6}_{-0.4} \times 10^{-3}$	$3.18^{+0.09}_{-0.08}$	9.1×10^{-9}	1.89(6)
NTD4	$1.4^{+0.2}_{-0.2} \times 10^{-3}$	$3.07^{+0.06}_{-0.06}$	8.5×10^{-9}	1.45(4)
common fit	$2.0^{+0.4}_{-0.4} \times 10^{-3}$	$3.14^{+0.07}_{-0.07}$		

5.4.4 Phase I - Glue conductance measurement

Also this time we regulated the temperature with one of the 39C NTD present on the slab and we selected three temperatures to perform the measurements: 15 mK, 20 mK and 25 mK. We have not been able to use the low resistance NTD to regulate the temperature because during its characterisation we found that its resistance was of the order of the cable resistance and we concluded that it was not reliable. We used the heater on the slab to provide the power needed for the temperature regulation. As in the previous measurement, for each point we checked the slab temperature with one of the other NTD present on the slab. We always found a coherent feedback.

Fig. 5.26 presents the result obtained from the glue conductance measurement. The fit of the data was performed simultaneously for the three temperatures with the root GMinuit package in the case of the phonon-temperature central value and in the case of the positive and negative temperature deviations. We left as free parameters: α_{glue}, g_{glue} and the three base temperatures considered. In this measurement we found a good agreement between the surface of the glue spots and the conductance value: a larger surface corresponds to a higher glue conductance in Table 5.10. The average glue conductance at 20 mK is 9.0 nW/K with a dispersion of 4.4 %. Renormalising the average glue conductance for the average glue surface we obtain:

$$G_{glue} = 1.2(5) \times 10^{-3}\ T[K]^{3.1(1)}\ [W/(K\ mm^2)], \tag{5.6}$$

comparing this value (properly renormalised for the spot dimension) with the one reported in Ref. [117] and discussed in Sec. 2.5, we find that the exponents are compatible while there is a factor two difference in the coefficients.

5.4.5 Phase II - Electron-phonon conductance measurement

We repeated the electron-phonon conductance measurement at 15 mK, 20 mK and 25 mK with the same analysis used in the previous measurement (see Sec. 5.2). Fig. 5.27 shows the load curves acquired during this data campaign at the three different temperatures. The curve at 15 mK for the NTD1 has an unusual behaviour for higher bias. These data have been acquired twice to verify the presence of possible mistakes in the measurement but this behaviour was reproducible. These data have been included in the analysis. Fig. 5.28 (*top*) shows the temperature of the electrons as a function of the temperature of the phonons. The data of NTD1 introduce a spread with respect to the others NTDs at 15 mK probably because of their uncommon tendency for higher bias currents.

Three fits were performed: for the central value and in the case of under and over-estimated temperature deviations. Also in this case, each of the fits — done with the root gMinuit package — considers the data acquired at 15 mK, 20 mK and 25 mK at the same time. The free parameters of the fit were: α_{el-ph}, g_{el-ph} and the three base temperatures. Contrary to the previous measurement, the parameters obtained by the fit of the average temperature $\overline{T}$ are not included in the interval formed by the ones

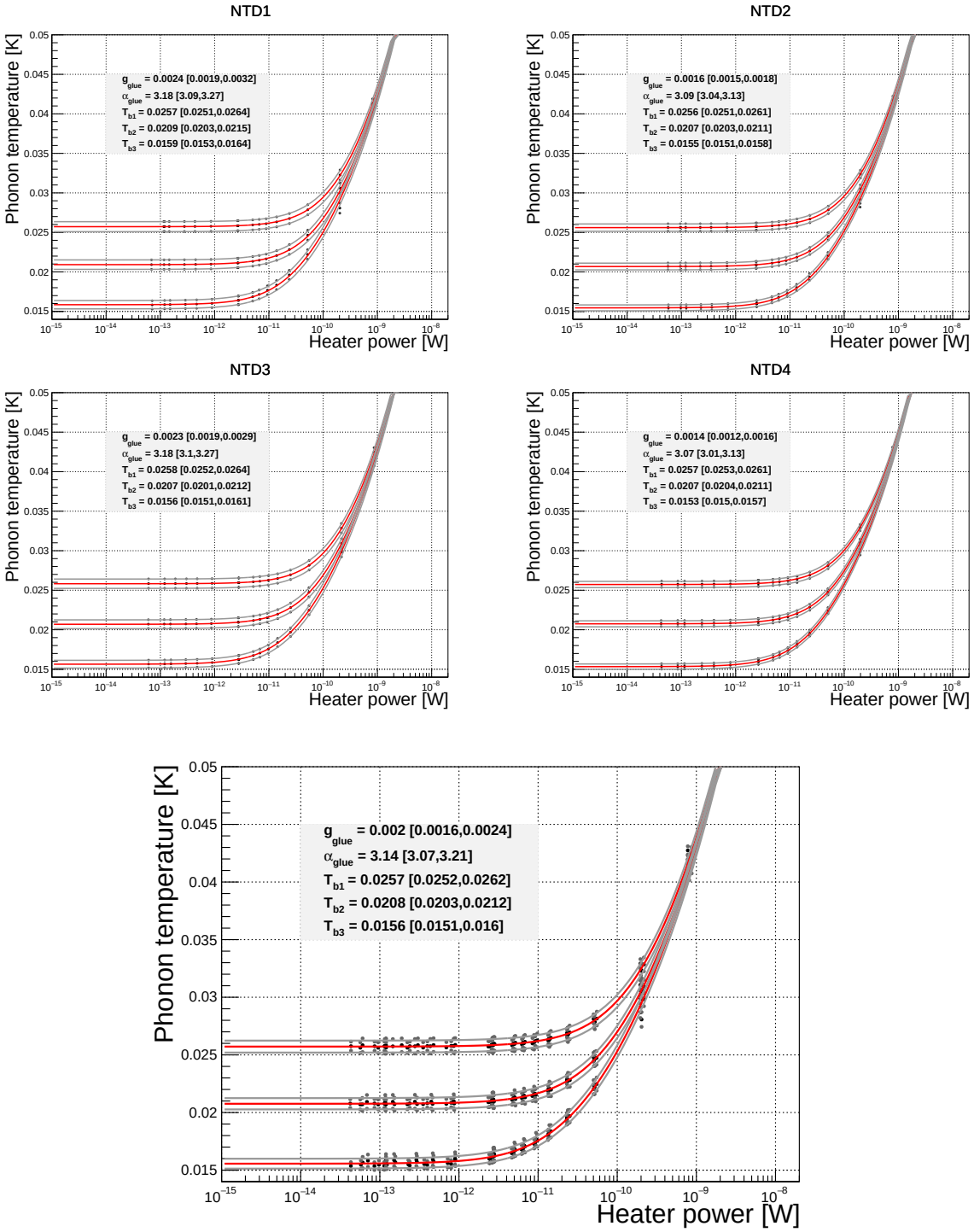

Fig. 5.26: Phonon temperature as a function of the power injected with the heater for three temperatures: 15 mK, 20 mK and 25 mK. *Top panel*: glue conductance analysis for each NTD. *Bottom panel*: common fit of the glue conductance with all the NTDs.

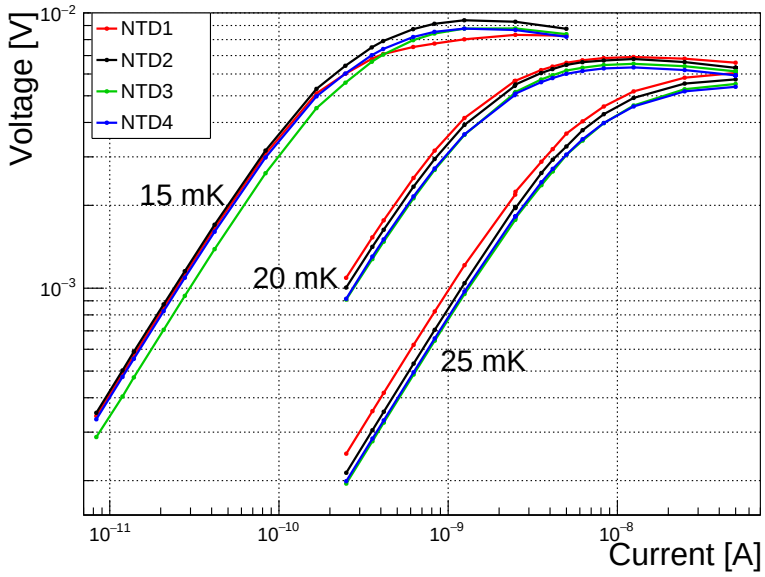

Fig. 5.27: Voltage as a function of the current for all the NTDs at 15 mK, 20 mK and 25 mK.

measured from $\overline{T} - \sigma_T$ and $\overline{T} + \sigma_T$. Nevertheless the parameters corresponding to the $\overline{T}$ gives rise to an electron-phonon conductance included in the band spanned by the parameters corresponding to the over and under-estimated temperatures in Fig. 5.28 (*bottom*). The resulting electron-phonon conductance is:

$$G_{el-ph}[\text{NTD39C}] = 12.2\ T[K]^{5.3}[W/K]. \tag{5.7}$$

The electron-phonon conductance at 20 mK corresponds to 1.3 nW/(K mm^3) with an error of 34 % and it becomes 11 nW/(K mm^3) with 32 % of uncertainty at 30 mK. This last value can be compared with the ones reported in literature (Table 2.1).

5.4.6 Dynamic measurements

Two dynamic measurements have been acquired with the couple NTD1-NTD3 and then with the couple NTD2-NTD4 stabilised at 20 mK on the detector floating plate. A simultaneous acquisition of all the NTD was not possible because of the organisation of the cabling lines of the cryostat. These couples were selected during the mounting to acquire simultaneously one NTD close to an α source and one distant and study position dependences.

The bias of each NTD was chosen maximising the signal-to-noise ratio, the working currents and resistances are reported in Table 5.11. The following DAQ parameters were selected to maximise output signal and improve the pulse shape reconstruction: gain of 1403, dynamic range ± 1 V, sampling frequency 20 kHz. A heater pulse was injected in the slab each 5 minutes to check the stability of the measurement. Fig. 5.29 (*top*) shows the muon distribution for the four NTDs, the inset on each plot presents the heater peak position. The energy distribution presents an event increase at low energies because the data were not cut to preserve the muon distribution shape. As it has been explained in the set-up description, two uranium sources have been positioned below the slab to study the detector response. The measurement of NTD1 and NTD3 collected around 5.6 hours of data and the one of NTD2 and NTD4 gathered 27.8 hours,

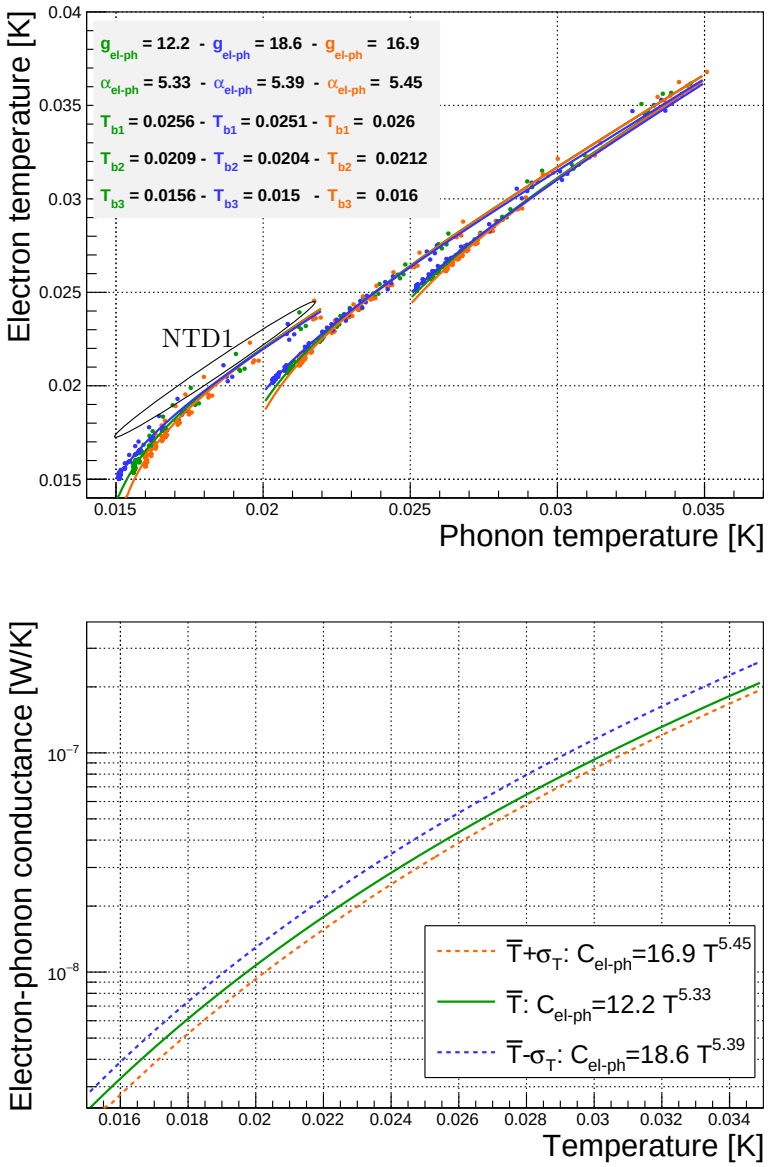

Fig. 5.28: *Top panel*: electron temperature as a function of the phonon one. *Bottom panel*: electron-phonon conductance as a function of the temperature for the measure (*solid line*) and considering the systematics (*dashed lines*).

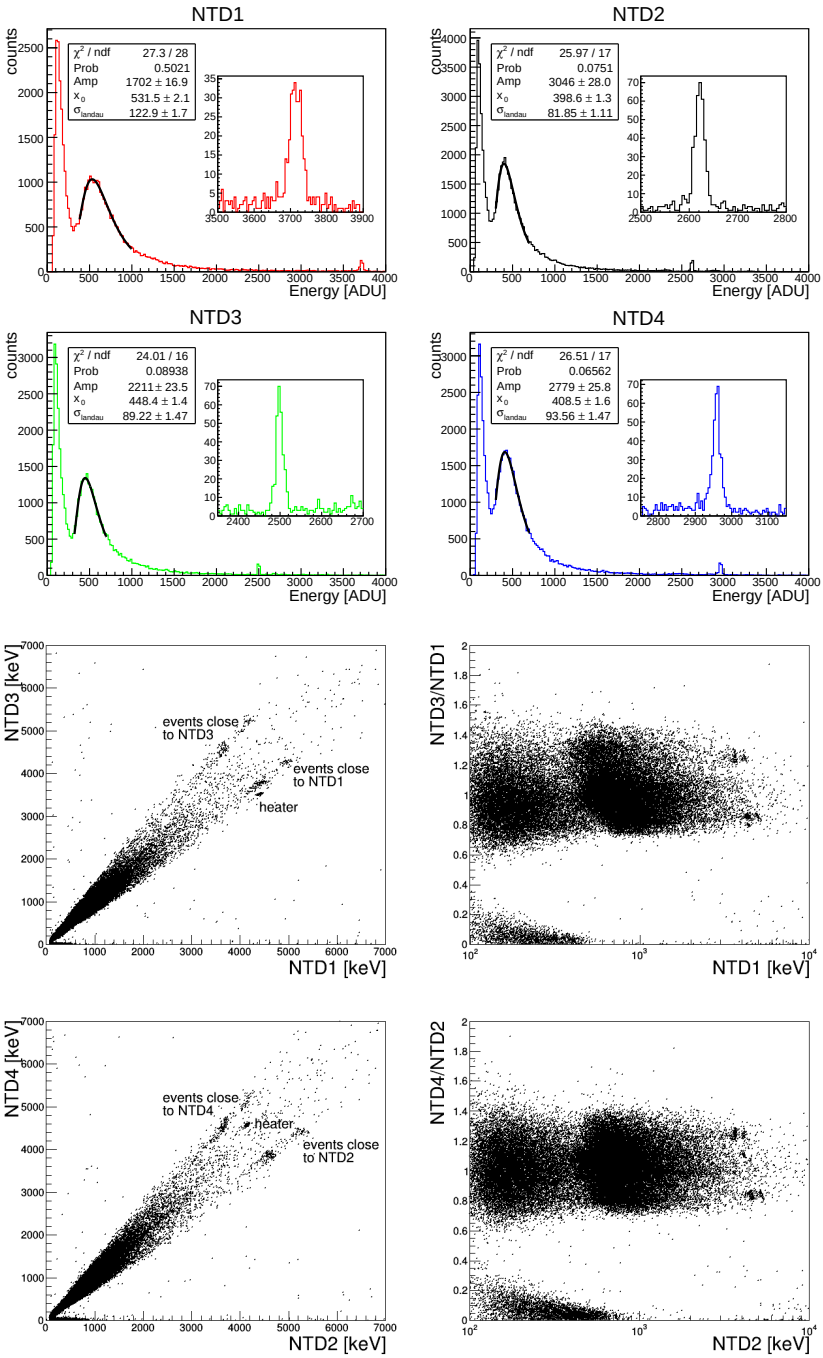

Fig. 5.29: *Top panel*: muon spectra obtained by each NTD with an inset of the heater peak. *Bottom panel*: scatter plot (*left*) and Q-plot (*right*) of the two couples of NTDs measured together (NTD1-NTD3 and NTD2-NTD4).

Tab. 5.11: Working points chosen for the dynamic measurement optimising the signal-to-noise ratio. The NTD1 has a particularly low bias because surprisingly the noise was increasing for higher currents.

	bias current [nA]	resistance [MΩ]	sensitivity [nV/keV]
NTD1	0.83	3.8	18
NTD2	8.3	0.8	14
NTD3	6.2	1.0	15
NTD4	6.2	1.0	14

but it was not possible to reconstruct the α events position in both cases because of the energy-resolution enlargement due to the position dependence. The sensitivities of the various NTDs measured with the muon peak are reported in Table 5.11. The muons were used for the sensitivity evaluation because they hit the detector uniformly, therefore we can consider that on average the result does not depend on the impact point. The energy of the Landau distribution maximum has been simulated with a Monte Carlo for a TeO_2 slab as the one used in this test. The energy of the maximum corresponds to an energy of 632 keV for our slab thickness.

As it is visible from the insets in Fig. 5.29 (*top*), the heater peak energy depends strongly by the distance between the sensor and the heater. The NTD1 and NTD4 are closer to the heater (see also the scheme in Fig. 5.18) and present the heater peak at higher energies. This phenomenon has two possible explanations:

- the sensors read the athermal signal from the heater, therefore the distance between the chips influence the measured energy amount;

- this effect is due to the mounting structure. The strong conductance between the slab and the bath generates a thermal gradient in the slab and the effects of heat propagations in the slab are important. The heat is evacuated before being measured by the farther NTDs, in this case we do not need to invoke athermal effects.

The α events are visible in the scatter plot and Q-plot in Fig. 5.29 (*bottom*). These data have been calibrated with the muons distribution and, also in this case, no cuts were applied to data. The α events seen by the close NTD are characterised by a higher amplitude with respect to the nominal α energy (4.3 MeV and 4.7 MeV) while the farther NTD measures a lower energy. The same effect is visible for the heater events: they have a higher energy when measured by NTD1 for the couple NTD1-NTD3 and they are almost equidistant from NTD2 and NTD4, this perfectly reflects the reciprocal positions of the NTDs and heater presented in Fig. 5.18. These are further confirmations of presence of energy losses through the grease conductance and/or presence of athermal signals.

Fig. 5.30 (*top*) presents some selected pulses from the 4270-keV α events, each panel shows the same not calibrated event seen by two different NTDs. The title of the plots specifies the NTD to which the source was closer. As it was also clear from the scatter plots in Fig. 5.29 (*bottom*), the events closer to the sources are characterised by a higher amplitude. Fig. 5.30 (*bottom*) shows five pulses for each NTD, the events are selected from the source opposite to the acquired NTD. The pulse outputs (converted in a volts) of NTD2, NTD3 and NTD4 are characterised by similar amplitudes and time constants. This effect is not visible for NTD1: it has a higher amplitude and a longer decay time. This is due to its different working point at a lower bias, characterised by a higher sensitivity and a smaller electro-thermal feedback (see Sec. 2.5).

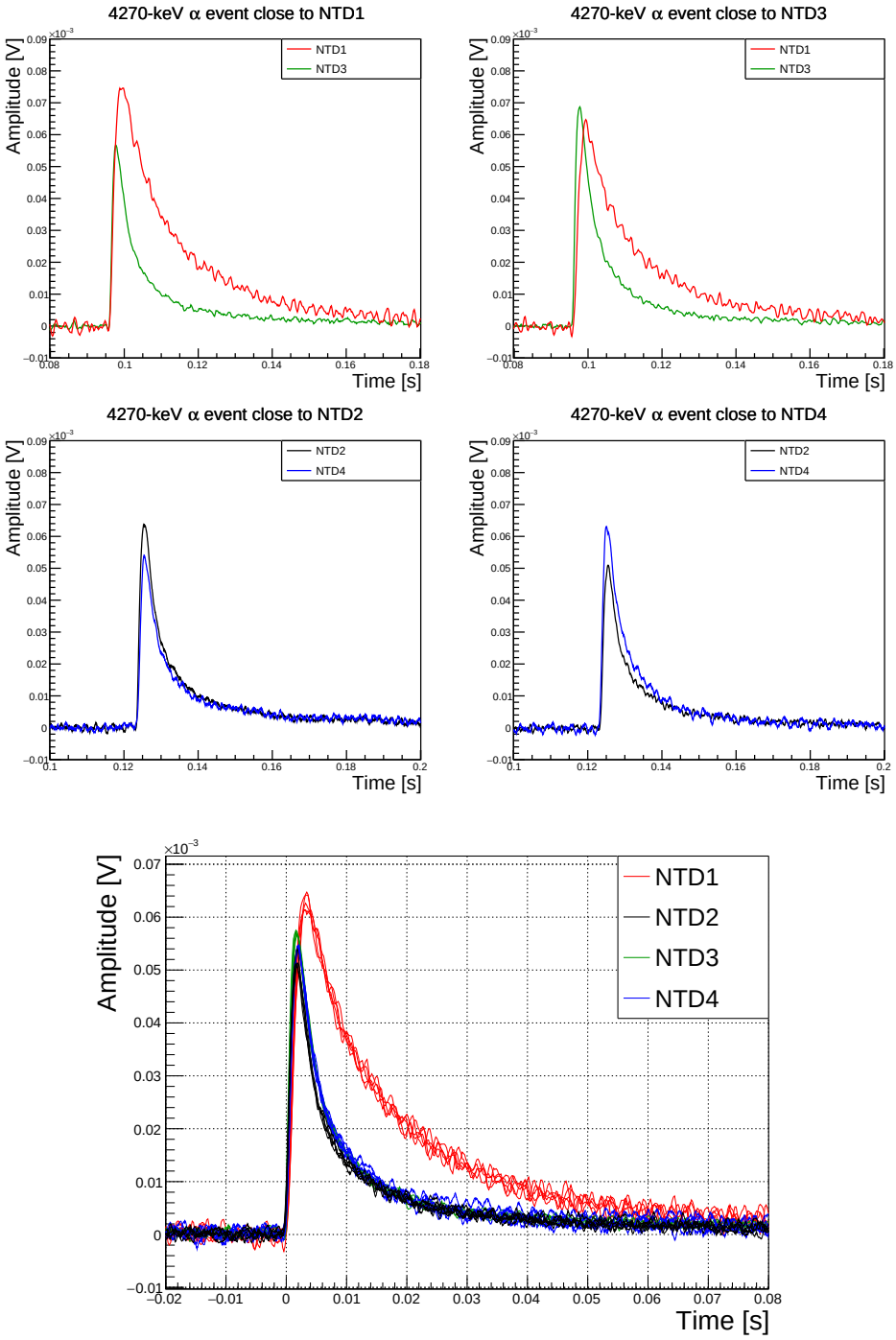

Fig. 5.30: *Top panel*: the same 4270-keV α event registered by a couple of NTDs. The amplitude of the event is correlated with the position of the event. *Bottom panel*: five 4270-keV α events for each NTD recorded from the source farther from the measuring NTD. More information are presented in the text.

Tab. 5.12: Summary of the parameters used in the simulation.

	NTD1	NTD2	NTD3	NTD4
G_{el-ph} [W/K]	$12.2\ T[K]^{5.33}$			
G_{glue} [W/K]	$2.4 \times 10^{-3}\ T[K]^{3.18}$	$1.6 \times 10^{-3}\ T[K]^{3.09}$	$2.3 \times 10^{-3}\ T[K]^{3.18}$	$1.4 \times 10^{-3}\ T[K]^{3.07}$
G_{grease} [W/K]	8×10^{-7}			
R_0 [Ω]	1.4	1.31	1.3	1.4
T_0 [K]	4.7	4.64	4.62	4.55
P_{static} [pW]	0.048	0.051	0.060	0.052
$P_{dynamic}$ [pW]	39	38	2.6	56
C_{TeO_2} [J/K]	$3.7 \times 10^{-5}\ T^3$			
$C_{NTD\ latt}$ [J/K]	$2.2 \times 10^{-8}\ T^3$			
$C_{NTD\ elect}$ [J/K]	$8.8 \times 10^{-9}\ T$ [220]			

5.4.7 Simulations

As in the first case, we decided to simulate the behaviour of the set-up trying to reproduce the static and dynamic response. Table 5.12 summarises the parameters used in this new simulation, for a general description of the simulation refer to Sec. 5.3.8. In this case we tuned the heat capacity parameters with the mass that we directly measured before gluing them (for this reason they slightly differ from the previous simulation). We decided to use for each sensor its own glue conductance while we used a common electron-phonon conductance for all the sensors as in the previous case. In the static simulation a common bath temperature was used and we choose it equal to the temperature resulting from the fit in Fig. 5.12 since the same data will be used for the comparison with the simulation. Therefore we used 15.6 mK for the 15-mK measurement, 21 mK for the 20-mK one and 25.6 mK for the 25-mK one. Fig. 5.31 (*top*) reports the static result of the simulation for the three temperatures superimposed to the experimental data. The small mismatch between the measured point and the simulation can be corrected with a fine tuning of the base temperature for each sensor. The simulations correspond quite well to the measured data, except for the data of NTD1 at 15 mK. The values used in the simulation are extrapolated from an average system that does not take into account the different behaviour of NTD1 visible from the load curves in Fig. 5.27.

Fig. 5.31 (*bottom*) shows the dynamic simulation superimposed to real pulses. The pulses correspond to 4270-keV α events occurred in the source farther from reading NTD, this choice was done to minimise the presence of athermal signals. The real pulses present a higher amplitude and an extra fast decay time absent in the simulations also in this second conductance measurement. This time, we tried to simulate this effect with the introduction of an athermal phonon component using the program corresponding to the model in Ref. [219]. We managed to reproduce the extra amplitude but not the fast decay time because the programs consider the evacuation of the athermal energy as the thermal one using the same time constant. In order to reproduce this behaviour, probably a different energy loss mechanism should be considered in the case of athermal phonons.

5.4.8 Conclusions

In this second measurement, we decided to repeat the first measurement improving our set-up:

- we changed the gluing technique to improve the glue-spot uniformity and increase the number of glue spots to nine (as in the case of CUORE, even if with a smaller surface in our case). We also improved the statistics by gluing all the four NTDs with the same spot number.
- we polished the slab side opposed to the NTD in order to measure the spot dimensions in-situ.

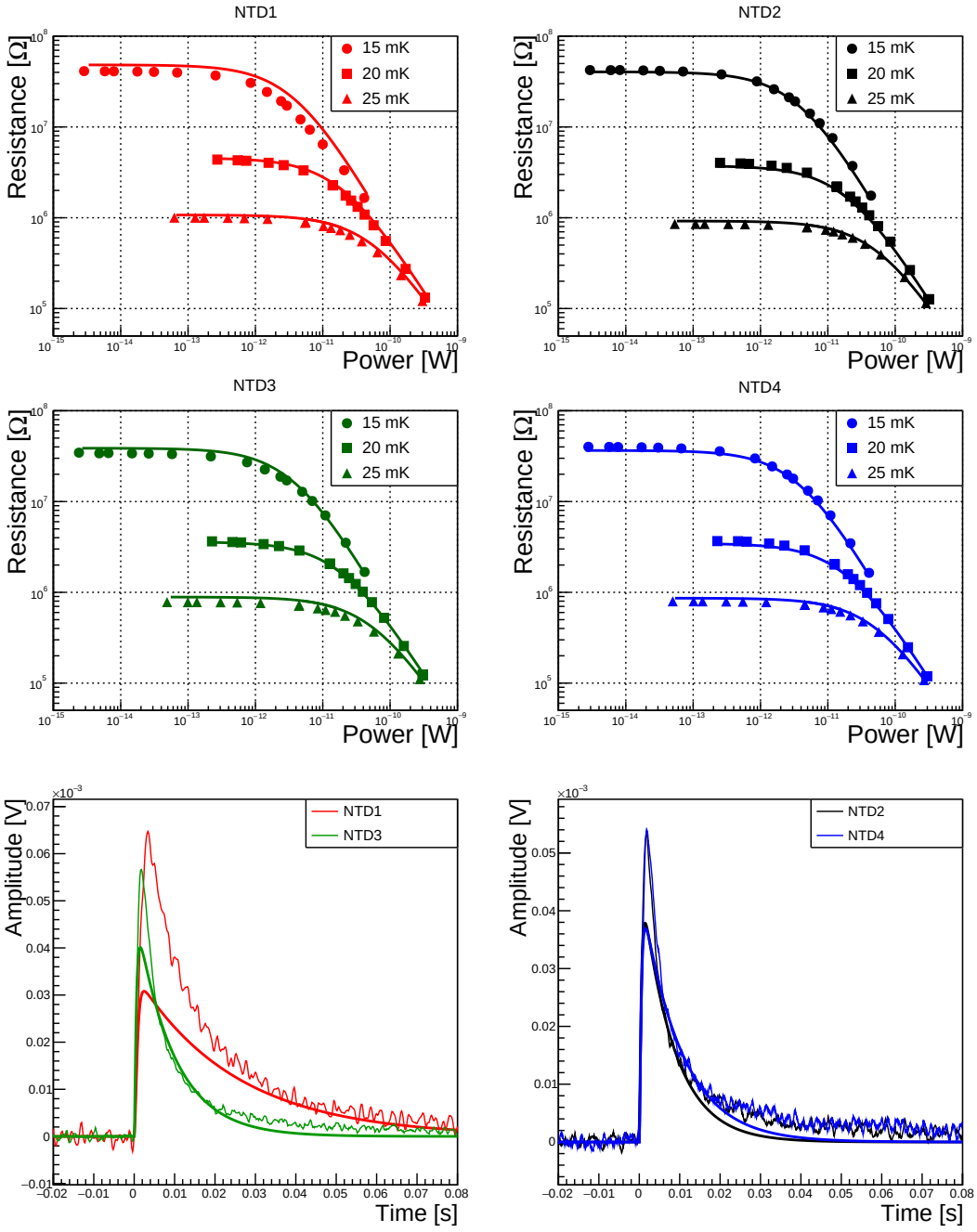

Fig. 5.31: *Top panel*: resistance-power curve data measured in our set-up and their simulation with the common electron-phonon conductance. *Bottom panel*: example of 4270-keV α event occurred in the farther source with respect to the measuring NTD and its simulation.

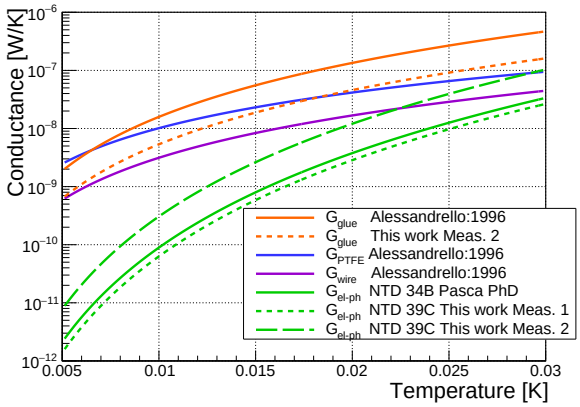

Fig. 5.32: Comparison between the conductance laws measured in this chapter and the ones reported in the introduction (Fig. 2.5). The conductance laws are reported in a $5 - 30$ mK temperature interval.

- we added a low-resistivity NTD (that was not working properly) and a heater to the slab to improve the slab temperature regulation.

- we included two α sources to study the position effect on our set-up.

The measurements have been repeated at three different working temperatures (15 mK, 20 mK and 25 mK) and all the data have been considered in the analysis. Fig. 5.25 demonstrates the absence of overheating in our measurement, that indeed prevented us to use the 14-mK measurement in the previous conductance measurement. This improvement was obtaining injecting a lower current in the NTD by changing the load resistors.

The glue conductance was measured for all the four NTDs. The analysis has been performed for each NTD and we have seen a correlation between the glue conductance and the glue-spot surface. Evaluating the glue conductance for each NTD at 20 mK, we obtained a mean value: $G_{glue} = 9.0(4)$ nW/K corresponding to an error of 4.4 %. The analysis has been repeated by fitting simultaneously the data from all the NTD. A glue conductance of $1.2(5) \times 10^{-3}$ T[K]$^{3.1(1)}$ [W/(K mm^2)] was obtained after the re-normalisation with respect to the glue surface. This value is coherent with the one measured in Ref. [117]: the exponents are compatible and the coefficient differs by a factor 2. We found a larger value of the glue conductance in this last measurement with respect to the previous.

The electron-phonon conductance has been re-measured with a combined fit of all the four NTDs at the three working temperatures. All the NTDs showed an uniform behaviour and pointed to the following electron-phonon conductance: $G_{el-ph} = 12.2$ T[K]$^{5.3}$ W/K. The coefficient renormalised by the sensor volume is: $g_0 = 1.44$ W/(K$^{6.3}$ mm^3). The electron-phonon conductance at 30 mK is 11 nW/(K mm^3) that can be compared with the measurements reported in literature (see Table 2.1). These values have a good spread: the average value is 3 ± 2 nW/(K mm^3) excluding Ref. [120], nevertheless it becomes 9 ± 19 nW/(K mm^3) including that measurement. By comparing the here-discussed electron-phonon conductance with the one obtained in the previous measurement, we find a reasonably compatible exponent but a difference of a factor 2 in the coefficient. If this discrepancy has to be attribute to a further systematic uncertainty in the temperature scale, we have to admit a difference of $3 - 4$ mK between the two measurements in the estimation of the temperature. A new measurement of the same set-up would allow a better understanding of this difference.

We acquired a few hours of stream data with the couple NTD1-NTD3 and NTD2-NTD4. The NTDs showed an uniform behaviour with similar sensitivities ($\sim 14 - 15$ nV/keV) and pulse shape parameters. The only exception concerns the NTD1, that was biased with a lower current and was characterised by a higher sensitivity and a longer decay time. An energy dependence as a function of the event position was observed thanks to the two α sources. The NTD closed to the source presented higher-amplitude pulses with respect to the farther one. The same behaviour was observed for the heater event fired during the acquisition. This effect has two possible explanations: heat diffusion effects are present in the slab during pulse formation; the signals present an athermal component that induces higher pulses in the closer NTD.

The set-up has been simulated with program described in Ref. [219] considering the new values obtained from the measurements. The static simulation reproduces well the data at the three different temperatures. The dynamic simulation — as in the previous measurement — does not manage to reconstruct the pulse amplitude and their initial fast decay time. The bigger amplitude can be due to the presence of athermal phonons that are not considered in the simulation and that may be consistent with the observed position effects.

When we introduced the thermal model in Sec. 2.5, we calculated the conductances characterising a general bolometer according to the parameters reported in literature (see Fig. 2.5). We considered a bolometer with a $3 \times 3 \times 1$-mm NTD thermistor from the batch 34C [123], that was glued with nine glue spots [117]. At this point, we can compare this example with our results in Fig. 5.32. Concerning the electron-phonon conductance, we have to notice that the sensors considered belong to two different batches: 34C and 39C with a consequent different doping. However, both NTDs were prepared and studied in the framework of the CUORE experiment.

6 Neganov-Trofimov-Luke light detectors

In this chapter the characterisations and the results obtained with NTL light detectors are presented. After a short presentation of the devices in Sec. 6.1, an aboveground characterisation is presented in Sec. 6.2. The two following sections show the results obtained in two underground measurements coupling NTL-assisted light detectors with TeO_2 bolometers. In particular, Sec. 6.3 presents the performance of two devices coupled to two enriched $^{130}TeO_2$ bolometers at the Laboratori Nazionali del Gran Sasso (L'Aquila, Italy). Then Sec. 6.4 illustrates the measurement performed in the Laboratoire Souterrain de Modane (Modane, France): one NTL-based light detector was coupled to a CUORE-size TeO_2 bolometer. The following two sections show two other possible applications of these high-performance devices: the pile-up rejection in Sec. 6.5 and the light-signal boost of set-ups with a poor light yield in Sec. 6.6. Furthers studies about NTL-assisted light detectors noise are presented in Sec. 6.7.

6.1 Neganov-Trofimov-Luke-assisted light detectors

Six NTL-assisted light detectors have been employed in this work. A general description of the detector assembly and the wafer coating can be found in Sec. 3.2. They present the same structure but some of them are characterised by different mounting features. Table 6.1 reports a schematic description summarising the few differences between the devices and Fig. 6.1 shows their photographs.

Tab. 6.1: Comparison between the NTL-assisted light detectors employed in this work. The NTD batch information is missing for the detectors GeCo2, Luke2 and SID.

	GeCo1	GeCo2	GeCo3	GeCo2A	Luke2	SID
Absorber material	Ge	Ge	Ge	Ge	Ge	Si
Absorber coating	SiO	SiO	SiO	SiO	-	-
Support material	PTFE	Al_2O_3 balls	PTFE	PTFE	PTFE	PTFE
NTD, mass [mg]	34B, ~ 5	~ 5	34B, ~ 5	34B, ~ 2	~ 5	~ 5
Bonding to	Kapton	Kapton	Cu pins	Cu pins	Kapton	Kapton
Note	-	-	a NbSi sensor was glued on its surface (see Ch. 7)	-	-	-

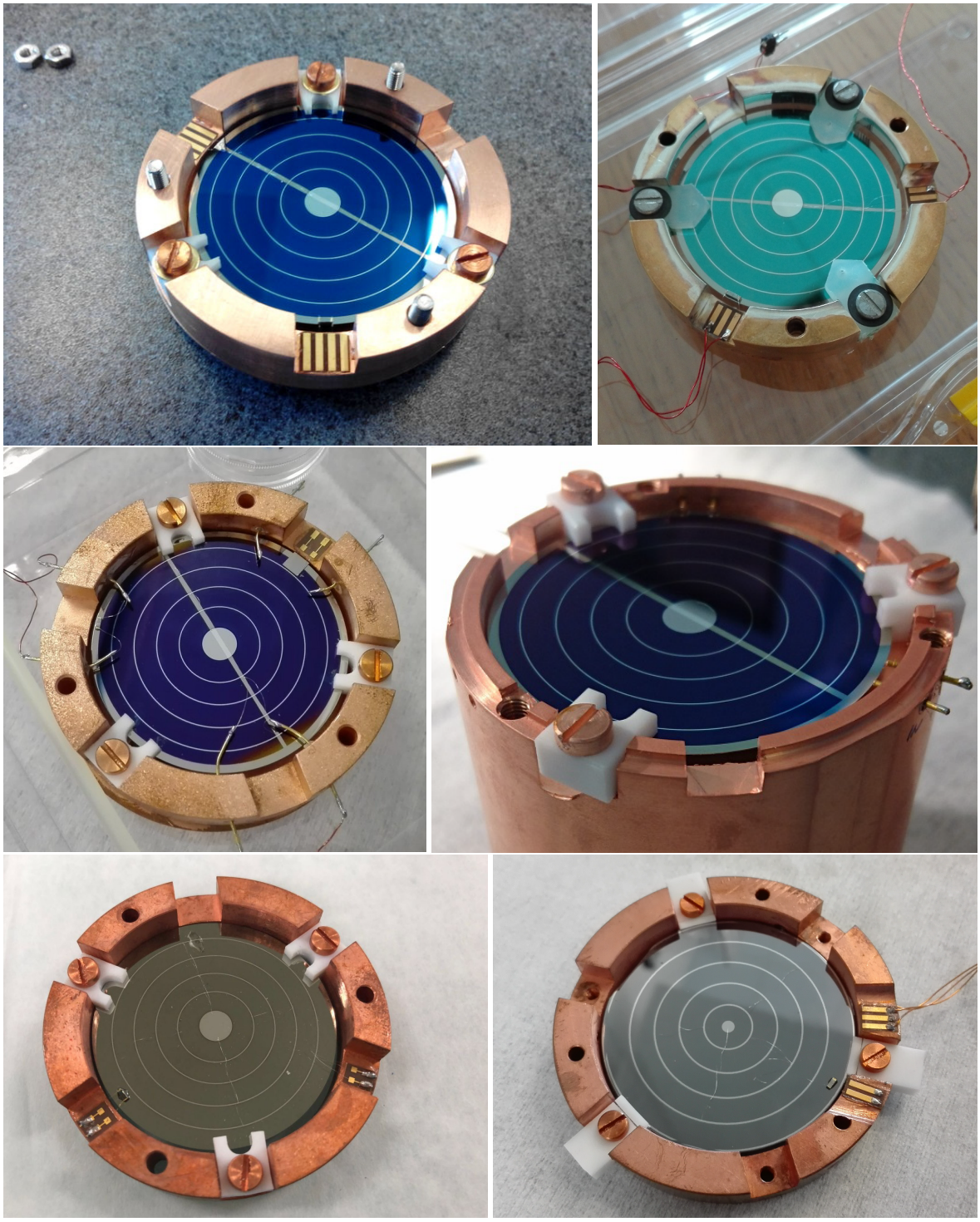

Fig. 6.1: Photographs of the NTL-assisted light detectors employed in this work. From the *top-left* photograph: GeCo1, GeCo2, GeCo3, GeCo2A, Luke2 and SID are shown in the order.

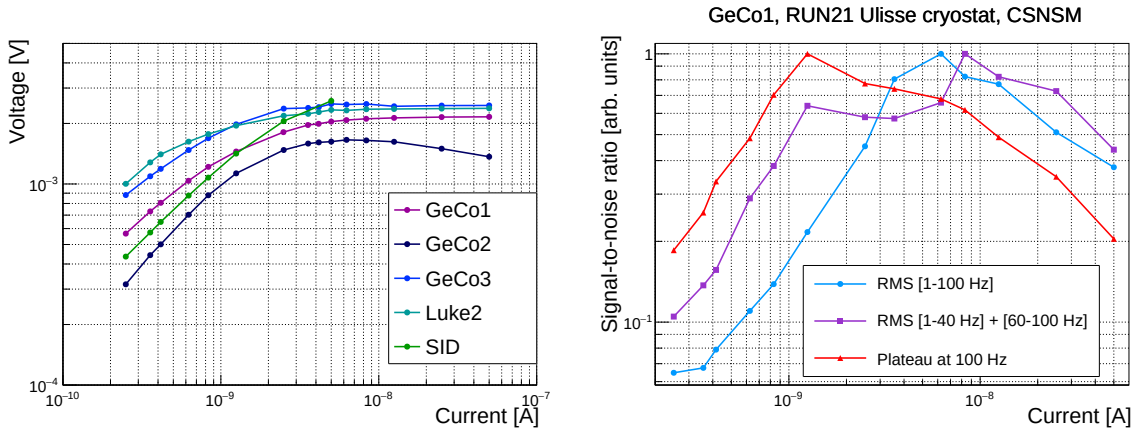

Fig. 6.2: *Left panel*: load curves of all the detectors measured at 18 mK. *Right panel*: signal-to-noise ratio renormalised for the light detector GeCo1 as a function of the bias current. Three different definitions of noise were considered: the baseline noise RMS in the frequency range $1-100$ Hz, the baseline noise RMS in the same range excluding the 50-Hz peak and the plateau value at 100 Hz in the noise power spectra.

6.2 Characterisation run with 5 Neganov-Trofimov-Luke-assisted light detectors

Five NTL-assisted light detectors (GeCo1, GeCo2, GeCo3, Luke2 and SID) were tested in the Ulisse cryostat — see Sec. 3.1.4 for the cryostat description — in order to check their performance in view of an underground measurement described in Sec. 6.3. They were stacked in a tower and each of them was equipped with a ^{55}Fe source and an optical fibre shining the light of a 820-nm LED operated at room temperature.

This run was carried out at 18 mK and Fig. 6.2 (*left*) shows the load curves of all the detectors at the working temperature. All the detector demonstrated a similar response to the static current bias. This measurement was characterised by a noise higher than 10 nV/$\sqrt{\text{Hz}}$ at low frequency and a big 50-Hz pick-up. The following description refers to Fig. 6.2 (*right*) that illustrates the signal-to-noise ratio of the GeCo1 light detector as a function of its current bias. Usually we define the best working point as the current bias that maximises the signal-to-noise ratio, where the noise is defined as the baseline noise RMS in the range $1-100$ Hz. The application of this definition requires to over-bias the detector to lower the noise but, in practice, it does not result in the choice of the best detector performance because the shape of the noise power spectra has to be taken into account too. Therefore we investigated different parametrisations of noise to see how the signal-to-noise ratio responded. At the beginning we removed the 50-Hz peak, considering the baseline noise RMS defined between $1-40$ Hz and $60-100$ Hz. The result did not change significantly. Then we tried to exclude the low frequency noise by considering only the noise plateau level at 100 Hz from the noise power spectra.

Table 6.2 presents the performance obtained by the light detectors during this characterisation run. The calibration has been performed at 0-V electrode bias with the ^{55}Fe source, while the muon distribution was used in the NTL regime. The results obtained are not the best achievable by these detectors because the measurement was affected by a low-frequency noise. Moreover the calibrations were highly disturbed by sets of event-like pulses: Fig. 6.3 (*top*) shows and example of a group of these recorded by Luke2. These events populated the low energy region ($1-10$ keV) and it was not possible to discriminate them by pulse shape. It has been noticed that these event-like pulses were absent from 1:20 AM to 5:00 AM, as it is visible in Fig. 6.3 (*bottom-left*). In these periods the only events at low energy where due to

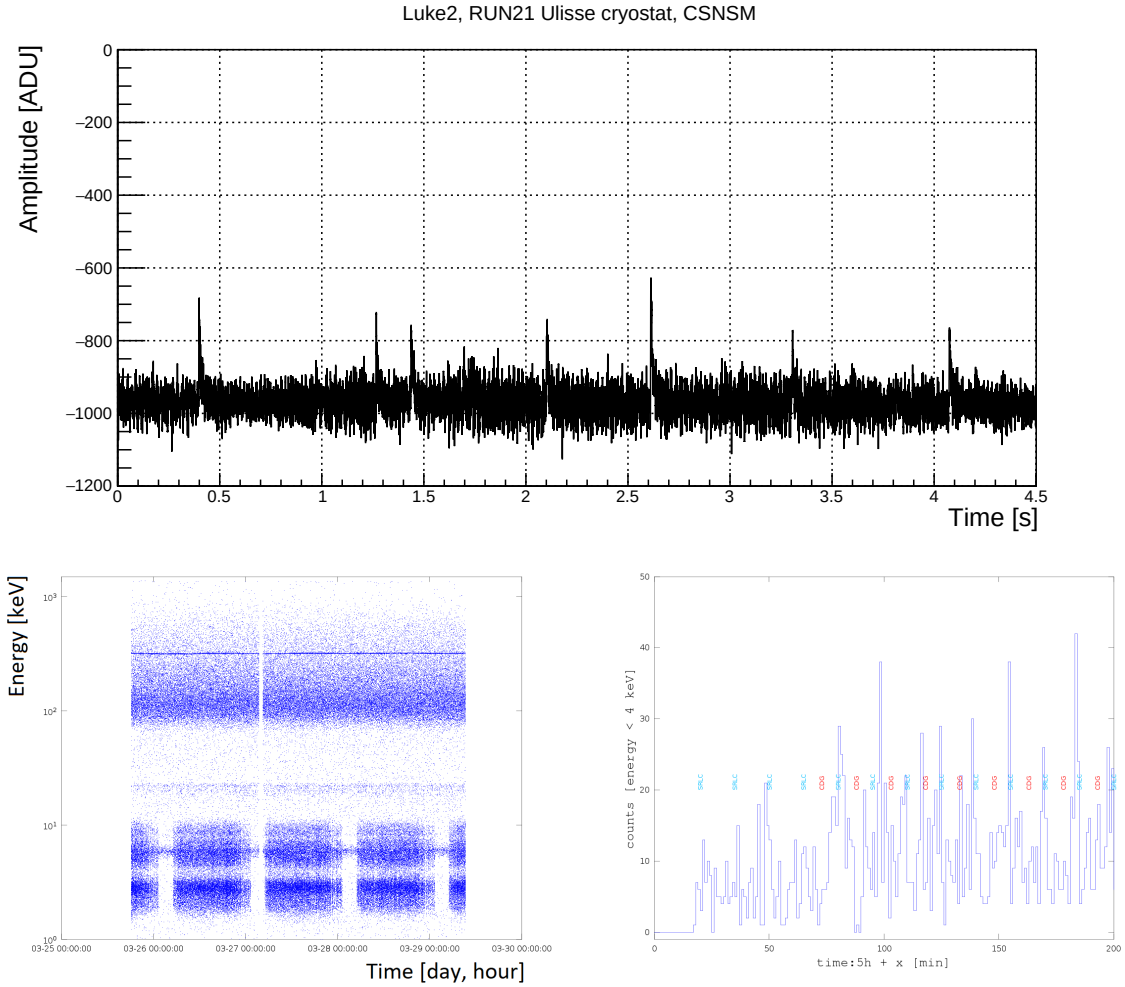

Fig. 6.3: *Top panel*: example of an event-like pulse set read by Luke2 and caused by the crossing of a RER train. *Bottom-left panel*: energy distribution of the events as a function of the time. This plot collects the data of around three days during Easter holidays. During the night the events below 10 keV disappear leaving only the line of the ^{55}Fe source. The lack of 1-h data during the 27$^{\text{th}}$ of March night is due to the switch between the standard and the daylight saving time. Two LED were operated during the run to shine all the ligt detectors. The intense line is due to the LED shining the light detector, the lower energy line is probably due to some reflections caused by the second LED. *Bottom-right panel*: event rate of pulses with an energy lower than 4 keV as a function of the passing time from 5:00 AM. The blue and red labels indicate the train crossing time, CDG (Charles de Gaulle) and SRLC (St Remy les Chevreuse) stand for the train direction.

Tab. 6.2: Working point and light detector performance in terms of sensitivity, baseline noise and energy resolution of the ^{55}Mn X-ray peak at 5.9 keV. The two light detectors with the best sensitivity (GeCo1 and Luke2) were tested in the NTL regime.

	run ID	current [nA]	resistance [MΩ]	NTL bias [V]	sensitivity [nV/keV]	noise RMS [eV]	RMS X-ray ^{55}Mn, 5.9 keV [keV]
GeCo1	M13	1.25	0.99	0	0.74	153	0.30
	M15	5	0.40	40	5.6	19	-
GeCo2	M14	5	0.59	0	0.58	109	0.37
GeCo3	M12	5	0.51	0	0.61	230	0.35
Luke2	M13	1.25	1.61	0	0.72	213	0.45
	M8	2.5	0.87	100	12.4	14	-
	M9	0.83	2.2	100	12.7	26	-
SID	M15	5	0.5	0	0.52	859	1.20
	M5	5	0.5	20	1.8	144	-
	M6	5	0.5	40	3.4	88	-
	M7	5	0.5	70	5.4	73	-

the calibration source. The time without events corresponded to the night interruption of the *Réseau Express Régional* (RER) train circulation. We tried to correlate the event rate with the time schedule of the RER trains passing through Orsay-ville station (the stop closer to the the laboratory hosting the set-up) and we found a reasonable correspondence in Fig. 6.3 (*bottom-right*). Probably this effect was due to an interference pick-up between the high voltage line of the train station and the cryostat ground.

Fig. 6.4 shows the gain and the signal-to-noise ratio as a function of the NTL bias for four detectors. These data were not acquired for SID light detector because of its poorer performance with respect to the others. The germanium-based light detectors present an uniform behaviour.

Since a baseline noise worsening is known to affect NTL-assisted devices at the increase of the electrode bias, we acquired a few minutes of stream data to evaluate its effect on the noise power spectra. Fig. 6.5 shows the noise power spectra of Luke2 for different electrode voltage bias. The noise worsens at low frequencies affecting the area where the bolometric signal develops. We suspect that it is caused by the presence of tiny pulses that are usually hidden in the noise, but they manage to stick out of it in presence of the NTL amplification. After this preliminary measurement, new tests about the noise caused by the NTL effect have been conducted, refer to Sec. 6.6.1 and 6.7 for further information.

GeCo1 and Luke2 were selected for the underground test with two enriched $^{130}TeO_2$ bolometers — described in the next section — because of their slightly better sensitivity.

6.3 Underground test with two 435-g enriched $^{130}TeO_2$ bolometers

This measurement — described in Ref. [173] — had to demonstrate the good bolometric performance of two enriched $^{130}TeO_2$ bolometers and to prove the separation achievable with the Cherenkov light detection using two NTL-assisted light detectors. This run has been performed in the CUORE/CUPID R&D cryostat hosted in Hall C at the Laboratori Nazionali del Gran Sasso, for more details about the cryostat see Sec. 3.1.4. The two $^{130}TeO_2$ crystals had a mass of 435 g each and were enriched in ^{130}Te up to 92 %. These two crystals have been produced in the framework of the R&D for the CUPID experiment with a view to the option of TeO_2 enriched in ^{130}Te. Previous attempt with enriched TeO_2 bolometers had been done in the MiBeta and CUORICINO experiments. Their bolometric performance was worst than the

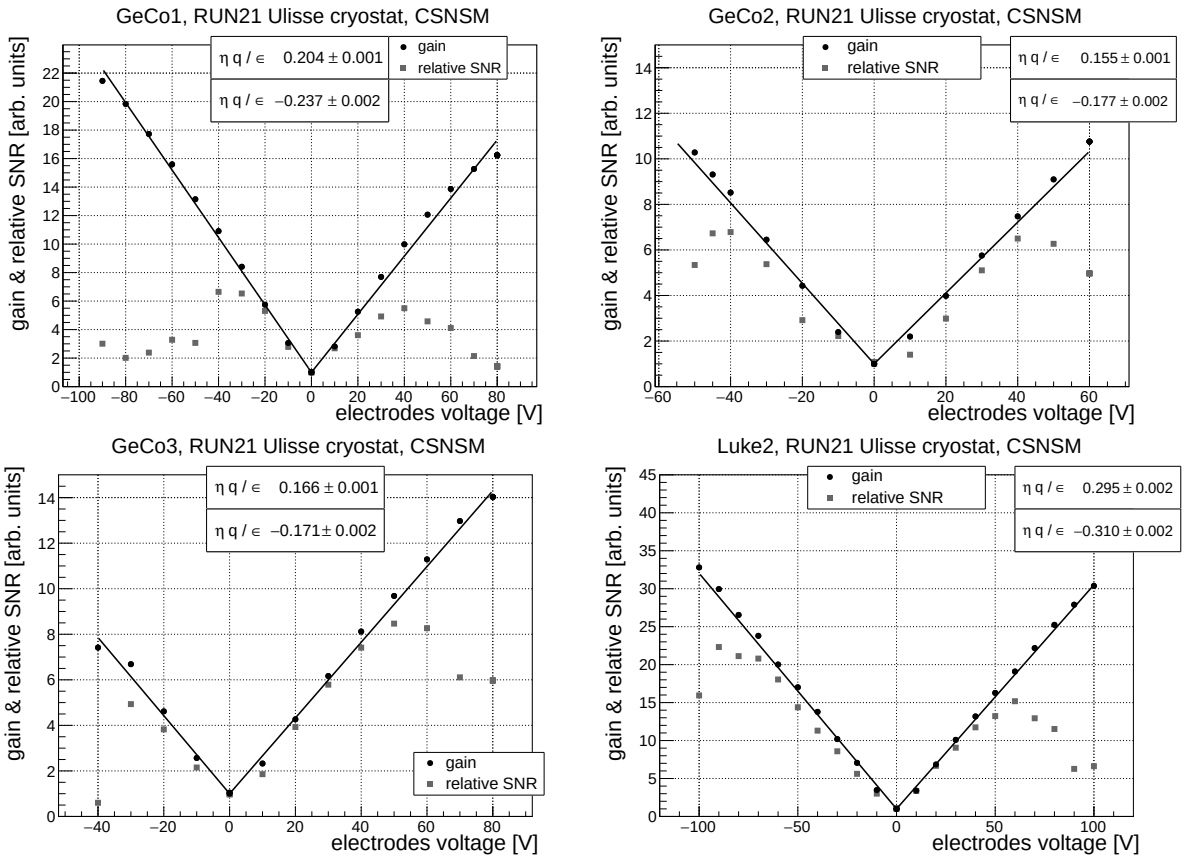

Fig. 6.4: Gain and signal-to-noise ratio as a function of the electrode bias measured for four NTL-assisted light detectors, in the order: GeCo1, GeCo2, GeCo3 and Luke2.

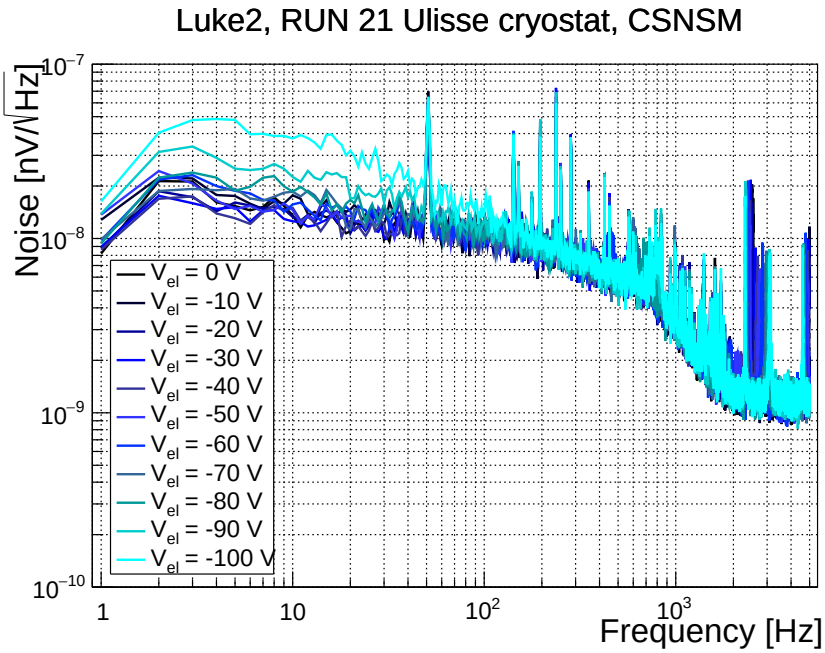

Fig. 6.5: Noise power spectra for the Luke2 light detector at different electrode biases.

Tab. 6.3: Light detector performance obtained in the CUPID R&D cryostat.

	resistance [MΩ]	sensitivity [μV/keV] (0-V bias)	noise RMS [eV] (0-V bias)	gain (NTL bias)	noise RMS [eV] (NTL bias)
GeCo1	2.3	1.32	87	8.9 (55 V)	25 (55 V)
Luke2	2.4	0.57	166	5.8 (25 V)	35 (25 V)

one of natural TeO_2 crystals [91, 221]. This measurement had also to test the bolometric performance of these devices. Each $^{130}TeO_2$ crystal was equipped with a $3 \times 3 \times 1$-mm NTD germanium thermistor and with a doped-silicon heater. The gluing of the thermal sensor has been performed with nine spots of Araldite glue. The $^{130}TeO_2$ bolometers were hold in a copper frame by S-shaped PTFE clamps and were surrounded on the sides and on the bottom by a plastic reflecting foil (3M Vikuiti(TM) ESR) to improve the light collection. The NTL-assisted light detectors have been mounted on the crystal top face with the electrodes facing the main bolometer. The photo-bolometers were equipped with a ^{55}Fe source for the calibration and a LED for the regeneration, that was performed every $2-4$ days depending on the type of run: background or calibration. We will refer to the main bolometer coupled to Luke2 as $^{130}TeO_2$-1 and as $^{130}TeO_2$-2 for the one coupled to GeCo1.

The light detectors and $^{130}TeO_2$ bolometers performance at 12 mK are reported respectively in Table 6.3 and 6.4. More information about the $^{130}TeO_2$-crystal radiopurity are discussed in Sec. 4.2. The calibration of the $^{130}TeO_2$ bolometers was done with a ^{232}Th source positioned inside of the cryostat lead shield. The light detector calibration has been done with the ^{55}Fe source when the electrodes were grounded. This calibration was used to calibrate the light output corresponding to the 2615-keV γ-quanta deposition in the main bolometer. The energy recorded in correspondence to these events was

Tab. 6.4: $^{130}TeO_2$ bolometer performance obtained in the CUPID R&D cryostat.

	resistance [MΩ]	noise FWHM [keV]	sensitivity [nV/keV]	γ-line ^{208}Tl, 2615 keV FWHM [keV]
$^{130}TeO_2$-1	200	3.5	135	4.3
$^{130}TeO_2$-2	145	4.2	95	6.5

(153 ± 4) eV and (160 ± 5) eV respectively for $^{130}TeO_2$-1 and $^{130}TeO_2$-2. The energy recorded by the light detectors is in a reasonable agreement with the ones measured in case of TeO_2 crystals of a similar size: 173 eV for a 177-g TeO_2 crystal [177] and 129 eV for a 285-g one [189]. The light signal thus calibrated is then used for the calibration of the light detector in the NTL regime, since the X-ray line of ^{55}Mn is no longer visible. The best signal-to-noise ratio working point in terms of electrode bias was identified by performing different calibrations: Luke2 was biased with 25 V and GeCo1 with 55 V. This measurement was characterised by a particularly bad noise for higher NTL biases, that was not observed in the aboveground test presented in Sec. 6.2. In fact Luke2 did not present a noise degradation for bias up to $70 - 80$ V in Fig. 6.5. We think that this was due to the presence of some radiation coming from the cold-electronic stage in the cryostat and affecting the light detector in the NTL regime. This topic is discussed further in Sec. 6.7, where some other aboveground tests are presented.

The discrimination power — defined as in Eq. (2.23) — was 2.65 for Luke2 and 3.5 for GeCo1. That corresponds to a $\beta(\gamma)$-event acceptance of 78.8 % in the case of Luke2 and of 98.3 % in the case of GeCo1 with an α rejection of 99.9 %. This measurement demonstrated that the use of enriched $^{130}TeO_2$ bolometers could be an interesting possibility in the upgrade of the CUORE experiment. In addition to the good bolometric performance achieved by the enriched crystals, the α background can be reduced by a factor more than 100 — the goal of the CUPID experiment — with a NTL-assisted device read by a NTD thermistor.

6.4 Underground test with a 784-g TeO_2 bolometer

In view of a tonne-scale experiment, the ability to fill the cryostat maximising the isotope mass inside the volume while maintaining a reasonable number of channels is indispensable. A huge number of detectors would become complicated both on the operation point of view and for the electronic lines needed for the detector read-out. A crystal mass of the order of $300 - 700$ g (depending on the material density) is a good compromise. A larger device would have a higher heat capacity that could affect the bolometric performance. But as we have seen in Sec. 4.2.1, the light-trapping probability increases with the crystal size and this can become an issue in case of crystals with a low light yield as the TeO_2. The $\beta(\gamma)$ and α separation performance achievable with the devices coupled to CUORE-size TeO_2 bolometer is here presented. This test was performed with a $50.8 \times 50.7 \times 50.7$-mm TeO_2 bolometer coupled to GeCo1 light detector. The crystal belonged to the ones used by the Cuoricino experiment, for this reason it was slightly larger than the ones presently used by CUORE. The results discussed in this section can be found in Ref. [196].

GeCo1 and the TeO_2 bolometer have been hosted in the EDELWEISS cryostat sharing the set-up with the EDELWEISS and the LUMINEU experiments. Stringent low-radioactivity conditions were required by both experiments. For this reason all the detector parts underwent a careful selection and cleaning procedure. All the copper pieces constituting the holder have been cleaned with the following procedure:

- washing in ultrasonic bath with ultra pure water mixed to an acid soap (*ELMA micro 60*) for 20 minutes to remove the grease on the surfaces;

- rinsing with ultra-pure water to remove the soap;
- etching with nitric acid concentrated at 30 % for 30 s, that was later removed by two consecutive immersions in ultra-pure water for 1 minute;
- water traces were removed with an immersion in ethyl alcohol for 1 minute and finally the copper pieces have been dried with a thermo-gun at 120 °C.

Also the PTFE pieces clamping the crystal have been cleaned as follows:

- washing in the ultrasonic bath with ultra-pure water and an acid soap (*ELMA micro 90*) for 20 minutes in order to remove eventual grease traces on their surface;
- rinsing with ultra-pure water to remove the soap traces and then with ethyl alcohol to remove possible water traces on surfaces.

After the cleaning procedure the holder has been coated with a ~ 0.1-μm-thick gold deposition in order to prevent copper oxidation. Moreover the holder surfaces facing the detector have been covered with a $\sim 1-3$-μm-thick silver layer in order to improve the light collection. Fig. 6.6 shows the holder and its cover after the coating procedure.

A cubic 783.94-g TeO_2 crystal was employed as absorber. The crystal surface had been ground with the same procedure employed for the crystals used by the CUORE experiment. Before mounting, the crystal surfaces have been cleaned with ethyl alcohol. The TeO_2 crystal has been fixed in the copper holder with five PTFE pieces: three L-shaped at the bottom and two S-shaped at the top positioned as reported in Fig. 6.8 (*left*). We tried to use four pieces for the bottom part, but one of them was not well fixed, so we decided to use three pieces in order to avoid microphonic noise.

CUORE-crystal lattice is characterised by a tetragonal structure with the following lattice orientations: <001>, <110> and <1-10> [157]. TeO_2 crystals have two hard faces and four soft ones [110]. The crystal orientation of soft faces is <110>; those faces expand in one direction and contract in the perpendicular direction during the cooling down. On the contrary, the hard-face crystal orientation is <100>; those faces contract in all the directions. The NTD have been glued on one of the soft faces: the crystal is placed inside the holder with the orientation reported in Fig. 6.8 (*right*).

We equipped the TeO_2 crystal with a low-resistance 34C NTD — previously belonging to a $Zn^{100}MoO_4$ crystal measured in run 310 at LSM [97] — and a heavily doped silicon meander as a heater [152]. The NTD and the heater were both glued with the Mylar mask method, the first one with a matrix of six-glue spots and the second one with only one spot. Fig. 6.9 shows the assembled detector before and after the chip gluing. The Kapton connectors were glued on the copper holder with a film of Araldite glue. The solderings on Kapton have been done with low radioactivity tin.

We used Ø25-μm gold bonding wire for the NTD and Ø25-μm aluminium bonding wire for the heater. We bonded the NTD with two wires for each pad in order to improve the thermal link, while the heater with only one wire for pad. We use the two internals pads for the heater because they had a better surface for bonding. Fig. 6.10 (*left*) shows the two chips bonded.

The TeO_2 holder cover was equipped with a ^{210}Po α source in Fig. 6.10 (*right*). The source has been implanted onto a copper tape that has been partially covered by three 6-μm-thick Mylar foils. The non-covered copper tape produced α particles at 5.31 MeV, that were used to stabilize the measurement and to calibrate the α spectrum. The covered tape produced smeared α in the region between 1 MeV and 3 MeV, that has been used to test the α-$\beta(\gamma)$ separation achieved with the help of the NTL effect. The description of a test dedicated to the evaluation of the source rate and smeared α energy region can be found in Appendix 9.1.

We coupled our TeO_2 bolometer to GeCo1: it is connected at the TeO_2 bottom face through the circular window in the holder. The electrodes are facing the crystal. Fig. 6.11 shows the GeCo1 light detector (*left*) and its thermal sensor (*right*) before the assembly with the TeO_2 bolometer. The TeO_2

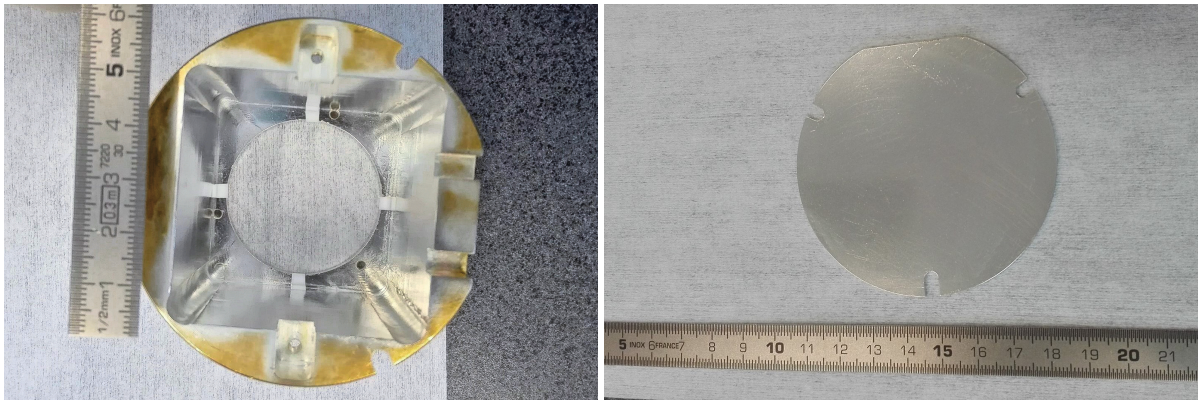

Fig. 6.6: *Left panel*: photograph of the detector copper holder coated with gold and silver. On the bottom of the holder there are four PTFE pieces used to seat the TeO_2 bolometer. *Right panel*: photograph of the holder cover coated with silver.

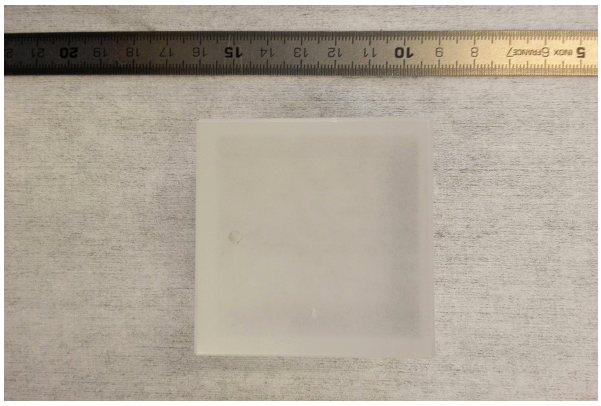

Fig. 6.7: Photograph of the 783.94-g TeO_2 crystal used in this measurement.

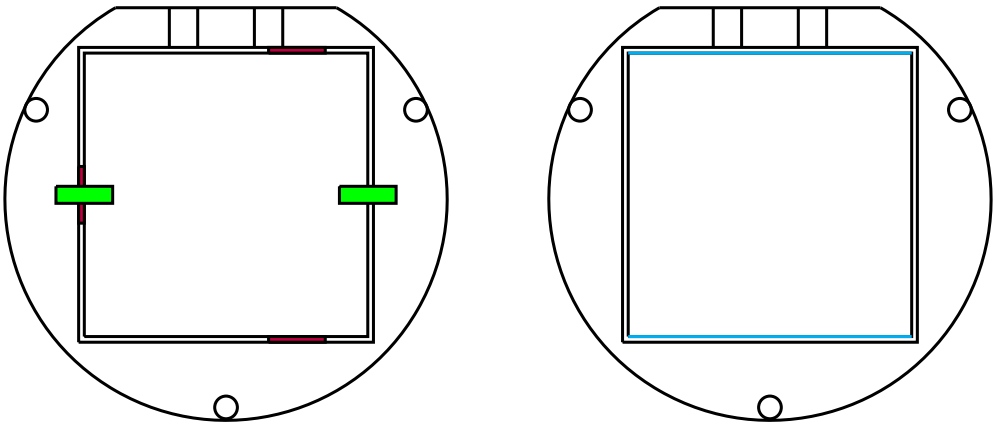

Fig. 6.8: *Left panel*: scheme of the PTFE clamp position, the L-shaped clamps are holding the crystal from below (*in purple*) and the S-shaped clamps are acting from above (*in green*). *Right panel*: position of the TeO_2 hard faces (*in cyan*) with respect to the holder.

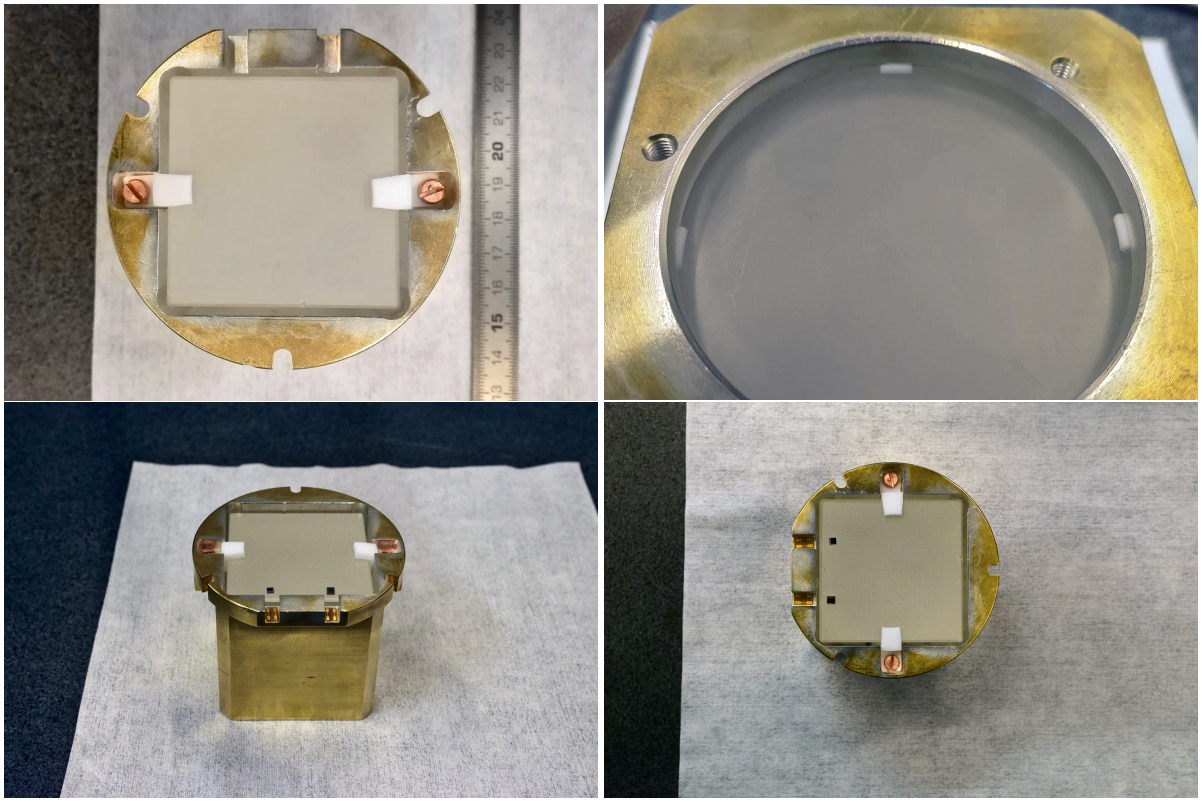

Fig. 6.9: *Top panel*: photograph of the position of the S-shaped (*left*) and L-shaped (*right*) PTFE pieces. *Bottom panel*: photographs of the crystal top view with the chips glued.

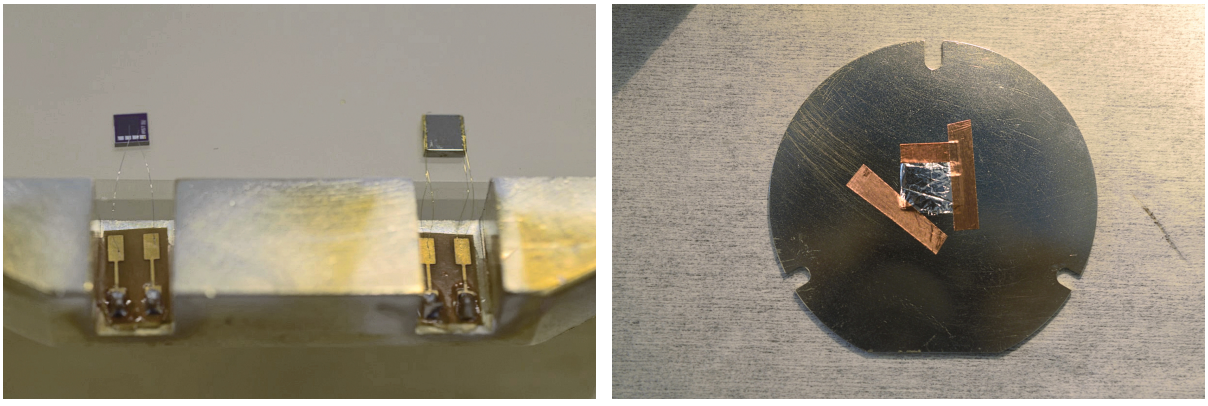

Fig. 6.10: *Left panel*: photograph of the bonded chips. The heater has been bonded with one aluminium wire for each pad, while the NTD has been bonded with two gold wires for each pad. *Right panel*: α source glued to the detector holder with copper tape. The source is implanted in a copper tape and two thirds of the source are covered with a three 6-μm-thick Mylar foils to smear the α's energy.

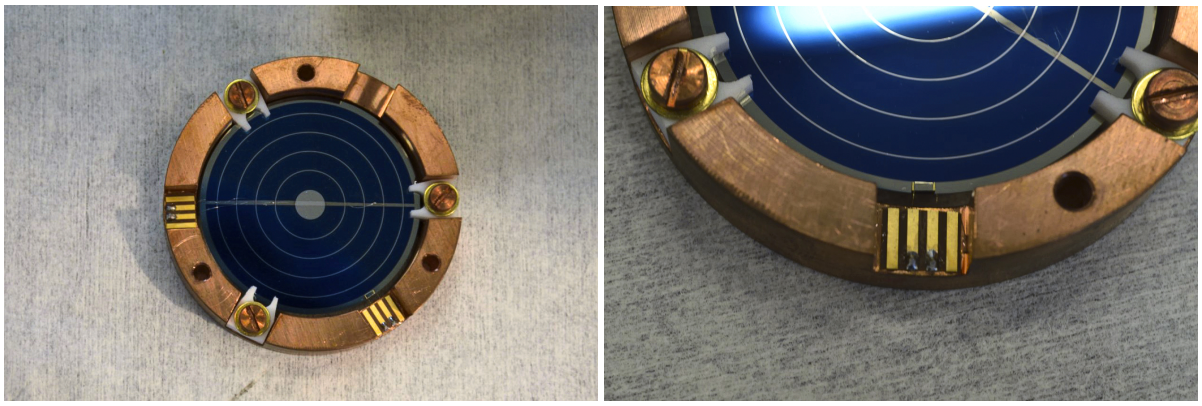

Fig. 6.11: Photograph of GeCo1 light detector (*left*) and its NTD thermistor (*right*).

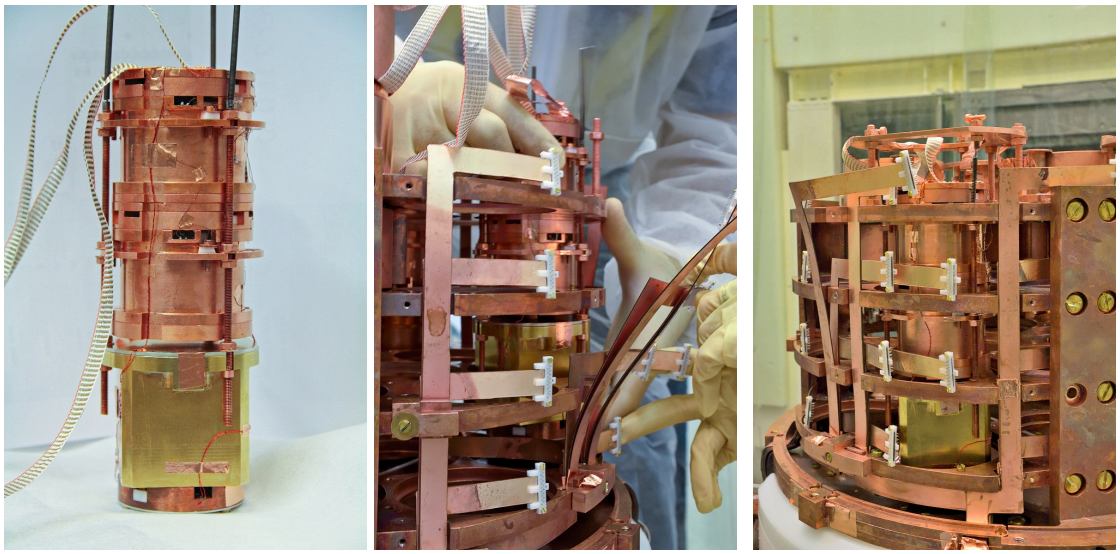

Fig. 6.12: *Left panel*: photograph of the second tower containing the TeO_2 detector in the lower position. The full tower has been mounted in CSNSM clean room and then transported to LSM. *Middle panel*: photograph of the second-tower installation in the EDELWEISS cryostat. The tower is inserted in the *galette* structure and then suspended from the top. *Right panel*: photograph of the second tower after its suspension.

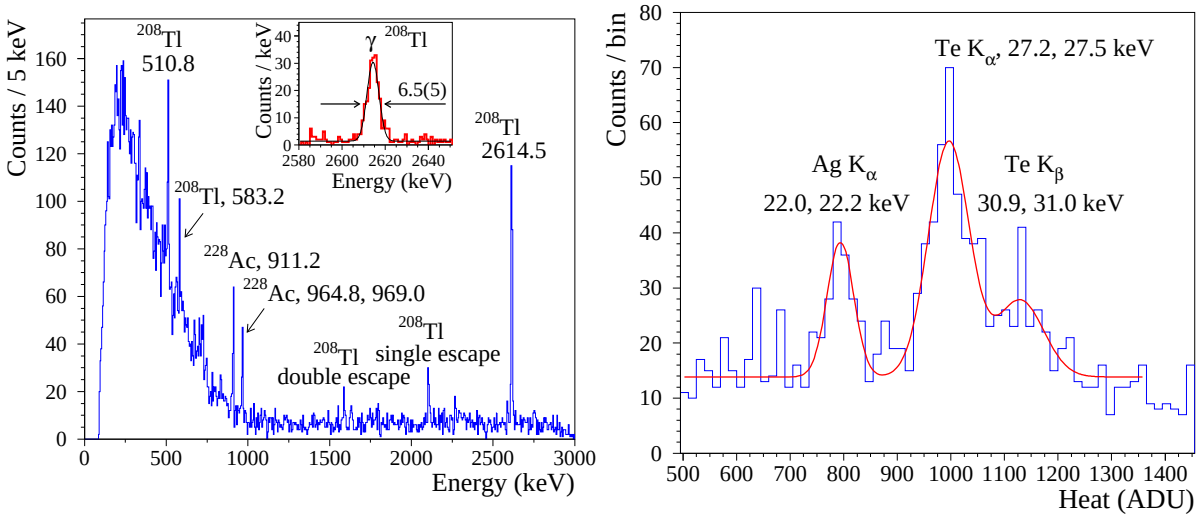

Fig. 6.13: *Left panel*: TeO_2 bolometer calibration with the ^{232}Th source over 148.3 h. The inset presents the fit of the 2615-keV γ-line from ^{208}Tl. *Right panel*: light detector calibration with the γ's induced by the ^{60}Co source.

detector and GeCo1 have been hosted by the EDELWEISS cryostat in the underground laboratory of Modane (France) during run 311. They were mounted with a $CdWO_4$ and a $ZnMoO_4$ detectors in a suspended tower used to reduce vibrations and consequently noise. The detectors were fixed at the bottom place of the tower in Fig. 6.12 (*left*). The detectors in the tower were hold together by three copper rods on the sides, that were placed with an angle of 120° in holders' guides. The TeO_2 holder was larger than the other two belonging to the tower, and for mechanical reasons it was not practical to put it in direct contact with the other two detectors above it. So the thermal link between this detector and the others has been done with a copper strip softened by annealing. The mounting of the tower has been completed at CSNSM and then it has been inserted in the cryostat in Fig. 6.12 (*middle*) once that all the *galette* structure was mounted. At the end, the tower was suspended from the top with three springs in Fig 6.12 (*right*).

The detector read-out was performed with the AC-electronics used by the EDELWEISS experiment, refer to Sec. 3.1.3 for more details. The GeCo1 electrodes were connected to the high-voltage system used by EDELWEISS to bias the NTL-based detectors [145].

The data here presented have been acquired in a week-long measurement at 17 mK. During the measurement, a low activity ^{232}Th source has been constantly employed to calibrate the TeO_2 bolometer. It has been positioned inside the cryostat lead shield and was characterised by a $\sim$ 300 Bq event rate. Fig. 6.13 (*left*) shows the energy spectra obtained by the TeO_2 bolometer, featuring an energy resolution of 6.5(5) keV at the 2615-keV γ quanta of ^{208}Tl. The light detector has been calibrated thanks to the fluorescence X-rays induced by an intense source ($\sim$ 200 kBq) of ^{60}Co in the material surrounding the light detector. This calibration has been performed with the electrodes grounded and lasted around 6.4 h. The X-ray lines produced by tellurium and silver are shown in Fig. 6.13 (*right*), they are respectively emitted by the TeO_2 crystal and the holder coating.

Over the 148.3-hour data acquired, 49.6 hours were performed with the light detector electrodes grounded. These data were used to prove the impossibility to obtain an α and $\beta(\gamma)$ separation without the enhancement of the NTL effect and to estimate the light energy output collected from the 2615-keV γ-quanta of ^{208}Tl thanks to the ^{60}Co calibration. In particular, only (70 ± 13) eV (corresponding to a

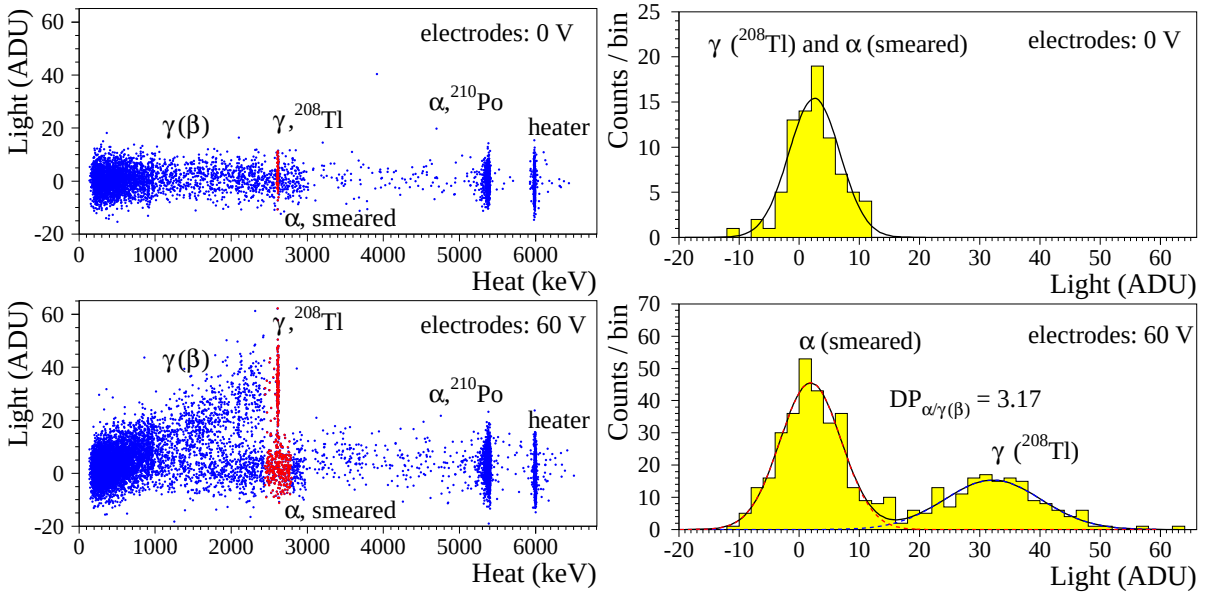

Fig. 6.14: Heat-light scatter plot and the corresponding histogram of the light output for the highlighted events. Two cases are presented: the light detector with grounded electrode (*top*) and with a 60-V NTL bias (*bottom*).

Tab. 6.5: GeCo1 performance obtained in the EDELWEISS cryostat.

	resistance [MΩ]	sensitivity [μV/keV] (0-V bias)	noise RMS [eV] (0-V bias)	gain (NTL bias)	noise RMS [eV] (NTL bias)
GeCo1	2	0.9	108	12.7 (60 V)	10(2) (60 V)

light yield of $\sim$ 27 eV/MeV) were collected by the light detector in correspondence of 2615-keV events in the heat channel. The light output has been evaluated from the fit of the light emitted by 2615-keV ^{208}Tl γ-quanta events in the main crystal with a 0-V electrode bias in Fig. 6.14 (*top*). Usually the light emitted by a 2615-keV deposition in a 5-cm-side TeO_2 bolometer is of the order of 100 eV, in particular 105(5) eV in Ref. [177] and 92 eV in Ref. [181]. The lower light collection in this measurement is due to a non-optimised geometric coupling between the light detector and the TeO_2 bolometer. In fact, the hole — through which the light detector sees the crystal — has an area that is around 40 % smaller than the main crystal face. This choice was imposed by space restrictions in the cryostat experimental volume.

In addition 98.7-hour data have been acquired enhancing the light detector performance with the NTL effect: 60 V were applied to the electrodes. The light detector performance are reported in Table 6.5. Fig. 6.14 shows the heat-light scatter plot and the light output both in case of grounded electrodes (*top*) and in case of NTL amplification (*bottom*). When the light detector is not in a NTL regime, it is not possible to discriminate between $\beta(\gamma)$ and α events. Only the improvement of the light signal-to-noise ratio in the NTL regime allows us to obtain a full separation. Table 6.6 summarises the results of the Gaussian fit performed on the light output in Fig. 6.14. In the case of grounded electrodes, a 34-keV energy interval has been considered around the 2615-keV peak for the $\beta(\gamma)$ events; the α events have been selected after the endpoint of natural γ radioactivity. When the NTL bias was applied, both for $\beta(\gamma)$ and α events has been considered the same energy interval. This measurement showed a discrimination power — defined as in Eq. (2.23) — of 3.17. If we assume to reject 99.9 % of α events — corresponding

Tab. 6.6: Results of the Gaussian fit performed on the light output at 0-V and 60-V electrode bias. For each energy interval of the heat channel, the mean value μ and the standard deviation σ are reported.

	0-V electrode bias			60-V electrode bias		
	Heat (keV)	Light μ (ADU)	Light σ (ADU)	Heat (keV)	Light μ (ADU)	Light σ (ADU)
Baseline	0	-0.05 ± 0.05	3.92 ± 0.04	0	0.005 ± 0.06	4.54 ± 0.06
$\beta(\gamma)$	$2598 - 2632$	2.5 ± 0.5	4.2 ± 0.3	$2440 - 2790$	32.1 ± 0.7	8.1 ± 0.7
α	$2640 - 2790$	0.1 ± 0.6	4.7 ± 0.4	$2440 - 2790$	1.9 ± 0.3	5.1 ± 0.3

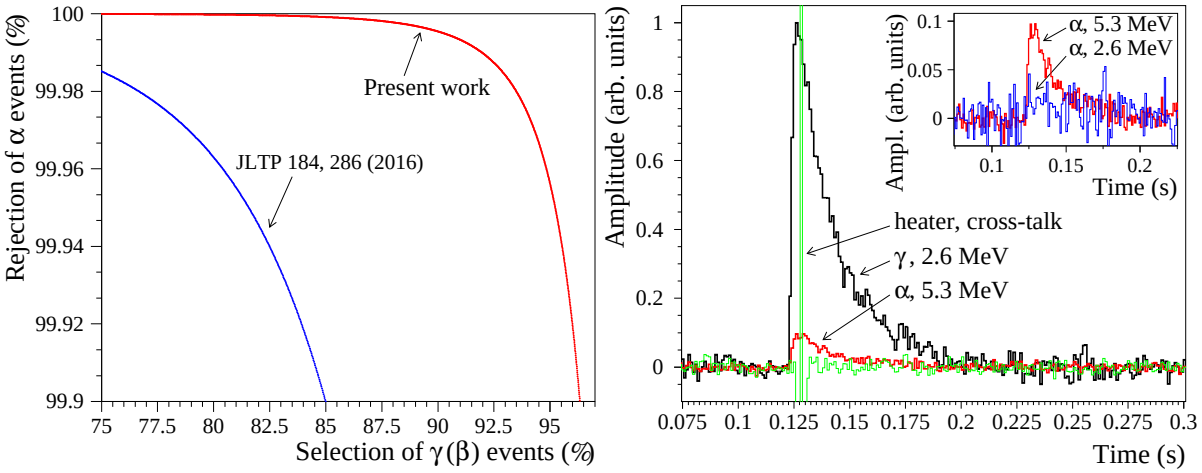

Fig. 6.15: *Left panel*: α events rejection as a function of the $\beta(\gamma)$ acceptance. *Right panel*: comparison of average pulses recored by the NTL-assisted light detector. The main plot compares average light pulse corresponding to the following events in the main bolometer: 2615-keV γ-quanta, a 5.3-MeV α and a heater-induced cross-talk. The inset compares an average of light events read in correspondance of a 2.6-MeV and a 5.3-MeV α event in the main crystal.

to lowering the α background by a factor 10^3 — we are able to accept 96 % of $\beta(\gamma)$ events. Fig. 6.15 (*left*) shows the α rejection ability as a function of the percentage of $\beta(\gamma)$ accepted comparing the results of this work with Ref. [181]. Both measurements have been carried out with a NTL-assisted light detector coupled to a CUORE-size TeO_2 bolometer, therefore with the same light output. The here-presented measurement demonstrated a notable improvement with respect to the previous one.

Fig. 6.14 shows that the light output in correspondence of α events is not compatible with no-light emission. Assuming that TeO_2 crystals do not scintillate at low temperatures, we would not expect Cherenkov light emission due to α events in the $1 - 5$-MeV region since the Cherenkov production threshold is much higher (see Sec. 4.2.1). Nevertheless, scintillation light from a TeO_2 crystal had already been observed in Ref. [194] but this result remained controversial. Some hints of scintillation light had already been observed [173, 181, 179, 189, 187, 182] without drawing conclusions. A large number of waveforms was mediated in Fig. 6.15 (*right*) in order to reduce the noise and verify whether some light was present in correspondence of α events or if it was an analysis artefact. We compared the average light output produced by 2615-keV γ-quanta events (333 waveforms) with the ones produced by 5.3-MeV α (3551 waveforms) — generated by the ^{210}Po-source part that was not smeared by the Mylar foils — and with cross-talk events induced by the heater (1608 waveforms). The inset presents also the

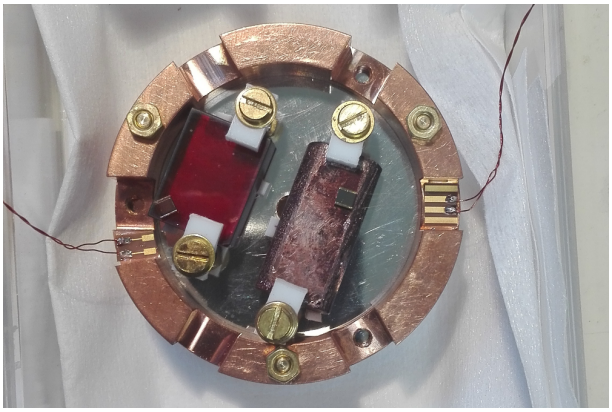

Fig. 6.16: Photograph of the mounting of $LiInSe_2$ (*left*) and GaSe (*right*) bolometers.

comparison between the average of 5.3-MeV α events with 2.6-MeV α events (668 waveforms). All the pulses are renormalised with respect to the γ pulse. We can clearly state that we see a light output in correspondence of α events and that it is not an artefact due to cross-talk or the analysis. If we assume a quenching factor between the light signals induced by $\beta(\gamma)$ events and by α's of the order of 0.2 — as it is typical for many crystal scintillator [97] — we can evaluate the energy fraction due to scintillation light. The TeO_2 scintillation light contributes by $\sim$ 20 % to the total light output collected from a 2615-keV γ-quanta from ^{208}Tl event. Therefore the light yield of a scintillation event can be estimated to $\sim$ 5 eV/MeV.

6.5 Pile-up discrimination

The pile-up is an intrinsic and unavoidable issue for bolometric detectors with a slow response. It can even become a possible source of background in rare-event searches performed with NTD-based detectors. An example is the $2\nu2\beta$ decay of ^{100}Mo that can contribute to the background of $0\nu2\beta$ decay with $\sim 10^{-3} - 10^{-4}$ counts/(yr kg keV) depending on the crystal size and the effectiveness of the pulse shape discrimination algorithms [222]. This issue has been studied and simulated for the $2\nu2\beta$ decay of $Zn^{100}MoO_4$ and $Li_2{}^{100}MoO_4$ crystals [222, 209] demonstrating that NTL-assisted light detectors are a promising solution. In fact these devices are characterised by a faster response — intrinsic to light detectors thanks to their low heat capacity — and an improved signal-to-noise ratio. The presence of only the first feature would not be sufficient because events occurring with a time resolution shorter than the pulse rise time would be hidden in the noise. However the NTL amplification and the improvement of the signal-to-noise ratio permit the identification of these events thanks to the pulse-shape analysis [223, 224]: a longer rise time is expected.

An aboveground test of a $LiInSe_2$ bolometer has provided a good opportunity to show the potentialities of NTL-assisted light detectors in the pile-up rejection. Fig. 6.16 shows a photograph of the bolometer: a $8 \times 15 \times 19$-mm 10.3-g $LiInSe_2$ bolometer provided by MIT. This crystal is particularly interesting for the forbidden β decay of ^{115}In. In fact the investigation of its β spectra at low energies can provide information on the effective values of the axial-vector coupling constant g_A [225, 226]. The $LiInSe_2$ bolometer was coupled to Luke2 light detector. The main crystal has been fixed to a standard light detector holder with 3 L-shape PTFE clamps on the bottom and two on the top. The bottom part of the holder was coated with silver in order to improve the light collection. The $LiInSe_2$ crystal has been

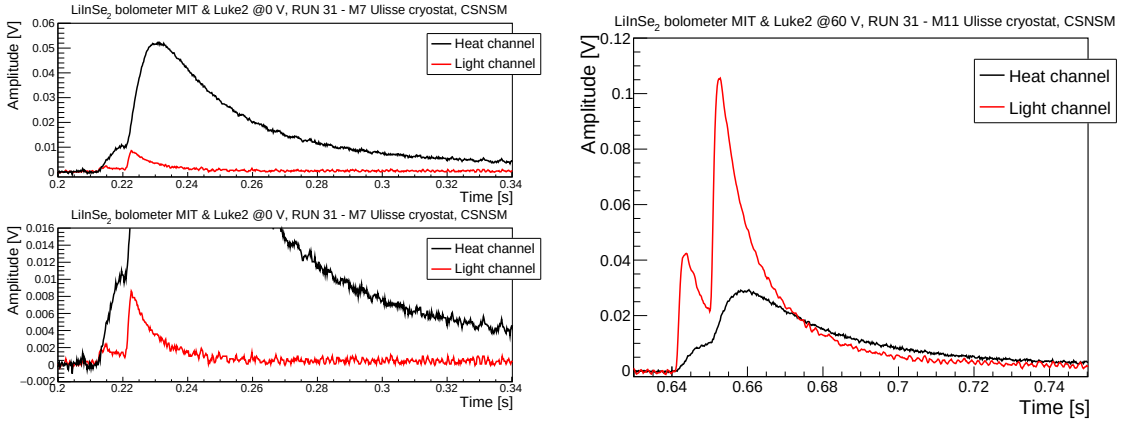

Fig. 6.17: *Left panel*: pile-up event in the heat channel compared to the light channel read with the grounded electrodes (*top*) with a zoom on the light event (*bottom*). *Right panel*: an equivalent-energy pile-up event in the heat channel compared to the light channel read with 60-V electrodes bias.

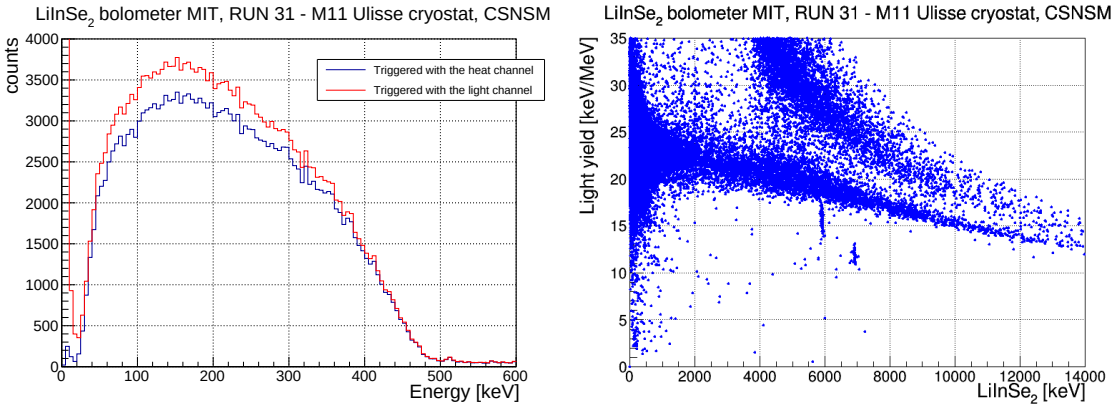

Fig. 6.18: *Left panel*: ^{115}In spectrum triggered with the heat (*in blue*) and light (*in red*) channel. *Right panel*: light yield of the $LiInSe_2$ detector as a function of its energy.

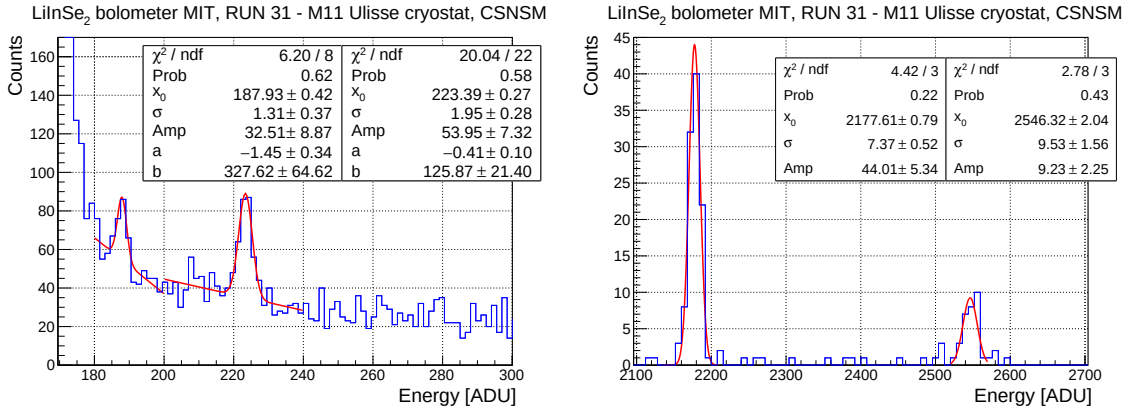

Fig. 6.19: *Left panel*: annihilation peak and ^{214}Bi γ quanta used for the β calibration of $LiInSe_2$ in measurement M11. *Right panel*: ^{6}Li neutron capture and ^{210}Po peaks of $LiInSe_2$.

Tab. 6.7: $LiInSe_2$ detector characterisation. The bolometer was biased with 12.5 nA to improve its linearity at low energy.

run	resistance	T_{base}	^{6}Li(n,t)α 4783 keV	ext ^{210}Po 5304 keV	^{210}Bi 609.3 keV	annihilation peak 511 keV
ID	[MΩ]	[mK]	FWHM [keV]	FWHM [keV]	FWHM [keV]	FWHM [keV]
M6	0.2	20	48(12)	low statistics	low statistics	low statistics
M7	-	18	68(124)	14(8)	low statistics	low statistics
M11	0.2	20	42(3)	49(8)	12(2)	6(2)

equipped with a NTD from the 41B batch[1] also provided by MIT. The thermistor has been glued with 6 glue spots of Araldite with the Mylar-mask technique. The bolometer has not been equipped with a heater, we decided to perform the stabilisation with the optical fibre. The light detector electrodes were facing the detectors while its back was shined by a ^{55}Fe source used for calibration. The light detector was illuminated also by an optical fibre shining in the crystal cavity.

The $LiInSe_2$ crystal is characterised by a high event rate ($\sim$ 1 Hz for the sample size used) generated mainly by the β decay of ^{115}In, that has to be added to the cosmic radiation pulses present in an aboveground measurements. An example of two pile-up events — read by the heat and light channel and characterised by similar amplitudes — is reported in Fig. 6.17. The light pulse acquired with grounded electrodes in Fig. 6.17 (*left*) is barely standing outside of the noise. Even if it is possible to recognise the pile-up presence visually, a trigger performed on the light channel would not recognise all the small event because of its bad signal-to-noise ratio. But an amplified light channel would allow a better identification of pile-ups as in in Fig. 6.17 (*right*). Fig. 6.18 (*bottom-left*) presents a ^{115}In β spectrum triggered with the heat and light channel. In this latter case, a larger number of events have been recovered at low energies. Usually the trigger is performed with the heat channel because of its better signal-to-noise ratio, but an amplified light can be an interesting alternative to the identification of low energy events.

Fig. 6.18 (*bottom-right*) shows the $LiInSe_2$ light yield measured by the Luke2 light detector. The light-yield non linearity is due to a heat channel non-linearity generated by an over-biased working point. The muon cloud is present above the β/γ band, since the measurement has been carried out in an aboveground cryostat, while the ^{6}Li neutron capture and the ^{210}Po are visible below. The heat channel has been calibrated with the 511-keV annihilation peak and 609-keV ^{214}Bi γ-quanta in Fig. 6.19 (*left*). Fig. 6.19 (*right*) shows the fit of the ^{6}Li neutron capture and ^{210}Po peaks fit. Table 6.7 reports the energy resolutions obtained.

The Luke2 performance are listed in Table 6.8. The light detector has been calibrated with the ^{55}Fe source when the electrodes were grounded and with the muon distribution when the electrodes were biased. The scintillation light emitted by the ^{6}Li neutron capture has been calibrated with the ^{55}Fe in one measurement with the grounded electrodes. The ^{55}Mn X-ray line used for this calibration is shown in Fig. 6.20 (*left*). The collected light had an energy of 77.4 keV in the case of ^{6}Li neutron capture and 63.7 keV in the case of ^{210}Po. This information was used to calibrate the measurement with 50-V bias on the electrodes in Fig. 6.20 (*right*). In the case of the scintillation light, the sensitivity and the baseline are improved with respect to the muon calibration. This is probably due to the fact that the detector working in the NTL regime starts to be non linear at the muon energies. In general it is better to calibrate the detectors with scintillation light because the light detector is used to detect signal with these energies, but this is not always possible.

[1] R_0 = 1.62(9) Ω and T_0 = 3.76(7) K characterised during this run directly glued on the crystal.

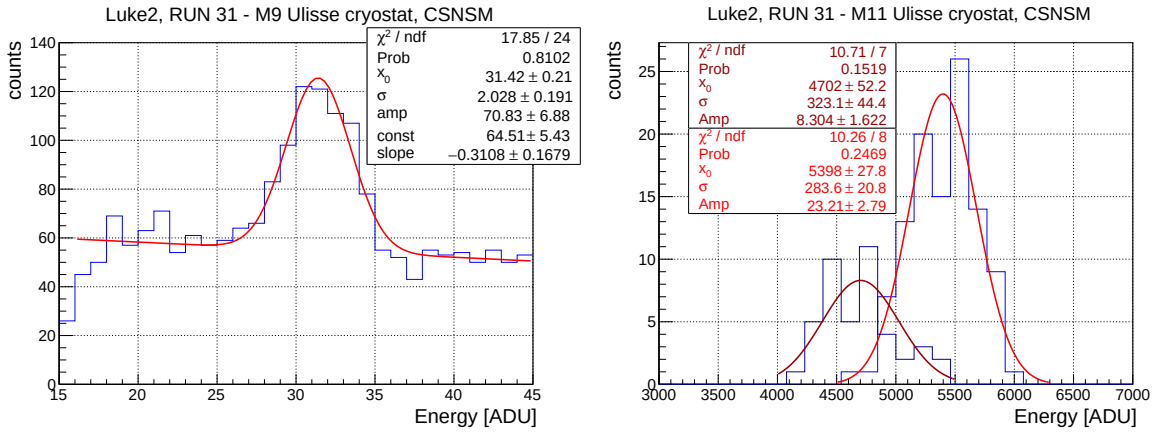

Fig. 6.20: *Left panel*: ^{55}Fe calibration of the Luke2 detector with grounded electrodes. *Right panel*: ^{6}Li neutron capture and ^{210}Po light collected by Luke2.

Tab. 6.8: Luke2 light detector performance obtained during the $LiInSe_2$ measurement.

run ID	current [nA]	resistance [MΩ]	T_{base} [mK]	NTL bias [V]	sensitivity [μV/keV]	noise RMS [eV]	RMS X-ray ^{55}Mn 5.9 keV [keV]
M6	5	0.45	20	60	7.7	15	fit on μ's
M7	5	$\sim$ 0.60	18	0	0.488	202	0.34
M9	1.25	1.5	20	0	0.758	264	0.38
M11	1.25	1.5	20	50	8.2	24	fit on μ's
					9.9	20	^{6}Li light

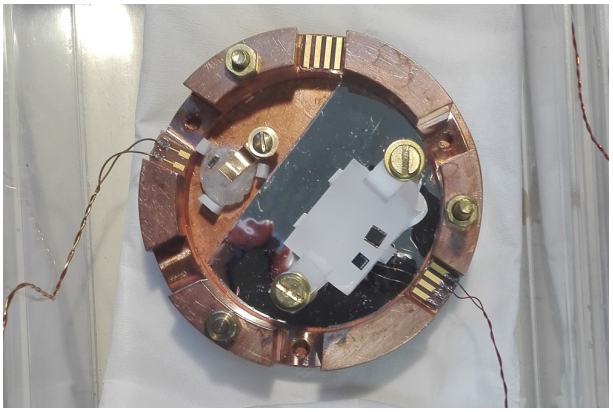

Fig. 6.21: Photograph of the mounting of $Na_2(MoO_3)_4O$ (*left*) and $Li_2Mg_2(MoO_4)_3$ (*right*) bolometers.

6.6 A boost for bolometers with a poor light collection

The amplification and the improved signal-to-noise ratio of NTL light detector could be also exploited with bolometric set-ups characterised by a poor light collection to improve the $\beta(\gamma)$ and α separation. We had the opportunity to test a small crystal of $Na_2(MoO_3)_4O$ (provided by MIT) with GeCo2 light detector. $Na_2(MoO_3)_4O$ could be an interesting compound for the search of $0\nu2\beta$ decay as an alternative of Li_2MoO_4 with a view to a CUPID experiment based on ^{100}Mo. The main crystal was a small sample with a size of Ø7 × 6 mm and a mass of 1.6 g, its irregular shape complicated the mounting. The $Na_2(MoO_3)_4O$ crystal was positioned in a light detector holder seated on three L-shaped PTFE pieces — that have been glued to the copper holder with a rapid glue — and blocked with a copper-beryllium clamp from above. The reflecting foil is not present below the $Na_2(MoO_3)_4O$ bolometer because the initial plan was to glue the crystal directly to the copper of the holder but this technique did not succeed. The $Na_2(MoO_3)_4O$ crystal was equipped with 1/3 of NTD belonging to the batch 34C, in order to not cover all his top surface reducing its light yield. The NTD was glued with one Araldite spot without applying any pressure on the NTD to avoid the creation of a glue film. We did not equip this crystal with a heater because its top surface was not big enough to host it. The upper surface of the crystal was partially covered by the NTD and the copper-beryllium clamp, therefore the light collection of the set-up was really poor. Fig. 6.21 shows a photograph of the final $Na_2(MoO_3)_4O$ detector mounting. A ^{210}Po α source was positioned close to the $Na_2(MoO_3)_4O$ bolometer. The light detector had the SiO side facing the detectors in order to improve the light collection and it was equipped with a ^{55}Fe source on the opposite side. The light detector was illuminated also by the optical fibre shining the detector cavity.

Fig. 6.22 shows the heat-light scatter-plot performed with the GeCo2 light detector without (*top-left*) and with (*top-right*) the bias applied on the electrodes. The light channel is calibrated in both plots: an improvement in the $\beta(\gamma)$ and α separation is clear in presence of the NTL regime. In these plots, two families of events are highlighted in different colors, these two groups of events are characterised by a different correlation as it is visible from Fig. 6.22 (*bottom-left*). We think that the presence of these two different event families is due to the structure of that sample of $Na_2(MoO_3)_4O$ crystal that was not a uniform mono-crystal but it was composed by a poli-crystalline structure constituted by two main crystals.

The heat channel has been calibrated with the α spectra presented in Fig. 6.22 (*bottom-right*). The presence of the ^{210}Po source, the fact that the measurement was carried out aboveground and the mount-

Tab. 6.9: GeCo2 light detector performance obtained during the measurement of the $Na_2(MoO_3)_4O$ bolometer.

run ID	current [nA]	resistance [MΩ]	T_{base} [mK]	NTL bias [V]	sensitivity [μV/keV]	noise RMS [eV]	RMS X-ray ^{55}Mn 5.9 keV [keV]
M2	2.5	0.68	20	0	0.679	219	0.36
M3	5	$\sim$ 0.46	19.5	0	0.831	98	0.31
M5	5	$\sim$ 0.46	19.5	60	11	14	fit on μ's

ing not optimised for a radioclean measurement prevents us from drawing conclusion on the crystal radiopurity. The light detector has been calibrated with the ^{55}Fe source when the electrodes were grounded and with the muon distribution when the electrodes were biased. Table 6.9 summarises the main performance obtained by the GeCo2 light detector during the run.

6.6.1 Photon tightness improvement

As it was stated in Sec. 6.2 and 6.3, we suspected that the noise deterioration for NTL high-voltage bias was due to a photon noise: the NTL effect amplifies signal that are usually hidden in the noise. We supposed that there were events — coming from warmer stages of the cryostat — that were able to reach our detectors. Therefore we painted the cryostat 50-mK shield — the one just surrounding the detectors — with a black painting, in order to reduce the reflection of the radiation in the inner screen hosting the detectors. This intervention has been carried out in Ulisse cryostat before this run with the $LiInSe_2$ and the $Na_2(MoO_3)_4O$ bolometers.

The GeCo2 and Luke2 gain and signal-to-noise ratio has been tested in this new run showing the results reported in Fig 6.23. A comparison between the gain curve slope in this measurement and in the first characterisation shows an improvement of 18 % in case of Luke2 and of 30 % for GeCo2. This result points out the importance that the environment plays on the performance achievable by these devices. The black painting — that cannot be applied on a radio-clean set-up — could be substituted by a photon-tight holder protecting the light detector from wandering radiation.

6.6.2 An alternative calibration with photon statistic

During the run with the $LiInSe_2$ and $Na_2(MoO_3)_4O$ bolometers, we calibrated one of our light detectors with the photon statistic technique described in Ref. [227]. This method exploits the fact that the photons have a Poissonian distribution whose width depends on the number of events. In our case, since a large number of events was collected, the Poissonian distribution was approximated with a Gaussian.

This measurement was performed with the GeCo2 light detector. First of all, its linearity was tested: GeCo2 maintained a linear behaviour for amplitudes below 180 mV as shown in Fig. 6.24 (*top-left*). The NTD sensor was biased with a 5-nA current and the temperature was regulated at 20 mK. The electrode bias was set to 50 V, that corresponded to a gain of around 13 according to Fig. 6.23. The following DAQ settings were selected: dynamic range to $\pm$5 V, the sampling frequency to 10 kHz, the Bessel frequency to 675 Hz and the gain to 1072. A 820-nm LED was employed with an average photon energy of 1.5 eV. We injected a LED pulse with an amplitude of 1 V each 0.5 s. It had been proven in previous studies carried out in CSNSM [151] that the LED energy is linear with the width of the square-pulse driving the LED but not with respect to its amplitude. For this reason, around 3000 pulses were acquired driving the LED with 10 different widths: 20 μs, 18 μs, 15 μs, 13 μs, 10 μs, 7 μs, 5 μs, 3 μs, 1 μs and 0.6 μs. We decided to measure around 3000 pulses in order to have an uncertainty on the Gaussian width of 1.3 %,

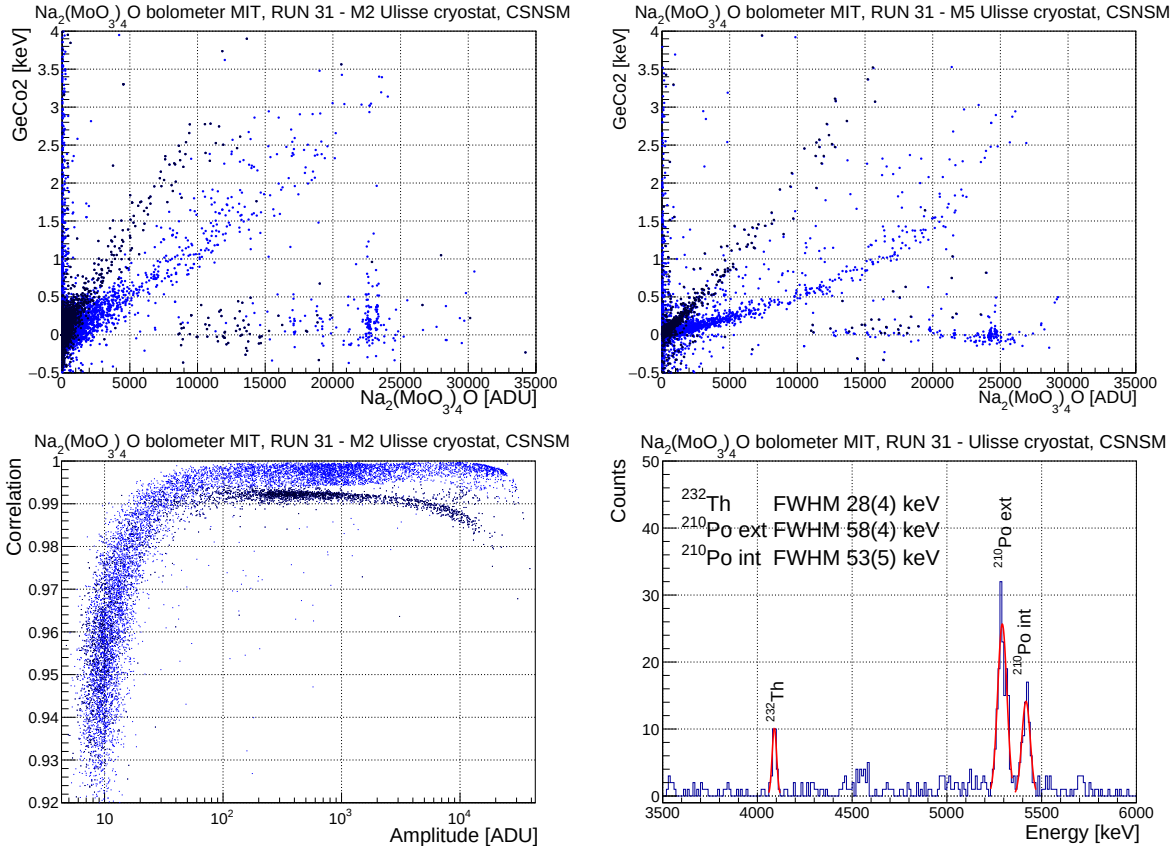

Fig. 6.22: *Top panel*: scatter plot of $Na_2(MoO_3)_4O$ detector coupled to GeCo2 with grounded electrodes (*left*) and at 60 V (*right*). *Bottom panel*: correlation as a function of the energy (*left*) and α spectrum (*right*) of $Na_2(MoO_3)_4O$ detector.

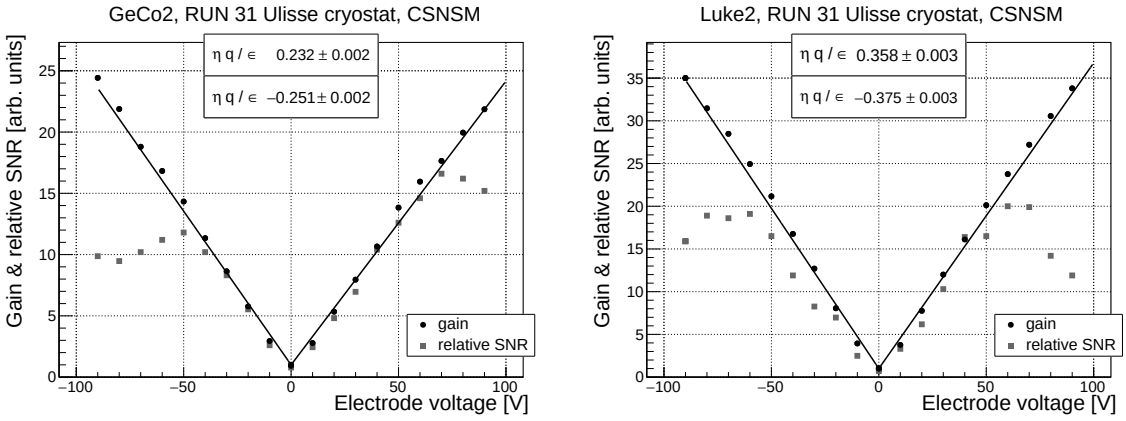

Fig. 6.23: Gain and relative signal-to-noise ratio as a function of the NTL bias for the GeCo2 (*left*) and Luke2 (*right*) light detectors.

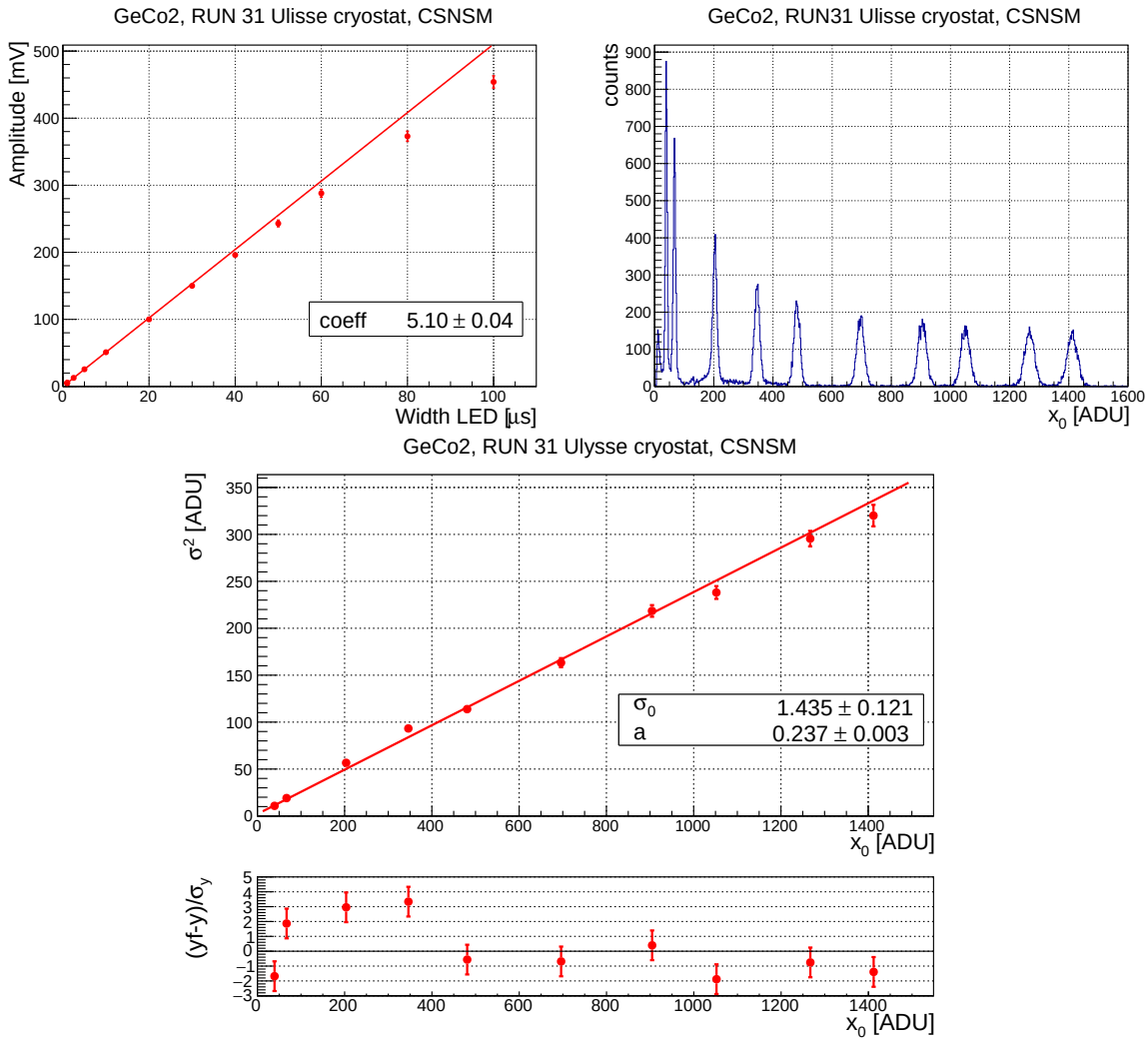

Fig. 6.24: *Top-left panel*: linearity test for the light detector GeCo2. The detector pulse amplitude is illustrated as a function of the width of the square wave driving the LED. *Top-right panel*: histogram of the LED events with 10 different energies. The peak widths are enlarged for higher energies. *Bottom panel*: photon calibration for light detector GeCo2 with 50 V on the electrodes.

in fact its error is given by:

$$d\sigma = \frac{1}{\sqrt{2(N-1)}}. \tag{6.1}$$

By increasing the width of the square pulse driving the LED, we inject pulses with a higher energy. The amplitude of the pulse x_0 is proportional to the the number of photon N injected multiplied by a scaling factor a:

$$x_0 = N\ a. \tag{6.2}$$

The pulses at a given energy are distributed around the mean value with a Poissonian distribution that can be approximated to a Gaussian since a large number of events are considered. Fig. 6.24 (*top-right*) shows the Gaussian peaks acquired: it is possible to see the width enlargement for higher energies. The Gaussian width σ depends on two factors: a contribution is due to the baseline noise σ_0 and the other to the photon statistic σ_{ph}, a larger number of photons widens the width:

$$\sigma^2 = \sigma_0^2 + \sigma_{ph}^2. \tag{6.3}$$

The Poissonian statistics ensures us that the most probable value x_0 is also equal to the variance σ^2, so we can deduce from Eq. (6.2):

$$\sigma_{ph} = a\ \sigma_N = a\sqrt{N} = \sqrt{a\ x_0}. \tag{6.4}$$

Therefore we can write Eq. (6.3) as:

$$\sigma^2 = \sigma_0^2 + ax. \tag{6.5}$$

We fitted the Gaussians distributions in Fig. 6.24 (*top-right*) and we plot the σ^2 of each peak as a function of the x-position of the peak in Fig. 6.24 (*bottom*). The curve was fitted with Eq. (6.5). The energy of the events corresponding to the first peak at 39.39 ADU was produced by 166 photons. Multiplying the number of photon for the energy of one photon we get the energy of the peak, in that case 252 eV. From this information we measure the detector sensitivity, in this case 22 μV/keV with 50-V electrode bias, that divided by the gain (~ 13) gives 1.7 μV/keV for a 820-nm LED. This measurement has been performed only at 50-V-electrode bias.

All the parameters set on the square pulse generator driving the LED were chosen to have the peak with the highest voltage output lower than 180 mV to work in the linear region. Nevertheless, the three points at higher energy are below the fit-line, this suggests the beginning of a non-completely linear region.

The sensitivity of these data has been evaluated also with the muon calibration. The resulting sensitivity is a factor two lower than the one measured with the here-described method. This effect could be explained if we consider that the electron-hole pair production is different for LED and the muon energies (see Sec. 2.7) and that non linearities can be present in the muon energy region (that is located well beyond the last peak used for the photon calibration).

6.7 A few more considerations on the noise

In the case of an aboveground test of the new module geometry for the CUPID-Mo demonstrator, further noise tests were performed on a NTL-assisted light detector: GeCo2A. The new copper holder hosted both the main crystal and the light detector in order to reduce the volume occupied by the detectors in the cryostat. After a short description of the new-module performance, other tests on the noise will be presented. Fig. 6.25 shows the up and bottom view of the new structure. A 209.5-g $Li_2{}^{100}MoO_4$ crystal was used for this measurement. It has been equipped with a NTD sensor and a heater that were glued with Araldite with the Mylar-mask method: the thermistor with six glue spots and the heater with only one. The chips were bonded to copper pins with Ø25-μm gold wires.

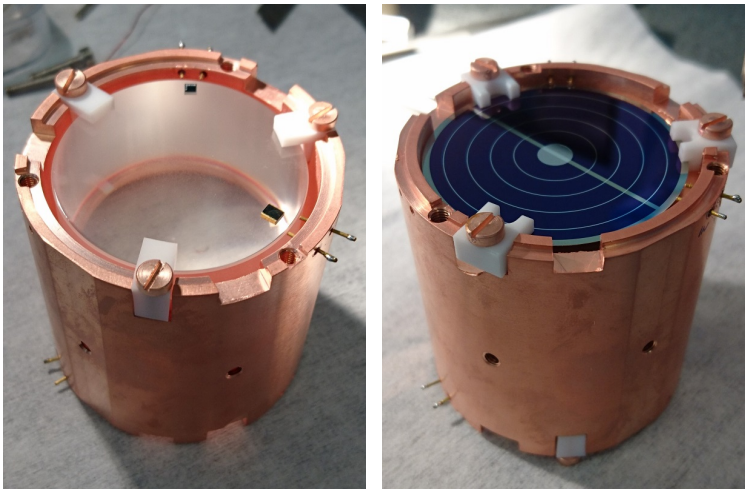

Fig. 6.25: *Left panel*: Enriched $Li_2^{100}MoO_4$ bolometer equipped with a heater and a NTD in the new copper holder. The light detector has been later mounted in the same copper holder on the opposite side. *Right panel*: GeCo2A light detector mounted in the new module for the CUPID-Mo demonstrator. The electrodes are mounted on the side opposite to the main crystal to simplify the bonding phase. This fact does not affect the scintillation-light amplification achievable by the light detector.

At the beginning of the measurement, the gain and the signal-to-noise ratio of GeCo2A were tested for different electrode bias configurations: with a symmetric bias on both electrode sets and with one electrode set grounded. Fig. 6.26 (*top*) shows the gain and the corresponding signal-to-noise ratio as a function of the applied bias on the electrodes. There is no significant difference between the different electrode configurations, but the most favourable one has been selected during the following measurements. Fig. 6.26 (*bottom*) shows the best working condition of the electrodes.

As we have seen in Sec. 6.1, GeCo2A has a reduced-size NTD in order to lower the light detector heat capacity and therefore increase its sensitivity. The NTD mass has been halved acting on the NTD-wafer thickness, that was reduced with a wire saw. Fig. 6.27 (*left*) shows the light detector load curves at different temperatures. Comparing the load curves to the ones in Fig. 6.2, we can see that the NTD mass reduction influences the resistance of around a factor 2.5. Fig. 6.27 (*right*) shows the signal-to-noise ratio as a function of the bias applied on the NTD of GeCo2A. This curve has been used to determine the best working point: the signal-to-noise ratio becomes flat for currents bigger than 0.83 nA, so these working points have been considered equivalent. We decided to work with a resistance around $1-2$ MΩ corresponding to a current range of $2.5-5$ nA at our working temperatures. Two different working point have been selected: 5 nA that has been tested at 0 V, 45 V and 50 V and 2.5 nA that has been measured with 0 V, 30 V and 60 V. Table 6.10 shows some performance obtained by GeCo2A light detector in these configurations. The large improvement in the detector performance between the measurement M5 and M10 is due to the substitution of the batteries used to bias the NTL electrodes. The old batteries were probably introducing some disturbances on the detector that contributed to the noise. It is difficult to strongly affirm it since the two measurements had a slightly different electrode bias, but an improvement of 38 % cannot be due to only a 5-V bias difference on the electrodes.

Since the module had to be installed in the EDELWEISS cryostat just after this test, a ^{55}Fe source was not included in the assembly. The calibration of the light detector has been carried out considering that muons deposit 100 keV at the maximum of the Landau distribution in a germanium wafer of our

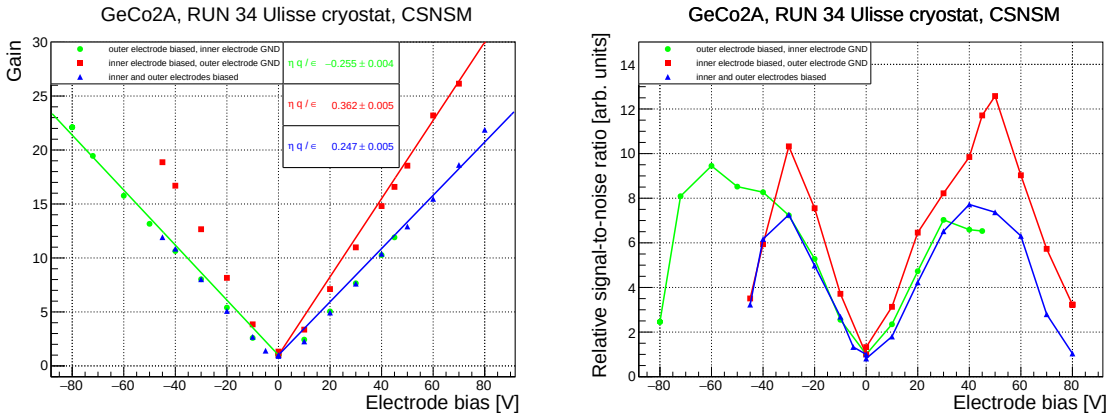

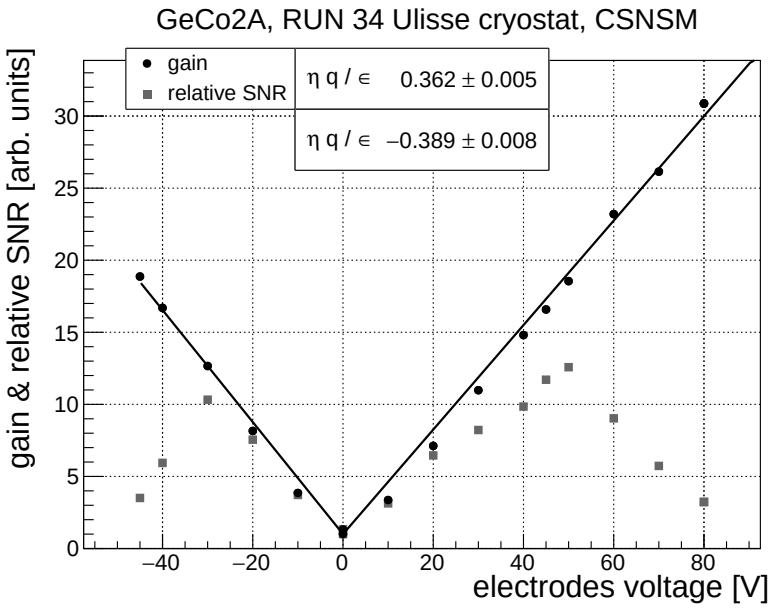

Fig. 6.26: *Top panel*: gain (*left*) and signal-to-noise ratio (*right*) as a function of the NTL bias in different configurations of the electrodes: a symmetric bias was applied to the two sets of electrodes and a combination of a grounded and a biased set. In the case of a symmetric bias, the x axis reports the total bias variation: a ±25 V on the electrodes corresponds to 50 V on the axis and ∓25 V to -50 V. *Bottom panel*: Gain and signal-to-noise ratio as a function of the bias applied on the electrodes in the best configuration.

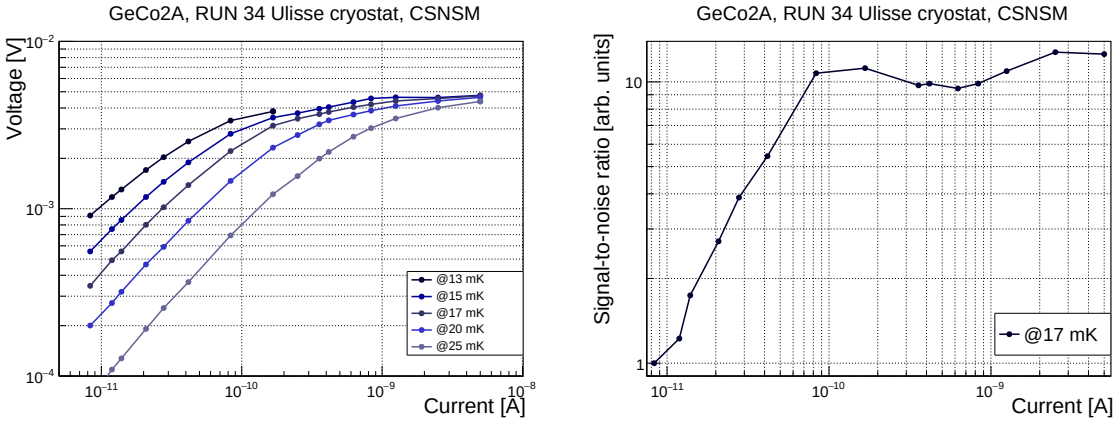

Fig. 6.27: *Left panel*: load curves of GeCo2A light detector at five different temperatures. *Right panel*: signal-to-noise ratio as a function of the current bias at 17 mK.

Tab. 6.10: GeCo2A performance in terms of sensitivity and baseline noise RMS. The light detector was calibrated both with the muon distribution and the scintillation light emitted in correspondence of the ^{6}Li neutron capture. For this reason, the sensitivity and the noise at 0-V electrode bias is omitted in the case of the scintillation light calibration, since they should be equal for construction.

run ID	current [nA]	resistance [MΩ]	T_{base} [mK]	NTL bias [V]	μ's light sensitivity [μV/keV]	μ's light noise RMS [eV]	^{6}Li(n,t)α light sensitivity [μV/keV]	^{6}Li(n,t)α light noise RMS [eV]
M4	5	0.95	17	0	1.1	149	-	-
M5	5	0.95	17	45	12.1	26	12.1	26
M10	5	0.95	17	50	13.4	16	13.0	16
M8	2.5	1.8	15	0	1.5	122.6	-	-
M7	2.5	1.8	15	30	10.8	23.9	11.4	23
M6	2.5	1.8	15	60	20.5	18.4	21.2	17

Tab. 6.11: Enr-$Li_2^{100}MoO_4$ energy resolution performance at 15 mK and a 1.25-nA bias on the NTD corresponding to a 2.2-MΩ resistance.

run ID	^{214}Pb 351.9 keV FWHM	annihilation 511 keV FWHM	^{214}Bi 609.3 keV FWHM	^{214}Bi 1764.5 keV FWHM	^{6}Li(n,t)α 4783 keV FWHM	heater FWHM	noise FWHM
M6-M7-M8	20.0 keV	15.4 keV	17.7 keV	30.7 keV	38.5 keV	58.6 keV	14.0 keV

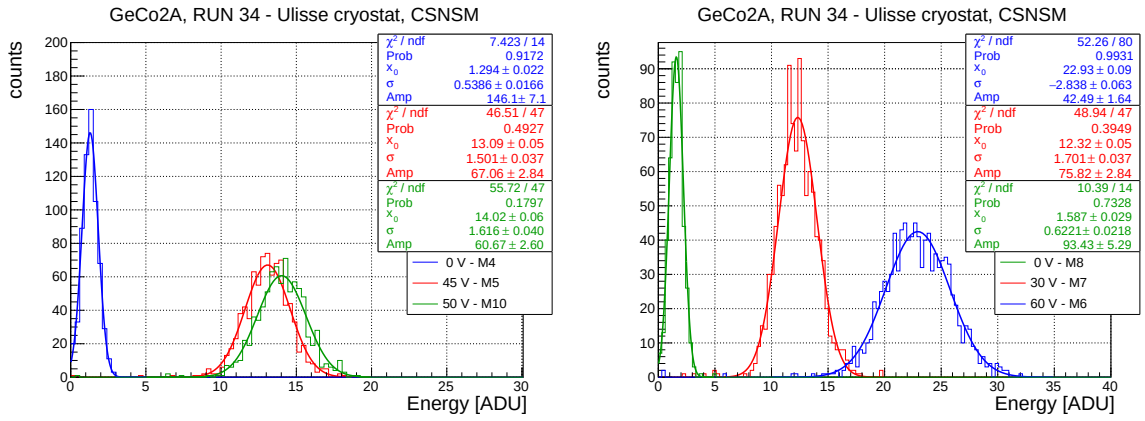

Fig. 6.28: ^{6}Li neutron-capture scintillation-light detected with GeCo2A at different electrode bias: 0 V, 45 V, 50 V (*left*) and 0 V, 30 V, 60 V (*right*), respectively at 17 mK and 15 mK.

thickness. The scintillation light emitted by ^{6}Li neutron capture was calibrated with the muons when the light detector electrodes were grounded. An energy deposition of $\sim$ 300 eV was found in the light detector in correspondence to ^{6}Li neutron capture events. The scintillation light and the muon distributions have been both employed to calibrate when a bias was applied on the light detector electrodes. Fig. 6.28 shows the calibration done with the scintillation light emitted by the ^{6}Li neutron capture for all the measurements considered in this run. The calibration results are summarised in Table 6.10. The two techniques are equivalent as expected from Fig. 2.8, there is not a big difference concerning the quantum efficiency.

The energy resolutions of the $Li_2{}^{100}MoO_4$ bolometer are listed in Table 6.11 and they have been obtained from the fits in Fig. 6.29. The energy resolutions are worst than the ones that can be obtained in an underground set-up because the higher event rate caused by cosmic rays impacts on the pile-up. The fit in Fig. 6.30 has been used to calibrate the β spectra in Fig. 6.31 (*top*). The heat-light scatter plot for the data acquired at 15 mK is reported in Fig. 6.31 (*bottom*). The light detector output has been converted in volt in order to compare the amplification factors on the $\beta(\gamma)$ band for different NTL bias applied on the electrodes. The cloud of green events above the β bands is due to not amplified muons from the 0-V acquisition. These events are shifted at higher energies in presence of the NTL bias in the other two measurements.

We have seen in Sec. 6.2, 6.3 and 6.6.1 that the detector performance strongly depends on the set-up conditions. It seems that a better shielding against warmer-stage radiation improves the detector performance in terms of gain and noise (see also Sec. 6.6.1). In order to understand better this phenomenon, the detector performance was studied in presence of two different constant photon fluxes. The photon fluxes were produced by shining the light detector with a constantly turned-on LED. We repeated the measurement of the gain and the signal-to-noise ratio for GeCo2A with the LED turned off and in the case of a weak and a strong LED photon flux. Fig. 6.32 summarises the data acquired in this measurement: the gain, the signal-to-noise ratio and the working resistance were measured for each NTL bias with the help of a constant LED pulse. The gain progressively decreases in presence of a higher photon flux. The gain reduction is probably due to a change in the detector working point, that is physically heated by the photon flux. At the same time, the signal-to-noise ratio has a progressively smaller improvement for higher photon fluxes, till the point in which it remains constant as a function of the NTL bias.

After these considerations we tried to measure the noise power spectra of the light detector without

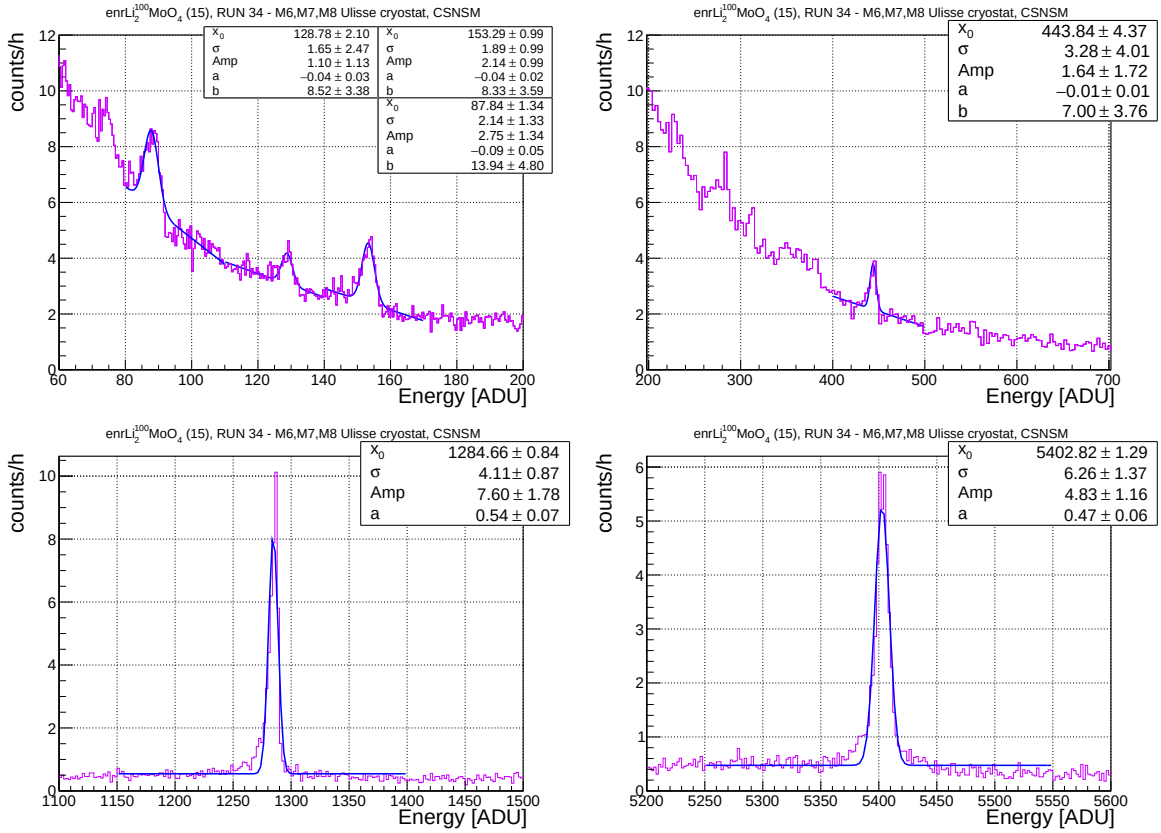

Fig. 6.29: *Top panel*: peaks used to calibrate the β region, the following peaks have been used: ^{214}Pb (351.9 keV), annihilation (511 keV), ^{214}Bi (609.3 keV) (*left*) and ^{214}Bi (1764.5 keV) (*right*). *Bottom panel*: ^{6}Li(n,t)α peak (*left*) and heater events (*right*). This measurement has been acquired at 15 mK with a bias of 1.25 nA on the NTD.

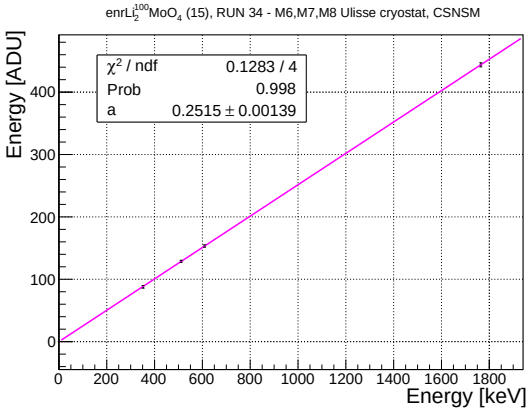

Fig. 6.30: Enr-Li$_2^{100}$MoO$_4$ final calibration, the detector is linear.

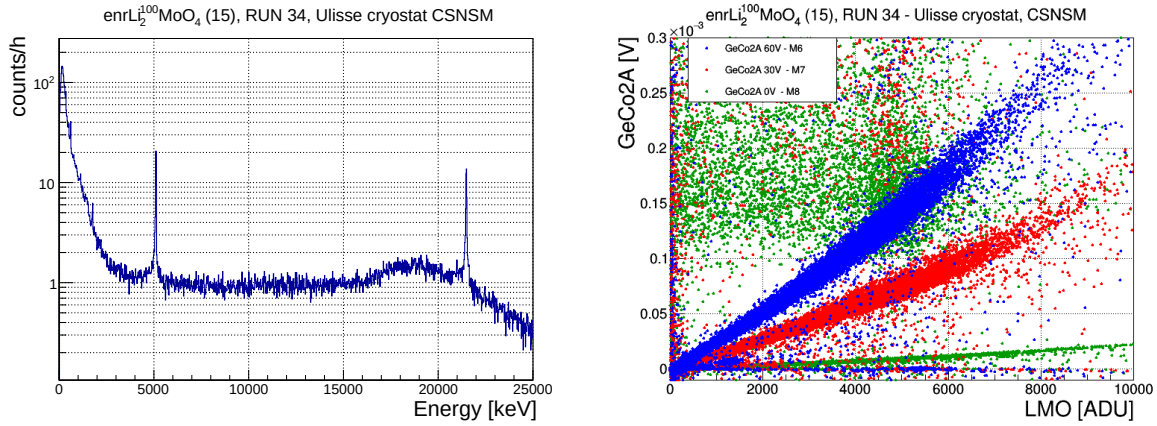

Fig. 6.31: *Left panel*: enr-$Li_2^{100}MoO_4$ energy spectra. *Right panel*: heat-light scatter plot with three different electrode bias: 0 V, 30 V and 60 V.

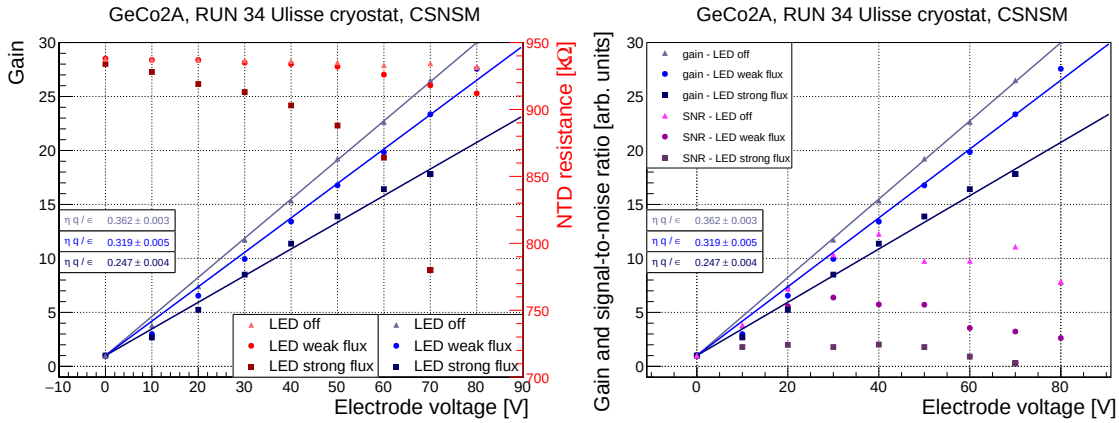

Fig. 6.32: *Left panel*: the gain of GeCo2A has been tested with and without a constant photon flux (*in blue*). For the same points the NTD resistance has been measured (*in red*). *Right panel*: the gain of GeCo2A has been tested with and without a constant photon flux (*in blue*) and for the same points the signal-to-noise ratio is reported (*in violet*).

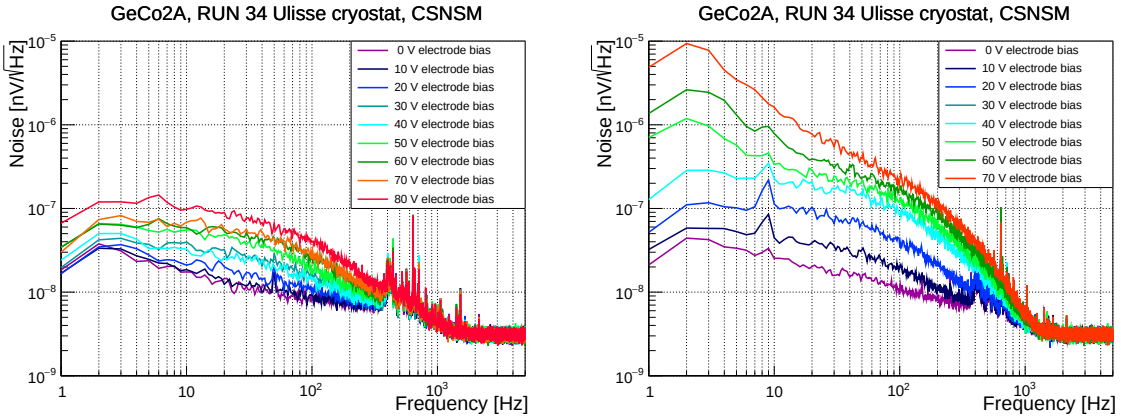

Fig. 6.33: Noise spectra at different electrode bias (*left*) and the same measurement repeated in presence of a constant flux of photons (*right*).

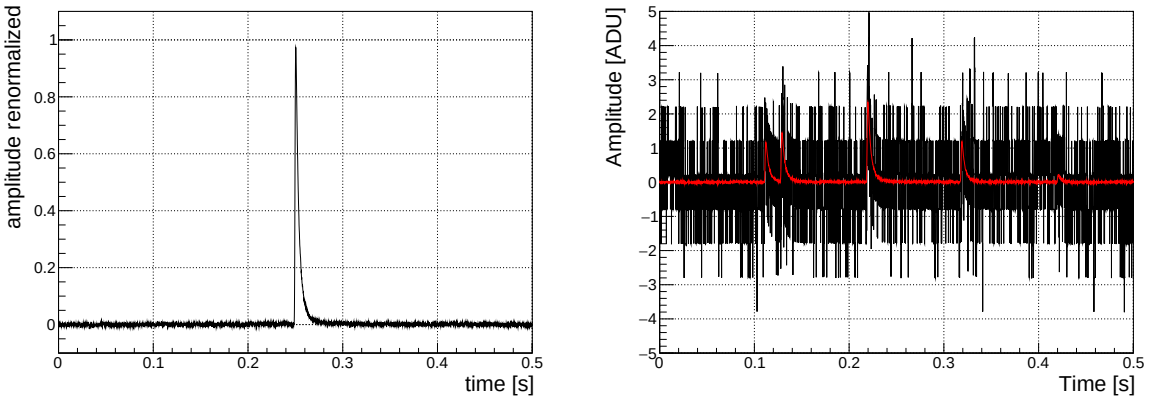

Fig. 6.34: *Left panel*: mean pulse obtained averaging a large number of LED pulses. *Right panel*: noise acquired with grounded electrodes with five mean pulses added in *black*. These pulses have been plotted over the noise in *red* to help their identification.

and with a constant photon flux. Fig. 6.33 shows the noise spectra of the light detector that have been measured at different electrode bias with and without a constant photon flux, imitating a parasitic flux of photons from warmer stages of the cryostat. The noise increases in presence of a constant flux of photons and this noise populates the low-frequency region where the signals develop.

Some simulations have been performed in order to test this hypothesis. The idea was to verify how the baseline noise with grounded electrodes would have changed by adding pulses and if this could explain the noise worsening in the NTL regime. We expected to find that the noise worsening for higher NTL bias can be reproduced by injecting pulses with a higher amplitude keeping their rate constant. Real noise baselines — acquired with grounded electrodes for the measurement reported in Fig. 6.33 — were employed in the simulation. Mean pulses were added to these baselines in order to mimic the presence of hidden events. The mean pulse was averaged from real LED events detected by the light detector with no bias on the electrodes in Fig. 6.34 (*left*). 400 simulations have been considered where two parameters were varied: the number of events in the baseline and the maximum amplitude that pulses can assume. Each event had a random amplitude that was always lower than the maximum amplitude imposed in the simulation: we do not expect monochromatic photons. Obviously also the pulse position was randomised in the window. Fig. 6.34 (*right*) presents an example of mean pulses added to a real noise baseline. 5000 baselines with extra events were produced in each simulation and their noise power spectrum was calculated. The noise power spectra have been compared with the ones in Fig. 6.33 performing a simplified chi-square test:

$$\chi^2 = \sum_{i=0}^{N} (S_i^{sim} - S_i^{real})^2, \tag{6.6}$$

where S^{sim} and S^{real} are respectively the simulated noise spectra and the real one, and N is the number of points in the noise power spectrum. The χ^2 values as a function of the different maximum amplitudes and event numbers is shown in Fig. 6.35 (*top*). The χ^2 does not have a defined minimum, it has a valley of minima. In any case, we searched for the minimum χ^2 and we compared its noise power spectra with the one of measured data. Fig. 6.35 (*bottom*) reports the result for a few examples, showing a good agreement between the measurement and the simulation. Against our expectations, the minima was not always in correspondence of fixed event number. This is a symptom that additional and deeper studies should be undertaken. However, this simulation showed that the noise shape measured at higher NTD voltage can be reproduced by injecting events in the baseline. The result of this test suggests that the

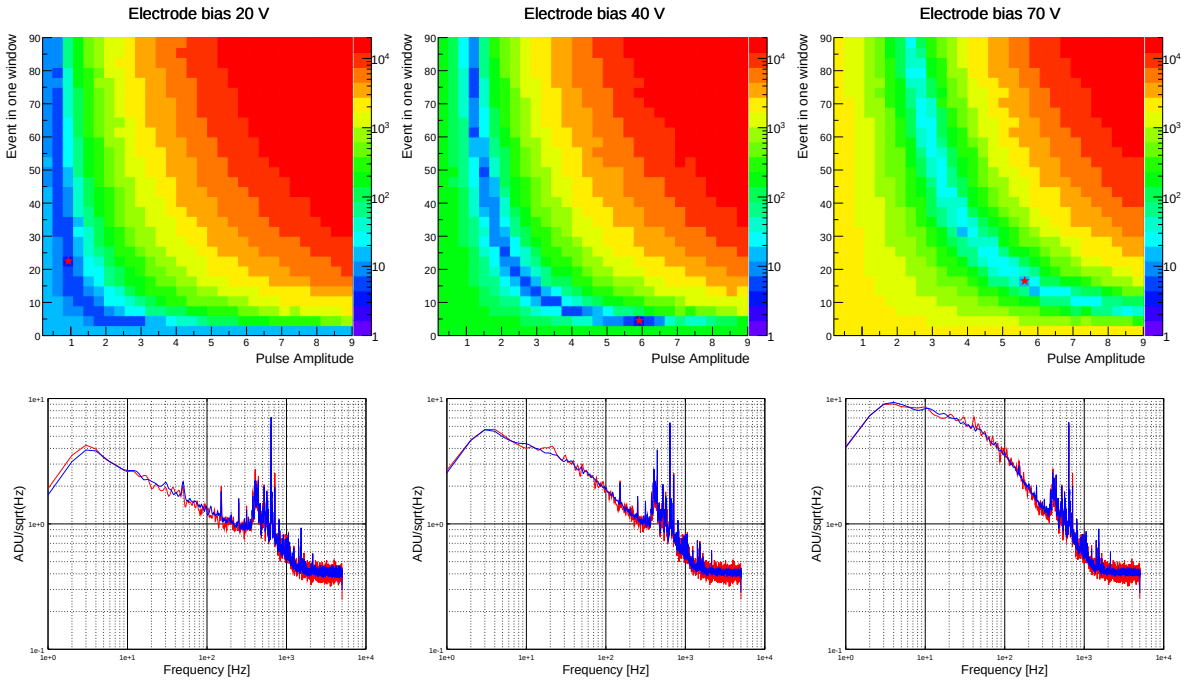

Fig. 6.35: *Top panel*: two-dimension χ^2 distributions as a function of the number of events added to the noise and their maximum amplitude. The χ^2 plot of the simulations compared with the data at 20 V, 40 V and 70 V is shown as an example. The *red star* indicates the minimum χ^2 identified, unluckily it was not always in correspondence to a similar number of events. *Bottom panel*: comparison between the measured noise spectra (*blue*) and the simulated ones (*red*) corresponding to the plots reported in the *top panel*. All this analysis has been performed considering the noises in ADU without converting it to volt.

increase can be originated by photons leaking from warmer stages of the cryostat.

7 High-impedance TES detectors

High-performance light detectors are needed for the α-background rejection exploiting the Cherenkov light emission of TeO_2 bolometers. Different technologies have been investigated as reported in Sec. 4.2. In this framework and according to the R&D program of LUMINEU, another kind of light detector sensors was studied during this work: high-impedance NbSi TES. These devices are interesting because of their normal state resistance of the order of 100 kΩ – 5 MΩ. As a consequence, their read-out could be performed with the same electronics used by the CUORE experiment without the need to implement a more complicated read-out system based on SQUIDs. This technology is still at an initial stage but the results are interesting. This chapter presents the performance obtained in two tests. The first measurement is reported in Sec. 7.1: a NbSi TES deposited on a germanium support has been glued to a NTL-assisted light detector. The second measurement in Sec. 7.2 has been done with a large-area NbSi TES directly deposited on a silicon substrate.

7.1 Test of a NbSi TES deposited on a germanium carrier

A batch of NbSi meanders — characterised by a length of 14.8 mm, a width of 18 μm and a thickness of 50 nm — have been deposited on a Ø44 × 0.17-mm germanium wafer. They had a niobium percentage of 13.3 %, that with the film thickness contributes to establish a defined critical temperature as discussed in Sec. 2.3. Fig. 7.1 (*left*) shows a picture of the meander geometry used for the sensors. Some non-uniformities in the deposition were expected for the sensors on the wafer edge since the surface of the deposition was quite large. For this reason, ten TESs have been selected in different position of the wafer to test their response. A part of them have been annealed at different temperatures for 1 hour in order to lower their transition temperature and operate them at temperatures of the order of 20 mK. The ten sensors were mounted on the sample holder in Fig. 7.1 (*right*) and characterised in the Mulet Modane cryostat, a description of the set-up can be found in Ref. [151]. The transition of three sensors biased by 100 μV is presented in Fig. 7.2 (*left*) as an example. Two of them belonged to the center of the wafer and one was selected closer to the border. The curves of the TESs close to the center have a sharp transition. One of the two samples — characterised by a lower transition temperature — was annealed at 90 °C while the other one was not. The transition of the TES taken from the wafer side is not sharp as the other ones and is characterised by a higher transition temperature even if it was annealed at 120 °C. This is due to the fact that its transition temperature results from a combination of several film sections featuring different critical temperatures because of a non-uniform NbSi deposition. The same samples were measured also with a 200-μV bias to check the presence of transition shifts due to sensor over-heating, but the transition was found in the same position showing the absence of over-heating effects in our characterisation.

The central sensor — characterised by a transition at around 42 mK — was selected to be mounted on GeCo3, a NTL-assisted light detector presented in Sec. 6.1. We decided to install the sensor on a well-performing light detector in order to compare the performance of the two technologies. Refer

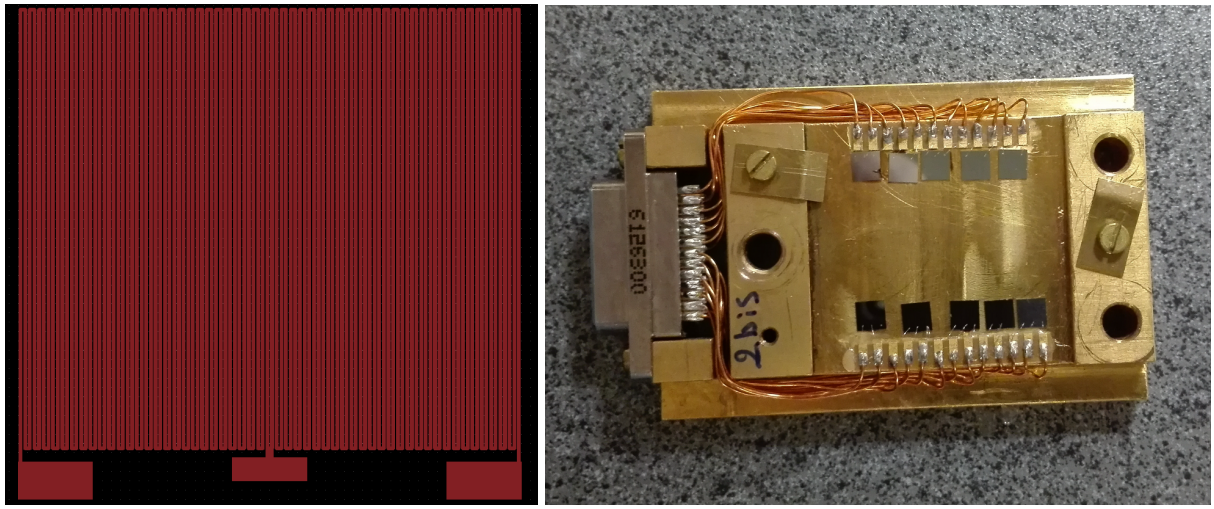

Fig. 7.1: *Left panel*: geometry used for the production of the NbSi sensor batch here discussed. *Right panel*: photograph of the ten sensors glued on a sample holder with varnish before their preliminary characterisation.

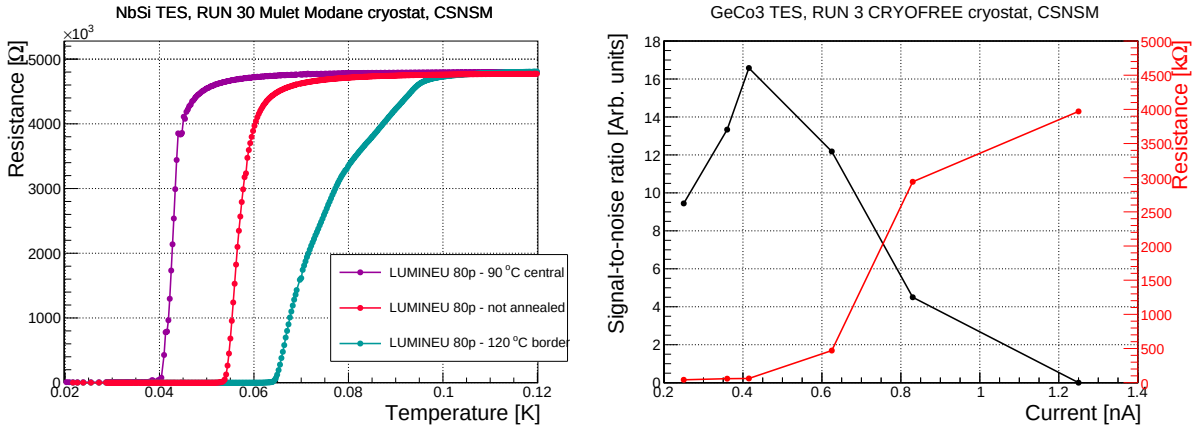

Fig. 7.2: *Left panel*: TES superconductive transitions of three NbSi samples. *Right panel*: signal-to-noise ratio and resistance as a function of the bias current for the TES glued on GeCo3.

Tab. 7.1: Performance obtained by the NTD and the TES glued on GeCo3 during a couple of measurements.

sensor	NTD		TES	
run ID	M1	M3	M1	M3
current [nA]	5	1.25	0.42	0.42
resistance [kΩ]	~ 410	693	129	129
sensitivity [μV/keV]	0.38	0.27	0.2	0.074
noise RMS [keV]	0.26	0.46	1.8	1.4
RMS X-ray ^{55}Mn, 5.9 keV [keV]	0.42	0.56	2.2	1.6

to Fig. 6.1 for a photograph of GeCo3 equipped with the NbSi TES. This sensor was glued with an Araldite film corresponding to an amount of glue equivalent to nine spots. The NbSi TES was bonded with Ø25-μm aluminium wire. The light detector was equipped with a ^{55}Fe source and was illuminated with an optical fibre, that was operated with a room temperature 950-nm LED. GeCo3 was tested in the CRYOFREE cryostat, a description of the set-up is present in Sec. 3.1.4. At the beginning of the measurement, the best signal-to-noise-ratio working point was identified at 0.4 pA in Fig. 7.2. The TES had a resistance of 129 kΩ in the best working point: it was operated at the foot of the transition curve.

Fig. 7.3 (*top-left*) shows the comparison of the same 120-keV event measured by the TES and the NTD sensor. The NTD thermistor is characterised by a better signal-to-noise ratio — given by both a higher amplitude and a lower noise — and a faster decay time. We tried to compare the noise power spectra of the two sensors and we found a higher noise on the TES in Fig. 7.3 (*top-right*), whose origin is not understood yet. It could be due to something intrinsic in the sensor but it could be also due to a more noisy cabling line. The origin of the longer decay time of the TES pulses was also investigated. We have seen in Sec. 2.5 that NTDs are characterised by a negative electro-thermal feedback that tends to shorten the pulse decay time for higher bias. A similar effect is also present in the TESs but we speak about positive electro-thermal feedback in this case. In fact the derivative of the resistance with respect to the temperature is positive and tends to extend the decay time for higher biases (see Sec. 2.5). Fig. 7.3 (*bottom-left*) shows the decay time for three different biases (41 pA, 250 pA and 400 pA). The influence of the bias on the decay time is negligible for bias below 250 nA. After these considerations, we concluded that probably the long decay time was due to the thermal configuration of the detector. The heat evacuation from the germanium support hosting the TES is mainly done through the NTD gold bonding wire, since the TES bonding is done with aluminium wires. A thermal link would be needed also in the TES germanium support or, even better, the NbSi sensor should be deposited directly on the light detector substrate. Considering the average of many pulses in order to reduce the noise, it is possible to notice the hint of an athermal component on the top of the pulse in Fig. 7.3 (*bottom-right*). TES are usually sensitive to athermal phonons contrary to the NTD that should be only sensitive to thermal signals in theory. We can only speak about a hint because the extra peak is practically hidden in the noise: it appears after the average of many pulses. The athermal component is negligible with respect to the thermal one probably because of the glue-interface presence between the light detector and the TES support.

We acquired a few measurements operating both sensors, the performance are reported in Table 7.1. The cryostat temperature was regulated in order to have the TES at the best working point of its transition. Consequently, the NTD working point was not optimised and its performance are poorer than the usual ones. In any case, the results obtained by the TES were even worse than the NTD ones. A simple trigger on the TES was not sufficient to extract the ^{55}Mn X-ray line because of the high noise. In order to extract the information about this line, TES data were triggered with the NTD trigger file. Fig. 7.4

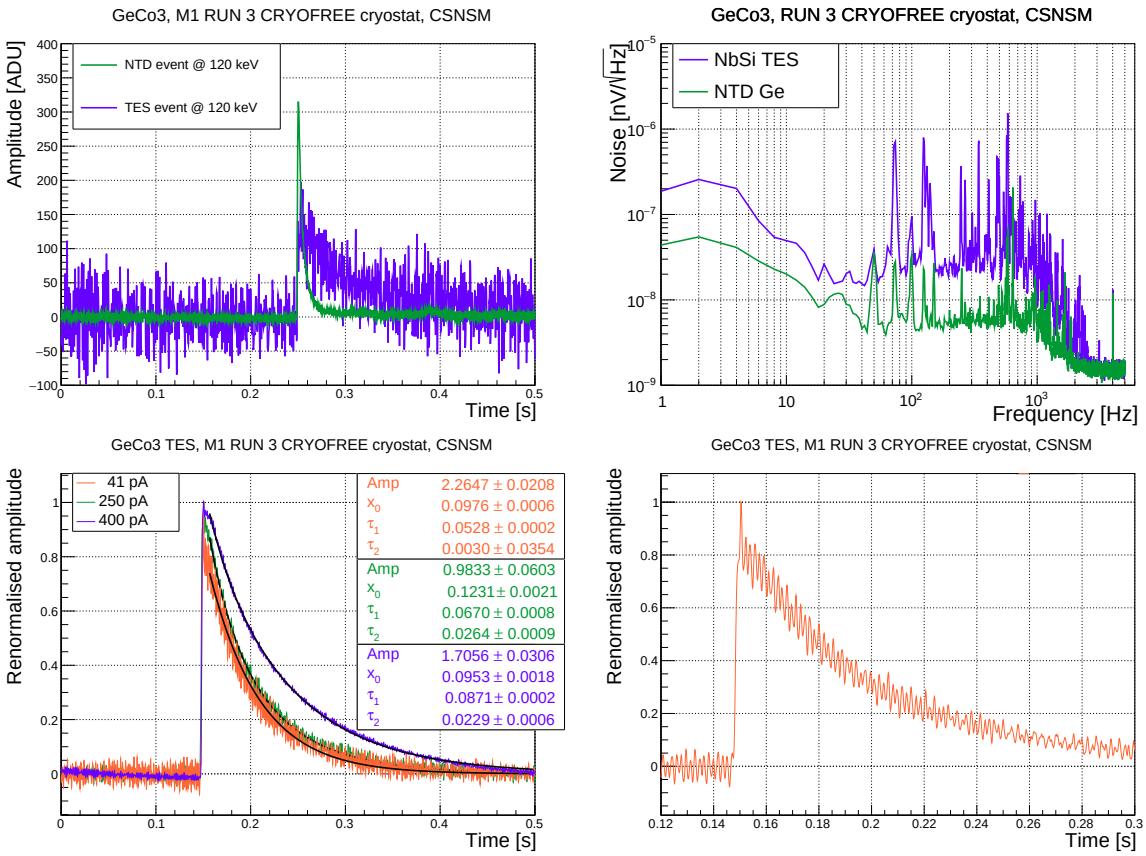

Fig. 7.3: *Top-left panel*: comparison between a NTD and a TES pulse corresponding to an energy of 120 keV. *Top-right panel*: NTD and TES noise power spectra comparison. *Bottom-left panel*: comparison between three mean pulses acquired at three different biases. The decay time increases for higher current bias because of the positive electro-thermal feedback. *Bottom-right panel*: mean pulse acquires with a 41-pA bias. It shows a hint of the athermal phonon presence as an extra small peak on the top of the pulse.

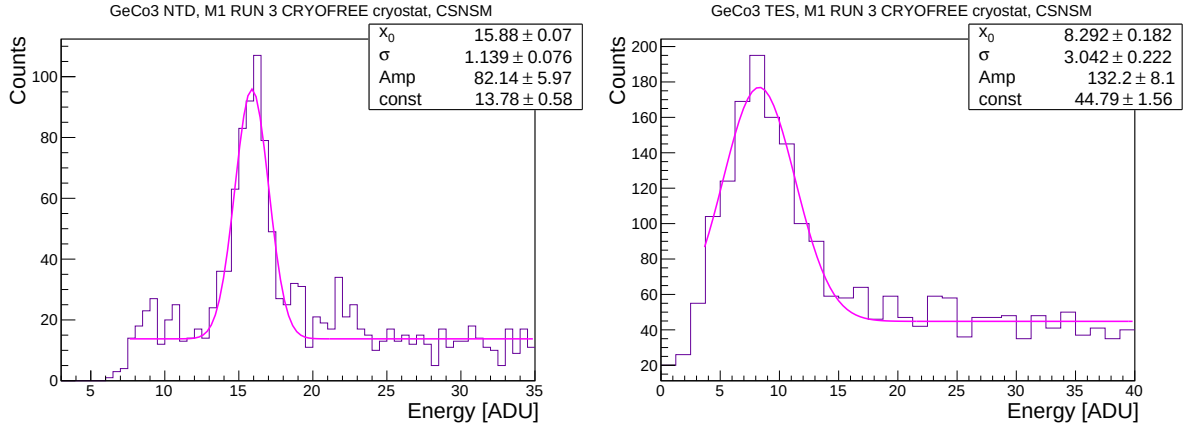

Fig. 7.4: ^{55}Mn X-ray line used for the detector calibration for the NTD (*left*) and for the TES (*right*). The line has been extracted from the TES data thanks to a trigger performed with the NTD.

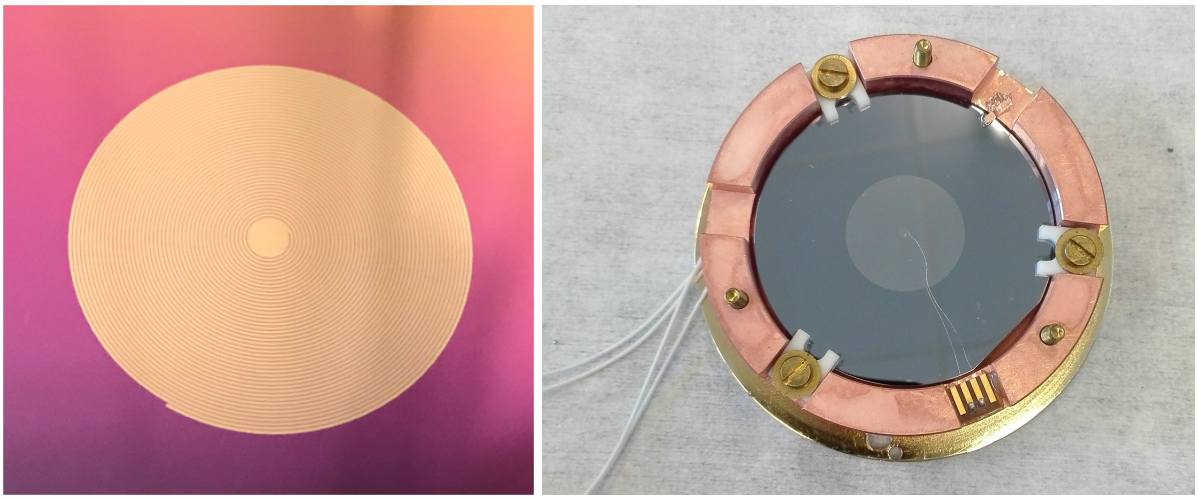

Fig. 7.5: *Left panel*: photograph of the spiral NbSi meander. *Right panel*: photograph of the complete light detector.

shows the ^{55}Mn X-ray line measured with the NTD and the TES. In order to improve the results here obtained the TES thermal evacuation has to be improved or the sensor should be directly deposited on the detector absorber.

7.2 Test of a large-area NbSi TES

The measurement of a larger-area NbSi sample directly deposited on a light detector absorber is here presented. The NbSi TES had a thickness of 500 Å and a niobium percentage corresponding to 13.20 %. These two parameters contribute to the definition of the TES transition temperature as presented in Sec. 2.3. This TES has been directly deposited on a silicon wafer with the size Ø50.8 × 0.2 mm. The absorber was mounted in a light detector copper casing and hold by three PTFE clamps. The TES was bonded with Ø25-μm aluminium wire to the Kapton pads placed on the holder. Considering the issues of the previous measurement with the long decay time, a good thermal leak has been made with a small copper strip glued between the silicon wafer and the copper holder. The gluing has been done with Araldite glue. Usually the thermal leak passes through the gold bonding wire that in this case were not present. Fig. 7.5 presents the new sensor geometry and its final mounting. The light detector was equipped with a ^{55}Fe source for the calibration and an optical fibre shining the light of a 820-nm LED.

Before acquiring data, we spanned the temperatures close to the transition temperature in order to search for the best working point. In this process, we acquired the detector temperature, its resistance and the amplitude of a LED pulse. This procedure has been repeated at different bias currents. Fig. 7.6 (*top*) shows the LED-pulse amplitude as a function of the cryostat base temperature for different bias currents. The detector sensitivity increases with the bias applied. At the same time, the best working point is concentrated in a smaller temperature span as soon as the current bias increases. A very precise temperature regulation is needed in order to operate the detector always in the same working point. The maximum amplitude of the data acquired with 25 nA (*in black*) was in such a small interval of temperatures that the slow cool-down employed to map the transition prevented us from sampling the center of the transition. The curves maximum moves to lower temperatures for higher bias, this effect is due to the detector over-heating induced by the bias. This effect is also clear in Fig. 7.6 (*bottom-left*), where the

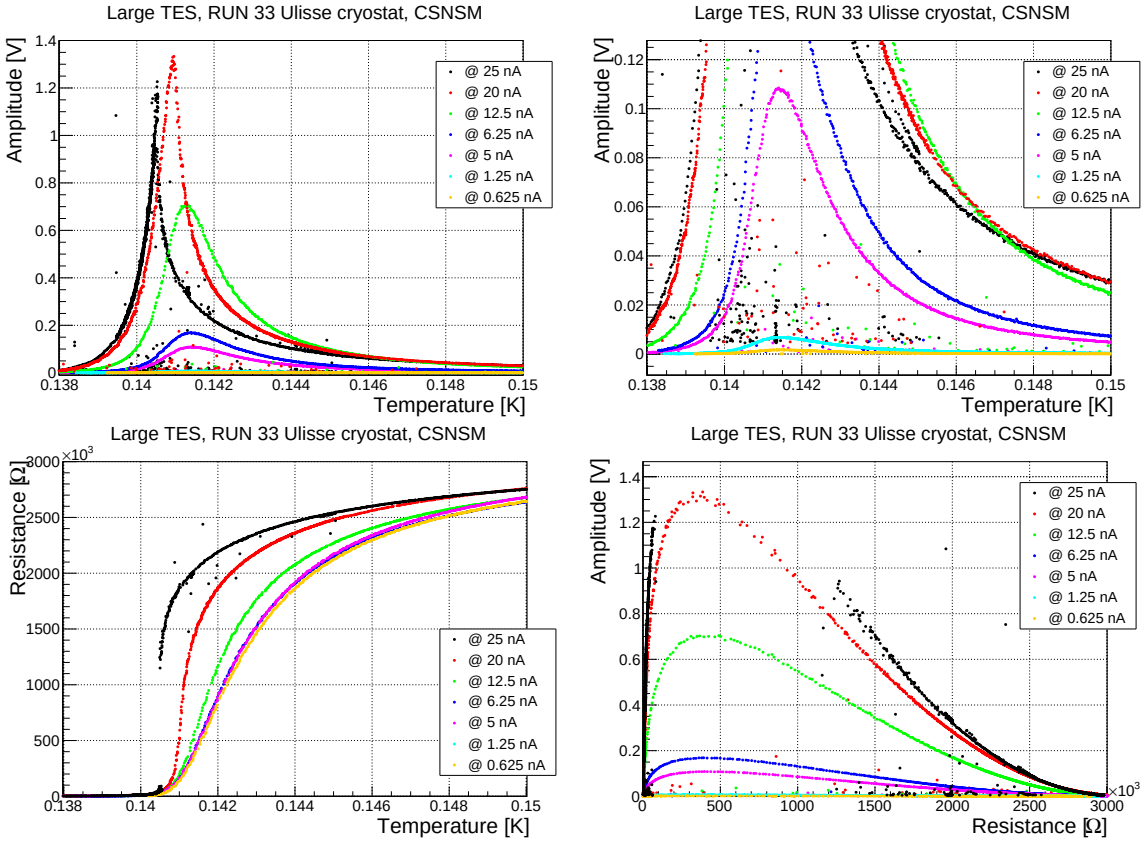

Fig. 7.6: *Top panel*: the amplitude of the same LED pulse as a function of the mixing chamber temperature for different bias currents applied on the TES (*left*) and its zoom for low amplitudes (*right*). *Bottom panel*: TES superconductive transitions for different bias currents applied on the sensor (*left*). The LED amplitude as a function of the TES resistance for different bias currents applied on the sensor (*right*).

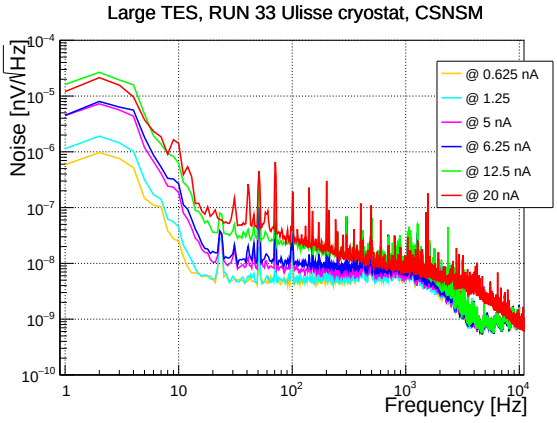

Fig. 7.7: Noise in the optimal working point acquired at different current biases.

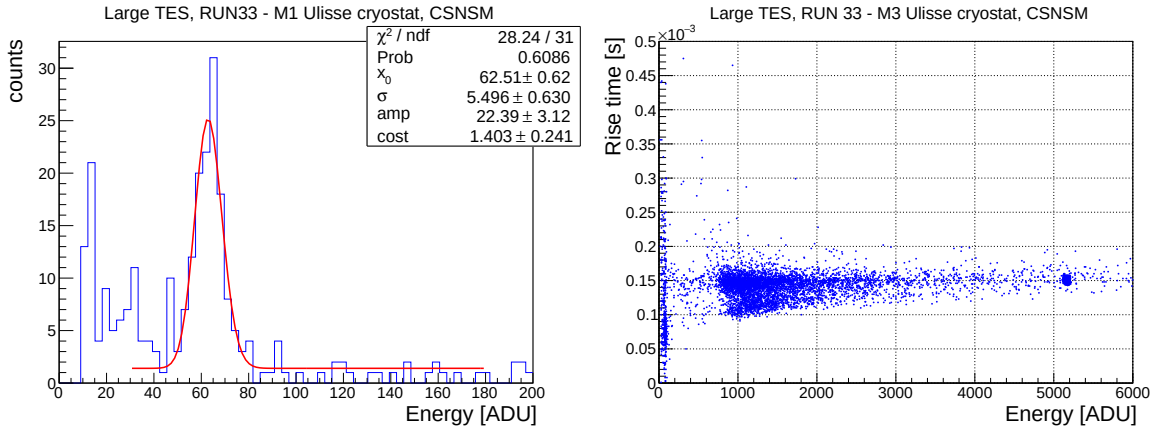

Fig. 7.8: *Left panel*: ^{55}Fe calibration peak measured by the large TES detector. *Right panel*: rise time as a function of the energy. There is a hint of the presence of two populations with different rise time. We suspect that it is an analysis artefact due to a difficult determination of the pulse starting point.

TES transitions are presented. In fact, the TES is not heated by bias up to 6.25 nA and all the transition curves lay one over the others. With 12.5 nA and higher bias, the TES is heated up and this temperature increase induces an apparent lowering of the sensor transition temperature. The transition temperature of the sensor is around 140 mK. This sensor reaches a resistance of around 3 MΩ at the normal state. We did not measure the 0-Ω resistance in the super-conductive state because this measurement has been performed with only two wires. Therefore we were able to measure the cryostat wiring resistance when the TES was in the superconducting state. Fig. 7.6 (*bottom-right*) shows the LED-pulse amplitude as a function of the resistance. The resistance of the device around the best working point is of the order of 400 kΩ, placing the operational point around the foot of the transition. These measurements have been performed with the semi-vintage electronics when the bias currents was below 20 nA, the other two bias (20 nA and 25 nA) were provided by an older front-end card. In Fig. 7.6, some points do not belong to the curves and populate the area below the measured points. They are due to not-LED event (as muons events) that appeared during the baseline acquisition and were not cut during the analysis.

During the measurements we noticed a noise increase for higher bias, this issue was investigated acquiring a few minutes of stream data. The obtained noise spectra for different bias conditions are reported in Fig. 7.7. The noise at low frequencies increases for bias above 1 nA on the TES. Except the noise at 20 nA that has been measured with the old electronic module, all the others have been measured with the semi-vintage electronics. This results clear from the roll-off frequency: the noise measured with the semi-vintage electronics has a cut frequency at the Bessel frequency (675 Hz), the other is filtered after 1 kHz. We were not able to stabilize the sensor in its best working point at 25 nA as it is visible from Fig. 7.6, so we decided to not acquire its spectra.

A few measurements have been acquired with different current biases. Table 7.2 illustrates the performances of the light detector for the analysed ones. It results evident that with the increase of the bias the sensitivity improves but at the same time the noise worsen. Three measurements were acquired with a bias of 12.5 nA but at slightly different temperatures: the sensitivity is strongly influenced by the working temperature. Fig. 7.8 (*left*) shows the ^{55}Fe peak of a two-hour-long measurement.

Usually we acquire data with a Bessel filter of 675 Hz for light detectors because they are characterized by fast pulses. In this case the detector was faster than an usual light detector, so we had to remove the Bessel filter in order to measure its real rise time. We substituted the Bessel filter with a Stanford amplifier, setting a low-pass filter at 10 kHz with a 6-dB attenuation. The acquisition has

Tab. 7.2: Detector performance listed for increasing biases.

ID run	bias [nA]	temperature [mK]	sensitivity [μV/keV]	noise RMS [eV]	RMS X-ray ^{55}Mn 5.9 keV [eV]
M11	5	141.4	0.474	393	566
M7	8.33	141.47	0.980	326	495
M1	12.5	140.4	1.51	235	519
M3	12.5	141.5	1.93	233	710
M8	12.5	141.2	1.36	226	984
M10	20	140.96	3.81	273	708
M5	25	140.7	4.27	173	476

been performed at 50 kHz, with a gain of 1072 and a dynamic range of $\pm$5 V. We biased the sensor with 12.5 nA and we regulated the cryostat temperature at 141.5 mK to keep the detector in its best working point. Fig. 7.8 (*right*) shows the rise time as a function of the amplitude acquired in these conditions: this detector presented an average rise time of 150 μs. In this plot we can distinguish the ^{55}Fe peak below 100 ADU, the cosmic rays bumps around 1500 ADU and the LED peak above 5000 ADU.

This device obtained amazing sensitivity performance considering its working temperature around 140 mK. The silicon absorber should be equipped with a heater in order to employ this detector at base-cryostat temperatures of the order of 20 mK, more proper for standard bolometric operations. Otherwise this device should be annealed in order to lower its transition temperature and operate it at lower temperatures. This technology is still at an initial stage but the performance achieved demonstrates that the R&D studies are worthwhile.

8 Conclusions and perspectives

CUORE is the first tonne-scale bolometric experiment. It searches for the neutrinoless double-β decay of ^{130}Te. Its detector is constituted by 988 TeO_2 bolometers with a size of $5 \times 5 \times 5$ cm. This work aimed at the study of its sensitivity enhancement in view of a possible upgrade: the CUPID experiment. This target has been pursued with two parallel studies: the reduction of the CUORE dominant background — degraded-energy α events close to the detector surfaces — thanks to the Cherenkov light tagging and the study of the thermal model of the single CUORE module with two dedicated experimental measurements.

The core of this work consists in the demonstration that we have developed a technology capable to reject the α background (at the level of 10^3 keeping a very high signal acceptance) for a possible CUORE upgrade based on TeO_2 bolometers. This result was obtained thanks to NTD-based light detectors enhanced by the Neganov-Trofimov-Luke (NTL) effect, that have been developed in CSNSM. During this work, these detectors have been tested in different environments and conditions, both in aboveground and underground facilities. The aboveground tests have been used to assess the performance of all the studied devices. They showed similar performance in terms of sensitivity (~ 0.9 μV/keV), resolution at the 5.9-keV X-ray line of ^{55}Mn (~ 300 eV RMS) and gain in the NTL regime (~ 13 at 50 V), demonstrating that the technology is mature and the results are reproducible.

Two underground measurements have been carried out coupling these devices to TeO_2 bolometers to test their performance concerning the α-background rejection. The first underground measurement was performed at the Laboratori Nazionali del Gran Sasso (Italy). Two NTL-assisted light detectors have been tested with two 435-g enriched $^{130}TeO_2$ bolometers. The two $^{130}TeO_2$ bolometers showed good bolometric performance (4.3 and 6.5 keV FWHM at the 2615-keV γ quanta of ^{208}Tl) and a high radiopurity (^{228}Th and ^{226}Ra < 3.1 μBq/kg). The light detectors were operated in NTL regime obtaining a baseline noise of 25 and 35 eV respectively with a bias of 55 and 25 V. The α-background tagging capability was proved in this measurement: a $\beta(\gamma)$-event acceptance of 78.8 % and 98.3 % was achieved with an α rejection of 99.9 %. This measurement demonstrated that the technology needed by a tellurium-based CUPID experiment can be based — with very good prospects — on NTD-equipped germanium light detectors with NTL amplification. A second underground measurement was carried out in the Laboratoire Souterrain de Modane (France). A NTL-enhanced light detector was coupled to a CUORE-size TeO_2 bolometer, that was characterized by a lower light yield with respect to the previous two because of its larger mass (784 g). The light detector reached a baseline noise of 10 eV and a gain of 12.7 in the NTL regime with a bias of 60 V. This high performance permitted the acceptance of 96 % of $\beta(\gamma)$ signals with the rejection of 99.9 % of α events. The complete separation between α and $\beta(\gamma)$ events has been obtained for the first time with a TeO_2 bolometer as the ones used by the CUORE experiment. We demonstrated that the α background could be reduced by a factor 10^3 by adding NTL-boosted light detectors keeping the present configuration of CUORE.

The improved signal-to-noise ratio and low threshold of these devices in the NTL regime can be exploited also for other applications, as for example, the pile-up rejection in detectors characterised by a high event rate. For this purpose a NTL-assisted light detector was coupled to a 10.3-g $LiInSe_2$ bolometer.

This detector was interesting for the β decay of ^{115}In, whose shape at low energies can constrain the axial coupling constant g_A. The difficulty of this measurement consisted in the high event rate ($\sim$ 1 Hz) and the consequent high pile up, that modified the energy-spectrum shape. The improved signal-to-noise ratio and faster signals of the light channel allowed us to recover a larger number of events at low energies.

Another application of these devices is the improvement of the light collection in set-ups characterised by a poor light yield. The light collection can be enhanced thanks to the amplification achievable by these photo-bolometers. A 1.6-g $Na_2(MoO_3)_4O$ bolometer has been tested as a possible compound for a $0\nu2\beta$ next-generation experiment. The sample was so tiny that the NTD sensor on its top was reducing the light collection. We have shown that a better discrimination can be achieved exploiting the NTL amplification.

Also another kind of light detectors — equipped with a different temperature sensor based on high-resistance NbSi TES — has been investigated in this work. The measurement of the first large surface TES directly deposited on the main absorber presented good performance: a sensitivity of 4.3 μV/keV was achieved with a baseline noise of 173 eV RMS and a risetime of 150 μs. The drawback of this device was its high transition temperature ($\sim$ 140 mK). This device could be interesting for the pile up rejection thanks to its high sensitivity and fast signals, but a lower transition temperature would be indispensable to be compatible with the bolometric applications described in this work. Its baseline noise do not make it a good candidate for the detection of the tiny-Cherenkov-light signal produced by TeO_2 bolometers. New R&D studies are needed.

Furthermore, a more technical study on the CUORE-detector thermal model has been carried out with two cryogenic measurements. Two thermal parameters have been measured in a CUORE-like set-up: the glue and the electron-phonon conductances. In the first measurement, an electron-phonon conductance $G_{el-ph} = 0.74\ T[K]^{5.5}$ [W/(K mm^3)] was found. Concerning the glue conductance, we encountered an unexpected issue: its value was not scaling with the surface of the glue. We supposed that this was due to our gluing technique: the process was not reproducible. Therefore, a second measurement was performed changing the gluing technique. This time, the glue conductance results were coherent and consistent: $G_{glue} = 1.2(5) \times 10^{-3}\ T[K]^{3.1(1)}$ [W/(K mm^2)]. The electron-phonon conductance was measured again obtaining: $G_{el-ph} = 1.44\ T[K]^{5.3}$ [W/(K mm^3)]. There is a discrepancy between the electron-phonon conductance measured in the first and the second measurement that cannot be explained with the systematic errors evaluated in this work. But both measurement demonstrated an internal coherence and self consistence. We did not find any good reason to reject and exclude one of the two measurement from this work. The discrepancy in the electron-phonon-conductance measurement — supported also by the spread on the parameter reported in literature — reveals the intrinsic difficulty of this measurement. The systematics — due to the absolute temperature measurement and parasitic powers — are not completely understood. This measurements showed that the conductance exponent is not significantly sensitive to these systematics while the coefficient is more affected. Since bolometric measurements require long time for the detector and set-up preparation, the fabrication of macro bolometers has not been fully optimised. Several details in the construction have been maintained over time without being questioned. A better understanding of the parameters regulating the heat flux inside of bolometers would open the way to a more reliable modelisation, that can be used to enhance the sensitivity of the next-generation bolometers.

At this point we can try to evaluate the sensitivity achievable by a Te-based CUPID experiment employing NTL-assisted light detectors. We have seen that degraded-energy α particles are the dominant background of the CUORE experiment by contributing with 1.4×10^{-2} counts/(keV kg yr) in the region of interest [68]. The NTD-boosted light detectors demonstrated the possibility to reduce this background at the level of 10^{-5} counts/(keV kg yr) in a CUORE-like detector by exploiting the amplification of the NTL effect [196].

After the operation of the CUORE detector with an exposure of 86.3 kg yr, a preliminary study of the

Tab. 8.1: Summary of the sensitivities and the limits on the Majorana neutrino mass achievable in the case of a Te-based and a Mo-based experiment. The same detector volume (123500 cm^3) is assumed for both isotopes. More information on the calculations can be found in the text.

Isotope	background index [counts/(keV kg yr)]	isot. abund. [%]	5-year lifetime sensitivity [yr]	5-year lifetime mass [meV]	10-year lifetime sensitivity [yr]	10-year lifetime mass [meV]
^{130}Te	2.6×10^{-3}	34.2	1.7×10^{26}	$38 - 100$	2.4×10^{26}	$32 - 84$
^{130}Te	2.6×10^{-3}	92	4.6×10^{26}	$23 - 61$	6.5×10^{26}	$19 - 51$
^{130}Te	1.0×10^{-4}	92	1.6×10^{27}	$13 - 33$	2.45×10^{27}	$10 - 26$
^{100}Mo	1.0×10^{-4}	96.9	8.4×10^{26}	$12 - 33$	1.37×10^{27}	$9 - 26$

background model has been carried out [228]. The background-source position has been investigated and the γ contribution to the background has been evaluated of the order of 2.5×10^{-3} counts/(keV kg yr) [228, 68].

At this point, to fix the ideas, we can imagine the following three possible scenarios and calculate the sensitivity that could be reached employing our NTL-assisted light detectors:

- non-enriched TeO_2 bolometers are employed with the present background adding only NTL light detectors;
- enriched $^{130}TeO_2$ bolometers are used with the present background with the addition of NTL light detectors;
- enriched $^{130}TeO_2$ bolometers are operated with NTL light detectors, but the γ background is reduced from $\sim 2.5 \times 10^{-3}$ counts/(keV kg yr) to 10^{-4} counts/(keV kg yr).

For the sake of simplicity, we will consider the same structure of the CUORE experiment and a 10-keV region around the $Q_{\beta\beta}$ of the transition in all the cases. In case of non-enriched TeO_2 bolometers, a crystal density of 6.04 g/cm^3 [157] and an isotopic abundance of 34.2 % [156] were used in the calculation. For the enriched $^{130}TeO_2$, a 6.1 g/cm^3 (evaluated from Ref. [173]) and a 92 % [173] isotopic abundance were employed. In both cases the considered efficiency is the one reported by the CUORE collaboration in Ref. [68]: a total 94 % (excluded the $\beta\beta$ containment) and a 88.35 % including anti-coincidence cuts and the $\beta\beta$ containment. The upper limit on the number of double-β-decay counts was calculated at 90 % C.L.: as a Poissonian fluctuation in the case of a background of 2.5×10^{-3} counts/(keV kg yr) and with method reported in Ref. [229] for a background of 10^{-4} counts/(keV kg yr). Eq. (1.19) is used to calculate the sensitivity to the $0\nu2\beta$ decay employing the phase space factor of Ref. [53] and the nuclear matrix elements in Ref. [230, 231, 232, 233, 234, 52]. Two different experimental live time have been considered: 5 and 10 years. The resulting sensitivities and limits on the Majorana neutrino mass are reported in Table 8.1. The inverted hierarchy could be completely investigated — and the CUPID requirements accomplished [82]— only in the third case: an experiment employing enriched $^{130}TeO_2$ bolometers with a background of 10^{-4} counts/(keV kg yr). Nevertheless reaching such a low background would require, for the tellurium case, the replacement of some parts of the cryostat where the ^{232}Th contamination is present.

The CUORE collaboration announced at the conference NEUTRINO 2018 that $Li_2{}^{100}MoO_4$ scintillating bolometers had been identified as a promising baseline for the upgrade of the CUORE experiment, adding that $^{130}TeO_2$ is a mature and viable alternative [228]. At this point, we can compare this result with the one achievable with a Mo-based equivalent experiment constituted by $Li_2{}^{100}MoO_4$ bolometers. For sake of simplicity we assume the same detector structure. In this case, we consider a background index of 10^{-4} counts/(keV kg yr) that can be achieved more easily thanks to the ^{100}Mo Q-value higher than the

γ natural radioactivity and the particle identification accomplished with scintillating bolometers. The CUORE background seems to indicate that a background level of the order of 10^{-4} counts/(keV kg yr) is already achievable at 3 MeV in the current cryostat like it is. The density of the enriched $Li_2{}^{100}MoO_4$ compound is 3.08 g/cm^3 (evaluated from Ref. [97]) and an isotopic abundance of 96.9 % [97] can be obtained by centrifugation. The detector efficiency considered in this evaluation is 75 % from Ref. [97]. The procedure used for this evaluation is the same as in the previous case with the phase-space factor from Ref. [53] and the nuclear matrix elements from Ref. [235, 230, 231, 232, 233, 234, 52]. The result is summarised in Table 8.1 to facilitate the comparison. We assumed that the internal crystal radiopurity, both in the case of tellurium- and molibdenum-based bolometers, is compatible with a background index lower than 10^{-4} counts/(keV kg yr). This, any way, was already demonstrated in both cases.

Considering the same background index (10^{-4} counts/(keV kg yr)) for an enriched Te-based and Mo-based solution for the CUPID experiment, a higher sensitivity to $0\nu2\beta$-decay half life can be achieved with TeO_2 bolometers. This is due to the higher density of the material, that increases the isotope nuclei number for an equal volume. Nevertheless, the limits on the Majorana neutrino mass are comparable for both solutions thanks to a more favourable nuclear-matrix-element set in the case of $Li_2{}^{100}MoO_4$ bolometers.

9 Appendix

9.1 Test of the α source used in the 784-g TeO_2 bolometer measurement

The α source — used in the underground measurement described in Sec. 6.4 — has been made by implanting ^{218}Po atoms (produced by the ^{222}Rn decay) in a copper tape. The ^{218}Po and its daughters decay quickly to ^{210}Pb, that has a half life of 22.3 years. Its β decay leads to ^{210}Po that constitutes our 5.3-MeV α source. The copper tape was covered by two thirds with a mask in order to produce at the same time smeared α's with the covered part and a ^{210}Po peak with the uncovered part. The peak is useful to calibrate the α spectrum and to stabilize the measurement if needed, while the smeared α events were used to test the α and $\beta(\gamma)$ separation in 2.6-MeV region. The mask consisted of three 6(1)-μm-thick superimposed Mylar foils. Two photographs of the source are presented in Fig. 9.1. The source was tested in a vacuum chamber with a 300-μm-thick silicon diode in order to estimate its activity and the smeared α energy before the underground measurement. The silicon diode surface protection had been removed to be sensitive to α particles. The silicon diode had a surface (~ 324 mm^2) bigger than the source one (~ 196 mm^2). Refer to Fig. 9.2 for the following set-up description. The silicon diode was read-out by a Canberra charge pre-amplifier that was supplied by a Schlumberger type-7126 HV board. The silicon detector was biased with 36 V supplied by four 9-V external batteries. Since signals were fast, they were slowed down with a filter contained in the module: Standford Research System SR560 low-noise pre-amplifier. A pass band filter was implemented in the range $0.1 - 300$ Hz with a 6-dB attenuation and a gain of 10. The data were acquired with a PXI-NI4472 National Instruments card with a sampling frequency of 100 kHz. A test pulse was sent each 30 s to the Canberra pre-amplifier. These events had a pulse-shape mimicking α events — in particular they had a rise time in the range $60 - 64$ μs — but a larger signal amplitude (~ 210 mV). Since we found the vacuum broken at the end of the first test, the vacuum chamber has been pumped during all the following measurements.

The first measurement was dedicated to a 3.46-hour-long background measurement in order to identify a possible contamination of the set-up. Then 18.64 hours were acquired with the α source. Fig. 9.3 shows the comparison between the two spectra renormalized by time and bin energy (20 keV). The low-energy events are due to cosmic rays and natural radioactivity that were not shielded in this set-up. The 5.3-MeV peak is due to the ^{210}Po α decay produced by the one-third of the source that was not covered by the Mylar mask. The events in the range $1 - 3$ MeV are generated by the ^{210}Po α's whose energy is smeared by the 3-layer Mylar mask. The test pulses are not present in the spectra because they formed a peak at around 9 MeV. There are a few events around 7.7 MeV probably due to the α decay of ^{214}Po (a ^{222}Rn daughter).

The source-detector configuration can be easily modelled with a square-base truncated pyramid. The smaller base represents the 14-mm-side source while the bigger base would be the 18-mm-side silicon detector. The height of the pyramid, around 5 mm, corresponds to the distance between the detector

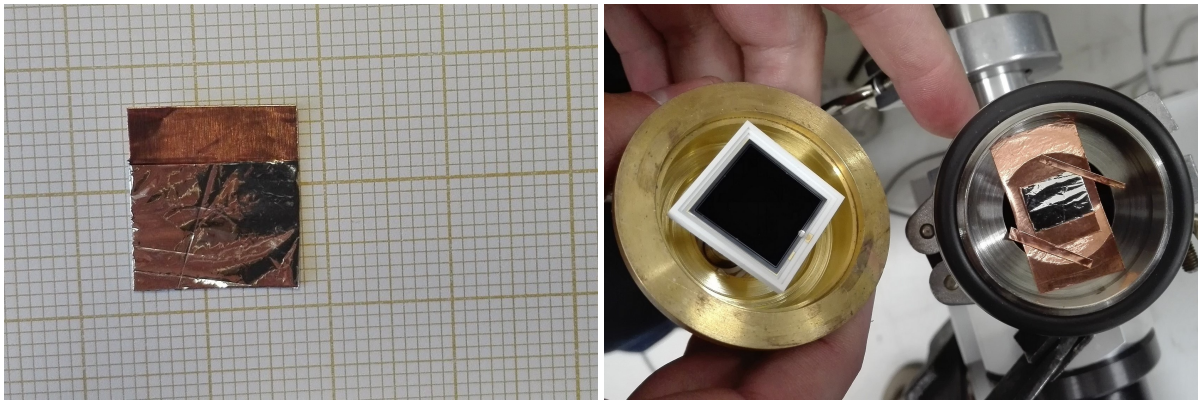

Fig. 9.1: *Left panel*: ^{210}Po α source implanted in a copper tape. It is covered by two thirds with three Mylar foils of 6(1) μm in order to have a smearing of the α's energy. *Right panel*: photograph of the silicon diode (*left*) with the α source (*right*) installed in the vacuum chamber. The detector surface is bigger than the source one.

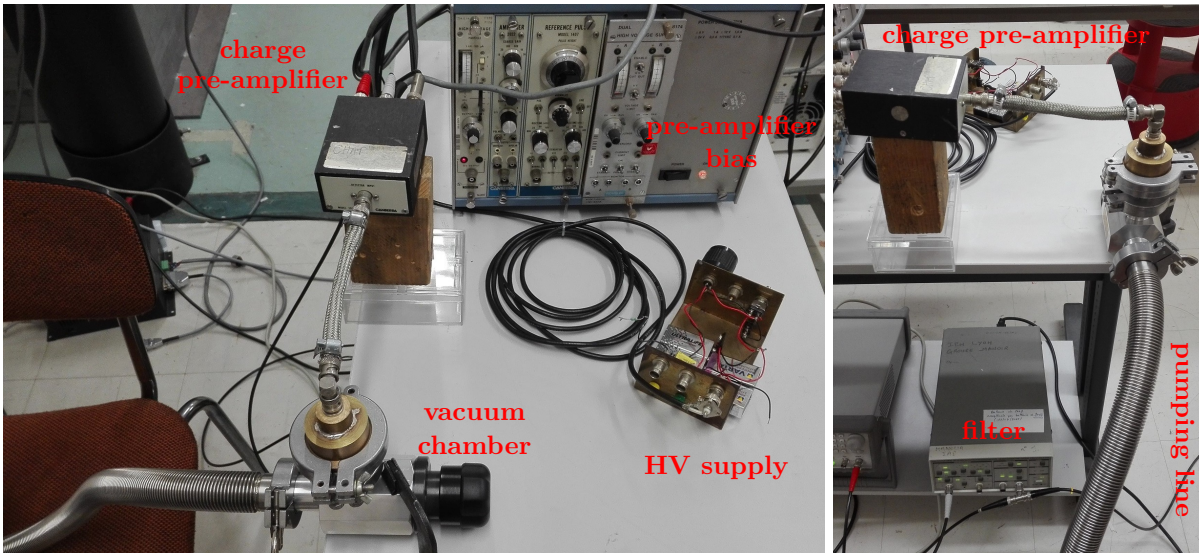

Fig. 9.2: Photographs of the set-up used in the α source test. *Left panel*: the vacuum chamber containing the source and the silicon diode is shown in the foreground on the left. The detector is connected to the Canberra charge pre-amplifier by a coaxial cable, that is biased by the chassis in the background. The high voltage supply used to bias the silicon diode is visible on the right part of the foreground. *Right panel*: the vacuum chamber and the charge pre-amplifier are present on the top of the photograph. The vacuum chamber is connected with a tombac to an external pump. The SR560 pre-amplifier of Stanford Research System is shown in the lower part of the photograph.

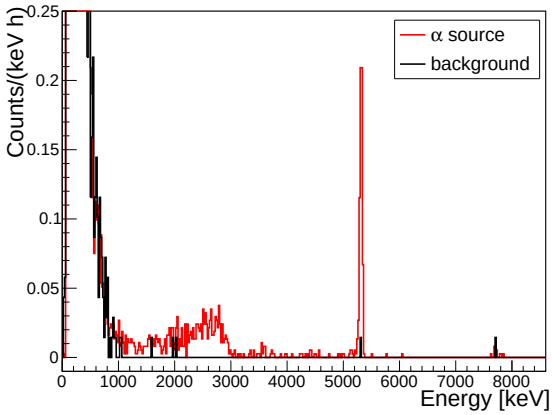

Fig. 9.3: Source (*red*) and background (*black*) spectra superimposed.

Tab. 9.1: Summary of the activity in different energy intervals.

energy interval [MeV]	activity [mBq]	event rate [counts/h]
$1-3$	0.0079(3)	29(1)
$2-3$	0.0052(3)	19(1)
$1-5.2$	0.0088(4)	32(1)
$5.2-5.4$	0.0036(2)	13.1(8)
$1-5.4$	0.0124(4)	45(2)

and the source. 10^6 events were simulated in order to calculate the geometrical efficiency of the set up. We supposed that α particles can leave the source from a random point of the surface and that they do not have a preferential direction: they can be emitted in a random direction in a demi sphere with a random origin on the source surface. With these assumptions, only 58 % of the particles emitted hits the detector.

In order to estimate the source activity we tried to evaluate the dead time of the system. In order to calculate a dead time upper limit after each event, the distribution of the time interval between two successive events for all the events recorded was plotted. Fig. 9.4 shows its zoom for small time intervals. This plot highlights that 0.08 s is the minimum time interval between two events. This dead time is due to the acquisition-card time employed to record events after each trigger. The acquisition systems records 8192 points for each event, of which 2048 points constitute the pre-trigger. The pulse is registered in 6144 points, where a second pulse cannot be triggered. The sampling frequency was set to 100 kHz, therefore after each trigger we cannot have other event for 0.06 s. The previously estimated dead time is reasonably in agreement with the dead time induced by the acquisition card. The source measurement recorded 15705 events in 67106 s. The total dead time is 1256 s, that corresponds to 1.9 % of the total time.

After the background spectrum subtraction from the source one, the activity was estimated in different energy intervals: the results are reported in Table 9.1. We considered a total time of measurement (excluding the dead time) of 65850 s but we neglected the geometrical efficiency in the calculation. The

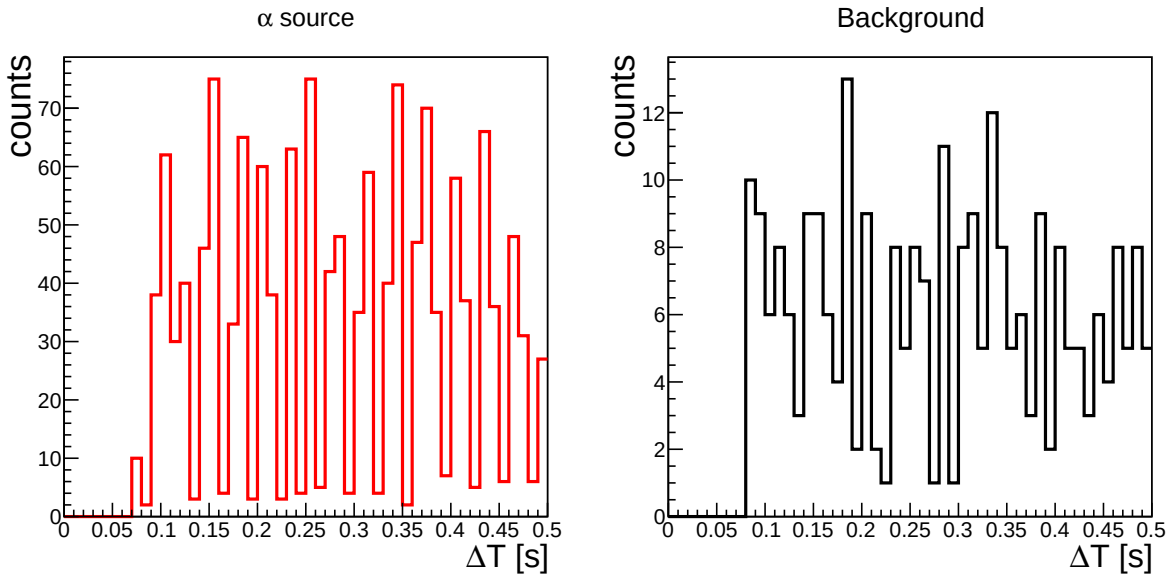

Fig. 9.4: Distribution of the time interval between two consecutive events in the measurement with the source (*left*) and without (*right*). This distribution has been used to experimentally estimate the dead time after each event.

event rate generated by this source is compatible with an underground bolometric measurement. It is sufficiently high to acquire a good statistics in few hours without affecting the detector performance by inducing pile-ups. This test also demonstrated that the optimal number of Mylar foil was three in order to have smeared α in the energy range of $1 - 3$ MeV. This energy interval was chosen to compare the α and $\beta(\gamma)$ separation close to the $0\nu2\beta$ Q-value for the ^{130}Te isotope.

Bibliography

[1] C. Sutton, *Spaceship neutrino.* Cambridge University Press, 1992.

[2] L. M. Brown, *The idea of the neutrino*, *Phys. Today* **31** (1978) 23.

[3] J. Chadwick, *The existence of a neutron*, *Proc. R. Soc. Lond. A* **136** (1932) 692.

[4] E. Fermi, *Tentativo di una teoria dei raggi β*, *Nuovo Cim.* **11** (1934) 1.

[5] B. Pontecorvo, *National research council of Canada report P.D. 205*, Chalk River Laboratory, 1946.

[6] C. L. Cowan et al., *Detection of the free neutrino: a confirmation*, *Science* **124** (1956) 103.

[7] F. Reines and C. L. Cowan, *Detection of the free neutrino*, *Phys. Rev.* **92** (1953) 830.

[8] H. A. Bethe, *Energy production in stars*, *Phys. Rev.* **55** (1939) 434.

[9] M. Salaris and S. Cassisi, *Evolution of stars and stellar populations.* Wiley, 2005.

[10] R. Davis, *Solar neutrinos. II. Experimental*, *Phys. Rev. Lett.* **12** (1964) 303.

[11] R. Davis, *Attempt to detect the antineutrinos from a nuclear reactor by the $Cl^{37}(\bar{\nu}, e^-)A^{37}$ reaction*, *Phys. Rev.* **97** (1955) 766.

[12] J. N. Bahcall and R. K. Ulrich, *Solar models, neutrino experiments, and helioseismology*, *Rev. Mod. Phys.* **60** (1988) 297.

[13] R. Davis, *Proc. IAU Colloq.*, in *Inside the Sun*, vol. 121, (Plenum, New York), p. 171, G. Berthomieu and M. Cribier, 1989.

[14] W. Hampel et al., *GALLEX solar neutrino observations: results for GALLEX IV*, *Phys. Lett. B* **447** (1999) 127.

[15] M. Altmann et al., *Complete results for five years of GNO solar neutrino observations*, *Phys. Lett. B* **616** (2005) 174.

[16] J. N. Abdurashitov et al., *Solar neutrino flux measurements by the Soviet-American Gallium Experiment (SAGE) for half the 22-year solar cycle*, *J. Exp. Theor. Phys.* **95** (2002) 181.

[17] J. N. Bahcall, *Gallium solar neutrino experiments: absorption cross sections, neutrino spectra, and predicted event rates*, *Phys. Rev. C* **56** (1997) 3391.

[18] B. Pontecorvo, *JINR Preprint P-95*, Dubna, 1957.

[19] S. Fukuda et al., *The Super-Kamiokande detector*, *Nucl. Instrum. Meth. A* **501** (2003) 418.

[20] J. Boger et al., *The Sudbury Neutrino Observatory*, *Nucl. Instrum. Meth. A* **449** (2000) 172.

[21] Y. Ashie et al., *Measurement of atmospheric neutrino oscillation parameters by Super-Kamiokande I*, *Phys. Rev. D* **71** (2005) 112005.

[22] B. Aharmim et al., *Combined analysis of all three phases of solar neutrino data from the Sudbury Neutrino Observatory*, *Phys. Rev. C* **88** (2013) 025501.

[23] M. Tanabashi et al., *The review of particle physics (2018)*, *Phys. Rev. D* **98** (2018) 030001.

[24] E. Majorana, *Teoria simmetrica dell'elettrone e del positrone*, *Nuovo Cim.* **14** (1937) 171.

[25] N. Aghanim et al., *Planck 2018 results. VI. Cosmological parameters*, *arXiv preprint* (2018) , [1807.06209].

[26] V. N. Aseev et al., *Upper limit on the electron antineutrino mass from the Troitsk experiment*, *Phys. Rev. D* **84** (2011) 112003.

[27] C. Kraus et al., *Final results from phase II of the Mainz neutrino mass searchin tritium β decay*, *Eur. Phys. J. C* **40** (2005) 447.

[28] J. Angriki et al., *KATRIN design report 2004*, FZKA Scientific Report 7090, 2004.

[29] M. Kleesiek et al., *β-decay spectrum, response function and statistical model for neutrino mass measurements with the KATRIN experiment*, *arXiv preprint* (2018) , [1806.00369].

[30] A. A. Esfahani et al., *Determining the neutrino mass with cyclotron radiation emission spectroscopy-Project 8*, *J. Phys. G: Nucl. Part. Phys.* **44** (2017) 054004.

[31] F. Gatti, *Microcalorimeter measurements*, *Nucl. Phys. B - Proc. Suppl.* **91** (2001) 293.

[32] C. Arnaboldi et al., *Measurement of the p to s wave branching ratio of ^{187}Re β decay from beta environmental fine structure*, *Phys. Rev. Lett.* **96** (2006) 042503.

[33] E. Ferri et al., *The status of the MARE experiment with ^{187}Re and ^{163}Ho isotopes*, *Phys. Procedia* **61** (2015) 227.

[34] P. T. Springer et al., *Measurement of the neutrino mass using the inner bremsstrahlung emitted in the electron-capture decay of ^{163}*Ho, *Phys. Rev. A* **35** (1987) 679.

[35] L. Gastaldo et al., *The electron capture in ^{163}Ho experiment – ECHo*, *Eur. Phys. J.* **226** (2017) 1623.

[36] B. Alpert et al., *HOLMES*, *Eur. Phys. J. C* **75** (2015) 112.

[37] A. Nucciotti, *Statistical sensitivity of ^{163}Ho electron capture neutrino mass experiments*, *Eur. Phys. J. C* **74** (2014) 3161.

[38] K. Assamagan et al., *Upper limit of the muon-neutrino mass and charged-pion mass from momentum analysis of a surface muon beam*, *Phys. Rev. D* **53** (1996) 6065.

[39] R. Barate et al., *An upper limit on the τ neutrino mass from three- and five-prong tau decays*, *Eur. Phys. J. C* **2** (1998) 395.

[40] M. Goeppert-Mayer, *Double beta-disintegration*, *Phys. Rev.* **48** (1935) 512.

[41] M. G. Inghram and J. H. Reynolds, *Double beta-decay of* Te^{130}, *Phys. Rev.* **78** (1950) 822.

[42] S. R. Elliott et al., *Direct evidence for two-neutrino double-beta decay in* ^{82}Se, *Phys. Rev. Lett.* **59** (1987) 2020.

[43] K. S. Krane, *Introductory nuclear physics*. Wiley, 1987.

[44] W. H. Furry, *On transition probabilities in double beta-disintegration*, *Phys. Rev.* **56** (1939) 1184.

[45] S. Dell'Oro et al., *Neutrinoless double beta decay: 2015 review*, *Adv. High Energy Phys.* **2016** (2016) 2162659.

[46] M. Fukugita and T. Yanagida, *Baryogenesis without grand unification*, *Phys. Lett. B* **174** (1986) 45.

[47] J. T. Suhonen, *Value of the axial-vector coupling strength in β and $\beta\beta$ decays: a review*, *Front. Phys.* **5** (2017) 55.

[48] E. Caurier et al., *The shell model as a unified view of nuclear structure*, *Rev. Mod. Phys.* **77** (2005) 427.

[49] J. Suhonen and O. Civitarese, *Weak-interaction and nuclear-structure aspects of nuclear double beta decay*, *Phys. Rep.* **300** (1998) 123.

[50] J. P. Elliott, *The interacting boson model of nuclear structure*, *Rep. Prog. Phys.* **48** (1985) 171.

[51] P. K. Rath et al., *Neutrinoless $\beta\beta$ decay transition matrix elements within mechanisms involving light majorana neutrinos, classical majorons, and sterile neutrinos*, *Phys. Rev. C* **88** (2013) 064322.

[52] T. R. Rodríguez and G. Martínez-Pinedo, *Energy density functional study of nuclear matrix elements for neutrinoless $\beta\beta$ decay*, *Phys. Rev. Lett.* **105** (2010) 252503.

[53] J. Kotila and F. Iachello, *Phase-space factors for double-β decay*, *Phys. Rev. C* **85** (2012) 034316.

[54] T. Iida, *First result of the CANDLES III experiment searching for double beta decay of ^{48}Ca*, June, 2018. Neutrino 2018, Heidelberg, Germany.

[55] S. Umehara et al., *Neutrino-less double-β decay of* ^{48}Ca *studied by* CaF_2*(Eu) scintillators*, *Phys. Rev. C* **78** (2008) 058501.

[56] R. Arnold et al., *Measurement of the double-beta decay half-life and search for the neutrinoless double-beta decay of* ^{48}Ca *with the NEMO-3 detector*, *Phys. Rev. D* **93** (2016) 112008.

[57] M. Agostini et al., *Improved limit on neutrinoless double-β decay of ^{76}Ge from GERDA Phase II*, *Phys. Rev. Lett.* **120** (2018) 132503.

[58] V. Guiseppe, *New results from the MAJORANA DEMONSTRATOR experiment*, June, 2018. Neutrino 2018, Heidelberg, Germany.

[59] S. Pirro, *New results on double beta decay with CUPID-0*, July, 2018. Neutrinos and Dark Matter, Daejeon, Korea.

[60] R. Arnold et al., *Final results on ^{82}Se double beta decay to the ground state of ^{82}Kr from the NEMO-3 experiment*, *arXiv preprint* (2018) , [1806.05553].

[61] J. Argyriades et al., *Measurement of the two neutrino double beta decay half-life of Zr-96 with the NEMO-3 detector*, *Nucl. Phys. A* **847** (2010) 168.

[62] R. Arnold et al., *Results of the search for neutrinoless double-β decay in ^{100}Mo with the NEMO-3 experiment*, *Phys. Rev. D* **92** (2015) 072011.

[63] D. V. Poda, *^{100}Mo-enriched Li_2MoO_4 scintillating bolometers for $0\nu2\beta$ decay search: from LUMINEU to CUPID-0/Mo projects*, *AIP Conf. Proc.* **1894** (2017) 020017.

[64] D. V. Poda, *Mo-100 double-beta decay search in the CUPID-Mo experiment with enriched scintillating bolometers*, June, 2018. Neutrino 2018, Heidelberg, Germany.

[65] A. S. Barabash et al., *Final results of the Aurora experiment to study 2β decay of ^{116}Cd with enriched $^{116}CdWO_4$ crystal scintillators*, *Phys. Rev. D* **98** (2018) 092007.

[66] R. Arnold et al., *Measurement of the $2\nu\beta\beta$ decay half-life and search for the $0\nu\beta\beta$ decay of ^{116}Cd with the NEMO-3 detector*, *Phys. Rev. D* **95** (2017) 012007.

[67] F. A. Danevich et al., *Search for 2β decay of cadmium and tungsten isotopes: final results of the Solotvina experiment*, *Phys. Rev. C* **68** (2003) 035501.

[68] C. Alduino et al., *First results from CUORE: a search for lepton number violation via $0\nu\beta\beta$ decay of ^{130}Te*, *Phys. Rev. Lett.* **120** (2018) 132501.

[69] A. Gando et al., *Search for Majorana neutrinos near the inverted mass hierarchy region with KamLAND-Zen*, *Phys. Rev. Lett.* **117** (2016) 082503.

[70] J. B. Albert et al., *Search for neutrinoless double-beta decay with the upgraded EXO-200 detector*, *Phys. Rev. Lett.* **120** (2018) 072701.

[71] R. Arnold et al., *Measurement of the $2\nu\beta\beta$ decay half-life of ^{150}Nd and a search for $0\nu\beta\beta$ decay processes with the full exposure from the NEMO-3 detector*, *Phys. Rev. D* **94** (2016) 072003.

[72] H. V. Klapdor-Kleingrothaus et al., *Evidence for neutrinoless double beta decay*, *Mod. Phys. Lett. A* **16** (2001) 2409.

[73] C. Aalseth et al., *Neutrinoless double beta decay and direct searches for neutrino mass*, *arXiv preprint* (2004) , [hep-ph/0412300].

[74] V. I. Tretyak, *False starts in history of searches for 2β decay, or discoverless double beta decay*, *AIP Conf. Proc.* **1417** (2011) 129.

[75] G. Orebi Gann, *SNO+*, June, 2018. Neutrino 2018, Heidelberg, Germany.

[76] C. Grant, *The discovery potential of THEIA*, June, 2018. Neutrino 2018, Heidelberg, Germany.

[77] J. Martín-Albo et al., *Sensitivity of NEXT-100 to neutrinoless double beta decay*, *J. High Energy Phys.* **2016** (2016) 159.

[78] X. Chen et al., *PandaX-III: searching for neutrinoless double beta decay with high pressure ^{136}Xe gas time projection chambers*, *Sci. China Phys. Mech. Astron.* **60** (2017) 061011.

[79] M. Yoshida, *AXEL — a high pressure xenon gas TPC for $0\nu\beta\beta$ search*, June, 2018. Neutrino 2018, Heidelberg, Germany.

[80] N. Abgrall et al., *The large enriched germanium experiment for neutrinoless double beta decay (LEGEND)*, *AIP Conf. Proc.* **1894** (2017) 020027.

[81] R. Arnold et al., *Probing new physics models of neutrinoless double beta decay with SuperNEMO*, *Eur. Phys. J. C* **70** (2010) 927.

[82] G. Wang et al., *CUPID: CUORE (Cryogenic Underground Observatory for Rare Events) Upgrade with Particle IDentification*, *arXiv preprint* (2015) , [1504.03599].

[83] V. Alenkov et al., *Technical design report for the AMoRE 0$\nu\beta\beta$ decay search experiment*, *arXiv preprint* (2015) , [1512.05957].

[84] A. Giuliani, *The mid and long term future of neutrinoless double beta decay*, June, 2018. Neutrino 2018, Heidelberg, Germany.

[85] J. B. Albert et al., *Sensitivity and discovery potential of the proposed nEXO experiment to neutrinoless double-β decay*, *Phys. Rev. C* **97** (2018) 065503.

[86] A. Gando, *KamLAND-Zen*, June, 2018. Neutrino 2018, Heidelberg, Germany.

[87] C. E. Aalseth et al., *Search for neutrinoless double-β decay in ^{76}Ge with the MAJORANA DEMONSTRATOR*, *Phys. Rev. Lett.* **120** (2018) 132502.

[88] S. Rahaman et al., *Q values of the ^{76}Ge and ^{100}Mo double-beta decays*, *Phys. Lett. B* **662** (2008) 111.

[89] A. J. Zsigmond, *New results from GERDA Phase II*, June, 2018. Neutrino 2018, Heidelberg, Germany.

[90] K. Zuber, *COBRA — double beta decay searches using CdTe detectors*, *Phys. Lett. B* **519** (2001) 1.

[91] S. Pirro et al., *Present status of MI-BETA cryogenic experiment and preliminary results for CUORICINO*, *Nucl. Instrum. Meth. A* **444** (2000) 71.

[92] E. Andreotti et al., *^{130}Te neutrinoless double-beta decay with CUORICINO*, *Astropart. Phys.* **34** (2011) 822.

[93] K. Alfonso et al., *Search for neutrinoless double-beta decay of ^{130}Te with CUORE-0*, *Phys. Rev. Lett.* **115** (2015) 102502.

[94] V. Nanal, *Search for neutrinoless double beta decay in ^{124}Sn*, *Eur. Phys. J. Web Conf.* **66** (2014) 08005.

[95] J. W. Beeman et al., *The LUCIFER project: achievements and near future prospects*, *J. Low Temp. Phys.* **184** (2016) 852.

[96] O. Azzolini et al., *First result on the neutrinoless double-β decay of ^{82}Se with CUPID-0*, *Phys. Rev. Lett.* **120** (2018) 232502.

[97] E. Armengaud et al., *Development of ^{100}Mo-containing scintillating bolometers for a high-sensitivity neutrinoless double-beta decay search*, *Eur. Phys. J. C* **77** (2017) 785.

[98] H. Park, *The AMoRE: search for neutrinoless double beta decay in ^{100}Mo*, *Nucl. Part. Phys. Proc.* **273** (2016) 2630.

[99] R. Arnold et al., *Technical design and performance of the NEMO 3 detector*, *Nucl. Instrum. Meth. A* **536** (2005) 79.

[100] H. Ejiri et al., *MOON for neutrino-less double beta decays*, *Eur. Phys. J. Special Topics* **162** (2008) 239.

[101] H. Iwase et al., *The DCBA/MTD experiments for neutrinoless double beta decay search*, *Proc. 12th Asia Pacific Phys. Conf. (APPC12)* **1** (2014) 013023.

[102] E. Fiorini and T. O. Niinikoski, *Low-temperature calorimetry for rare decays*, *Nucl. Instrum. Meth. Phys. Res.* **224** (1984) 83.

[103] D. L'Hote, *Les bolometres pour la detection de particules*, tech. rep., Ecole internationale Joliot-Curie de physique nucleaire, Maubuisson, France, 1994.

[104] J. Joffrin, *Introductions aux phonons, interaction électron-phonon*, tech. rep., Détection de rayonnements à très basse température, 3ème ecole thematique, Aussois, France, 1996.

[105] A. Juillard, *Thermalisation des phonons dans un bolomètre massif*, tech. rep., Détection de rayonnements à très basse température, 5ème ecole thematique, Oléron, France, 2002.

[106] N. F. Mott, *Conduction in non-crystalline materials*, *Phil. Mag.* **19** (1969) 835.

[107] S. Marnieros, *Couches minces d'isolant d'Anderson. Application à la bolométrie à très basse température*, Ph.D. thesis, Université de Paris-Sud XI, 1998.

[108] S. Marnieros, *Détecteurs cryogéniques et leurs applications en astrophysique et astroparticules*, Habilitation à Diriger des Recherches, Centre de Sciences Nucléaires et de Sciences de la Matière, 2014.

[109] O. Crauste, *Étude des transitions de phases quantiques supraconducteur - isolant, métal - isolant dans des matériaux amorphes désordonnés proches de la dimension 2.*, Ph.D. thesis, Université de Paris-Sud XI, 2010.

[110] C. Alduino et al., *CUORE-0 detector: design, construction and operation*, *J. Instrum.* **11** (2016) P07009.

[111] J. C. Mather, *Bolometer noise: nonequilibrium theory*, *Appl. Opt.* **21** (1982) 1125.

[112] K. M. van Vliet, *Noise limitations in solid state photodetectors*, *Appl. Opt.* **6** (1967) 1145.

[113] A. Giuliani and S. Sanguinetti, *Phonon-mediated particle detectors: physics and materials*, *Mater. Sci. Eng.* **11** (1993) 1.

[114] E. Olivieri et al., *Vibrations on pulse tube based dry dilution refrigerators for low noise measurements*, *Nucl. Instrum. Meth. A* **858** (2017) 73.

[115] R. Maisonobe et al., *Vibration decoupling system for massive bolometers in dry cryostats*, *J. Instrum.* **13** (2018) T08009.

[116] P. L. Kapitza, *The study of heat transfer in helium II*, *J. Phys.(Moscow)* **4** (1941) 181.

[117] A. Alessandrello et al., *Development and optimization of a modular bolometer to search for rare decays*, *Czechosl. Journ. Phys.* **46** (1996) 2893.

[118] N. Wang et al., *Electrical and thermal properties of neutron-transmutation-doped Ge at 20 mK*, *Phys. Rev. B* **41** (1990) 3761.

[119] J. Soudée et al., *Hot electrons effect in a #23 NTD Ge sample*, *J. Low Temp. Phys.* **110** (1998) 1013.

[120] A. Alessandrello et al., *Workshop on semiconductor thermistor for mK operation*, 1991.

[121] É. Aubourg et al., *Measurement of electron-phonon decoupling time in neutron-transmutation doped germanium at 20 mK*, *J. Low Temp. Phys.* **93** (1993) 289.

[122] E. Pasca et al., *Measurement of electron-phonon decoupling in NTD31 germanium*, *Adv. Tech. Part. Phys.* **1** (2002) 684.

[123] E. Pasca, *Low temperature properties of neutron transmutation doped germanium*, Ph.D. thesis, Università degli studi di Firenze, 2004.

[124] A. Saporta-Druesnes, *Développement de détecteurs cryogéniques bas-seuil nouvelle génération pour la recherche de matière noire légère avec l'expérience EDELWEISS-III*, Master's thesis, Université de Lyon, 2016.

[125] M. Pedretti, *The single module for CUORICINO and CUORE detectors: tests, construction and modelling*, Ph.D. thesis, Università dell'Insubria, 2004.

[126] G. Angloher et al., *Results on light dark matter particles with a low-threshold CRESST-II detector*, *Eur. Phys. J. C* **76** (2016) 25.

[127] G. Angloher et al., *The COSINUS project: perspectives of a NaI scintillating calorimeter for dark matter search*, *Eur. Phys. J. C* **76** (2016) 441.

[128] S. Cebrián et al., *The ROSEBUD experiment at Canfranc : 2001 report*, *Nucl. Phys. B - Proc. Suppl.* **110** (2002) 97.

[129] L. Hehn et al., *Improved EDELWEISS-III sensitivity for low-mass WIMPs using a profile likelihood approach*, *Eur. Phys. J. C* **76** (2016) 548.

[130] R. Agnese et al., *Nuclear-recoil energy scale in CDMS II silicon dark-matter detectors*, *Nucl. Instrum. Meth. A* **905** (2018) 71.

[131] L. Gironi, *Development of cryogenic detectors for rare event searches*, Ph.D. thesis, Università degli studi di Milano-Bicocca, 2010.

[132] S. Nagorny et al., *Quenching factor for alpha particles in ZnSe scintillating bolometers*, *IOP Conf. Mater. Sci. Eng.* **169** (2017) 012011.

[133] S. Koc, *The quantum efficiency of the photo-electric effect in germanium for the 0.3-2 μ wavelength region*, *Czechosl. Journ. Phys.* **7** (1957) 91.

[134] B. S. Neganov and V. N. Trofimov, *Colorimetric method measuring ionizing radiation*, *Otkryt. Izobret.* **146** (1985) 215.

[135] P. N. Luke, *Voltage-assisted calorimetric ionization detector*, *J. Applied Phys.* **64** (1988) 6858.

[136] E. Olivieri et al., *Space-and-surface charge neutralization of cryogenic Ge detectors using infrared LEDs*, *AIP Conf. Proc.* **1185** (2009) 310.

[137] O. V. Lounasmaa, *Experimental principles and methods below 1 K*. Academic Press, 1974.

[138] G. Frossati, *Obtention d'ultrabasses températures en régime continu, par dilution ^{3}He-^{4}He classique : application aux méthodes de réfrigération transitoire ; thermométrie et étude de quelques systèmes physiques*, Ph.D. thesis, Université Joseph Fourier (Grenoble), 1978.

[139] D.-M. Mei and A. Hime, *Muon-induced background study for underground laboratories*, *Phys. Rev. D* **73** (2006) 053004.

[140] S. Pirro, *Further developments in mechanical decoupling of large thermal detectors*, *Nucl. Instrum. Meth. A* **559** (2006) 672.

[141] M. Mancuso et al., *An aboveground pulse-tube-based bolometric test facility for the validation of the LUMINEU $ZnMoO_4$ crystals*, *J. Low Temp. Phys.* **176** (2014) 571.

[142] C. Arnaboldi et al., *The cold preamplifier set-up of CUORICINO: towards 1000 channels*, *Nucl. Instrum. Meth. A* **559** (2006) 826.

[143] C. Arnaboldi et al., *The front-end readout for CUORICINO, an array of macro-bolometers and MIBETA, an array of μ-bolometers*, *Nucl. Instrum. Meth. A* **520** (2004) 578.

[144] E. Armengaud et al., *Development and underground test of radiopure $ZnMoO_4$ scintillating bolometers for the LUMINEU $0\nu2\beta$ project*, *J. Instrum.* **10** (2015) P05007.

[145] E. Armengaud et al., *Performance of the EDELWEISS-III experiment for direct dark matter searches*, *J. Instrum.* **12** (2017) P08010.

[146] M. Tenconi, *Development of luminescent bolometers and light detectors for neutrinoless double beta decay search*, Ph.D. thesis, Université Paris-Sud, 2015.

[147] M. Koláč et al., *Low temperature heat release from copper: ortho-para conversion of hydrogen*, *J. Low Temp. Phys.* **59** (1985) 547.

[148] T. Shutt et al., *A solution to the dead-layer problem in ionization and phonon-based dark matter detectors*, *Nucl. Instrum. Meth. A* **444** (2000) 340.

[149] B. Censier, *Étude et optimisation de la voie ionisation dans l'expérience EDELWEISS de détection directe de la matière noire* , Ph.D. thesis, Université Paris-Sud, 2006.

[150] M. Mancuso et al., *An experimental study of antireflective coatings in Ge light detectors for scintillating bolometers*, *Eur. Phys. J. Web Conf.* **65** (2014) 04003.

[151] M. Mancuso, *Development and optimization of scintillating bolometers and innovative light detectors for a pilot underground experiment on neutrinoless double beta decay*, Ph.D. thesis, Université Paris-Sud, 2016.

[152] E. Andreotti et al., *Production, characterization, and selection of the heating elements for the response stabilization of the CUORE bolometers*, *Nucl. Instrum. Meth. A* **664** (2012) 161.

[153] A. Alessandrello et al., *Methods for response stabilization in bolometers for rare decays*, *Nucl. Instrum. Meth. A* **412** (1998) 454.

[154] E. Gatti and P. F. Manfredi, *Processing the signals from solid-state detectors in elementary-particle physics*, *Riv. Nuovo Cim.* **9** (1986) 1.

[155] D. R. Artusa et al., *Searching for neutrinoless double-beta decay of ^{130}Te with CUORE*, *Adv. High Energy Phys.* **2015** (2015) 879871.

[156] M. A. Fehr et al., *Application of MC-ICPMS to the precise determination of tellurium isotope compositions in chondrites, iron meteorites and sulfides*, *Int. J. Mass Spectrom.* **232** (2004) 83.

[157] C. Arnaboldi et al., *Production of high purity TeO_2 single crystals for the study of neutrinoless double beta decay*, *J. Cryst. Growth* **312** (2010) 2999.

[158] M. Barucci et al., *Measurement of low temperature specific heat of crystalline TeO_2 for the optimization of bolometric detectors*, *J. Low Temp. Phys.* **123** (2001) 303.

[159] C. Arnaboldi et al., *New limit on the neutrinoless $\beta\beta$ decay of ^{130}Te*, *Phys. Rev. Lett.* **95** (2005) 142501.

[160] M. Redshaw et al., *Masses of ^{130}Te and ^{130}Xe and double-β-decay Q value of ^{130}Te*, *Phys. Rev. Lett.* **102** (2009) 212502.

[161] E. E. Haller, *Advanced far-infrared detectors*, *Infrared Phys. Technol.* **35** (1994) 127.

[162] C. Rusconi, *Optimisation of the bolometric performances of the CUORE-0/CUORE and LUCIFER detectors for the neutrinoless double beta decay search*, Ph.D. thesis, Università degli studi dell'Insubria, 2011.

[163] E. Andreotti et al., *The low radioactivity link of the CUORE experiment*, *J. Instrum.* **4** (2009) P09003.

[164] C. Ligi et al., *The CUORE cryostat: a 1-ton scale setup for bolometric detectors*, *J. Low Temp. Phys.* **184** (2016) 590.

[165] A. Alessandrello et al., *Measurements of internal radioactive contamination in samples of Roman lead to be used in experiments on rare events*, *Nucl. Instrum. Meth. B* **142** (1998) 163.

[166] J. S. Cushman et al., *The detector calibration system for the CUORE cryogenic bolometer array*, *Nucl. Instrum. Meth. A* **844** (2017) 32.

[167] C. Alduino et al., *The projected background for the CUORE experiment*, *Eur. Phys. J. C* **77** (2017) 543.

[168] F. Alessandria et al., *Validation of techniques to mitigate copper surface contamination in CUORE*, *Astropar. Phys.* **45** (2013) 13.

[169] E. Buccheri et al., *An assembly line for the construction of ultra-radio-pure detectors*, *Nucl. Instrum. Meth. A* **768** (2014) 130.

[170] G. Benato et al., *Radon mitigation during the installation of the CUORE $0\nu\beta\beta$ decay detector*, *J. Instrum.* **13** (2018) P01010.

[171] C. Alduino et al., *CUORE sensitivity to $0\nu\beta\beta$ decay*, *Eur. Phys. J. C* **77** (2017) 532.

[172] G. Wang et al., *R&D towards CUPID (CUORE Upgrade with Particle IDentification)*, *arXiv preprint* (2015) , [1504.03612].

[173] D. R. Artusa et al., *Enriched TeO_2 bolometers with active particle discrimination: towards the CUPID experiment*, *Phys. Lett. B* **767** (2017) 321.

[174] T. Tabarelli de Fatis, *Cerenkov emission as a positive tag of double beta decays in bolometric experiments*, *Eur. Phys. J. C* **65** (2010) 359.

[175] N. Casali, *Model for the Cherenkov light emission of TeO_2 cryogenic calorimeters*, *Astropar. Phys.* **91** (2017) 44.

[176] N. Uchida, *Optical properties of single-crystal paratellurite (TeO_2)*, *Phys. Rev. B* **4** (1971) 3736.

[177] N. Casali et al., *TeO_2 bolometers with Cherenkov signal tagging: towards next-generation neutrinoless double-beta decay experiments*, *Eur. Phys. J. C* **75** (2015) 12.

[178] D. R. Artusa et al., *First array of enriched $Zn^{82}Se$ bolometers to search for double beta decay*, *Eur. Phys. J. C* **76** (2016) 364.

[179] J. W. Beeman et al., *Discrimination of α and β/γ interactions in a TeO_2 bolometer*, *Astropart. Phys.* **35** (2012) 558.

[180] N. J. Coron et al., *Highly sensitive large-area bolometers for scintillation studies below 100 mK*, *Opt. Eng.* **43** (2004) 43.

[181] L. Pattavina et al., *Background suppression in massive TeO_2 bolometers with Neganov-Luke amplified light detectors*, *J. Low Temp. Phys.* **184** (2016) 286.

[182] L. Gironi et al., *Cerenkov light identification with Si low-temperature detectors with sensitivity enhanced by the Neganov-Luke effect*, *Phys. Rev. C* **94** (2016) 054608.

[183] M. Stark et al., *Application of the Neganov-Luke effect to low-threshold light detectors*, *Nucl. Instrum. Meth. A* **545** (2005) 738.

[184] C. Isaila et al., *Low-temperature light detectors: Neganov-Luke amplification and calibration*, *Phys. Lett. B* **716** (2012) 160.

[185] X. Defay et al., *Cryogenic silicon detectors with implanted contacts for the detection of visible photons using the Neganov–Trofimov–Luke effect*, *J. Low Temp. Phys.* **184** (2016) 274.

[186] X. Defay et al., *Silicon PIN diodes as Neganov–Trofimov–Luke cryogenic light detectors*, *J. Low Temp. Phys.* (2018).

[187] M. Willers et al., *Neganov-Luke amplified cryogenic light detectors for the background discrimination in neutrinoless double beta decay search with TeO_2 bolometers*, *J. Instrum.* **10** (2015) P03003.

[188] G. Angloher et al., *EURECA conceptual design report*, *Phys. Dark Univ.* **3** (2014) 41.

[189] K. Schäffner et al., *Particle discrimination in TeO_2 bolometers using light detectors read out by transition edge sensors*, *Astropart. Phys.* **69** (2015) 30.

[190] R. Hennings-Yeomans et al., *Controlling T_c of iridium films using interfacial proximity effects*, *arXiv preprint* (2017) , [1711.03648].

[191] C. Hassel et al., *Recent results for the ECHo experiment*, *J. Low Temp. Phys.* **184** (2016) 910.

[192] D. Gray et al., *The first tests of a large-area light detector equipped with metallic magnetic calorimeters for scintillating bolometers for the LUMINEU neutrinoless double beta decay search*, *J. Low Temp. Phys.* **184** (2016) 904.

[193] L. Cardani et al., *Al/Ti/Al phonon-mediated KIDs for UV-VIS light detection over large areas*, *Supercond. Sci. Tech.* **31** (2018) 075002.

[194] N. Coron et al., *Scintillating and particle discrimination properties of selected crystals for low-temperature bolometers: from LiF to BGO*, *Nucl. Instrum. Meth. A* **520** (2004) 159.

[195] P. de Marcillac. private communication.

[196] L. Bergé et al., *Complete event-by-event $\alpha/\gamma(\beta)$ separation in a full-size TeO_2 CUORE bolometer by Neganov-Luke-magnified light detection*, *Phys. Rev. C* **97** (2018) 032501(R).

[197] C. Nones et al., *Superconducting aluminum layers as pulse shape modifiers: an innovative solution to fight against surface background in neutrinoless double beta decay experiments*, *J. Low Temp. Phys.* **167** (2012) 1029.

[198] L. Canonica et al., *Rejection of surface background in thermal detectors: the ABSuRD project*, *Nucl. Instrum. Meth. A* **732** (2013) 286.

[199] D. L. Lincoln et al., *First direct double-β decay Q-value measurement of ^{82}Se in support of understanding the nature of the neutrino*, *Phys. Rev. Lett.* **110** (2013) 012501.

[200] M. Berglund et al., *Isotopic compositions of the elements 2009 (IUPAC Technical Report)*, *Pure Appl. Chem.* **83** (2011) 397.

[201] J. W. Beeman et al., *Performances of a large mass ZnSe bolometer to search for rare events*, *J. Instrum.* **8** (2013) P05021.

[202] L. Cardani, *Scintillating bolometers for rare events searches: the LUCIFER experiment*, *J. Low Temp. Phys.* **176** (2014) 973.

[203] O. Azzolini et al., *CUPID-0: the first array of enriched scintillating bolometers for $0\nu\beta\beta$ decay investigations*, *Eur. Phys. J. C* **78** (2018) 428.

[204] I. Dafinei, *The LUCIFER project and production issues for crystals needed in rare events physics experiments*, *J. Cryst. Growth* **393** (2014) 13.

[205] J. Meija et al., *Isotopic compositions of the elements 2013 (IUPAC Technical Report)*, *Pure Appl. Chem.* **88** (2016) 293.

[206] S. Nagorny et al., *$^{arch}PbMoO_4$ scintillating bolometer as detector to searches for the neutrinoless double beta decay of ^{100}Mo*, *J. Phys. Conf. Ser.* **841** (2017) 012025.

[207] L. Gironi et al., *Performance of $ZnMoO_4$ crystal as cryogenic scintillating bolometer to search for double beta decay of molybdenum*, *J. Instrum.* **5** (2010) P11007.

[208] L. Cardani et al., *First bolometric measurement of the two neutrino double beta decay of ^{100}Mo with a $ZnMoO_4$ crystals array*, *J. Phys. G: Nucl. Part. Phys.* **41** (2014) 075204.

[209] D. M. Chernyak et al., *Rejection of randomly coinciding events in $Li_2{}^{100}MoO_4$ scintillating bolometers using light detectors based on the Neganov-Luke effect*, *Eur. Phys. J. C* **77** (2016) 3.

[210] S. Rahaman et al., *Double-beta decay Q values of ^{116}Cd and ^{130}Te*, *Phys. Lett. B* **703** (2011) 412.

[211] F. A. Danevich et al., *The research of 2β decay of ^{116}Cd with enriched $^{116}CdWO_4$ crystal scintillators*, *Phys. Lett. B* **344** (1995) 72.

[212] F. A. Danevich et al., *Search for double beta decay of ^{116}Cd with enriched $^{116}CdWO_4$ crystal scintillators (Aurora experiment)*, *J. Phys. Conf. Ser.* **718** (2016) 062009.

[213] A. S. Barabash et al., *First test of an enriched $^{116}CdWO_4$ scintillating bolometer for neutrinoless double-beta-decay searches*, *Eur. Phys. J. C* **76** (2016) 487.

[214] F. A. Danevich, *Radiopure tungstate and molybdate crystal scintillators for double beta decay experiments*, *Int. J. Mod. Phys. A* **32** (2017) 1743008.

[215] A. S. Barabash et al., *Low background detector with enriched $^{116}CdWO_4$ crystal scintillators to search for double β decay of ^{116}Cd*, *J. Instrum.* **6** (2011) P08011.

[216] D. V. Poda, *Search for 2β decay of ^{116}Cd with the help of enriched $^{116}CdWO_4$ crystal scintillators*, *Eur. Phys. J. Web Conf.* **65** (2014) 01005.

[217] A. Giuliani et al., *A multi-isotope 0ν2β bolometric experiment*, *Eur. Phys. J. C* **78** (2018) 272.

[218] G. Ventura et al., *Thermal conductivity of the normal and superconducting Al/Si 1 % alloy*, *Nucl. Phys. B - Proc. Supp.* **61** (1998) 576.

[219] S. Sangiorgio, *Modellizzazione e ottimizzazione di rivelatori bolometrici per la ricerca del decadimento ββ0ν del ^{130}Te*, Master's thesis, Università degli studi di Milano, 2003.

[220] M. Pedretti et al., *Measurement of thermal properties for modeling and optimization of large mass bolometers*, *Physica B* **329** (2003) 1614.

[221] A. Alessandrello et al., *New experimental results on double beta decay of ^{130}Te*, *Phys. Lett. B* **486** (2000) 13.

[222] D. M. Chernyak et al., *Rejection of randomly coinciding events in $ZnMoO_4$ scintillating bolometers*, *Eur. Phys. J. C* **74** (2014) 2913.

[223] H. Spieler, *Semiconductor detector systems*. Oxford University Press, 2005.

[224] D. M. Chernyak et al., *Random coincidence of 2ν2β decay events as a background source in bolometric 0ν2β decay experiments*, *Eur. Phys. J. C* **72** (2012) 1989.

[225] A. Leder, *Measurement of quenched axial vector coupling constant in In-115 beta decay and its impact on future 0νββ searches*, June, 2018. Neutrino 2018, Heidelberg, Germany.

[226] M. Haaranen et al., *Spectrum-shape method and the next-to-leading-order terms of the β-decay shape factor*, *Phys. Rev. C* **95** (2017) 024327.

[227] C. Isaila et al., *Scintillation light detectors with Neganov-Luke amplification*, *Nucl. Instrum. Meth. A* **559** (2006) 399.

[228] J. Ouellet, *Latest results from the CUORE experiment*, June, 2018. Neutrino 2018, Heidelberg, Germany.

[229] G. J. Feldman and R. D. Cousins, *Unified approach to the classical statistical analysis of small signals*, *Phys. Rev. D* **57** (1998) 3873.

[230] D.-L. Fang et al., *Neutrinoless double-β decay of deformed nuclei within quasiparticle random-phase approximation with a realistic interaction*, *Phys. Rev. C* **83** (2011) 034320.

[231] A. Faessler et al., *Nuclear matrix elements for neutrinoless double-beta decay and double-electron capture*, *J. Phys. G: Nucl. Part. Phys.* **39** (2012) 124006.

[232] J. Suhonen and O. Civitarese, *Review of the properties of the 0νββ-nuclear matrix elements*, *J. Phys. G: Nucl. Part. Phys.* **39** (2012) 124005.

[233] J. Barea et al., *Nuclear matrix elements for double-β decay*, *Phys. Rev. C* **87** (2013) 014315.

[234] P. K. Rath et al., *Uncertainties in nuclear transition matrix elements for neutrinoless ββ decay within the Projected-Hartree-Fock-Bogoliubov model*, *Phys. Rev. C* **82** (2010) 064310.

[235] J. Menéndez et al., *Disassembling the nuclear matrix elements of the neutrinoless ββ decay*, *Nucl. Phys. A* **818** (2009) 139.

université PARIS-SACLAY | ÉCOLE DOCTORALE PHENIICS

Title: Sensitivity enhancement of the CUORE experiment via the development of Cherenkov hybrid TeO_2 bolometers
Keywords: neutrino physics, double beta decay, cryogenic detectors

CUORE is the first tonne-scale experiment searching for the neutrinoless double beta decay with TeO_2 bolometers. The discovery of this nuclear transition would have decisive consequences on the present physics scene. The following questions would find an answer: why is matter dominant in the Universe? which is the neutrino mass? has the neutrino a Majorana or a Dirac nature? This work presents two different approaches for the enhancement of the CUORE sensitivity with a view to its upgrade: the CUPID experiment. In the first part, a study of the thermal model describing NTD-based bolometers is presented with the objective to achieve a better comprehension of the response of the CUORE detectors. Bolometers are amazing detectors used for a large number of applications because of their impressive high performance, but their modelisation and simulation is far to be completely understood. Two measurements have been performed for an experimental evaluation of two thermal-model parameters: the glue and the electron-phonon conductances. In the second part, the possibility to detect the tiny Cherenkov light emitted by TeO_2 to reject α event — the main background of the CUORE experiment — is studied. The challenge consists in the detection of a 100-eV light signal with a NTD-based light detector that usually is characterised by a baseline noise of the order of 100 eV. This issue is solved with the employment of the Neganov-Trofimov-Luke (NTL) effect to lower the energy threshold of the light detector and improve its signal-to-noise ratio. This effect exploits the presence of an electric field to amplify bolometric thermal signals. The full rejection of the α background has been proved with one NTL-assisted photo-bolometer coupled to a CUORE-size TeO_2 bolometer. A convincing solution for the α background rejection has been demonstrated with a view to the CUPID experiment.

Title : Amélioration de la sensibilité de l'expérience CUORE par le développement de bolomètres de TeO_2 hybrides à lumière Cherenkov
Keywords : physique des neutrinos, double décroissance bêta, détecteurs cryogéniques

CUORE est la plus grande expérience qui recherche la double désintégration bêta sans neutrino avec des bolomètres de TeO_2. La découverte de cette transition nucléaire aurait des conséquences décisives sur la scène actuelle de la physique. Les questions suivantes trouveraient une réponse : pourquoi la matière est-elle dominante dans l'Univers? Quelle est la masse du neutrino? Le neutrino est il une particule de Majorana ou de Dirac? Ce travail présente deux approches différentes pour l'amélioration de la sensibilité de CUORE en vue de sa prochaine phase : CUPID. Dans la première partie de ce travail, une étude du modèle thermique pour les bolomètres équipés avec des NTDs est présentée dans le but de mieux comprendre la réponse des détecteurs de CUORE. Les bolomètres sont des détecteurs extraordinaires utilisés pour un grand nombre d'applications en raison de leurs performances remarquables, mais leur modélisation et leur simulation sont loin d'être complètement comprises. Deux mesures ont été effectuées pour évaluer expérimentalement deux paramètres du modèle thermique : la conductance de la colle et celle entre les électrons et les phonons. Dans la deuxième partie de ce travail, la possibilité de détecter la faible lumière Cherenkov émise par le TeO_2 est étudiée à fin de rejeter des événements α, le fond principal de l'expérience CUORE. Le défi consiste dans la détection d'un signal de lumière de 100 eV à moyen d'un détecteur équipé avec un NTD qui a normalement un bruit de l'ordre de 100 eV. Cette question peut être résolue grâce à l'effet Neganov-Trofimov-Luke (NTL) qui a permis de baisser le seuil du détecteur de lumière et d'améliorer son rapport signal-sur-bruit. Cet effet exploite la présence d'un champ électrique pour amplifier les signaux thermiques des bolomètres. Le rejet complet du fond α a été prouvé avec un photo-bolomètre amélioré par l'effet NTL et couplé à un bolomètre de TeO_2 comme ceux utilisés par CUORE. Une solution convaincante pour le rejet de fond α a été démontrée en vue de l'expérience CUPID.

Université Paris-Saclay
Espace Technologique / Immeuble Discovery
Route de l'Orme aux Merisiers RD 128 / 91190 Saint-Aubin, France